UNIVERSITAT POLITÈCNICA DE VALÈNCIA

I.U.I. CMT - CLEAN MOBILITY & THERMOFLUIDS
PhD program in Propulsion Systems for Transport

DOCTORAL THESIS:

"Study of oxy-fuel combustion-based power plants with in-situ O_2 production and carbon capture"

Presented by: D. Vitor Hugo Farias da Silva
Supervised by: Dr. Francisco José Arnau Martínez

in fulfillment of the requirements for the degree of

Doctor of Philosophy

Valencia, June 2024

Doctoral Thesis

"Study of oxy-fuel combustion-based power plants with in-situ O_2 production and carbon capture"

Presented by: D. Vitor Hugo Farias da Silva
Supervised by: Dr. Francisco José Arnau Martínez

THESIS EXAMINERS

Dr. D. José Martín Herreros Arellano
Dr. D. Chaitanya Yashvant Patil

DEFENSE COMMITTEE

Chairman: Dr. D. José Galindo Lucas
Secretary: Dr. Dña. Leonor Hernández López
Member: Dr. D. Chaitanya Yashvant Patil

Valencia, June 2024

Abstract

In recent years, a worldwide concern with respect to an increase in anthropogenic greenhouse gas emissions has pushed transport and energy industries towards the development of sustainable technologies with low or zero pollutant emissions from powerplants. Within this scenarios, oxy-fuel combustion arises as one of the most promising methods to mitigate the environmental footprint of powerplants, by eradicating their pollutant tailpipe emissions, in addition to enabling carbon dioxide (CO_2) capture from their flue gas. In this case, pure oxygen (O_2) is diluted with recirculated exhaust gas to react with fuel for the combustion process and, thereby, the exhaust stream, mainly composed of CO_2 and water vapor, may be subjected to elementary cooling and pressurizing steps for capturing high-purity CO_2 at ambient temperature.

Therefore, in this thesis, a self-sustaining oxy-fuel carbon-capture layout model is developed for a 2.2 liter turbocharged and direct-injection multi-cylinder compression ignition engine (CIE) as a feasibility demonstration of this proposed concept considering its potential application for development of zero-emission high-duty powerplants. In such circumstances, a mixed ionic-electronic conducting membrane is employed to generate O_2 from air in-situ. For this purpose, exhaust gas wasted energy is recovered via a tailored Brayton cycle in order to provide suitable conditions for proper membrane operation in terms of temperature and feed-permeate pressure ratio. Also, an in-situ carbon capture system (CC), composed essentially of two reciprocating compressors, three cooling units with liquid separation (flashes) and a CO_2 storage tank, is designed taking into account the flash out temperatures and operating pressure of the last CO_2 purification step.

Firstly, the oxy-fuel layout model with engine and its auxiliary components (heat exchangers and turbochargers) is designed and then assessed under oxy-fuel combustion conditions for the engine full-load curve from 1250 rpm to 3500 rpm in the absence of the CC, contrasting its outputs against the baseline conventional multi-cylinder CIE behavior. Secondly, the oxy-fuel powerplant load operation map is extended until system stability limits by modifying oxygen-fuel ratio and exhaust gas temperature for three engine speeds. Finally, the CC is designed and then coupled to the O_2 generation unit, recycling water and excess of O_2 from CC back to engine intake. In this regard, start of injection and recirculated water mass flow are swept in order to find out optimum operating point concerning the trade-off between powerplant performance and

additional cooling power at 3500 rpm.

Thereafter, the complete oxy-fuel carbon-capture layout model is enhanced and adapted for realistic application at laboratory scale and experimental proof of concept, following same trade-off philosophy. Although the final oxy-fuel carbon-capture engine layout presents slight deterioration in performance if compared to the baseline conventional multi-cylinder CIE at 3500 rpm, this proposed novel concept may be still energy-efficient competitive as an emerging technology which might contribute for conception of zero-emission powerplant on commercial industrial scale.

Keywords: Oxy-fuel combustion; Membrane; Energy recovery; Carbon capture; Water recirculation; Zero emissions

Resumen

En los últimos años, la preocupación mundial con el aumento de las emisiones antropogénicas de gases de efecto invernadero ha motivado a las industrias del transporte y la energía a moverse hacia el desarrollo de tecnologías sostenibles con bajas o nulas emisiones de contaminantes de plantas de generación de potencia. Con este escenario, la oxicombustión surge como uno de los métodos más prometedores para mitigar la huella ambiental de plantas de generación de potencia, al erradicar sus emisiones contaminantes del tubo de escape, además de permitir la captura de dióxido de carbono (CO_2) de sus gases producidos en la combustión. De esta manera, el oxígeno puro (O_2) se diluye con el gas de escape recirculado para que reaccione con el combustible en el proceso de combustión y, de este modo, la corriente de gases de escape, compuesta principalmente por CO_2 y vapor de agua, puede ser sometida a etapas elementales de enfriamiento y presurización para capturar CO_2 de alta pureza a temperatura ambiente.

Dado este contexto, en esta tesis, se desarrolla un modelo de sistema autosostenible a oxicombustión con captura de carbono para un motor policilíndrico de encendido por compresión (MEC) de 2,2 litros turboalimentado y de inyección directa como demostración de viabilidad de este concepto propuesto, considerando su aplicación potencial para el desarrollo de plantas de potencia de altas prestaciones con cero emisiones. En tales circunstancias, se emplea una membrana conductora mixta iónica-electrónica para generar O_2 a partir del aire local. Para ello, se recupera la energía residual de los gases de escape mediante un ciclo Brayton adaptado con el fin de proporcionar las condiciones adecuadas para el correcto funcionamiento de la membrana en términos de temperatura y relación de presión alimentación-permeado. Asimismo, se diseña un sistema de captura de carbono (CC) local, compuesto esencialmente por dos compresores alternativos, tres unidades de refrigeración con separación de líquidos (flashes) y un tanque de almacenamiento de CO_2, teniendo en cuenta las temperaturas de salida de los flashes y la presión de funcionamiento de la última etapa de purificación del CO_2.

En primer lugar, se diseña el modelo del sistema de oxicombustión con el motor y sus componentes auxiliares (intercambiadores de calor y turbocompresores) y, a continuación, el sistema es evaluado bajo condiciones de oxicombustión para la curva de plena carga del motor desde 1250 rpm hasta 3500 rpm en ausencia del CC, contrastando sus resultados con el comporta-

miento del MEC convencional de referencia. En segundo lugar, se amplía el mapa de funcionamiento de carga del motor de oxicombustión hasta los límites de estabilidad del sistema modificando el dosado oxígeno-combustible y la temperatura de los gases de escape para tres regímenes del motor. Por último, se diseña el CC y se lo acopla a la unidad de generación de O_2, reciclando el agua y el exceso de O2 del CC de nuevo a la admisión del motor. A este respecto, un barrido es llevado a cabo sobre el inicio de la inyección y el flujo másico de agua recirculada para encontrar el punto de funcionamiento óptimo a 3500 rpm con respeto a la compensación entre las prestaciones del motor y la potencia de refrigeración adicional.

A continuación, se mejora y adapta el modelo del sistema completo de oxicombustión con captura de carbono para una aplicación realista a escala de laboratorio y una prueba de concepto experimental, siguiendo la misma filosofía de compensación. Aunque el diseño final del motor de oxicombustión con captura de carbono presenta un ligero empeoramiento de prestaciones comparado con el MEC convencional de referencia a 3500 rpm, este nuevo concepto propuesto puede seguir siendo competitivo desde el punto de vista de la eficiencia energética como tecnología emergente que puede contribuir a la concepción de plantas de generación de potencia con emisiones cero a escala industrial comercial.

Resum

En els darrers anys, la preocupació mundial amb l'augment de les emissions antropogèniques de gasos d'efecte hivernacle ha motivat les indústries del transport i l'energia a moure's cap al desenvolupament de tecnologies sostenibles amb baixes o nul · les emissions de contaminants de plantes de generació de potència. Dins aquest escenari, l'oxicombustió sorgeix com un dels mètodes més prometedors per mitigar l'empremta ambiental de plantes de generació de potència, en eradicar les emissions contaminants del tub d'escapament, a més de permetre la captura de diòxid de carboni (CO_2) dels seus gasos produïts a la combustió. En aquest cas, l'oxigen pur (O_2) es dilueix amb el gas d'escapament recirculat perquè reaccioni amb el combustible en el procés de combustió i, així, el corrent de gasos d'escapament, compost principalment per chCO2 i vapor d'aigua, pot ser sotmesa a etapes elementals de refredament i pressurització per capturar CO_2 d'alta puresa a temperatura ambient.

Per tant, en aquesta tesi, es desenvolupa un model de sistema autosostenible a oxicombustió amb captura de carboni per a un motor policilíndric d'encesa per compressió (MEC) de 2,2 litres turboalimentat i d'injecció directa com a demostració de viabilitat d'aquest. concepte proposat, considerant-ne l'aplicació potencial per al desenvolupament de plantes de potència d'altes prestacions amb zero emissions. En aquestes circumstàncies, es fa servir una membrana conductora mixta iònica-electrònica per generar O_2 a partir de l'aire local. Per això, es recupera l'energia residual dels gasos d'escapament mitjançant un cicle Brayton adaptat per tal de proporcionar les condicions adequades per al funcionament correcte de la membrana en termes de temperatura i relació de pressió alimentació-permeat. Així mateix, es dissenya un sistema de captura de carboni (CC) local, compost essencialment per dos compressors alternatius, tres unitats de refrigeració amb separació de líquids (flaixos) i un tanc d'emmagatzematge de CO_2, tenint en compte les temperatures de sortida dels flaixos i la pressió de funcionament de l'última etapa de purificació del CO_2.

En primer lloc, es dissenya el model del sistema d'oxicombustió amb el motor i els seus components auxiliars (intercanviadors de calor i turbocompressors) i, a continuació, el sistema és avaluat sota condicions d'oxicombustió per a la corba de plena càrrega del motor des de 1250 rpm fins a 3500 rpm en absència del CC, contrastant els seus resultats amb el comportament del MEC convencional de referència. En segon lloc, s'amplia el mapa de funci-

onament de càrrega del motor d'oxicombustió fins als límits d'estabilitat del sistema modificant el dosatge oxigen-combustible i la temperatura dels gasos d'escapament per a tres règims del motor. Finalment, es dissenya el CC i l'acobla a la unitat de generació de O_2, reciclant l'aigua i l'excés de O2 del CC de nou a l'admissió del motor. Referent a això, un escombrat és dut a terme sobre l'inici de la injecció i el flux màssic d'aigua recirculada per trobar el punt de funcionament òptim a 3500 rpm amb respecte a la compensació entre les prestacions del motor i la potència de refrigeració addicional.

A continuació, es millora i s'adapta el model del sistema complet d'oxicombustió amb captura de carboni per a una aplicació realista a escala de laboratori i una prova de concepte experimental, seguint la mateixa filosofia de compensació. Tot i que el disseny final del motor d'oxicombustió amb captura de carboni presenta un lleuger empitjorament de prestacions comparat amb el MEC convencional de referència a 3500 rpm, aquest nou concepte proposat pot continuar sent competitiu des del punt de vista de l'eficiència energètica com a tecnologia emergent que pot contribuir a la concepció de plantes de generació de potència amb emissions zero a escala industrial comercial.

List of publications

Vitor Hugo Farias da Silva is co-author of the publications exposed in this section, with the supervision of other members of the I.U. CMT-Clean Mobility and Thermofluids (CMT). The origin of these publications were the research activities performed during the candidate's doctorate, which was supervised by Prof. Francisco José Arnau Martínez, oriented and discussed with the other co-authors of the papers. The respondent carried out several research activities, which were analyzed and processed in order to back up the studies and assumptions pretended, as well as the development of models presented in the publications. The analysis and discussion of results and procedures were done in collaboration with the thesis director (Prof. Francisco José Arnau Martínez) and with the co-authors of each publication. Each author's contribution to each study is specified in the "contributions description section" in the different studies. Any requirement to guarantee the fulfilment of the Ph.D. works, such as materials, software licenses and test benches were provided by the UPV and CMT.

The results of all these works have been compiled, ordered, completed, and further discussed in the present thesis manuscript. All parts, analyses, or conclusions from these or whatever other publications, have been appropriately referred along with the paper. Nevertheless, for the sake of readiness and to protect the thesis writing style, the publications of this list may not have been specifically cited every time, as part of the contents, figures and discussions have been directly imposed from my publications. This disclaimer corrects, compensates, and justifies the fact that being the PhD candidate, the experimental work of my thesis and the origin of the innovation component have resulted in the publications mentioned in this section, therefore compiling my thesis.

The PhD candidate is always the last signer of the CMT members in every publication since the protocol among CMT members is signing by seniority order, first the doctors, and last the PhD candidate.

[1] J. Serrano, F. Arnau, L. García-Cuevas, and V. Farias. "Oxy-fuel combustion feasibility of compression ignition engines using oxygen separation membranes for enabling carbon dioxide capture". *Energy Conversion and Management* 247 (Nov. 2021), p. 114732. DOI: 10.1016/j.enconman.2021.114732

[2] F. Arnau, G. Bracho, L. García-Cuevas, and V. Farias. "A strategy to extend load operation map range in oxy-fuel compression ignition engines with oxygen separation membranes". *Applied Thermal Engineering* 226 (2023), p. 120268. ISSN: 1359-4311. DOI: https://doi.org/10.1016/j.applthermaleng.2023.120268. URL: https://www.sciencedirect.com/science/article/pii/S1359431123002971

[3] J. Luján, F. Arnau, P. Piqueras, and V. Farias. "Design of a carbon capture system for oxy-fuel combustion in compression ignition engines with exhaust water recirculation". *Energy Conversion and Management* 284 (May 2023), p. 116979. DOI: 10.1016/j.enconman.2023.116979

Acknowledgments

In first place, words can not express my gratitude to God, to whom I owe everything in my life. In fact, he has always been my fundamental support and aim behind everything I have been done in all circumstances of my life.

Additionally, this endeavor would not have been possible without my parents Paulo and Vera, my brother Joao Paulo, my nephews Pietro and Lorenzo, my sister-in-law Natacha, and all my family members. Their belief in me has kept my spirit high during this enjoyable journey. Indeed, they have been a great source of motivation in personal and professional aspects.

I would specially like to thank my wife Beatriz since, even though she was pregnant of our first son, she has stood by me the whole time and helped me in a lot os ways for finalizing my thesis, mainly during my last year in which I started to work in a company and write my thesis manuscript at same time.

Finally, I wish to thank Dr. Francisco José Arnau Martínez and Dr. José Ramón Serrano Cruz for their precious time and dedication in sharing their knowledge and guidance through the sinuous path that has been this thesis. I feel very blessed indeed to have been given the chance to work and learn with them. And, of course, I would also like to thank all the staff in CMT-Clean Mobility and Thermofluids and my Ph.D student mates that made of this great researching institute my home for three years. At last, the Ph.D. candidate has been funded by Generalitat Valenciana, Spain (GRISOLIAP/2020/078).

Valencia, April 2024.

"The things that we love tell us what we are."

Thomas Aquinas

Contents

List of Tables

List of Figures

List of symbols

Latin characters

A	Pre-exponential Factor of the Oxygen Mass Transfer	$mol \cdot m^{-1} \cdot K^{-1} \cdot s^{-1}$
c_p	Specific Molar Heat Capacity at Constant Pressure	$J \cdot mol^{-1} \cdot K^{-1}$
E_a	Activation Energy of the Oxygen Mass Transfer	$J \cdot mol^{-1}$
F	Molar Flow	$mol \cdot s^{-1}$
h	Specific Molar Enthalpy	$J \cdot mol^{-1}$
H	Sensible Enthalpy	kW
HR	Heat Released by Combustion	kW
J_{O_2}	Molar Flux of Oxygen	$mol \cdot m^{-2} \cdot s^{-1}$
k_{ij}	Binary Interaction Parameter between Species i and j	
L	Membrane Thickness	m
$\dot{m}$	Mass Flow	$kg \cdot s^{-1}$
$\dot{m}^*$	Mass Flow per Engine Cycle	$kg \cdot s^{-1} \cdot rpm^{-1}$
n	Number of Components	
P	Pressure	Pa
P_{feed,O_2}	Oxygen Partial Pressure at Feed Side	Pa
$P_{permeate,O_2}$	Oxygen Partial Pressure at Permeate Side	Pa
Q	Heat Power	kW
R	Universal Gas Constant	$J \cdot mol^{-1} \cdot K^{-1}$
T	Temperature	K
v	Molar Volume	$m^3 \cdot mol^{-1}$
x	Liquid Mole Fraction	
y	Vapor Mole Fraction	
z	Overall Mole Fraction	

Greek characters

γ	Heat capacity ratio
λ	Oxygen–fuel Equivalence Ratio
ω	Acentric Factor
ϕ	Fugacity Coefficient
σ, ε, Ω, Ψ	Constants for Cubic Equations of State

ζ	Vapor Mole Ratio

Sub- and Superscripts

0	Reference Condition
$air, in, MIEC$	MIEC Feed Side Inlet
$air, in, system$	System Air Inlet
c	Critical Point
$C-1$	Cooler C-1
dew	Dew Point
exh	Exhaust gas
htw	Convective Heat Losses at Cylinder Walls
i	Component i
in	Inlet Condition
liq	Liquid Phase
$MIEC, real$	Heat Transferred to Air from System Entry until MIEC Feed Side Inlet
out	Outlet Condition
$pipes$	Convective Heat Losses at Exhaust Pipes
r	Reduced Variable
vap	Vapor Phase

Acronyms

0D	Zero Dimensional
3D	Three Dimensional
ACT	Apparent Combustion Time
BSCF	$Ba_{0.5}Sr_{0.5}Co_{0.8}Fe_{0.2}O_{3-\delta}$ Membrane
BSFC	Brake Specific Fuel Consumption
BPV	Back Pressure Valve
CAD	Crank Angle Degree
CAS	Cryogenic Air Separation
CC	Carbon Capture
CFD	Computational Fluid Dynamics
CIE	Compression Ignition Engine
CO	Carbon Monoxide
CO_2	Carbon Dioxide
CR	Compression Ratio

CS	Control System
EGR	Exhaust Gas Recirculation
EOS	Equation of State
Exp	Experimental Data
GHG	Greenhouse Gas Emission
HE	Heat Exchanger
HEN	Heat Exchange Network
HRL	Heat Released Law
ICE	Internal Combustion Engine
MIEC	Mixed Ionic-Electronic Conducting Membrane
Mod	Model Data
N_2	Nitrogen
NO_x	Nitrogen Oxides
O_2	Oxygen
OC	Oxidation Catalyst
PID	Proportional-Integral-Derivative Controller
PMEP	Pumping Mean Effective Pressure
PR	Peng-Robinson
RK	Redlich-Kwong
SC	Single Cylinder
SIE	Spark Ignition Engine
SOC	Start of Combustion
SOI	Start of Injection
SRK	Soave-Redlich-Kwong
TF	Flash Outlet Temperature
VEMOD	Virtual Engine Model
VLE	Vapor-Liquid Equilibrium
VGT	Variable Geometry Turbocharger
WIC	With a Cooler before Intake Manifold
WIR	With Water Recirculation
WMF	Water Mass Flow
WOC	Without a Cooler before Intake Manifold
WOR	Without Water Recirculation

Chapter 1

Introduction

Contents

1.1 Background

Currently, as emission regulation standards are increasingly getting stricter regarding anthropogenic greenhouse gas (GHG) release into atmosphere, many of the main governments and industry stakeholders around the world are looking for new technological solutions based on sustainable development. Indeed, total GHG emissions have ramped up 0.4 gigatonnes of carbon dioxide (CO_2) equivalents (1.3%) per year from 1970 to 2000, and achieving a increment of 2.2% per year over 2000 to 2010. Likewise, around 78% of those total GHG emissions during that period corresponds to CO_2 emissions from industrial processes and fossil fuel combustion [4]. Also, the global monitoring laboratory estimated in the latest published CO_2 emission data in 2022 that the CO_2 atmospheric concentration is approximately 417 parts per million (ppm) with a constant growth trend over past few decades [5]. In order to illustrate that concern, the European Union has defined ambitious targets for 2030 such as at least 40% cuts in GHG emissions with at least 32.5% improvement in energy efficiency [6].

Also, one of the main global objectives is to improve the life in cities reducing harmful emissions (CO, HC, NOx, particulate matter, etc) which causes local air quality deterioration. Among the indicated substances, nitrogen oxides NOx emissions are generated due to the presence of N_2 in the air, usually used as oxidizer in combustion processes, and the high temperatures reached in the combustion chamber that facilitate its oxidation [7]. However, NOx may lead to harsh respiratory effects including asthma and airway inflammation. In fact, NOx may combine with volatile organic compounds (VOC), ammonia and other substances to form fine particles which may penetrate into deep parts of the lung causing respiratory diseases like bronchitis and emphysema. In addition, ground-level ozone, which is formed from VOC-NOx reaction in stagnant air and sunlight, may block pollution from escaping to higher atmosphere [8].

As shown in Figure 1.1, around 25% of the world's power is provided by internal combustion engines (ICE) operating with fossil fuel oil, generating around 10% of the world's GHGs [9]. The transport sector represents almost 25% of Europe's GHGs and the road transport constitutes the most considerable amount of overall transport emissions (it emitted more than 70 % of all domestic and international transport GHG in 2019) [10] [11]. Moreover, road transport dominates overall emissions from global transport sector with

conventional engines in automobiles emitting approximately 4.6 metric tons of CO_2 per year [12]. Besides that, European Environment Agency states that the major sources of NOx emissions were energy production and distribution (23%) and road transport (41%) in 2011 [13].

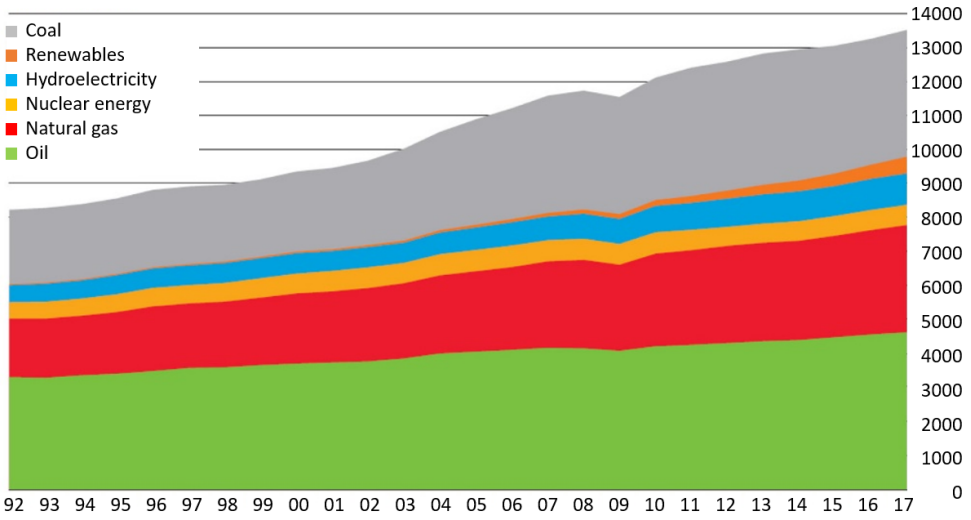

Figure 1.1: World energy consumption by source (millions of Petroleum equivalent) from 1992 to 2017. About 70% of fossil oil is consumed in ICEs [9].

Thus, effective low-zero-emission solutions are claimed to reduce GHG and NOx emissions from ICEs and powerplants such as system adaptation to fuel-cell, hybrid electric and solar-powered arrangements, synthesis of e-fuels (synthetic fuel with low environmental impact), and development of carbon capture (CC) technologies [14] [15] [16].

1.2 Motivation

Each of those low-zero solutions has its conveniences and drawbacks. Nevertheless, in order to utterly eradicate CO_2 emissions from ICEs to atmosphere, low-cost and sustainable alternatives are necessary. Thus, CC technologies have a high potential to reach net-zero emissions still enabling the use of fossil fuels and, thereby, not being affected by electricity supply limitations [17]. Indeed, fossil fuel-fired power stations and coal-fired integrated gasification

combined cycle plants have envisaged carbon capture solutions to cut CO_2 emissions applying pre-combustion, post-combustion and oxy-fuel combustion CO_2 capture methods. In the pre-combustion approach, CO_2 is removed from fuel prior to combustion generating syngas in natural gas reforming or coal gasification processes. In contrast, post-combustion method relates to CO_2 capture from the exhaust gas after fuel-air combustion. In the oxy-fuel combustion concept, the fuel is burnt in a highly oxygen-enriched nitrogen-free environment to facilitate the CO_2 capture from exhaust gas by essentially condensing the water vapor [18] [19].

Regarding the latter, oxy-fuel combustion arises as one of the most promising strategies to achieve net-zero emissions without huge reduction in energy conversion efficiency and useful power supply [7]. When considering its application to ICEs, as in-chamber temperature achieved in pure-oxygen combustion could be much higher than in standard air operation, exhaust gas recirculation (EGR) should be used to dilute oxygen (O_2), preventing overheating issues [20] [21]. Furthermore, once nitrogen (N_2) is not present at intake gas, NO_x emissions may be entirely eliminated and the trade-off in combustion optimization between NOx and particle matter control disappears. Consequently, sophisticated-and-expensive NO_x after-treatment systems may be completely removed. Besides, as engine may be operated in learn burn conditions (the fuel is burned with excess of O_2), CO and soot emissions could be virtually eliminated and, thereby, combustion products are mainly CO_2 and H_2O.

Nowadays, oxy-fuel combustion is mainly mature in large-scale power generation plants, but at the cost of penalizing the process thermal efficiency [22] by using cryogenic air separation (CAS) units to generate O_2. In fact, that system involves a relevant energy penalty and a high capital investment which complicates its proximity to market [23] [24]. Also, other industrial segments are evaluating the usage of oxy-fuel combustion for their processes such as refining industry [25], biomass-fired power plants [26] and cement production [27]. Considering means-of-transport engines, the pure-O_2 acquisition is one of the main obstacles for the oxy-fuel combustion implementation since it requires more complex and high-priced systems to supply a high-purity O_2 on board. Moreover, the off-board O_2 acquisition may not be a profitable solution for the industry due to storage and transport costs, and especially for the transport sector, that would entail an huge increment of weight in vehicles leading to a fuel consumption deterioration.

In such a context, oxygen transport membranes such as mixed ionic-electronic

conducting membranes (MIECs), appear as an alternative to CAS, since they achieve economic saving of 10.5-17.5% and energy consumption reduction of 0.5-9% compared to CAS [24]. Despite some challenges in the MIEC pathway towards industrial production due to some chemical and thermal stability issues under extreme environments [28] [29], growing breakthrough in performance of membranes indicates its potential application for in-situ and low-cost O_2 generation [30]. The MIEC transports O_2 from the feed side to the permeate one by way of temperature and a partial pressure gradient between both sides, so O_2 molecules are adsorbed onto a porous, electrically conductive coating and dissociated into O_2 ions, which are transported through the non-porous electrolyte [31]. Once O_2 ions have reached the permeate side, they recombine to form O_2 molecules and desorb from the membrane surface. Moreover, electrons are transported at the same time in the opposite direction to keep the electrical neutrality of the MIEC [32]. Besides, sweep gas may be employed to heat up the MIEC and reduce the O_2 partial pressure at permeate side, improving O_2 transport driving force (Figure 1.2). Thus, MIECs appear as a reasonable approach for in-situ O_2 separation in ICE using the flue gas as a sweep gas at permeate side and exploiting its waste heat to produce enough temperature and pressure on MIEC feed side to generate the O_2 necessary for proper engine operation under oxy-fuel combustion environment.

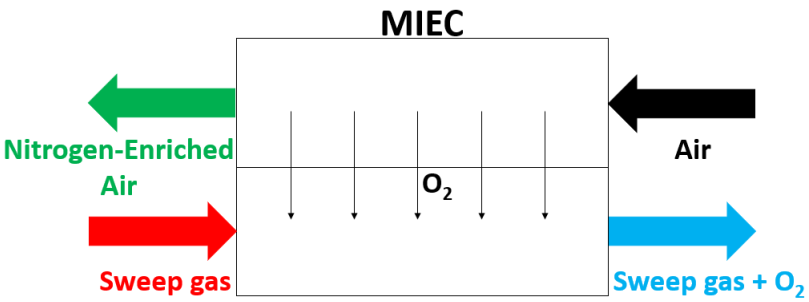

Figure 1.2: Macroscopic schematic representation of O_2 permeation through MIEC

Some approaches have been evaluated through experimental and modeling assessments to control combustion process in oxy-fuel spark ignition engines (SIEs) and compression ignition engines (CIEs) in order to maximize engine efficiency and minimize emissions [33] [34]. Most of those approaches are entrenched in actuating on process key variables such as EGR [35], O_2 concentration [36], supplement fuel [37], compression ratio (CR) [38] and water injection [39] [40]. Thus, some of those techniques may be also exploited in

oxy-fuel ICEs considering membrane-based on-site O_2 generation and CC to achieve zero-emissions without high penalties in system efficiency.

1.3 Objectives

The main objective of the current work is to highlight the high feasibility potential of MIEC-based oxy-fuel combustion in ICEs/powerplants to enable CC and eliminate NO_x, H_xC_y, CO and soot emissions. For this purpose, an automotive multi-cylinder CIE is considered to evaluate this technology, which may be also applicable to engines for power generation and in heavy-duty vehicles such as ships, trains and trucks. In this scenario, a conventional turbocharged CI engine model validated with an experimental campaign carried out at CMT Researching Institute is used as baseline to build up a oxy-fuel combustion layout with on-site O_2 generation and a CC system. Therefore, the sub-objectives may be summarized as follows:

- Adaptation of an in-house calculation system for predicting real gas behavior within this thesis scope.
- Development of an oxy-fuel engine layout with integrated MIEC and exhaust gas wasted-energy recovery system for on-site O_2 generation.
- Assessment of the proposed oxy-fuel engine layout operating map in order to find out system limitations and demonstrate its feasibility.
- On-site CC system development and integration into the oxy-fuel engine layout.
- Assessment of the carbon-capture oxy-fuel engine layout at maximum-power operating point and tentative system adaption for prototype construction.

1.4 Thesis outline

The main content of this thesis is distributed into 7 chapters which are described bellow:

- In the current chapter 1, global scenario is presented regarding emissions from ICEs and their environmental impacts. Also, the need for zero-low emission solutions is outlined and, hence, oxy-fuel combustion with on-site O_2 production and CC is proposed to fight GHG emissions and air quality deterioration caused by ICEs operation.

- State of the art and literature review about oxy-fuel combustion for net-zero emissions in ICEs are included in chapter 2. Moreover, a brief review of previous works regarding O_2 generation methods, mainly using O_2 separation membranes, is discussed. In addition, current CC approaches related to oxy-fuel combustion are described. Finally, some methods for engine control under oxy-fuel combustion conditions are presented considering CIEs and SIEs.

- In chapter 3, the oxy-fuel CIE model with MIEC-based O_2 generation is built up and studied. In this case, exhaust gas wasted energy is recovered for producing O_2 needed for engine operation by heating up the MIEC, and two types of EGR control systems (CS), used to regulate the in-cylinder temperature, are compared. Furthermore, a virtual engine model is employed in this study to build and analyze the proposed oxy-fuel engine model, which has its baseline version calibrated with experimental data. Thus, the engine and its auxiliary components (turbochargers and heat exchangers) are assessed under oxy-fuel combustion conditions for the engine full load operation points from 1250 rpm to 3500 rpm.

- A strategy is proposed in chapter 4 to extend the load operation map range of the oxy-fuel engine model defined in chapter 3. The strategy consists of modifying exhaust gas temperature (T_{exh}) and oxygen-fuel equivalence ratio (λ), generating temperature-lambda maps to decide the optimal combination in terms of engine performance. Thus, the system behavior is analyzed at three engine speeds (1250 rpm, 2500 rpm and 3500 rpm) with different load levels and CR of 20. Furthermore,

specific parameters are investigated to verify whether the system produces enough energy to heat up the MIEC, generating the necessary O_2. Indeed, a few of them have been found very useful as design parameters for finding out oxy-fuel engine operation limits and estimating MIEC design features.

- In chapter 5, a CC system is connected to the oxy-fuel engine layout studied in chapter 4 at its tailpipe outlet. Therefore, the carbon capture system is designed considering flash-out temperatures and operating pressure of the last CO_2 purification step. The additional cooling power required by the system is also contemplated. In addition, a mixer model is developed to recirculate part of the water condensed in the carbon capture unit towards the cylinder inlet to lower the intake gas temperature and increase the oxidizer heat capacity ratio (γ). From this layout, an optimum setup for SOI and recirculated water mass flow is found considering the trade-off between additional cooling power and engine performance at full-load 3500 rpm.
- The carbon-capture oxy-fuel layout developed in chapter 5 is more detailed and specified in chapter 6 taking into account more realistic operating conditions at full-load 3500 rpm in preparation for an upcoming setting-up of a prototype. Thus, the combustion model is improved and the reciprocating compressors are directly modeled in VEMOD for considering the system wave dynamic during the CO_2 capture. Moreover, the recirculating flows from CC unit to oxy-fuel layout are redesigned in order to simplify the system.
- chapter 7 summarizes the main findings and conclusions present in this PhD dissertation. In addition, potential studies and future works are pointed out in the aim of carrying out an experimental campaign for a carbon-capture oxy-fuel ICE prototype.

Chapter 1 Bibliography

[4] I. P. on Climate Change. *AR5 Climate Change 2014: Mitigation of Climate Change*. URL: https://www.ipcc.ch/report/ar5/wg3/ (cit. on p. 2).

[5] G. M. Laboratory. *Trends in Atmospheric Carbon Dioxide*. URL: https://gml.noaa.gov/ccgg/trends/global.html# (cit. on p. 2).

[6] E. Commission. *2030 climate and energy framework in European Union*. URL: https://ec.europa.eu/clima/policies/strategies/2030_en (cit. on p. 2).

[7] B. Buhre, L. Elliott, C. Sheng, R. Gupta, and T. Wall. "Oxy-fuel combustion technology for coal-fired power generation". *Progress in Energy and Combustion Science* 31 (Dec. 2005), pp. 283–307. DOI: 10.1016/j.pecs.2005.07.001 (cit. on pp. 2, 4).

[8] A. D. of Environmental Quality. *Nitrogen Oxide Pollution*. URL: https://azdeq.gov/nitrogen-oxide-nox-pollution#:~:text=The%20nitrogen%20oxides%20family%20can,disease%2C%20leading%20to%20premature%20death. (cit. on p. 2).

[9] R. D. Reitz et al. "IJER editorial: The future of the internal combustion engine". *International Journal of Engine Research* 21.(1) (2020), pp. 3–10. DOI: 10.1177/1468087419877990. URL: https://doi.org/10.1177/1468087419877990 (cit. on pp. 2, 3).

[10] European Commission. *An european strategy for low-emission mobility*. URL: https://ec.europa.eu/clima/policies/transport_en#tab-0-0 (cit. on p. 2).

[11] E. E. Agency. *Greenhouse Gas Emissions from Transport in Europe*. URL: https://www.eea.europa.eu/ims/greenhouse-gas-emissions-from-transport (cit. on p. 2).

[12] United States Environmental Protection Agency. *Greenhouse gas emissions from a typical passenger vehicle*. URL: https://www.epa.gov/greenvehicles/greenhouse-gas-emissions-typical-passenger-vehicle (cit. on p. 3).

[13] E. E. Agency. *Nitrogen Oxides Emissions*. URL: https://www.eea.europa.eu/data-and-maps/indicators/eea-32-nitrogen-oxides-nox-emissions-1/assessment.2010-08-19.0140149032-3 (cit. on p. 3).

[14] R. Babayev, A. Andersson, A. Dalmau, H. Im, and B. Johansson. "Computational optimization of a hydrogen direct-injection compression-ignition engine for jet mixing dominated nonpremixed combustion". *International Journal of Engine Research* 23.(5) (Dec. 2021), pp. 754–768. DOI: 10.1177/14680874211053556 (cit. on p. 3).

[15] M. S. Wooldridge, R. Singh, L. G. Gutierrez, and S. Clancy. "Survey of strategies to reduce cold-start particulate, CO, NOx,and hydrocarbon emissions from direct-injection spark-ignition engines". *International Journal of Engine Research* (2022). DOI: 10.1177/14680874211068576. URL: https://doi.org/10.1177/14680874211068576 (cit. on p. 3).

[16] J. V. Pastor, J. M. García-Oliver, C. Micó, and A. Garcia. "An experimental study with renewable fuels using ECN spray A and D nozzles". *International Journal of Engine Research* (July 2021), p. 146808742110312. DOI: 10.1177/14680874211031200 (cit. on p. 3).

[17] S. Bouzalakos and M. Maroto-Valer. "Overview of carbon dioxide (CO2) capture and storage technology". In: vol. 2. June 2010, pp. 1–24. ISBN: 1 84569 533 X. DOI: 10.1533/9781845699574.1 (cit. on p. 3).

[18] X. Li, Z. Peng, T. Ajmal, A. Aitouche, R. Mobasheri, Y. Pei, B. Gao, and M. Wellers. "A feasibility study of implementation of oxy-fuel combustion on a practical diesel engine at the economical oxygen-fuel ratios by computer simulation". *Advances in Mechanical Engineering* 12 (Dec. 2020), p. 168781402098018. DOI: 10.1177/1687814020980182 (cit. on p. 4).

[19] M. Kanniche, R. Gros-Bonnivard, P. Jaud, J. Valle-Marcos, J.-M. Amann, and C. Bouallou. "Pre-combustion, Post-combustion and Oxy-combustion in thermal power plant for CO capture". *Applied Thermal Engineering* 30 (Jan. 2010), pp. 53–62. DOI: 10.1016/j.applthermaleng.2009.05.005 (cit. on p. 4).

[20] M. Pamminger, W. Buyu, C. Hall, R. Vojtech, and T. Wallner. "The impact of water injection and exhaust gas recirculation on combustion and emissions in a heavy-duty compression ignition engine operated on diesel and gasoline". *International Journal of Engine Research* 21 (Jan. 2019), pp. 1555–1573. DOI: 10.1177/1468087418815290 (cit. on pp. 4, 17).

[21] R. Mobasheri and S. Khabbaz. "Modeling the Effects of High EGR Rates in Conjunction with Optimum Multiple Injection Techniques in a Heavy Duty DI Diesel Engine". *SAE Technical Papers* 1 (Apr. 2014). DOI: 10.4271/2014-01-1124 (cit. on pp. 4, 17).

[22] A. Simpson and A. Simon. "Second law comparison of oxy-fuel combustion and post-combustion carbon dioxide separation". *Energy Conversion and Management* 48 (Nov. 2007), pp. 3034–3045. DOI: 10.1016/j.enconman.2007.06.047 (cit. on p. 4).

[23] C. N. del Medio Ambiente CONAMA 10. *CAPTURA Y ALMACENAMIENTO DE CO_2*. URL: http://www.conama10.conama.org/conama10/download/files/GTs\%202010/2_final.pdf (cit. on p. 4).

[24] E. Portillo, B. Alonso-Fariñas, F. Vega, M. Cano, and B. Navarrete. "Alternatives for oxygen-selective membrane systems and their integration into the oxy-fuel combustion process: A review". *Separation and Purification Technology* 229 (June 2019), p. 115708. DOI: 10.1016/j.seppur.2019.115708 (cit. on pp. 4, 5, 22).

[25] A. Escudero, S. Espatolero, and L. Romeo. "Oxy-combustion power plant integration in an oil refinery to reduce CO_2 emissions". *International Journal of Greenhouse Gas Control* 45 (Feb. 2016), pp. 118–129. DOI: 10.1016/j.ijggc.2015.12.018 (cit. on pp. 4, 16).

[26] X. Wei, V. Manovic, and D. Hanak. "Techno-economic assessment of coal-or biomass-fired oxy-combustion power plants with supercritical carbon dioxide cycle". *Energy Conversion and Management* 221 (July 2020), p. 113143. DOI: 10.1016/j.enconman.2020.113143 (cit. on p. 4).

[27] F. Carrasco Maldonado, R. Spörl, K. Fleiger, V. Hoenig, J. Maier, and G. Scheffknecht. "Oxy-fuel combustion technology for cement production - State of the art research and technology development". *International Journal of Greenhouse Gas Control* 45 (Feb. 2016), pp. 189–199. DOI: 10.1016/j.ijggc.2015.12.014 (cit. on pp. 4, 16).

[28] A. Leo, S. Liu, and J. Costa. "Development of mixed conducting membranes for clean coal energy delivery". *International Journal of Greenhouse Gas Control* 3 (July 2009), pp. 357–367. DOI: 10.1016/j.ijggc.2008.11.003 (cit. on p. 5).

[29] S. Hashim, A. Mohamed, and S. Bhatia. "Oxygen separation from air using ceramic-based membrane technology for sustainable fuel production and power generation". *Renewable and Sustainable Energy Reviews* 15 (Feb. 2011), pp. 1284–1293. DOI: 10.1016/j.rser.2010.10.002 (cit. on p. 5).

[30] R. Kriegel, L. Kiesel, R Kircheisen, and U Pippardt. "Performance of various Archetypes of Oxygen Membranes for local Oxygen Supply." In: *DKG-Jahrestagung, 10. München*. Apr. 2018, p. 10. DOI: 10.13140/RG.2.2.16996.83842 (cit. on p. 5).

[31] F. Wu, M. Argyle, P. Dellenback, and M. Fan. "Progress in O_2 separation for oxy-fuel combustion–A promising way for cost-effective CO_2 capture: A review". *Progress in Energy and Combustion Science* 67 (July 2018), pp. 188–205. DOI: 10.1016/j.pecs.2018.01.004 (cit. on pp. 5, 23).

[32] A. Arratibel, A. Labella, Y. Liu, N. Porras, D. Tanaka, M. Annaland, and F. Gallucci. "Mixed Ionic-Electronic Conducting Membranes (MIEC) for Their Application in Membrane Reactors: A Review". *Processes* 7 (Mar. 2019), p. 128. DOI: 10.3390/pr7030128 (cit. on p. 5).

[33] X. Li, Z. Peng, Y. Pei, T. Ajmal, K. Rana, A. Aitouche, and R. Mobasheri. "Oxy-fuel combustion for carbon capture and storage in internal combustion engines – A review". *International Journal of Energy Research* 46 (Aug. 2021), pp. 505–522. DOI: 10.1002/er.7199 (cit. on pp. 5, 16, 18, 21).

[34] X. Li, Y. Pei, Z. Peng, T. Ajmal, K.-J. Rana, A. Aitouche, and R. Mobasheri. "Numerical study on the effects of intake charge on oxy-fuel combustion in a dual-injection spark ignition engine at economical oxygen-fuel ratios". *International Journal of Engine Research* 23 (May 2021). DOI: 10.1177/14680874211022292 (cit. on pp. 5, 18).

[35] A. Van Blarigan, D. Kozarac, R. Seiser, R. Cattolica, J.-Y. Chen, and R. Dibble. "Experimental Study of Methane Fuel Oxycombustion in a Spark-Ignited Engine". *Journal of Energy Resources Technology* 136 (Mar. 2013), p. 9. DOI: 10.1115/1.4024974 (cit. on pp. 5, 18, 46).

[36] Z. Wu, Z. Kang, D. Jun, H. Zongjie, and L. Li. "Effect of oxygen content on n-heptane auto-ignition characteristics in a HCCI engine". *Applied Energy* 184 (Dec. 2016). DOI: 10.1016/j.apenergy.2016.10.050 (cit. on p. 5).

[37] H.-W. Wu, R.-H. Wang, Y.-C. Chen, D.-J. Ou, and T.-Y. Chen. "Influence of port-inducted ethanol or gasoline on combustion and emission of a closed cycle diesel engine". *Energy* 64 (Jan. 2013). DOI: 10.1016/j.energy.2013.11.027 (cit. on pp. 5, 20, 21, 25).

[38] Y. Gao, L. Li, X. Yu, J. Deng, and Z. Wu. "Effect of Compression Ratio on Internal Combustion Rankine Cycle Based on Simulations". In: vol. 328. Jan. 2015, pp. 129–138. ISBN: 978-3-662-45042-0. DOI: 10.1007/978-3-662-45043-7_14 (cit. on p. 5).

[39] Z. Kang, S. Chen, Z. Wu, J. Deng, Z. Hu, and L. Li. "Simulation Study of Water Injection Strategy in Improving Cycle Efficiency Based on a Novel Compression Ignition Oxy-Fuel Combustion Engine". *SAE International Journal of Engines* 11 (Apr. 2018). DOI: 10.4271/2018-01-0894 (cit. on pp. 5, 20, 21, 46).

[40] R. Bilger and Z. Wu. "Carbon Capture for Automobiles Using Internal Combustion Rankine Cycle Engines". *Journal of Engineering for Gas Turbines and Power* 131 (May 2009), p. 034502. DOI: 10.1115/1.3077657 (cit. on pp. 5, 21, 25).

Chapter 2

State of the art

Contents

2.1 Mature oxy-fuel combustion technologies and applications

The oxy-fuel combustion may be defined as a process in which the fuel is burnt with highly oxygen-enriched ambient without N_2, preventing NOx emissions and facilitating the CO_2 capture from flue gas. In 1982, Abraham et al. were the first ones to propose the oxy-fuel combustion concept which was focused on enhanced oil recovery (EOR) removing the CO_2 purification required in flue gases recovery [41]. Currently, the oxy-fuel combustion technology is especially applied to thermal power generation industry focused on coal-fired power plant [42] [43] [44] and high-velocity oxy-fuel coating processes [45]. Moreover, its usage is assessed to be employed for refining sector [25] and cement production [27]. By way of illustration, Figure 2.1 shows a typical oxy-fuel combustion configuration applied to power generation with CC.

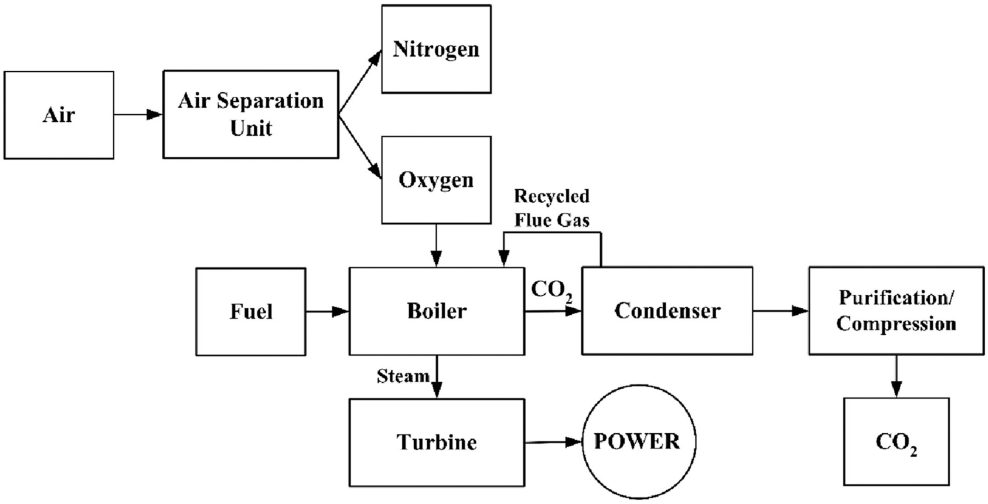

Figure 2.1: Typical flow chart of a power generation plant with CC and operating in oxy-fuel combustion mode [33].

The oxy-fuel concept in combustors and furnaces has been widely investigated and recent progress has been reported. For example, Guo et al. presented a large-scale experimental study of oxy-fuel combustion and showed that this concept performs properly with a special burner system designed for conditions with an initial O_2 concentration of 28% in the oxidant [46] . Also, the influence of high CO_2 concentration has been evaluated in oxy-fuel plants

for different reaction temperatures and equivalence ratios [47]. Actually, the high combustion temperatures maybe be controlled by using a thermal buffer, normally the EGR composed of CO_2 and water vapor, to prevent overheating issues [20] [21]. Several fuels have been tested in burning processes with oxy-fuel combustion, yielding high CO_2 recovery rates with reasonable cycle efficiencies. For instance, Shi et al. [48] studied the oxy-fuel combustion based on circulating fluidized beds boiler firing lignite, sawdust and coal with a CO_2 capture rate greater than 97%. Also, Chaos et al. [49] combined oxy-fuel combustion and coal-O_2/CO_2 partial gasification in a combined cycle system, increasing plant efficiency from 45% to 48% when compared to an integrated gasification combined cycle and improving coal utilization. In that case, separation of more than 92% CO_2 of the flue gas with 95% purity is achieved. In fact, the oxy-fuel combustion may reduce the complexity of CC systems, once the exhaust gas stream essentially contains water vapor and CO_2, water may be easily separated through dehydration at near-standard temperature and pressure conditions, and the remaining CO_2 may be pressurized through compression stages and stored in supercritical-fluid phase at ambient temperature [50].

Cai et al. [51] studied a natural gas oxy-fuel combustion power plant using CO_2, steam or recycled flue gas as diluent to moderate the combustion temperature, reaching the best energy efficiency of 67.6% for the recycled flue gas case. Similarly, Liang et al. [52] analyzed the oxy-fuel combustion applied to a liquefied natural gas (LNG) power plant, comparing two combustion environments with either O_2/CO_2 or O_2/H_2O as thermal buffer, wherein two power generation sub-systems were implemented. Net efficiencies of 55% and 59% are seen for O_2/H_2O and O_2/CO_2 atmospheres respectively, capturing 94.8% of the produced CO_2 with a purity of 97.2%.

Alvarez et al. [53] investigated water-based and carbon-based oxy-fuel combustion power cycles with CC, in which the reacting flows were analyzed through Computational Fluid Dynamics (CFD) for reheated and dual recuperative power schemes. Although water-based recycling fluids present interesting temperature when considering overheating issues, carbon-based fluids yield better overall performance. On the one hand, a 34% minimum efficiency is found for water-based dual recuperative power operating in dry-cooling conditions. On the other hand, carbon-based reheated recuperative power operating in wet-cooling conditions provides a 47% maximum efficiency.

2.2 Oxy-fuel combustion for vehicle propulsion

Although the combination of CO_2 capture systems with oxy-fuel power generation is an established technology [54] [55], the use of such systems in ICEs dedicated to vehicle propulsion is still a major challenge. Even more if such systems are capable of generating their own O_2 considering the limited dimension and load capacity of vehicles. Thus, that technology employed in ICEs has a broad research field due to its novelty for enabling CO_2 capture from exhaust gas [33] [34].

In 2009, Osman et al. [56] proposed to apply the oxy-fuel concept to a single cylinder (SC) engine for the first time, injecting water and pure O_2 straightly into combustion chamber. Once water has high specific heat capacity, it is used as a working medium for heat absorption, which also controls the high in-cylinder temperature, and for gas expansion during the expansion stroke. They obtained an improvement in fuel-conversion efficiency reflected onto reduction in PM, CO, HC and NO_x emissions. An experimental campaign was carried out by Blarigan [35] to study the oxy-methane-fueled combustion in a spark-ignition (SI) engine. They analyzed the engine performance under both wet and dry EGR conditions with various O_2 concentrations comparing them to methane-in-air operation. It was noted that the peak fuel-conversion efficiency for both wet and dry EGR under oxy-fuel combustion condition is lower than for methane-in-air operation, because the EGR working fluids have lower ratio of specific heats when compared to air (with N_2).

Serrano et al. [57] evaluated the oxy-fuel technology in a SC SI engine through experimental and theoretical techniques considering thermal-mechanical constraints. Figure 2.2 depicts the oxy-fuel engine experimental setup used in their study with O_2 supply tank, which is typically employed in other works regarding the oxy-fuel combustion in ICEs. In this case, the O_2 dilution may be performed via either EGR or external CO_2 supply tank. They observed a decrease in indicated efficiency that may be balanced by knocking reduction, which fosters room for spark optimization with an EGR rate range from 60 % to 70 % to sustain combustion stability. Besides, Serrano et al. [58] optimized the combustion chamber geometry of a CI engine operating in oxy-fuel combustion mode with recirculated exhaust gas as thermal buffer, minimizing pollutant emissions to near-zero levels and maximizing engine efficiency as much as possible. Their results show that, although the optimized oxy-fuel combustion system yields lower indicated efficiency than the equiv-

alent engine operating under conventional diesel combustion (35.7% against 40.1%), soot emissions are reduced to a virtual zero.

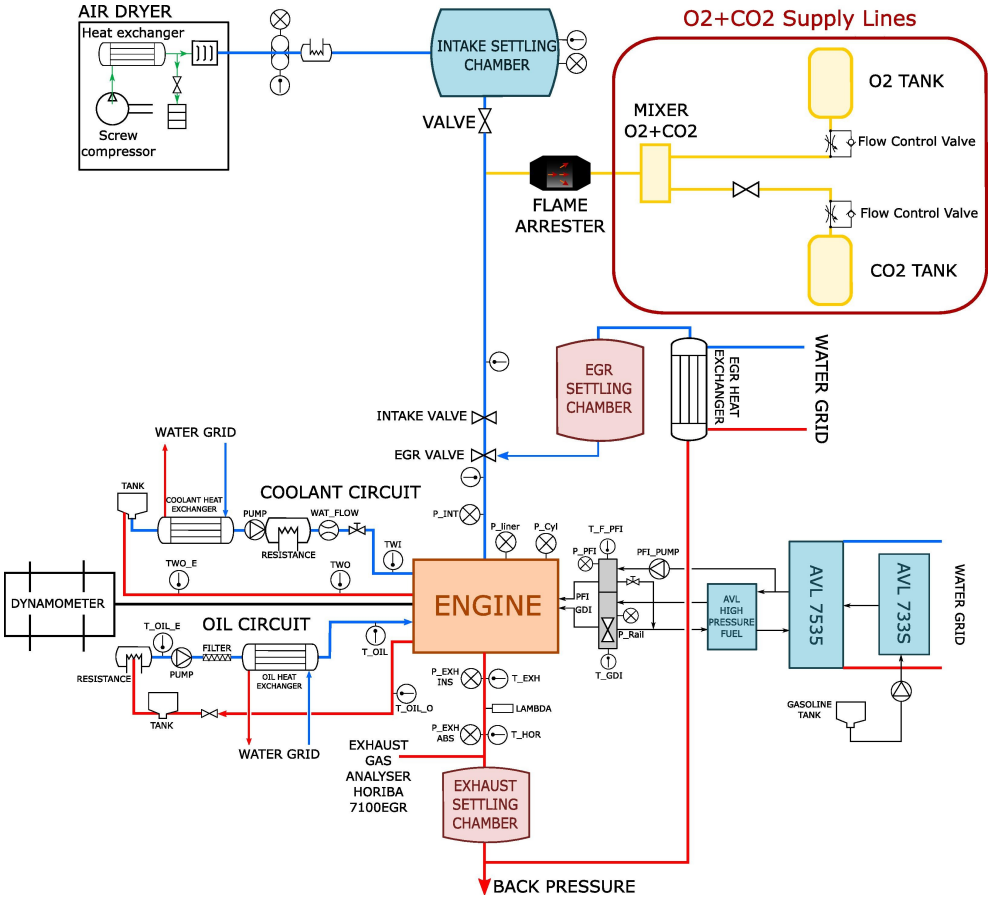

Figure 2.2: Typical layout of a SC oxy-fuel engine with O_2 supply tank [57].

Investigations have emerged motivated for simultaneously exploring the combined effects of oxy-fuel combustion and homogenous charge compression ignition strategies [59], since the latter presents low chamber temperature and lean equivalence ratio which increase the thermodynamic efficiency and decrease harmful soot emissions [60]. Mobasheri et al [61] have used CFD models to evaluate the influence of that combination on combustion characteristics and engine operating conditions in a diesel engine. In that research the intake gases are mainly O_2 and CO_2, so O_2 should be supplied from a commercial O_2 cylinder and CO_2 is captured by condensing and separating water vapor from

the exhaust gases, thereby some part of CO_2 is mixed with pure O_2 and the rest of CO_2 is compressed and stored in a designed tank. Among the main results, it may be noted that increasing the CO_2 concentration rises the overall specific heat capacity of intake flow which decreases the in-cylinder temperature and pressure during combustion phase, reducing the engine power and the thermal efficiency; and at low engine loads worsens the BSFC. Indeed, Abdulrahman Mohammed et al [62] found similar results investigating the oxy-fuel combustion in a SC engine under HCCI application through an experimental setup. The conclusions of their study show that the net indicated engine efficiency with O_2 and recirculated CO_2 is only 15% because mainly that case is operated under lower in-cylinder temperature compared to air combustion and, due to higher back pressure to produce required EGR, the pumping losses are also greater.

2.3 Parameters studied in oxy-fuel compression ignition engines

Also, some works have arisen studying several variables for oxy-fuel combustion application to CI engines such as varying the intake O_2 concentration [63], EGR rate [37], and water direct-injection and fuel injection parameters[39] in order to find out reasonable flame temperature, control combustion stability and verify pollutant emissions mitigation.

Hawley et al [64] [65] analyzed the performance limits of CIE operating on an atmosphere with 30% O_2 and 70% CO_2 on molar basis when pre-heated to 150 °C. Taking into account that their phenomenological models may estimate performance parameters of engines operating on such atmosphere within 5% certain limitations, their results show an increment in Brake Specific Fuel Consumption (BSFC) by 23-28% and a reduction in rated brake power by 20-23%. Besides, a marine four-cylinder four-stroke water-cooled CI engine was studied by Tan et al [66] varying the volumetric proportions of CO_2, O_2 and N_2 in the intake flow. The system was tested in idling and part-load operations for engine speed of 600 rpm and 800 rpm, respectively. They realized that NOx emission increases when N_2 concentration decreases for O_2/N_2 blends when engine runs without load. In addition, they conclude that the NOx/soot emission relationship is not broken regardless of $O_2/CO_2/N_2$ proportions. Nonetheless, NOx emissions are eradicated when the engine operates with nitrogen-free

O_2/CO_2 ratios, promoting combustion performance enhancement at the same time as O_2 concentration increases.

Traditionally, EGR technology was commonly used in CI engines for lowering combustion temperature and, hence, reducing NOx emissions. However, the EGR systems applied to oxy-fuel CI engines are currently focused on the absorption of smoke and CO_2 in order to clean the exhaust gas prior to recycling and mixing it with a fresh O_2 charge. Basically, the flue gas is cooled in a gas cooler, sent to an absorber for capturing part of the CO_2, then CO_2 and CO concentrations are measured, and subsequently flue gas recirculates back to cylinder intake blended with O_2 from the feeding system [67] [37]. Furthermore, the exhaust gas may be either directly recycled without external cooling in a hot EGR strategy or cooled down before its recirculation in a cold EGR strategy. The main benefits of the hot EGR rests on the combustion temperature improvement and low cost without the concern of NOx emissions, while cold EGR may enhance the volumetric efficiency by increasing intake charge density with lower temperature and, thereby, more O_2, H_2O and CO_2 are introduced at engine inlet [33].

Bilger et al.[40] proposed an internal combustion Rankine cycle (ICRC) with oxy-fuel combustion in which part of water condensed at CC system is recirculated and directly injected into the cylinders near top dead center, attaining a 56% ideal thermal efficiency with room for optimization. To improve the cycle efficiency based on oxy-fuel combustion in CI engine, Zhe Kang et al [39] studied the effect of water injection via CFD simulations analyzing the injection timing, injection temperature and water amount. Therefore, the purpose is to couple the Otto cycle with the Rankine cycle [40] [68] [69] because steam may work as the main working fluid. They have found an optimal injection strategy with 1:1.11 fuel-to-water ratio, 365^{o}CA timing and 160^{o}C temperature, enhancing the cycle efficiency by 5.2% compared to simulation without water injection. Accordingly, water injection may be considered a promising technique to control the in-cylinder temperature, improve the combustion phase and, as a consequence, increase engine efficiency [70] since the γ of water is higher than that of CO_2 in the working fluid [71]. In addition, Kang et al. [72] investigated the effect of direct water injection temperature on the ICRC concept with oxy-fuel combustion, reducing soot formation by around 25% if compared to a dry cycle, probably due to water-carbon reactions and water thermolysis.

Wu et al [37] studied with experiments and simulations the influence of a

port-inducted supplementary fuel (gasoline or ethanol) in an oxy-fuel CI engine using diesel as main fuel, which is directly injected into the combustion chamber. One may see among their main results that, even though port-induced ethanol emits more CO_2 at exhaust gas than port-induced gasoline due to the presence of O_2 in its chemical formula as a alcohol, its smoke emissions are lower than those for port-induced gasoline. In general, the integration of the port-injected gasoline or ethanol with the direct injection oxy-fuel CI engine reduces smoke and CO_2 emissions due to combustion performance improvement because the intake charge mixes more homogeneously with the fuel and the port-induced fuel contains less carbon.

2.4 Oxygen transport membranes

Although CAS is the most mature technology for O_2 production, it is highly energy-intensive process, motivating the research for alternatives. In such a context, MIECs may be considered as a promising solution to produce O_2 from the air with an O_2 selectivity of 100% and without crucial economic and energy penalties, being 10.5 % to 17.5 % more cost-effective than CAS with a power consumption abatement of 0.5 % to 9 % [24] due to the thermal integration of OTM systems within processes including available wasted hot streams. The arrangements of OTM modules may adopt either a 3-end or a 4-end approach for their integration within an industrial processes [73]. In a 3-end configuration, O_2 is collected by inducing vacuum on membrane permeate side, while a process hot stream (usually exhaust gas) is employed as sweep gas for carrying out O_2 separation and heating up the module in a 4-end mode [74].

In fact, Gutierrez *et al.* [75] compared CAS to ceramic membranes for O_2 production in the Graz cycle. The authors contemplated two cases for the membrane cycle coupled to Graz cycle regarding the method for decreasing O_2 partial pressure on the membrane permeate side: 3-end membrane with vacuum generation (Case 1) and 4-end membrane with gas sweeping (Case 2). They verify enhancements of 0.61% and 2.30% for cases 1 and 2 respectively in plant thermal efficiency with respect to baseline case (Graz cycle with cryogenic unit). Additionally, Serrano *et al.* [76] performed a thermo-economic analysis of a membrane-based O_2 production plant for a ceramic manufacturing factory. In this case, the whole cycle is powered by waste heat

from high temperature flue gas via a set of turbochargers. The authors state this approach is economically competitive when compared to O_2 acquisition in wholesale market, regarding O_2 purity, natural gas and electricity prices, with cost reduction between 34% and 38%.

As already explained in section 1.1, an O_2 partial pressure gradient between feed and permeate sides along with high temperature are the driving force for O_2 flux in those membranes in an eletroneutrality circuit regarding the transport of O_2 ions and electrons [31] as shown in Figure 2.3. Among the MIEC family structures, perovskite exhibits good electronic-ionic conductivity leading to an attractive O_2 transfer with [77]. Their crystal structure posses a typical cation-anion arrangement $ABO_{3-\delta}$ as depicted in Figure 2.4. According to results published by Shao and Teraoka [78] [79], $Ba_{0.5}Sr_{0.5}Co_{0.8}Fe_{0.2}O_{3-\delta}$ (BSCF) and $SrCo_{0.8}Fe_{0.2}O_{3-\delta}$ (SCF) provide the best O_2 transport properties of all perovskites and, hence, are interesting for material design in innovative O_2 separation technologies.

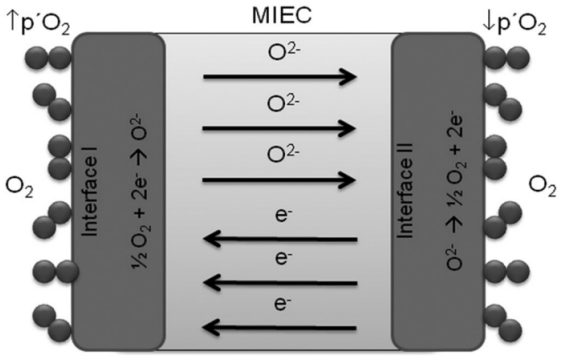

Figure 2.3: O_2 transport through a MIEC [77]

Although membrane modules based on BSCF present some limited stability, this material has a high O_2 flux with production capacity of up to $62\,mL\,min^{-1}\,cm^{-2}$ of O_2 at 1000 °C [80]. Indeed, Shubnikova et al. [81] states that the highest O_2 permeation for conventional membrane materials based on MIEC perovskites is seen for the BSCF oxide and its derivatives. Additionally, BSCF membranes would be suitable for being combined with oxy-fuel combustion applications since some studies have established a minimum O_2 permeation of $10\,mL\,min^{-1}\,cm^{-2}$ for their feasible utilization in this domain [82].

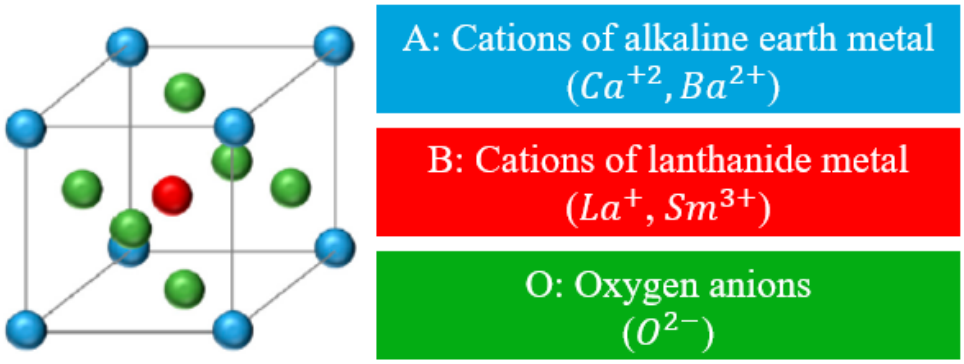

Figure 2.4: Perovskite crystal structure.

Serra et al. [74] conducted a characterization study of O_2 transport on BSCF MIEC based on an experimental and numerical assessment, analyzing some effects such as MIEC temperature, feeding flow, sweep inlet flow and sweep gas composition (O_2 dilution with CO_2, H_2O, He or Ar) on the MIEC performance. Their results show that increasing the temperature from 700 °C to 1000 °C improve the O_2 transport; the O_2 flux presents an asymptotic behavior regarding feed and sweep inlet flows; and the higher the molecular weight of the sweep gas is (such as CO_2 and H_2O), the better the O_2 is swept. Although CO_2 may hinder BSCF membrane performance, there are meaningful progresses in developing protective layers such as $Ce_{0.9}Gd_{0.1}O_{2-\delta}$ films which may be deposited on those membranes to improve their stability under CO_2-containing environments [83] [84].

Therefore, considering the oxy-fuel combustion technology to capture the CO_2, BSCF membranes arise as an O_2 separation way in ICE, using the exhaust gas as a sweep gas and taking advantage of its high thermal energy to generate enough pressure and temperature on MIEC feeding side to produce the needed O_2 for the proper engine performance under oxy-fuel combustion conditions. Arnau *et al.* [85] applied the oxy-fuel concept to a multi-cylinder SI engine using an oxygen transport membrane as an air separation unit to produce the O_2 needed by the engine operating requirements. Among the main simulation results, it may be noted that, in general, the oxy-fuel system efficiency is lower if compared to a conventional SI engine, but it is somewhat better at high speeds and high indicated mean effective pressures. In addition, Serrano *et al.* [86] evaluated the impact of the CR and the intake

O_2 concentration on the membrane-based oxy-fuel multi-cylinder SIE used in [85], but considering a similar heat exchanger network (HEN) to increase the air temperature on membrane feed side as proposed by Serrano *et al.* [1] and presented in this thesis dissertation. When compared to an air conventional combustion operation, they observed an improvement of 16.3% in fuel consumption for oxy-fuel combustion conditions with compression ratio of 20 and O_2 concentration of 30% at a medium engine speed. Moreover, these parameters are fixed and a full load study is carried out taking into account a wide range of engine speeds and, then, up to 21% lower fuel consumption than air combustion was reached.

2.5 Carbon capture application and modeling for internal combustion engines

In 2019, Sharma et all [87] proposed an on-board CO_2 capture and storage unit with ICE using a temperature swing adsorption integrated with a turbocharger system to compress and liquefy CO_2 (via Rankine cycle) using the heat of exhaust gases. By means of energy and exergy analyses of their study, they state that the proposed system may capture 90% of the emitted CO_2 from engine, without any energy penalty. Moreover, Wu et al [37] applied to a closed cycle diesel engine an absorption technique to reduce CO_2 emissions by washing the exhaust gas with an alkaline solution in a perforated T-type pipe.

In addition to reducing GHG, CC may provide the CO_2 as a product that offers new opportunities and challenges into a circular economy, converting it into carbon-based economically viable fuels [88] [50]. For instance, Oleksandr proposed the gradual rise of photocatalytic, CO_2 polymerization, biohybrid, and molecular machine technologies to enhance methods of electrocatalytic CO_2 transformation into chemical fuels [89]. In general, the CC technology has not been too exploited in ICE with oxy-fuel configuration and the existing investigations are particularly focused on the combustion process. At best, ideal schematic ICRC cycles are proposed, but without calculating effectively the CC energy specifications and CO_2 purification steps for the CC system coupled to ICE [68] [90] [40].

Anyway, accurate thermodynamic state models for multi-component CO_2 mixtures are essential for the operation and design of processes inside CC

and storage context, especially concerning the modeling of separation systems based on volatility difference [91]. Moreover, existing cubic equations of state (EOS), such as Redlich-Kwong (RK) [92], Soave-Redlich-Kwong (SRK) [93] and Peng-Robinson (PR) [94], may be considered a satisfactory way to predict the vapor-liquid phase equilibrium (VLE) for pure compounds and mixtures, giving reasonable results if their binary interaction parameters (k_{ij}) are calibrated with reliable experimental data [95]. Thus, considering the oxy-fuel combustion application for power plants, well-calibrated cubic EOS may be used to model the condensation steps as well as the CO_2 purification process to calculate the amount of CO_2 captured from the exhaust gas and the energy requirements for that purpose with reasonable accuracy.

EOSs are basically thermodynamic approaches to relate state variables (pressure, temperature and volume) and describe the states of a fluid and its properties [96]. Indeed, one of their primary applications is the prediction of the VLE for pure compounds and mixtures considering the non-ideality of the system [97]. In general, conventional EOS, such as RK, SRK and PR, may be expressed with the following generalized cubic formulation relating pressure (P), temperature (T) and molar volume (v):

$$P = \frac{RT}{v-b} - \frac{a(T)}{(v+\varepsilon b)(v+\sigma b)} \tag{2.1}$$

For a given EOS, parameters $b = \Omega\dfrac{RT_c}{P_c}$ and $a(T) = \Psi\dfrac{\alpha(T_r)R^2T_c^2}{P_c}$ are substance dependent with the temperature dependence of $\alpha(T_r)$ specific to each EOS considering the reduced temperature defined by $T_r = \dfrac{T}{T_c}$, and the acentric factor (ω), variable for quantifying the centricity of a molecule, and critical pressure (P_c) and temperature (T_c) of each substance. Moreover, σ, ε, Ω and Ψ are pure numbers specific to a particular EOS but independent of the substance. Table 2.1 summarizes the parameter assignments for each EOS [98].

Table 2.1: α-functions and parameters for cubic EOS

EOS	$\alpha(T_r)$	σ	ε	Ω	Ψ
RK	$T_r^{-1/2}$	1	0	0.08664	0.42748
SRK	$\alpha_{SRK}(T_r,\omega)$	1	0	0.08664	0.42748
PR	$\alpha_{PR}(T_r,\omega)$	$1+\sqrt{2}$	$1-\sqrt{2}$	0.07780	0.45724

$$\alpha_{SRK}(T_r,\omega) = \left[1+(0.480+1.574\omega-0.176\omega^2)(1-T_r^{1/2})\right]^2$$

$$\alpha_{PR}(T_r,\omega) = \left[1+(0.37464+1.574226\omega-0.26992\omega^2)(1-T_r^{1/2})\right]^2$$

When predicting the thermodynamic states for mixtures, the EOS for a pure substance may also be applied to them using the concept of a one-fluid mixture. For a mixture with given composition, an equivalent pure-compound behavior regarding temperature and pressure variations is assumed with some parameters adjusted to the mixture composition. Thus, empirical mixing rules are proposed, and some conventional ones may be expressed by Equation 2.2 and Equation 2.3, where parameters $a(T)$ and b have quadratic and linear, respectively, dependence on mole fraction z with binary parameter k_{ij} calibrated by fitting to experimental data for each pair of substances (ij) [98] [97]:

$$a(T) = \sum_{i=1}^{n}\sum_{j=1}^{n} z_i z_j \sqrt{a(T)_i a(T)_j}(1-k_{ij}) \tag{2.2}$$

$$b = \sum_{i=1}^{n} z_i b_i \tag{2.3}$$

Besides that, the parameter k_{ij} may also be formulated as temperature-dependent regarding the system in question [99]. Furthermore, other exact thermodynamic properties of interest in this work may be derived from EOS, such as fugacity coefficient (ϕ) and specific real enthalpy (h) calculated from a reference condition (0) for a given system [98]:

$$\ln\phi = \int_0^P \left(\frac{Pv}{RT}-1\right) d\ln P \tag{2.4}$$

$$h = h_0 + \sum_{i=1}^{n} z_i \int_{T_0}^{T} c_{p,i_0}\, dT - RT + Pv - \int_{\infty}^{v}\left[P - T\left(\frac{\partial P}{\partial T}\right)_v\right] dv \tag{2.5}$$

Finally, one of the fundamental criteria for achieving the thermodynamic equilibrium between vapor and liquid phases is when species, in an either pure or mixture system, have the same fugacity in every phase, and thereby, the following condition for each compound is necessary for equilibrium phase [100] considering the vapor and liquid Mole fraction of each specie, y_i and x_i, respectively:

$$y_i \phi_{i,vap} = x_i \phi_{i,liq} \tag{2.6}$$

Chapter 2 Bibliography

[1] J. Serrano, F. Arnau, L. García-Cuevas, and V. Farias. "Oxy-fuel combustion feasibility of compression ignition engines using oxygen separation membranes for enabling carbon dioxide capture". *Energy Conversion and Management* 247 (Nov. 2021), p. 114732. DOI: 10.1016/j.enconman.2021.114732 (cit. on pp. xii, 25, 40).

[20] M. Pamminger, W. Buyu, C. Hall, R. Vojtech, and T. Wallner. "The impact of water injection and exhaust gas recirculation on combustion and emissions in a heavy-duty compression ignition engine operated on diesel and gasoline". *International Journal of Engine Research* 21 (Jan. 2019), pp. 1555–1573. DOI: 10.1177/1468087418815290 (cit. on pp. 4, 17).

[21] R. Mobasheri and S. Khabbaz. "Modeling the Effects of High EGR Rates in Conjunction with Optimum Multiple Injection Techniques in a Heavy Duty DI Diesel Engine". *SAE Technical Papers* 1 (Apr. 2014). DOI: 10.4271/2014-01-1124 (cit. on pp. 4, 17).

[24] E. Portillo, B. Alonso-Fariñas, F. Vega, M. Cano, and B. Navarrete. "Alternatives for oxygen-selective membrane systems and their integration into the oxy-fuel combustion process: A review". *Separation and Purification Technology* 229 (June 2019), p. 115708. DOI: 10.1016/j.seppur.2019.115708 (cit. on pp. 4, 5, 22).

[25] A. Escudero, S. Espatolero, and L. Romeo. "Oxy-combustion power plant integration in an oil refinery to reduce CO_2 emissions". *International Journal of Greenhouse Gas Control* 45 (Feb. 2016), pp. 118–129. DOI: 10.1016/j.ijggc.2015.12.018 (cit. on pp. 4, 16).

[27] F. Carrasco Maldonado, R. Spörl, K. Fleiger, V. Hoenig, J. Maier, and G. Scheffknecht. "Oxy-fuel combustion technology for cement production - State of the art research and technology development". *International Journal of Greenhouse Gas Control* 45 (Feb. 2016), pp. 189–199. DOI: 10.1016/j.ijggc.2015.12.014 (cit. on pp. 4, 16).

[31] F. Wu, M. Argyle, P. Dellenback, and M. Fan. "Progress in O_2 separation for oxy-fuel combustion–A promising way for cost-effective CO_2 capture: A review". *Progress in Energy and Combustion Science* 67 (July 2018), pp. 188–205. DOI: 10.1016/j.pecs.2018.01.004 (cit. on pp. 5, 23).

[33] X. Li, Z. Peng, Y. Pei, T. Ajmal, K. Rana, A. Aitouche, and R. Mobasheri. "Oxy-fuel combustion for carbon capture and storage in internal combustion engines – A review". *International Journal of Energy Research* 46 (Aug. 2021), pp. 505–522. DOI: 10.1002/er.7199 (cit. on pp. 5, 16, 18, 21).

[34] X. Li, Y. Pei, Z. Peng, T. Ajmal, K.-J. Rana, A. Aitouche, and R. Mobasheri. "Numerical study on the effects of intake charge on oxy-fuel combustion in a dual-injection spark ignition engine at economical oxygen-fuel ratios". *International Journal of Engine Research* 23 (May 2021). DOI: 10.1177/14680874211022292 (cit. on pp. 5, 18).

[35] A. Van Blarigan, D. Kozarac, R. Seiser, R. Cattolica, J.-Y. Chen, and R. Dibble. "Experimental Study of Methane Fuel Oxycombustion in a Spark-Ignited Engine". *Journal of Energy Resources Technology* 136 (Mar. 2013), p. 9. DOI: 10.1115/1.4024974 (cit. on pp. 5, 18, 46).

[37] H.-W. Wu, R.-H. Wang, Y.-C. Chen, D.-J. Ou, and T.-Y. Chen. "Influence of port-inducted ethanol or gasoline on combustion and emission of a closed cycle diesel engine". *Energy* 64 (Jan. 2013). DOI: 10.1016/j.energy.2013.11.027 (cit. on pp. 5, 20, 21, 25).

[39] Z. Kang, S. Chen, Z. Wu, J. Deng, Z. Hu, and L. Li. "Simulation Study of Water Injection Strategy in Improving Cycle Efficiency Based on a Novel Compression Ignition Oxy-Fuel Combustion Engine". *SAE International Journal of Engines* 11 (Apr. 2018). DOI: 10.4271/2018-01-0894 (cit. on pp. 5, 20, 21, 46).

[40] R. Bilger and Z. Wu. "Carbon Capture for Automobiles Using Internal Combustion Rankine Cycle Engines". *Journal of Engineering for Gas Turbines and Power* 131 (May 2009), p. 034502. DOI: 10.1115/1.3077657 (cit. on pp. 5, 21, 25).

[41] B. Abraham, J. Asbury, E. Lynch, and A. Teotia. "Coal-Oxygen Process Provides CO_2 for Enhanced Recovery". *Oil and Gas Journal* 80 (Jan. 1982) (cit. on p. 16).

[42] D. Hanak, D. Powell, and V. Manovic. "Techno-economic analysis of oxy-combustion coal-fired power plant with cryogenic oxygen storage". *Applied Energy* 191 (Jan. 2017), 193–203. DOI: 10.1016/j.apenergy.2017.01.049 (cit. on p. 16).

[43] N. Kimura, K. Omata, T. Kiga, S. Takano, and S. Shikisima. "The characteristics of pulverized coal combustion in O_2/CO_2 mixtures for CO_2 recovery". *Energy Conversion and Management* 36 (Jan. 1996), pp. 805–808. DOI: 10.1016/0196-8904(95)00126-X (cit. on p. 16).

[44] W. Sanz, H. Jericha, B. Bauer, and E. Göttlich. "Qualitative and Quantitative Comparison of Two Promising Oxy-Fuel Power Cycles for CO_2 Capture". *Journal of Engineering for Gas Turbines and Power-transactions of The Asme - J ENG GAS TURB POWER-T ASME* 130 (May 2008). DOI: 10.1115/1.2800350 (cit. on p. 16).

[45] O. Biyiklioğlu and M. Tat. "Tribological assessment of NiCr, Al_2O_3/TiO_2 , and Cr_3C_2/NiCr coatings applied on a cylinder liner of a heavy-duty diesel engine". *International Journal of Engine Research* (July 2020), p. 146808742093016. DOI: 10.1177/1468087420930164 (cit. on p. 16).

[46] J. Guo, Z. Liu, X. Huang, T. Zhang, W. Luo, F. Hu, P. Li, and C. Zheng. "Experimental and numerical investigations on oxy-coal combustion in a 35MW large pilot boiler". *Fuel* 187 (2017), pp. 315–327. ISSN: 0016-2361. DOI: https://doi.org/10.1016/j.fuel.2016.09.070 (cit. on p. 16).

[47] F. Hu, P. Li, W. Li, C. Ding, J. Guo, and Z. Liu. "Experimental and kinetic study of NO-reburning by syngas under high CO2 concentration in a jet stirred reactor". *Fuel* 304 (2021), p. 121403. ISSN: 0016-2361. DOI: https://doi.org/10.1016/j.fuel.2021.121403 (cit. on p. 17).

[48] S. Yan, Q. Liu, Y. Shao, and W. Zhong. "Energy and exergy analysis of oxy-fuel combustion based on circulating fluidized bed power plant firing coal, lignite and biomass". *Fuel* 269 (June 2020), p. 117424. DOI: 10.1016/j.fuel.2020.117424 (cit. on p. 17).

[49] C. Ye, Z. Ye, Z. Zhu, and Q. Wang. "Thermodynamic and Economic Analysis of Oxy-Fuel-Integrated Coal Partial Gasification Combined Cycle". *ACS Omega* XXXX (Feb. 2021). DOI: 10.1021/acsomega.0c05277 (cit. on p. 17).

[50] I. Mohsin, T. Al-Attas, K. Sumon, J. Bergerson, S. McCoy, and M. Kibria. "Economic and Environmental Assessment of Integrated Carbon Capture and Utilization". *Cell Reports Physical Science* 1 (July 2020), p. 100104. DOI: 10.1016/j.xcrp.2020.100104 (cit. on pp. 17, 25).

[51] L. Cai, L. Tan, Y. Liang, X. Yin, C. Liu, and Y. Guan. "Numerical study on sulfur-bearing natural gas oxy-fuel combustion power plant". *Applied Thermal Engineering* 196 (July 2021), p. 117292. DOI: 10.1016/j.applthermaleng.2021.117292 (cit. on p. 17).

[52] Y. Liang, L. Cai, Y. Guan, W. Liu, Y. Xiang, J. Li, and T. He. "Numerical study on an original oxy-fuel combustion power plant with efficient utilization of flue gas waste heat". *Energy* 193 (Dec. 2019), p. 116854. DOI: 10.1016/j.energy.2019.116854 (cit. on p. 17).

[53] J. Alvarez, A. Sleiti, W. Al-Ammari, and E. Fernández. "Study of recirculating water-based and carbon-based working fluids on the combustion flow field and the cycle performances of semi-CO2-capturing Brayton-derived cycles". *Applied Thermal Engineering* 218 (Sept. 2022), p. 119296. DOI: 10.1016/j.applthermaleng.2022.119296 (cit. on p. 17).

[54] S. Yadav and S. Mondal. "A review on the progress and prospects of oxy-fuel carbon capture and sequestration (CCS) technology". *Fuel* 308 (2022), p. 122057. ISSN: 0016-2361. DOI: https://doi.org/10.1016/j.fuel.2021.122057. URL: https://www.sciencedirect.com/science/article/pii/S0016236121019335 (cit. on p. 18).

[55] S. Yadav and S. Mondal. "Numerical investigation of 660 MW pulverized coal-fired supercritical power plant retrofitted to oxy-coal combustion". *International Journal of Greenhouse Gas Control* 105 (2021), p. 103227. ISSN: 1750-5836. DOI: https://doi.org/10.1016/j.ijggc.2020.103227. URL: https://www.sciencedirect.com/science/article/pii/S1750583620306526 (cit. on p. 18).

[56] A. Osman. "Feasibility Study of a Novel Combustion Cycle Involving Oxygen and Water". *SAE Technical Papers* (Nov. 2009), p. 14. DOI: 10.4271/2009-01-2808 (cit. on pp. 18, 46).

[57] J. R. Serrano, J. Martín, J. Gomez-Soriano, and R. Raggi. "Theoretical and experimental evaluation of the spark-ignition premixed oxy-fuel combustion concept for future CO2 captive powerplants". *Energy Conversion and Management* 244 (Sept. 2021), p. 114498. DOI: 10.1016/j.enconman.2021.114498 (cit. on pp. 18, 19).

[58] J. R. Serrano, G. Bracho, J. Gomez-Soriano, and C. Fernandes. "Development of an oxy-fuel combustion system in a compression-ignition engine for ultra-low emissions powerplants Using CFD and evolutionary algorithms". *Applied Sciences* 12.(14) (2022). ISSN: 2076-3417. DOI: 10.3390/app12147104. URL: https://www.mdpi.com/2076-3417/12/14/7104 (cit. on pp. 18, 71, 73, 78).

[59] R. Mobasheri, A. Abdel, Z. Peng, and X. Li. "A Numerical Study of the Effects of Oxy-Fuel Combustion under Homogeneous Charge Compression Ignition". *International Journal of Engine Research* (Feb. 2021). DOI: 10.1177/1468087421993359 (cit. on p. 19).

[60] T. Sharma, A. Rao, and M. K. "Homogeneous Charge Compression Ignition (HCCI) Engines: A Review". *Archives of Computational Methods in Engineering* 23 (May 2015). DOI: 10.1007/s11831-015-9153-0 (cit. on pp. 19, 46).

[61] R. Mobasheri, A. Aitouche, Z. Peng, and X. Li. "Influence of Oxy-Fuel Combustion on Engine Operating Conditions and Combustion Characteristics in a High Speed Direct Injection (HSDI) Diesel Engine under Homogenous Charge Compression Ignition (HCCI) Mode". In: *SAE Technical Paper*. WCX SAE World Congress Experience, Apr. 2020, p. 10. DOI: 10.4271/2020-01-1138 (cit. on pp. 19, 46).

[62] A. Mohammed, A. Elkhazraji, S. Jan, and B. Johansson. "A Study on the Performance and Emissions of HCCI Oxy-Fuel Combustion in a CFR Engine with Recirculated Carbon Dioxide". In: *SAE Powertrains, Fuels and Lubricants Meeting*. Sept. 2020, p. 13. DOI: 10.4271/2020-01-2065 (cit. on pp. 20, 46).

[63] Z. Kang, Z. Wu, Z. Zhang, J. Deng, Z. Hu, and L. Li. "Study of the Combustion Characteristics of a HCCI Engine Coupled with Oxy-Fuel Combustion Mode". *SAE International Journal of Engines* 10 (Mar. 2017). DOI: 10.4271/2017-01-0649 (cit. on p. 20).

[64] J. Hawley, G. Reader, M. Zheng, I. Potter, and O. Frauvel. "Investigations on Carbon Dioxide/Oxygen Breathing Diesel Engines—Results from an International Collaborative Project". *Underwater Technology: The International Journal of The Society for Underwater* 23 (Dec. 1998), pp. 109–121. DOI: 10.3723/175605498783259218 (cit. on p. 20).

[65] J Hawley, S Ashcroft, and M Patrick. "The Effects of Non-Air Mixtures on the Operation of a Diesel Engine by Experiment and by Simulation". *Proceedings of The Institution of Mechanical Engineers Part A-journal of Power and Energy - PROC INST MECH ENG A-J POWER* 212 (Feb. 1998), pp. 55–68. DOI: 10.1243/0957650981536691 (cit. on p. 20).

[66] Q. Tan and Y. Hu. "A study on the combustion and emission performance of diesel engines under different proportions of O2-N2-CO2". *Applied Thermal Engineering* 108 (July 2016). DOI: 10.1016/j.applthermaleng.2016.07.151 (cit. on p. 20).

[67] H.-W. Wu and C.-T. Shu. "Effects of operating parameters on steady and transient behaviors of a closed cycle diesel engine". *Energy Conversion and Management - ENERG CONV MANAGE* 47 (Sept. 2006), pp. 2070–2080. DOI: 10.1016/j.enconman.2005.12.023 (cit. on p. 21).

[68] Z. Wu, X. Yu, L. Fu, J. Deng, and L. Li. "Experimental study of the effect of water injection on the cycle performance of an internal-combustion Rankine cycle engine". *Proceedings of the Institution of Mechanical Engineers, Part D: Journal of Automobile Engineering* 228 (Mar. 2014), pp. 580–588. DOI: 10.1177/0954407013511069 (cit. on pp. 21, 25).

[69] X. Yu, Z. Wu, L. Fu, J. Deng, Z. Hu, and L. Li. "Study of Combustion Characteristics of a Quasi Internal Combustion Rankine Cycle Engine". *SAE Technical Papers* 11 (Oct. 2013). DOI: 10.4271/2013-01-2698 (cit. on p. 21).

[70] S. Zhu, B. Hu, S. Akehurst, C. Copeland, A. Lewis, H. Yuan, I. Kennedy, J. Bernards, and C. Branney. "A review of water injection applied on the internal combustion engine". *Energy Conversion and Management* 184 (Mar. 2019), pp. 139–158. DOI: 10.1016/j.enconman.2019.01.042 (cit. on p. 21).

[71] G. D. Perry R. *Perry's chemical engineers's handbook eighth edition.* McGraw-Hill, 2008 (cit. on pp. 21, 58, 113, 125).

[72] Z. Kang, S. Feng, Y. Lv, J. Wu, and Z. Wu. "Effect of direct water injection temperature on combustion process and thermal efficiency within compression ignition internal combustion Rankine engine". *Case Studies in Thermal Engineering* 28 (Oct. 2021), p. 101592. DOI: 10.1016/j.csite.2021.101592 (cit. on p. 21).

[73] S. Engels, F. Beggel, M. Michael, and H. Stadler. "Simulation of a membrane unit for oxyfuel power plants under consideration of realistic BSCF membrane properties". *Journal of Membrane Science - J MEMBRANE SCI* 359 (Sept. 2010), pp. 93–101. DOI: 10.1016/j.memsci.2010.01.048 (cit. on p. 22).

[74] D. Catalán Martínez, M. Santafé-Moros, J. Gozálvez-Zafrilla, J. García Fayos, and J. Serra. "Characterization of oxygen transport phenomena on BSCF membranes assisted by fluid dynamic simulations including surface exchange". *Chemical Engineering Journal* 387 (May 2020), p. 124069. DOI: 10.1016/j.cej.2020.124069 (cit. on pp. 22, 24, 40, 41, 70).

[75] F. Gutiérrez, L. García-Cuevas, and W. Sanz. "Comparison of cryogenic and membrane oxygen production implemented in the Graz cycle". *Energy Conversion and Management* 271 (Nov. 2022), p. 116325. DOI: 10.1016/j.enconman.2022.116325 (cit. on p. 22).

[76] J. Serrano, F. Arnau, L. García-Cuevas, and F. Gutiérrez. "Thermoeconomic analysis of an oxygen production plant powered by an innovative energy recovery system". *Energy* 255 (June 2022), p. 124419. DOI: 10.1016/j.energy.2022.124419 (cit. on p. 22).

[77] P. Lemes, G. Garcia, R. Machado, D. Hotza, and J. Costa. "Current Developments of Mixed Conducting Membranes on Porous Substrates". *Materials Research* 17 (Dec. 2012). DOI: 10.1590/S1516-14392013005000175 (cit. on p. 23).

[78] Z. Shao, G. Xiong, J. Tong, H. Dong, and W. Yang. "Ba effect in doped $SrCo_{0.8}Fe_{0.2}O_{3-\delta}$ on the phase structure and oxygen permeation properties of the dense ceramic membranes". *Separation and Purification Technology - SEP PURIF TECHNOL* 25 (Oct. 2001), pp. 419–429. DOI: 10.1016/S1383-5866(01)00071-5 (cit. on p. 23).

[79] Y. Teraoka, H.-M. Zhang, S. Furukawa, and N. Yamazoe. "Oxygen Permeation Through Perovskite-Type Oxides". *Chemistry Letters - CHEM LETT* 11 (Nov. 1985), pp. 1743–1746. DOI: 10.1246/cl.1985.1743 (cit. on p. 23).

[80] S. Baumann, J. Serra, M. Lobera, S. Escolástico, F. Schulze-Kuppers, and W. Meulenberg. "Ultrahigh Oxygen Permeation Flux Through Supported $Ba_0 \cdot {}_5Sr_0 \cdot {}_5Co_0 \cdot {}_8Fe_0 \cdot {}_2O_{3-\delta}$ Membranes". *Journal of Membrane Science* 377 (July 2011), pp. 198–205. DOI: 10.1016/j.memsci.2011.04.050 (cit. on p. 23).

[81] E. Shubnikova and A. Nemudry. "Perovskites Based on SCF and BSCF Oxides and Their Application as Membrane Materials and Electrodes for Solid Oxide Fuel Cells". *Membranes and Membrane Technologies* 3 (Nov. 2021), pp. 377–388. DOI: 10.1134/S251775162106007X (cit. on p. 23).

[82] M. Exter, W. Haije, and J. Vente. "Viability of ITM Technology for Oxygen Production and Oxidation Processes: Material, System, and Process Aspects". *Inorganic Membranes for Energy and Environmental Applications* (Jan. 2009). DOI: 10.1007/978-0-387-34526-0_2 (cit. on p. 23).

[83] M. Balaguer, C. Solís, J. García Fayos, E. Palafox, and J. Serra. "Progress in $Ce_{0.8}Gd_{0.2}O_{2-\delta}$ Protective Layers for Improving the CO_2 Stability of BSCF O2-Transport Membranes". *Sustainable Energy and Fuels* 4 (May 2020), pp. 3747–3752. DOI: 10.1039/D0SE00324G (cit. on p. 24).

[84] C. Solís, F. Toldrá Reig, M. Balaguer, S. Somacescu, J. García Fayos, E. Palafox, and J. Serra. "Mixed Ionic-Electronic Conduction in $NiFe_2O_4$−$Ce_{0.8}Gd_{0.2}O_{2-\delta}$ Nanocomposite Thin Films for Oxygen Separation". *ChemSusChem* 11 (July 2018), pp. 2818–2827. DOI: 10.1002/cssc.201800420 (cit. on p. 24).

[85] F. J. Arnau, R. Novella, L. M. García-Cuevas, and F. A. Gutierrez. "Adapting an internal combustion engine to oxy-fuel combustion with in-situ oxygen production". In: *Internal Combustion Engine Division Fall Technical Conference 2021*. Oct. 2021, p. 12. DOI: 10.1115/ICEF2021-67707 (cit. on pp. 24, 25).

[86] J. R. Serrano, F. J. Arnau, L. M. García-Cuevas, and F. A. Gutiérrez. "Coupling an oxygen generation cycle with an oxy-fuel combustion spark ignition engine for zero NOx emissions and carbon capture: A feasibility study". *Energy Conversion and Management* 284 (2023), p. 116973. ISSN: 0196-8904. DOI: https://doi.org/10.1016/j.enconman.2023.116973. URL: https://www.sciencedirect.com/science/article/pii/S0196890423003199 (cit. on p. 24).

[87] S. Sharma and F. Maréchal. "Carbon Dioxide Capture From Internal Combustion Engine Exhaust Using Temperature Swing Adsorption". *Frontiers in Energy Research* 7 (Dec. 2019), p. 143. DOI: 10.3389/fenrg.2019.00143 (cit. on p. 25).

[88] S. Valluri, V. Claremboux, and S. Kawatra. "Opportunities and challenges in CO2 utilization". *Journal of Environmental Sciences* 113 (2022), pp. 322–344. ISSN: 1001-0742. DOI: https://doi.org/10.1016/j.jes.2021.05.043. URL: https://www.sciencedirect.com/science/article/pii/S1001074221002217 (cit. on p. 25).

[89] O. Bushuyev, P. Luna, C. T. Dinh, L. Tao, G. Saur, J. Lagemaat, S. Kelley, and E. Sargent. "What Should We Make with CO_2 and How Can We Make It?" *Joule* 2 (Mar. 2018). DOI: 10.1016/j.joule.2017.09.003 (cit. on p. 25).

[90] Z. Wu, X. Yu, L. Fu, J. Deng, Z.-J. Hu, and L. Li. "A high efficiency oxyfuel internal combustion engine cycle with water direct injection for waste heat recovery". *Energy* 70 (June 2014). DOI: 10.1016/j.energy.2014.03.095 (cit. on p. 25).

[91] S. T. Munkejord, M. Hammer, and S. Løvseth. "CO2 transport: data and models – A review". *Applied Energy* 169 (May 2016), 499–523. DOI: 10.1016/j.apenergy.2016.01.100 (cit. on p. 26).

[92] O. Redlich and J Kwong. "On the Thermodynamics of Solutions: An Equation of State, Fugacities of Gaseous Solutions". *Chemical Reviews* 44 (Mar. 1949), pp. 233–44. DOI: 10.1021/cr60137a013 (cit. on p. 26).

[93] G. Soave. "Equilibrium Constants From a Modified Redlich-Kwong Equation of State". *Chemical Engineering Science* 27 (June 1972), pp. 1197–1203. DOI: 10.1016/0009-2509(72)80096-4 (cit. on p. 26).

[94] D. Peng and D. Robinson. "New Two-Constant Equation of State". *Industrial and Engineering Chemistry Fundamentals* 15 (Feb. 1976). DOI: 10.1021/i160057a011 (cit. on p. 26).

[95] H. Li, J. Jakobsen, O. Wilhelmsen, and J. Yan. "PVTxy properties of CO2 mixtures relevant for CO2 capture, transport and storage: Review of available experimental data and theoretical models". *Applied Energy* 88 (Apr. 2013), pp. 3567–3579. DOI: 10.1016/j.apenergy.2011.03.052 (cit. on p. 26).

[96] M. D. Bermejo and M. J. Cocero. "Supercritical water oxidation: a technical review". *American Institute of Chemical Engineers Journal* 52.(11) (2006), pp. 3933–3951. DOI: https://doi.org/10.1002/aic.10993. URL: https://aiche.onlinelibrary.wiley.com/doi/abs/10.1002/aic.10993 (cit. on p. 26).

[97] F. Mangold, S. Pilz, S. Bjelic, and F. Vogel. "Equation of state and thermodynamic properties for mixtures of H2O, O2, N2, and CO2 from ambient up to 1000 K and 280 MPa". *The Journal of Supercritical Fluids* 153 (Mar. 2019), p. 104476. DOI: 10.1016/j.supflu.2019.02.016 (cit. on pp. 26, 27).

[98] J. M. Smith, H. C. Van Ness, M. M. Abbott, and M. T. Swihart. *Introduction to chemical engineering thermodynamics*. Harvard, 2018 (cit. on pp. 26, 27).

[99] P. M. Mathias. "A versatile phase equilibrium equation of state". *Industrial & Engineering Chemistry Process Design and Development* 22.(3) (1983), pp. 385–391. DOI: 10.1021/i200022a008. URL: https://doi.org/10.1021/i200022a008 (cit. on p. 27).

[100] S. I. Sandler. *Chemical, biochemical and engineering thermodynamics*. Harvard, 2016 (cit. on pp. 28, 96).

Chapter 3

Oxy-fuel combustion layout with on-site O_2 production

Contents

3.1 Introduction

The works, analysis and ideas described in this chapter were the origins of publication number [1] from the publications list of the author of this thesis. In the sake of readiness and to protect the thesis writing style, the publication number [1] from author's list of publications have not been specifically cited every time that ideas, figures or discussions contained in it are bring to this chapter again. This disclaimer corrects, compensates and justify this fact; being the Ph.D. candidate and the works of his thesis are the origin of the innovation component in the publication number [1] listed in the referred section.

The main objective of this chapter is to highlight the high feasibility potential of the oxy-fuel combustion in CIE to eliminate NO_x, H_xC_y, CO and soot emissions, and to foster the capture of CO_2. Therefore, a CIE model is proposed and two EGR CSs are studied with different heat-exchanger-and-turbocharger disposals to recover the exhaust gas energy which shall be used for the O_2 production and to make possible upcoming CO_2 capture process. Basically, one of EGR CS uses a turbine on EGR line while the other one employs a turbine on cylinder exhaust line.

The ICE oxy-fuel combustion layouts studied in this chapter are based on the preferred realizations patented by Desantes et al. [101]. In addition, a BSCF MIEC 0D-model based on results obtained by Serra et al. [74] is employed as a from-air O_2 provider. Furthermore, a conventional air-combustion CIE model is calibrated with experimental data and used as baseline for oxy-fuel engine model. Finally, the oxy-fuel engine and its auxiliary components (turbochargers and heat exchangers) are assessed under oxy-fuel combustion conditions for the engine full load operation points from 1250 rpm to 3500 rpm.

3.2 System Description

All engine models used in this study are built and implemented in a non-commercial and in-house simulation software so-called Virtual Engine Model (VEMOD) [102] which has been developed by CMT-Clean Mobility and Thermofluids (CMT). VEMOD presents specific sub-models for the 1D gas dynamics, boosting system, air-charge and EGR coolers, throttle valves, heat transfer including gas-to-wall heat exchange and wall temperature prediction,

aftertreatment sub-models [103], etc. Also, VEMOD has been modified to add the 0D MIEC model proposed by Serra et al. [74] which is composed by two sub-models (feed and permeate sides) and, thereby, the molar flux of O_2 permeating the membrane may be expressed as a function of the MIEC temperature and O_2 partial pressure gradient as shown in Equation 3.1 and Equation 3.2. Thus, one may see that temperature has a key effect on O_2 production due mainly to its exponential dependence whereas the O_2 partial pressure ratio only has relevant impact when high MIEC temperatures (around 1000 °C) are employed as presented by Serra's work. Indeed, a geometric mean of inlet and outlet compositions is used to determine the concentration of each component for each side, and mass and energy balances are performed taking into account the heat transfer between both sides. All those mentioned sub-models are then integrated into VEMOD to simulate the engine under steady-state and speed-and-load transient conditions.

$$J_{O2} = K(T) \cdot \ln \frac{P_{feed,O_2}}{P_{permeate,O_2}} \cdot \frac{T}{L} \tag{3.1}$$

where the parameter $K(T)$ is given by:

$$K(T) = A \cdot exp\left(\frac{E_a}{T \cdot R}\right) \tag{3.2}$$

3.2.1 Validation study (Baseline)

A 2.2 L turbocharged and direct injection CIE is used as a baseline for the oxy-fuel combustion model. Thus, a model of this baseline power plant has been developed in VEMOD and calibrated using experimental data to reproduce a state-of-the-art Euro 6d full (E6d full) engine behavior. Once the model adjusted, an optimization procedure was carried out to analyze how far the engine performance could go if worked close to its thermal-mechanical restrictions with 2021 available state-of-the-art turbochargers. These results were thereby employed as optimized baseline engine to set limits and define objectives to be pursued with the oxy-fuel combustion power plant. Figure 3.1 shows the results of the calibration process for some of key parameters (torque and air mass flow) as well as the optimized (Opt) model points. One may see that the calibration of the engine model is good. Thus, that was considered

enough to guarantee a reliable extrapolation to the on-site O_2 generation concept studied for oxy-fuel combustion.

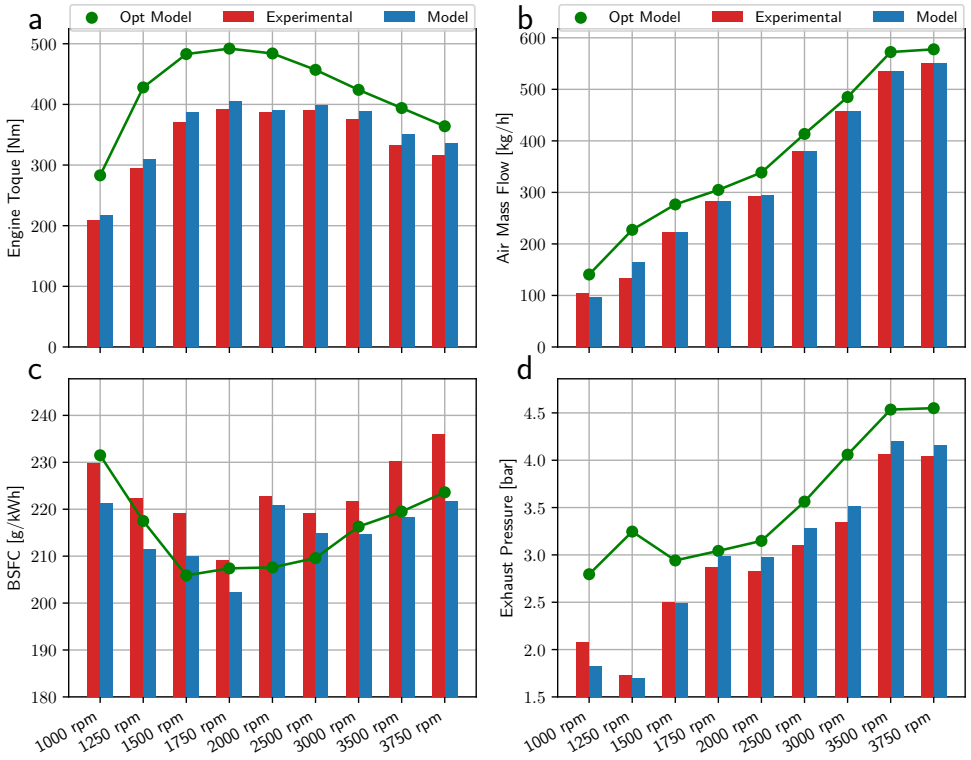

Figure 3.1: Comparison between Model and Optimized Model (Opt Model) results with experimental data for the base turbocharged IC standard air engine.

3.2.2 Implementation of the Oxy-fuel combustion concept

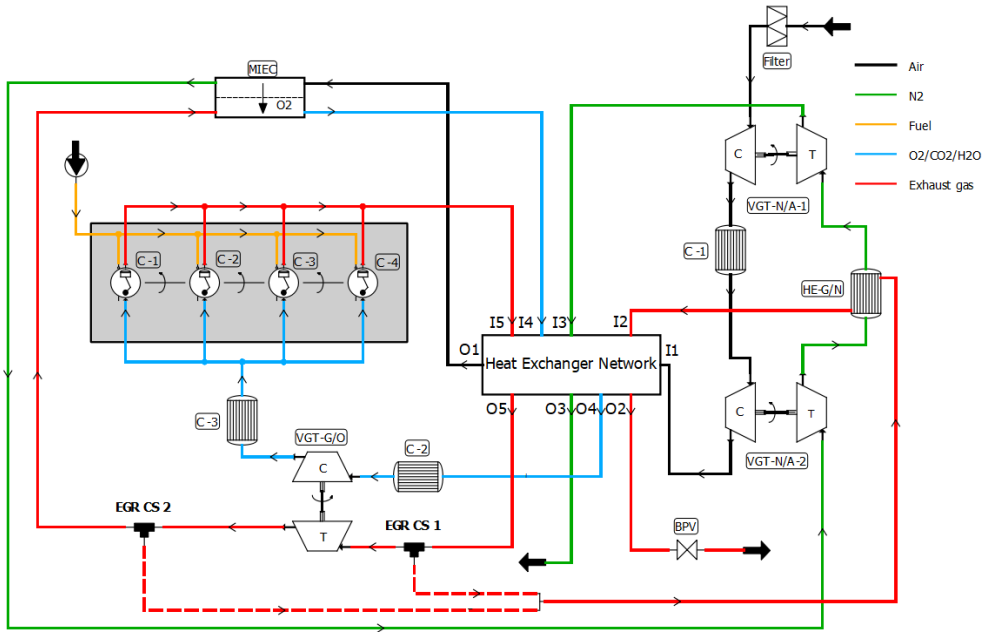

Figure 3.2: Implementation of the oxy-fuel combustion concept for two EGR CS: CS1 and CS2

After having the model calibrated, the four cylinders as well as the intake and exhaust systems of the baseline engine are preserved, and original supporting devices such as heat exchangers (HEs) and variable geometry turbocharger (VGT) are removed and replaced by a new heat-exchangers-and-turbochargers layout in order to adapt the original engine to the oxy-fuel combustion. Thus, using one of the preferred realizations from Desantes's patent [101] as baseline, the number of HEs and turbochargers as well as their sequence were tested by putting them in series, in parallel and combining both configurations, controlling the flow split by means of actuators on the valves. Finally, after testing several heat-exchangers-and-turbochargers layouts, the one that presents the best results in terms of energy recovery, power plant efficiency and packaging is analyzed in this study with two different EGR CSs (see Figure 3.2).

The different fluids are described as follows:

- The orange line represents the fuel flow.

- The black line represents air flow.
- The green line represents a nitrogen-enriched flow.
- The red line represents the exhaust gas flow composed mainly by CO_2 and water.
- The blue line, also called oxidizer line, represents a blend composed by O_2, CO_2 and water which enters the cylinders.

For details about the layout conception one may read previous Desantes's patent [101]. For the purpose of this manuscript and in short, once the membrane requires high pressure and high temperature on its feeding side, a regenerative Brayton cycle with intermediate cooling and reheating between compression and expansion stages, respectively, is formed by the black and green lines. Indeed, the system is similar to an external-combustion Brayton cycle with heat input via a HEN and with gas extraction at MIEC upstream the turbine. The regeneration in the Brayton cycle uses energy from nitrogen-enriched line but also regeneration is used to cool down oxidizer line and CO_2 + H_2O line for easier further CO_2 capture. Thus, the regenerative Brayton cycle is mainly composed by two turbochargers put in series at the system entry to compress air up to about 5 bars, and by several HEs distributed in order to recover heat from exhaust gas and raising the temperature on the feeding side of the MIEC up to about 900 °C.

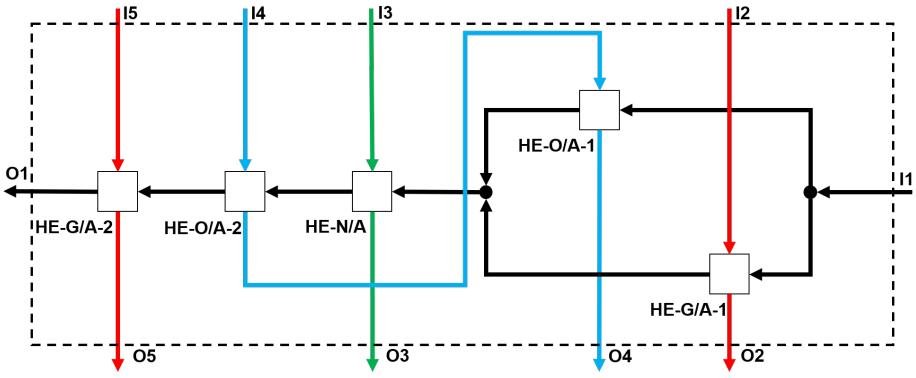

Figure 3.3: HEN

Therefore, air enters the system, pass through two compression steps with intercooler and, before reaching the MIEC feeding side, is heated up firstly by

a HEN (see Figure 3.3). The Cooler C-1 role is to avoid damaging the VGT-NA-1 compressor reducing its inlet temperature and to increase compression efficiency. The HEN is composed by two HEs in parallel and three HEs in series: HE G/A-1 and HE G/A-2 recover energy from exhaust gas line; HE O/A-1 and HE O/A-2 cool down the oxidizer line while they raise air temperature; and HE-N/A tries to heat up air with residual thermal energy of the N_2 line when HE G/A-1 and HE-O/A-1 may not supply enough energy. The nitrogen-enriched flow leaves the MIEC and is submitted to two expansion steps with intermediate reheating to convert the warmed-nitrogen energy into compression energy on the air compressors. For this purpose, the HE G/N retrieves the exhaust gases heat to enhance the VGT-N/A-1 performance increasing the inlet temperature of VGT-N/A-1.

The O_2 permeated in the MIEC is diluted by the EGR which lowers the O_2 partial pressure at permeate side, improving O_2 production driving force and controlling exhaust gases temperature (red line) at cylinders outlet below acceptable limits. Furthermore, the EGR maintains the high combustion temperature under reasonable levels. Afterwards, the oxygen-enriched oxidizer gas (blue line) is cooled down, primarily by air (at HE O/A-2 and HE O/A-1) and thereafter by the cooler C-2 before reaching the VGT-G/O compressor, whereby it is pressurized. In addition, before entering the cylinders, the O_2 is cooled down again by the cooler C-3 for improving the volumetric efficiency of the intake gas raising its density.

For EGR CS1, depicted in Figure 3.2, the combustion products leave the cylinders, rise the temperature upstream of the MIEC (at HE G/A-2), and are split off into two flows: the EGR and the exhaust gas which flows out of the system. The EGR flow is expanded into the VGT-G/O turbine, reducing the MIEC permeate side pressure. On the other hand, the exhaust gas leaving the system is twice cooled down, transferring its heat to regenerative Brayton cycle via HEN and HE G/N (see Figure 3.2), and pass through a back-pressure valve (BPV) which, along with the rack position of the VGT-G/O turbine, controls the T_{exh}.

The EGR control system 2 (EGR CS2), depicted in Figure 3.2, is similar to CS1 and the main difference between them is the VGT-G/O turbine location. Whereas CS1 has the turbine on EGR line, CS2 works with the turbine before the exhaust gas split and, thereby, their T_{exh} controls are different as it is further explained in subsection 3.2.3.

3.2.3 Model description

3.2.3.1 General specifications

For each engine speed, the combustion behavior is governed and imposed by the heat release law obtained from the optimized model of the original engine with air combustion but removing the pilots injections for the sake of simplification, since there was no available combustion law model properly adapted to oxy-fuel combustion application in available engine simulation software (neither in VEMOD nor in other standard commercial packages) when the work present in this chapter was published. In addition, the model used in this chapter is not able to predict the CO formation as well as soot emissions and, as a consequence, the hypothesis that the fuel is completely burned and oxidized is employed. This limitation is not relevant for the purpose of this work since, on the one hand, the literature shows examples of feasible and complete combustion in oxy-fuel combustion engines [56] [35] [39] [104] [60] [61] [62], and, on the other hand, the unique multi-cylinder engine analysis performed here at full loads (and with optimized heat release laws) is fully valid from the viewpoints of management of exhaust energy fluxes and gas dynamics, due to the low energy contained in CO and soot oxidation in CIEs.

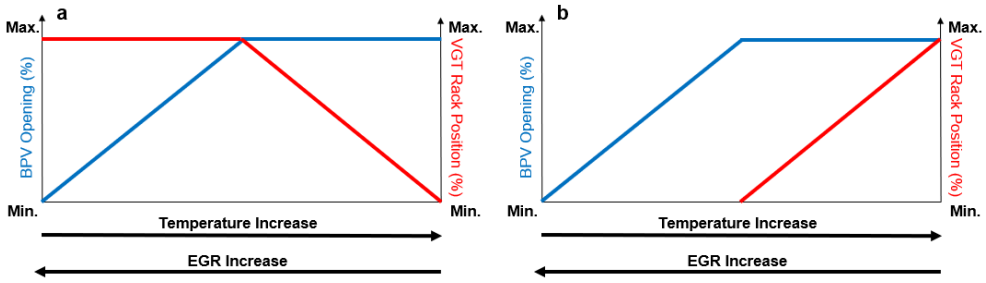

Figure 3.4: T_{exh} control. (a) CS1 ; (b) CS2.

In this study the value of the oxygen–fuel equivalence ratio (λ) is kept constant and equal to 1.1; because on the one hand, since the combustion is carried out by compression ignition with an heterogeneous mixture, high λ improves the in-chamber flame diffusion and reduces soot formation; on the other hand, the O_2 production is costly because the MIEC requires high thermal energy to operate properly which precludes very high λ usage. In addition, this parameter is controlled by the injected fuel as a function of the

amount of produced oxygen, which is a consequence of the boundary conditions imposed to the MIEC.

As mentioned above, high T_{exh} is one of the key factors which impacts the suitable MIEC performance. In this way, after preliminary analyses of area and temperature needed for the proper functioning of the MIEC, which is further detailed in subsubsection 3.2.3.2, T_{exh} is fixed at 1000 °C and is controlled by two actuators in series: the BPV lift and VGT-G/O turbine rack position. As seen in Figure 3.4, which shows the temperature control strategy applied for CS1 and CS2, if the CIE requires higher combustion temperature, the EGR rate must be reduced, increasing the cylinder inlet O_2 concentration and the combustion temperature as a result. For this purpose, the BPV is gradually open keeping the VGT rack at its maximum position for CS1 and at its minimum position for CS2, so at some moment, the BPV achieves the maximum opening and the rack position begins to be modified in a different way depending on CS in question. In CS1, the rack is little by little closed diminishing the EGR rate because the turbine starts to be operated as a throttling valve under quasi-shock conditions. Whilst in CS2, the rack is gradually open which decreases the turbine expansion ratio and, consequently, the compressor suction power, again reducing the EGR rate and CO_2 dilution.

The heat exchange and outlet temperatures of coolers and HEs are calculated based on a constant efficiency model (80% for coolers and 95% for HEs) and some simplifications are made such as the pressure drop on both sides of the HEs is negligible and the mass flow of coolant fluid used in the coolers (in this case water at room temperature) as well as its temperature are held constant. Those hypothesis are considered to calculate the transmitted power for defining specifications of HE facing a future component design. Since each turbocharger has a particular aim and specific flow conditions, their sizes must be different. Therefore, through similarity analysis [105], which may be automatically done by VEMOD defining a variable so-called "scale-factor", the turbocharger size may be either scaled up or scaled down with respect to reference one, in this case the baseline engine turbocharger is employed as reference. Thus, to find the best scale-factor for each turbocharger a multivariable optimization process was carried out using the power of the engine operating at 3500 rpm as objective function to be maximized.

Since the air-nitrogen turbochargers are equivalent on both CSs and the VGT-G/O size found in one case may be used to estimate the scale of the same turbocharge in other CS, the optimization process was only performed

for the CS2. Thus, the scales obtained for VGT-N/A-1 and VGT-N/A-2 are 1.15 and 0.75 respectively, whilst the optimum VGT-G/O scale is 1.70. With regard to CS1, the VGT-G/O scale was determined multiplying the EGR rate calculated in CS2 (70%) by the optimum VGT-G/O scale found in that case, which results the value 1.20.

After studying the rack position impact of the N_2 VGTs on power plant performance, it has been noted that when those turbines operate at the turbocharger maximum efficiency point, with rack lift around 60%, the engine power is maximum for each engine speed. Thus, those air VGTs, which were initially specified in this project, could be replaced by fixed geometry turbochargers (FGT) operating with N_2, which are relatively simpler and more robust at high temperature operation.

3.2.3.2 Membrane area, compression ratio and start of combustion studies

A membrane area study was performed to find out the minimum area needed to supply enough O_2 for the proper power plant operation at 3500 rpm full-load point. In fact, the O_2 flow rate required by the air-combustion conventional engine at 3500 rpm full-load point was specified as target for MIEC O_2 production in this study. Figure 3.5 shows on X axis the air temperature at the membrane entry and on Y axis the partial pressures ratio of O_2. This partial pressure ratio is defined as:

$$\Pi_{O2} = \frac{P_{feed,O_2}}{P_{permeate,O_2}} = \frac{P_{feed} \cdot X_{feed,O_2}}{P_{permeate} \cdot X_{permeate,O_2}} \tag{3.3}$$

where P is the absolute pressure of the gas at each side of the membrane and X the O_2 molar fraction.

The level curves represent the membrane area necessary to produce the required O_2 at the full power point (3500 rpm). Using very large membrane areas would hamper the packaging of the final prototype, however, very small sizes may limit O_2 production or require pressures and temperatures which are inadmissible by the membrane mechanical structure. Therefore, taking into account above considerations, it has been possible to carry out the simulations with a 10 m^2 surface membrane, an affordable size when making a prototype,

without loosing significant power and MIEC filtration efficiency, with a membrane inlet air temperature fixed at 1000 °C, the maximum temperature that the MIEC may withstand respecting its thermal-mechanical limits.

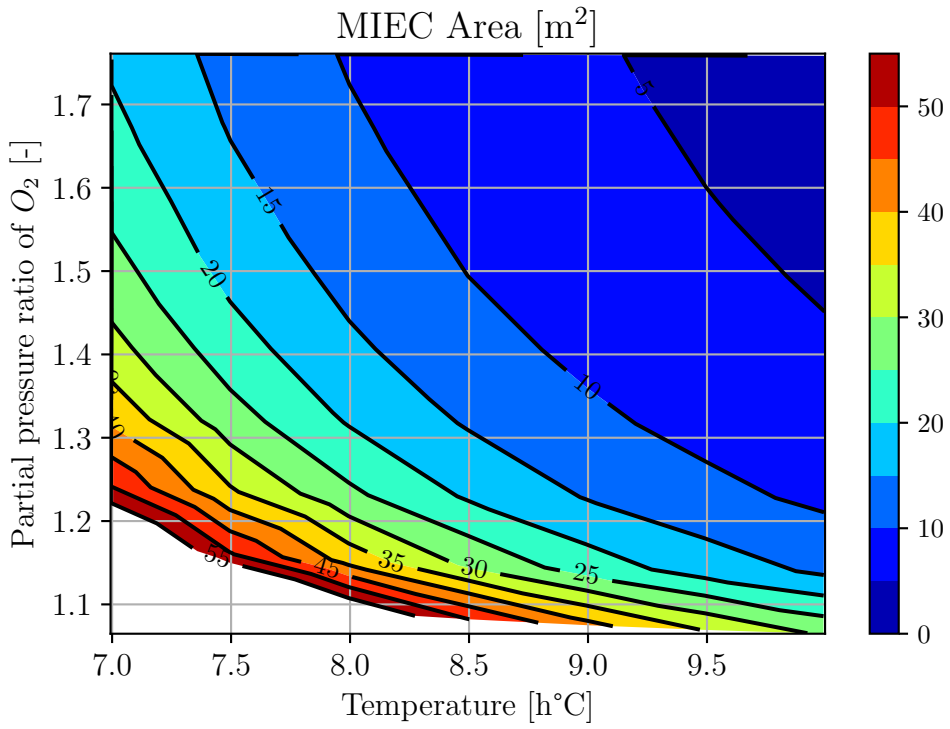

Figure 3.5: MIEC area needed to produce the maximum required O_2.

Since the baseline engine CR (original value = 16.2) had room for improvement due to lower trapped mass as a consequence of oxy-fuel combustion requirements (which means lower maximum in-cylinder pressure) and of engine efficiency, a sweep of CR was carried out taking into account the trade-off between the engine torque and effective efficiency at 2000 rpm (engine speed of minimum consumption for the optimized baseline engine), respecting the in-cylinder maximum pressure (180 bar) defined by the engine manufacturer. As shown in Figure 3.6, within a CR range from 26 to 30, torque and efficiency are maximum without significant differences and, thereby, CR equal 28 is assumed as the optimum one.

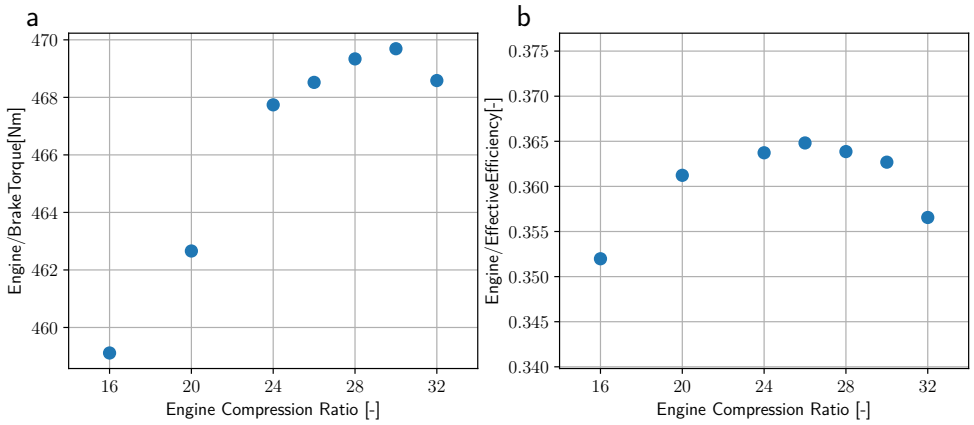

Figure 3.6: CR study at 2000 rpm full load. (a) Engine brake torque; (b) Engine effective efficiency

Likewise, in order to find the best Start of Combustion (SOC) and Start of Injection (SOI) for each engine speed and CS a SOC-based sweeping process with constraints (Maximum In-cylinder Pressure $\leq$ 180 bar and T_{exh} = 1000 °C) was carried out trying to maximize engine efficiency as well as torque as shown in Equation 3.4 and depicted in Figure 3.7, whereby red and blue points represent SOCs with pressures higher (penalized) and lower than 180 bar respectively, and green point denotes the optimum SOC which maximizes the objective function in Equation 3.4.

$$\max_{soc} \quad \text{ObjectiveFunction}(soc) = \text{Efficiency}(soc) \times \text{Torque}(soc) \tag{3.4}$$

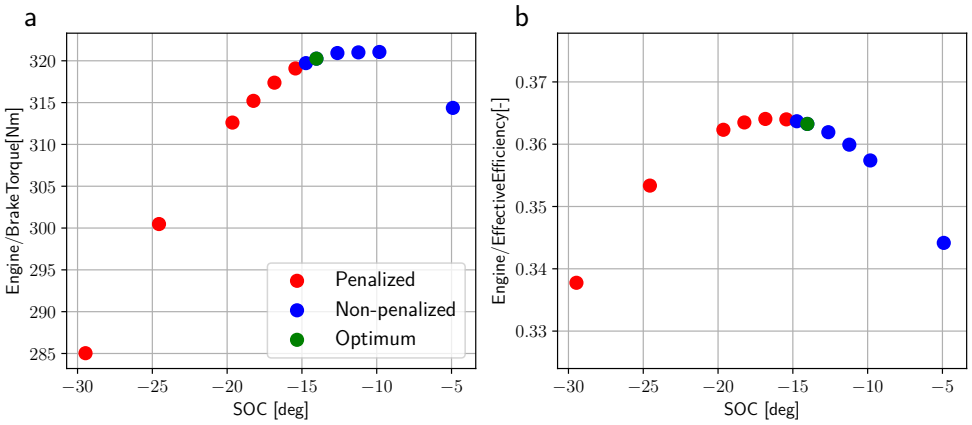

Figure 3.7: SOC-based sweeping study at full load for 3500 rpm

Finally, Table 3.1 summarizes the general model specification for each proposed CS.

Table 3.1: General specifications.

Parameter	**CS1**	**CS2**
VGT-N/A-1 scale	1.15	
VGT-N/A-2 scale	0.75	
VGT-G/O scale	1.20	1.70
VGT-G/O Min. Rack Position	5%	20%
VGT-G/O Max. Rack Position	100%	
Min. BPV lift	1%	
Max. BPV lift	100%	
T_{exh}	1000°C	
λ	1.10	
CR	28	
Membrane area	$10m^2$	

3.3 Results and discussion

After having fixed key parameters like CR and membrane area at 3500 rpm (see Table 3.1) and determined the power plant control procedure which is the same for each engine speed (using the BPV and VGT-G/O rack position to

control the T_{exh} at 1000 °C, fuel amount to control λ, and maximizing the engine effective efficiency actuating on SOC), a full load engine speeds sweeping was carried out from 1250 rpm to 3500 rpm. In this section temperature, pressure and mass flows diagrams are analyzed for 3500 rpm (subsection 3.3.1), instantaneous results for lowest and highest engine speeds are compared (subsection 3.3.2) and average results from 1250 rpm to 3500 rpm are discussed (subsection 3.3.3).

3.3.1 Temperature, pressure and mass flow diagrams

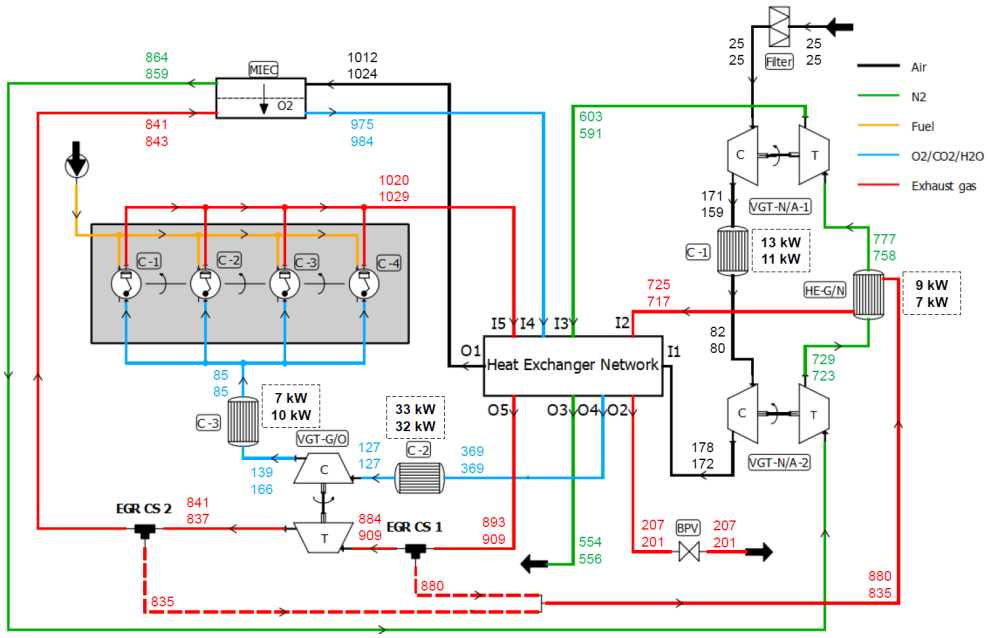

Figure 3.8: Power (in kW) and temperature (in °C) distribution diagram at 3500 rpm for EGR CS1 (top values) and EGR CS2 (bottom values)

Figure 3.8 shows the power and temperature diagram for each EGR CS at the maximum rated power engine speed whereby the energy requirements are more important. Numerical values representing the calculated temperatures in degrees Celsius is added next to each flow line with top values for CS1 and bottom ones for CS2. In addition, the heat power exchanged is shown next to each HE and cooler following the aforementioned sequence.

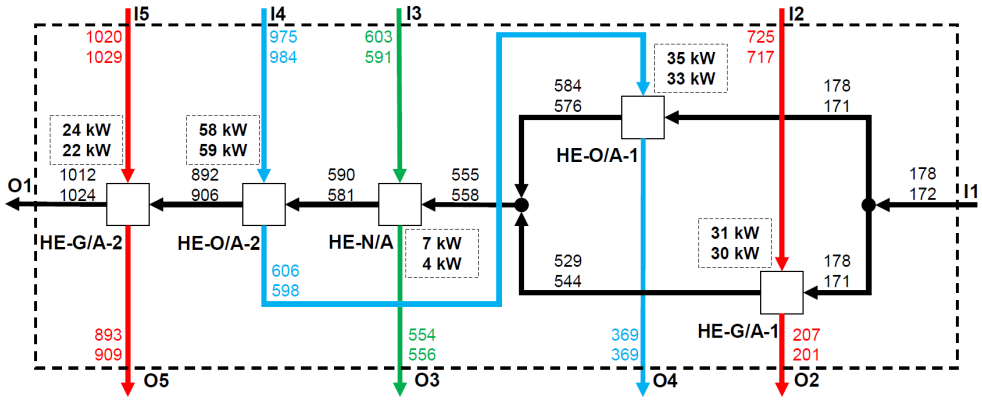

Figure 3.9: Power (in kW) and temperature (in °C) distribution diagram at 3500 rpm inside HEN for EGR CS1 (top values) and EGR CS2 (bottom values)

Also, the same power and temperature distribution is shown inside HEN (see Figure 3.9). In general, the two proposed CSs exhibit analogous results in terms of thermal energy distribution and, in both cases, the HE-O/A-2 is the biggest HE (with approximately 60 kW power), so it may be separated into two or more HE (in series or parallel) in forthcoming acquisition. Although the HE-G/A-2 is the most crucial HE, since its outlet and inlet temperatures are very high (1000 °C) that may be a technological limitation, the other HE possess temperatures within orders of magnitude of those found in the road transport sector.

Figure 3.10 and Figure 3.11 show the effect of each EGR CS on pressure distribution and mass flow distribution respectively following the same representation scheme as for temperature diagram (with top values for CS1 and bottom ones for CS2). Although EGR CS1 presents higher pressure than EGR CS2 in Brayton cycle, as the EGR CS2 may slightly yield higher temperature at MIEC feed side inlet and it posses lower MIEC permeate side pressure due to its VGT-G/O turbine expansion and BPV full opening which improve the MIEC filtration efficiency (comparing the mass fraction of O_2 at nitrogen-enriched line: 4% for CS1 and 2% for CS2), they produce similar amount of O_2 (around 101 kg h^{-1}). For both CSs, all engine speeds analyzed in this work present similar exhaust gas composition with mass fraction of O_2 of 6%. Moreover, as depicted on Figure 3.11, there is a mild difference (around 10 kg h^{-1}) between CSs in terms of mass flow at brayton and CI cycles lines.

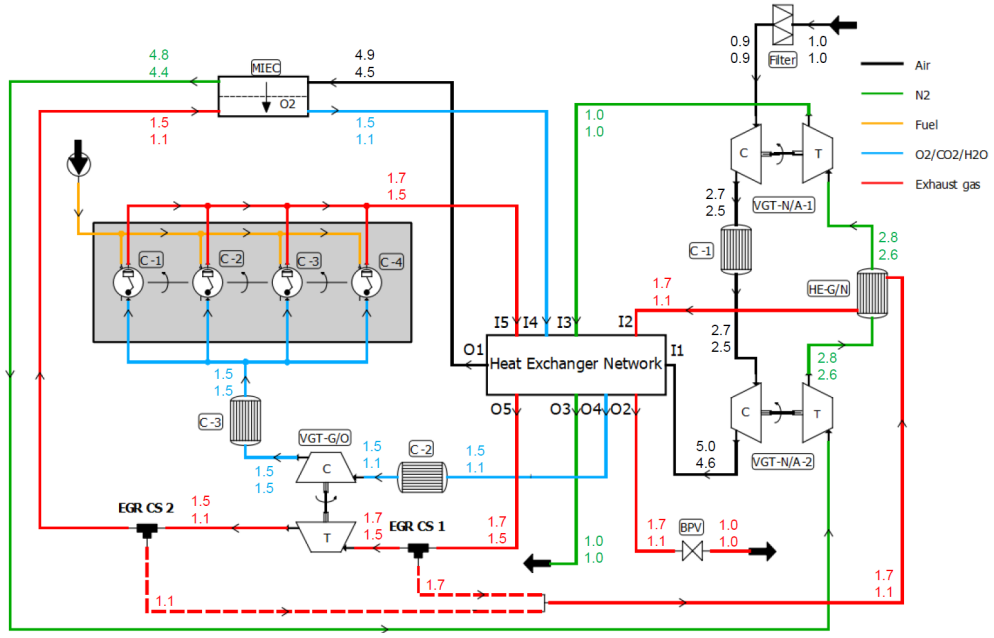

Figure 3.10: Pressure (in bar) distribution diagram at 3500 rpm for EGR CS1 (top values) and EGR CS2 (bottom values)

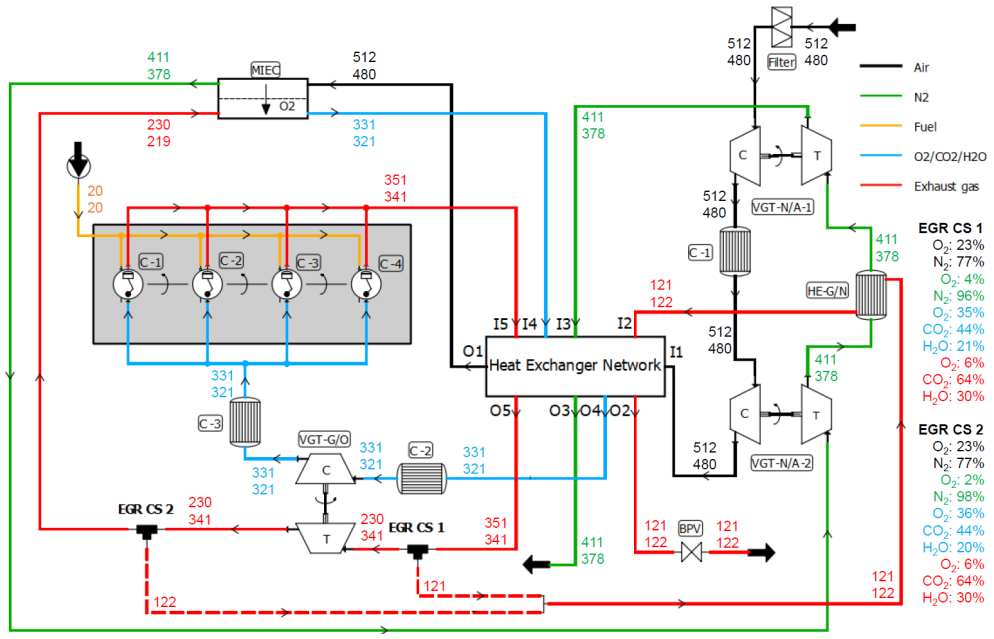

Figure 3.11: Mass flow (in $\mathrm{kg\,h^{-1}}$) distribution diagram at 3500 rpm for EGR CS1 (top values) and EGR CS2 (bottom values)

3.3.2 Instantaneous results

Figure 3.12 shows the main in-cylinder instantaneous results for the lowest and highest engine speeds. The two proposed CSs possess analogous outcomes that distinguish from optimized baseline results especially in terms of in-cylinder O_2 content (Figure 3.12d): the oxy-fuel combustion presents 15% more O_2 mass fraction than a conventional combustion, even though the trapped O_2 mass is lower in oxy-fuel combustion at 3500 rpm, since there is not enough thermal power in the exhaust gases to produce more O_2 in the MIEC at 1000 °C of T_{exh}. Although the in-chamber temperatures are greater in oxy-fuel combustion due to its lesser inert concentration, they are not outrageous if compared to optimized baseline case (Figure 3.12b).

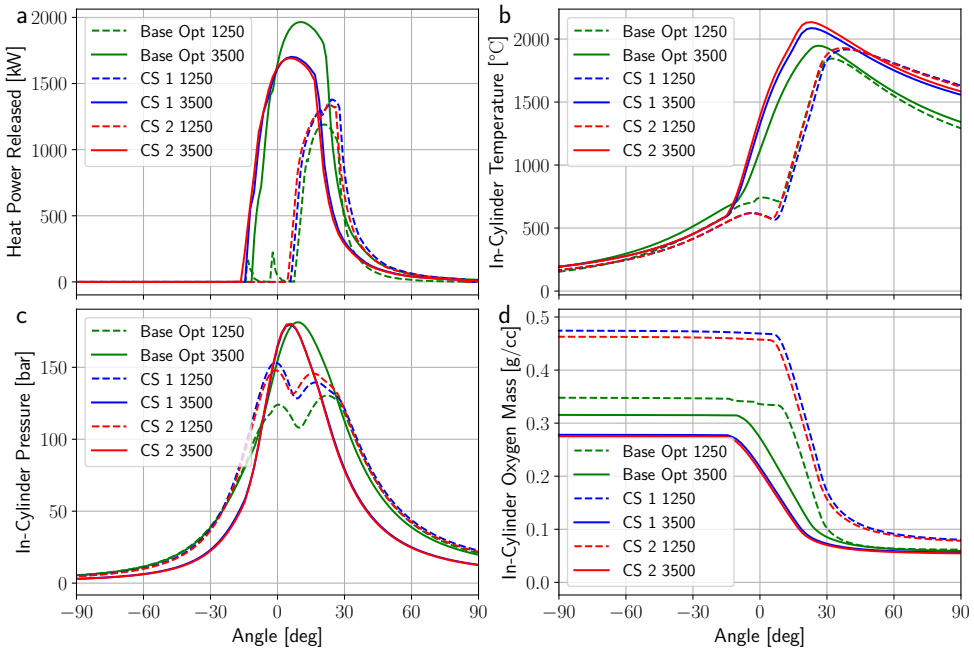

Figure 3.12: The instantaneous results of in-cylinder parameters at 1250 rpm and 3500 rpm full load

Figure 3.13b shows the indicator diagrams for the highest engine speed. The effect of the CR is observed in the minimum volume value of each cycle. The smaller amount of trapped mass combined with the characteristics of that trapped gas (with lower γ under oxy-fuel combustion conditions) lead to a smaller area enclosed by the high-pressure loop. However, part of this loss may be compensated by reducing pumping losses thanks to an air management system completely different from the conventional one.

As already mentioned, the SOC value has been optimized in terms of torque and efficiency by limiting the maximum pressure inside the cylinder to 180 bar. At high speed, despite the increase in CR in oxy-fuel combustion configurations, the lower in-cylinder pressure at IVC (Intake Valve Close) (Figure 3.13b) causes pressure and temperature reduction during the compression stage (compare Figure 3.12b and Figure 3.12c), this allows a slight advance of SOC compared to the conventional power plant without exceeding the maximum pressure limitation (Figure 3.12c). It is observed how the trapped O_2 is a little less than in the conventional case (Figure 3.12d) with the consequent

reduction of heat released power (Figure 3.12a). In addition, with the T_{exh} control, the oxy-fuel combustion cases present similar O_2 mass if compared to the conventional one, but with lower pressure at IVC (Figure 3.13b), which may indicate that less diluents are trapped (in next subsection that behavior is detailed) due to lesser CR and lower cylinders intake pressure (Figure 3.13b), which allows reaching a higher temperature at the end of the expansion (Figure 3.12b).

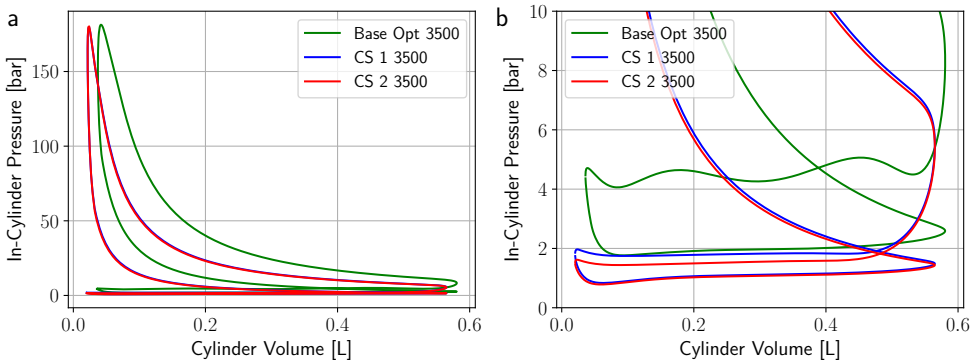

Figure 3.13: In-cylinder pressure-volume diagram at 3500 rpm full load. (a) Full diagram; (b) Zoom in on pumping loop

Finally, at low engine speeds, the supercharging effect on the conventional CIE is much lower and, thereby, at IVC the pressure and temperature conditions are similar. Such an effect, combined with the higher CR and the possibility of achieving high O_2 concentrations in oxy-fuel combustion conditions, allows higher pressure values at the end of the compression stage but without exceeding the in-chamber pressure threshold (180 bar) (Figure 3.12c). In addition, under these conditions the mass flows inside CI cycle are lower which decreases the membrane thermal requirements to produce the necessary oxygen. As may be seen in Figure 3.12d the trapped O_2 is much higher than the conventional case. However, the need to have energy in the membrane forces the system not to prioritize the CI cycle performance optimization, delaying combustion and not reaching the maximum pressure limit value. For this preliminary study, pilot combustion was not used in oxy-fuel combustion cases as it can be observed in the case of conventional combustion (Figure 3.12a). Therefore. a more in-depth study of pilot combustion shall to be carried out in future works.

3.3.3 Average results and Turbochargers maps

Although the oxy-fuel combustion presents lower torque than the optimized original power plant at high engine speeds (Figure 3.14a and b), if compared to original non-empowered engine, it provides similar brake power in such a zone and greater torque at low engine speed because the N_2 turbochargers, working at their maximum efficiency points, seek to supply the maximum air flow regardless of engine speed (Figure 3.14e). As the oxy-fuel combustion cases possess lower CR and cylinders intake pressure than the conventional one (Figure 3.15e), less oxidizer mass is trapped (Figure 3.14f). With respect to BSFC, even though the oxy-fuel combustion configurations present lower pumping losses than the air-based combustion ones (Figure 3.15b), it may be seen that only at high engine speeds the oxy-fuel power plants may achieve values similar to those offered by the conventional combustion engine with differences of around 30 g/kWh and 5 g/kWh at low and high engine speeds respectively (Figure 3.14c). That is due to the fact that there is less thermal power available in the exhaust gases at low engine speeds to generate enough O_2 and the power plant has to work under more delayed ignition conditions (Figure 3.14d) in order to convert more heat power released at combustion process into thermal energy for the exhaust gases than into mechanical power. Furthermore, as the specific heat ratio (γ) of the CO_2 and water mixture is lower than the γ of the N_2 [71], the engine indicated efficiency is lower for oxy-fuel combustion than for a conventional combustion. In addition, the oxy-fuel combustion temperature is higher which renders more heat losses (Figure 3.15a) at low engine speeds. Despite such higher consumption, it must be taken into account that the oxy-fuel combustion power plant is mainly designed to capture CO_2. Therefore, that purpose could compensate that energy consumption penalty, since BSFC is not correlated anymore with CO_2 emissions, and valorization of high-purity captured CO_2 could be used to partially compensate the increment in cost to owner due to higher BSFC.

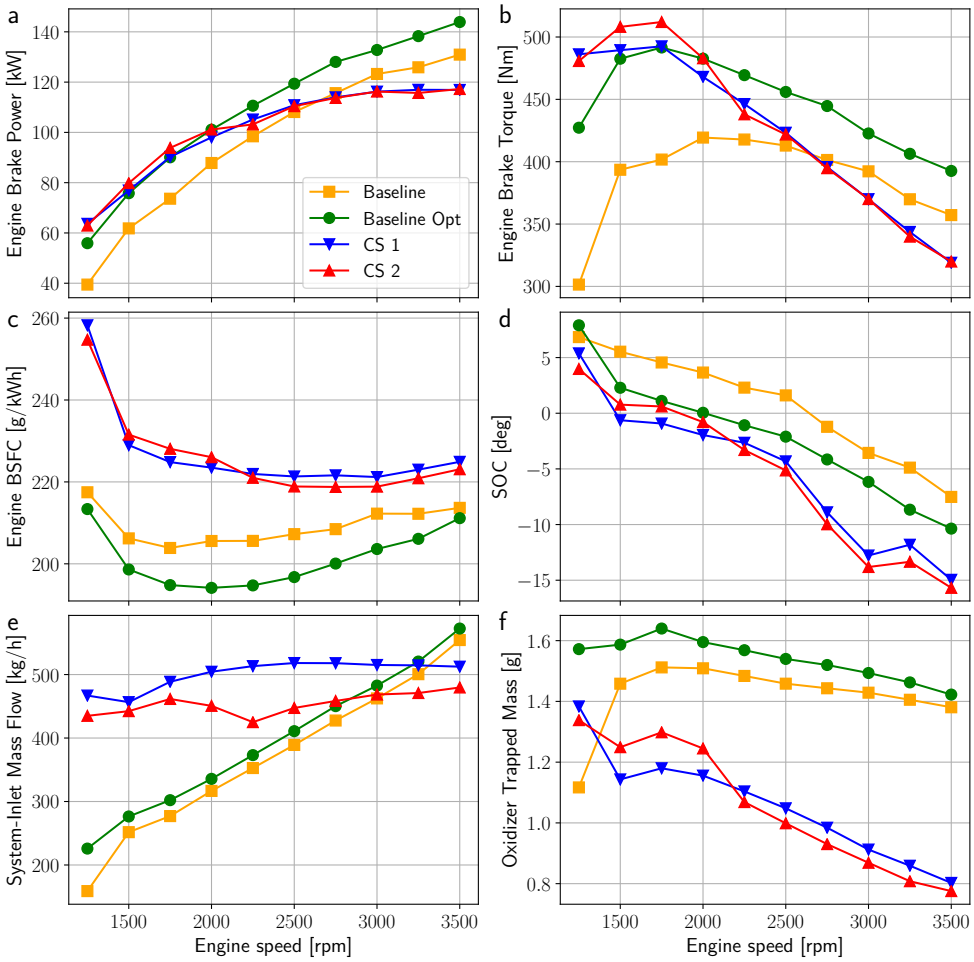

Figure 3.14: The average results of relevant average engine variables of oxy-fuel combustion EGR options (CS1 and CS2) compared to baseline and baseline optimized cases with air combustion engine (Baseline and Baseline Opt)

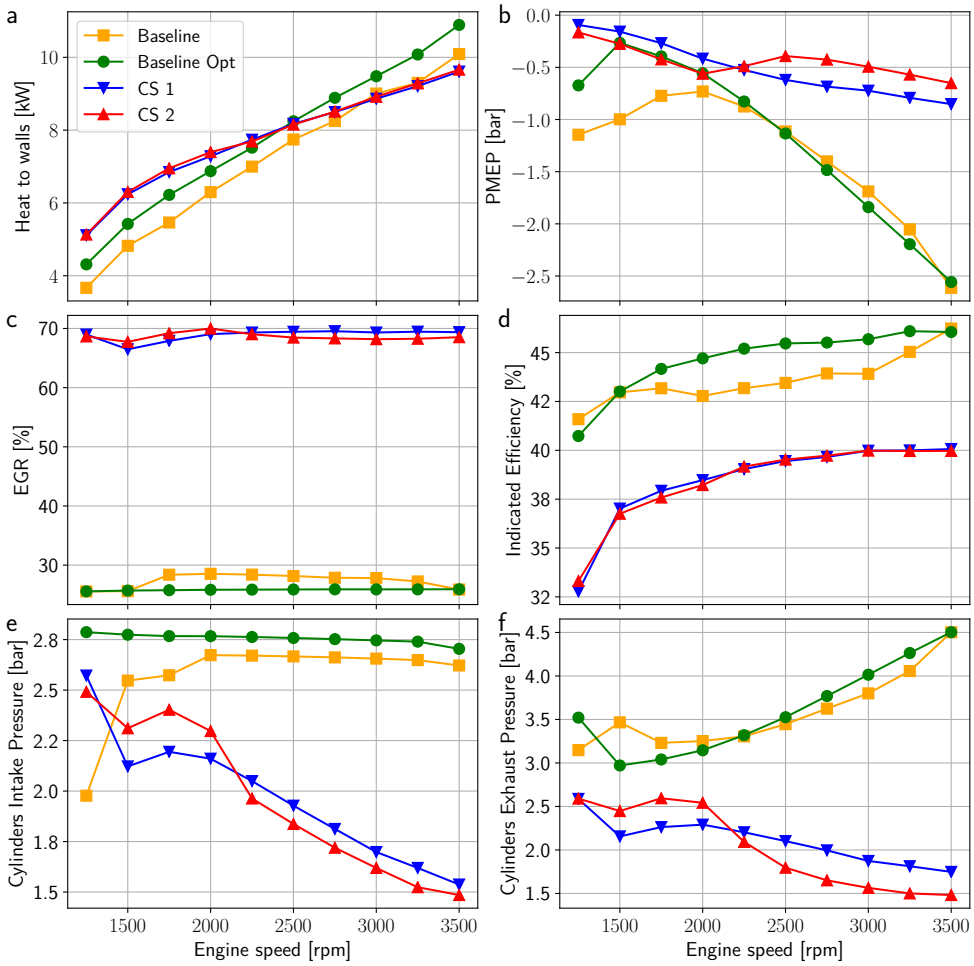

Figure 3.15: The average results of relevant average engine variables of oxy-fuel combustion options (CS1 and CS2) compared to baseline and baseline optimized cases with air combustion engine (Baseline and Baseline Opt)

For CS2, the MIEC filtration efficiency, defined by the ratio between the O_2 permeated in the MIEC and the total O_2 which enters the MIEC feed side, is almost constant at 90% when the back pressure valve (BPV) is fully open (Figure 3.16a and f), since the permeate pressure (also called back pressure) is low which entails a greater pressure gradient (Figure 3.16a, c, d and e). Nevertheless, whenever the back pressure valve is slightly closed, the permeate pressure increases, reducing the partial pressure of O_2 gradient which impairs the MIEC filtration even if high temperatures are observed at the end of the expansion stage (Figure 3.12b). Also, the mass flow of O_2 transferred in the MIEC varies in a similar way to engine power (Figure 3.14a and Figure 3.16b) with respect to engine speed, showing that the engine power only depends on total O_2 produced by MIEC (compare Figure 3.14a with Figure 3.16b).

In general, it has been noted that, for all engine speeds in both CSs, the EGR remains relatively constant at 70% to regulate the T_{exh}. However, as mentioned above, the O_2 production decreases at low engine speeds leading to less mass flow at MIEC permeate side, so the Brayton cycle air exchange less thermal power with the CI cycle hot gases (oxidizer and exhaust gas in Figure 3.3). Therefore, when that happens, the N_2 line (green line in Figure 3.2) energy becomes more useful to heat up the Brayton cycle air when the thermal powers provided by oxidizer and exhaust gases are insufficient, justifying by this way the HE N/A location (Figure 3.3 and Figure 3.17).

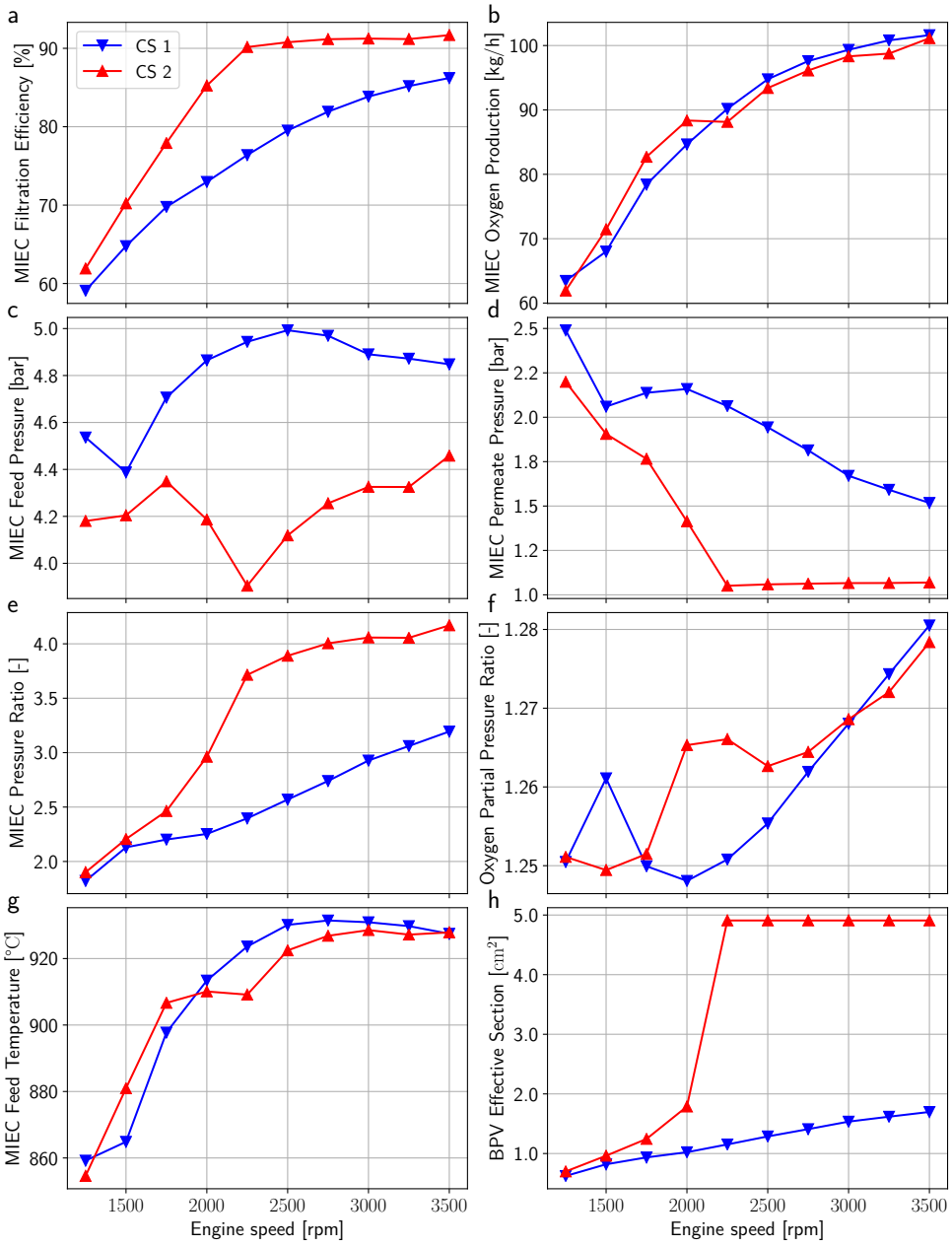

Figure 3.16: The average results comparing both EGR CSs: CS1 and CS2

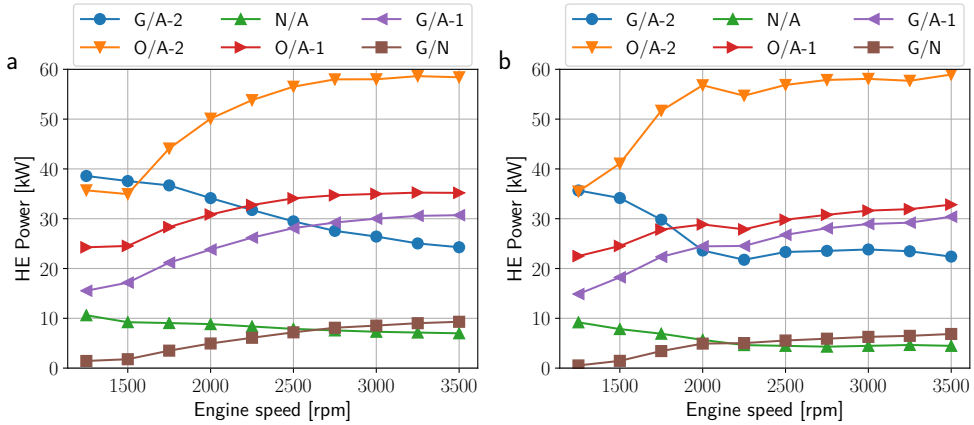

Figure 3.17: HE power average results: (a) CS1; (b) CS2

The compressors integrated in the Brayton cycle have the full load operating points gathered in small area of the maps (Figure 3.18e, f, g and h) which makes easier their future selection and purchase. Furthermore, those compressors operate close to their maximum efficiency points with high compression ratios (from 2 to 3). Figure 3.18c and d show the VGT-G/O maps of the CS2 and two operating zones may be observed: the high engine speeds zone whereby the EGR is controlled by the VGT-G/O rack; and the low engine speeds zone whereby the rack is fixed at its minimum position and the BPV regulates the T_{exh}.

Regarding the VGT-G/O of CS1 (see Figure 3.18a and b), it has been found that at full load points the T_{exh} is only controlled by the BPV working with the turbine completely open, which would be similar to not utilize any turbocharger in CS1. However, this turbocharger has been kept in the model in case its usage is required at other operating points (e.i. lowering the power plant load).

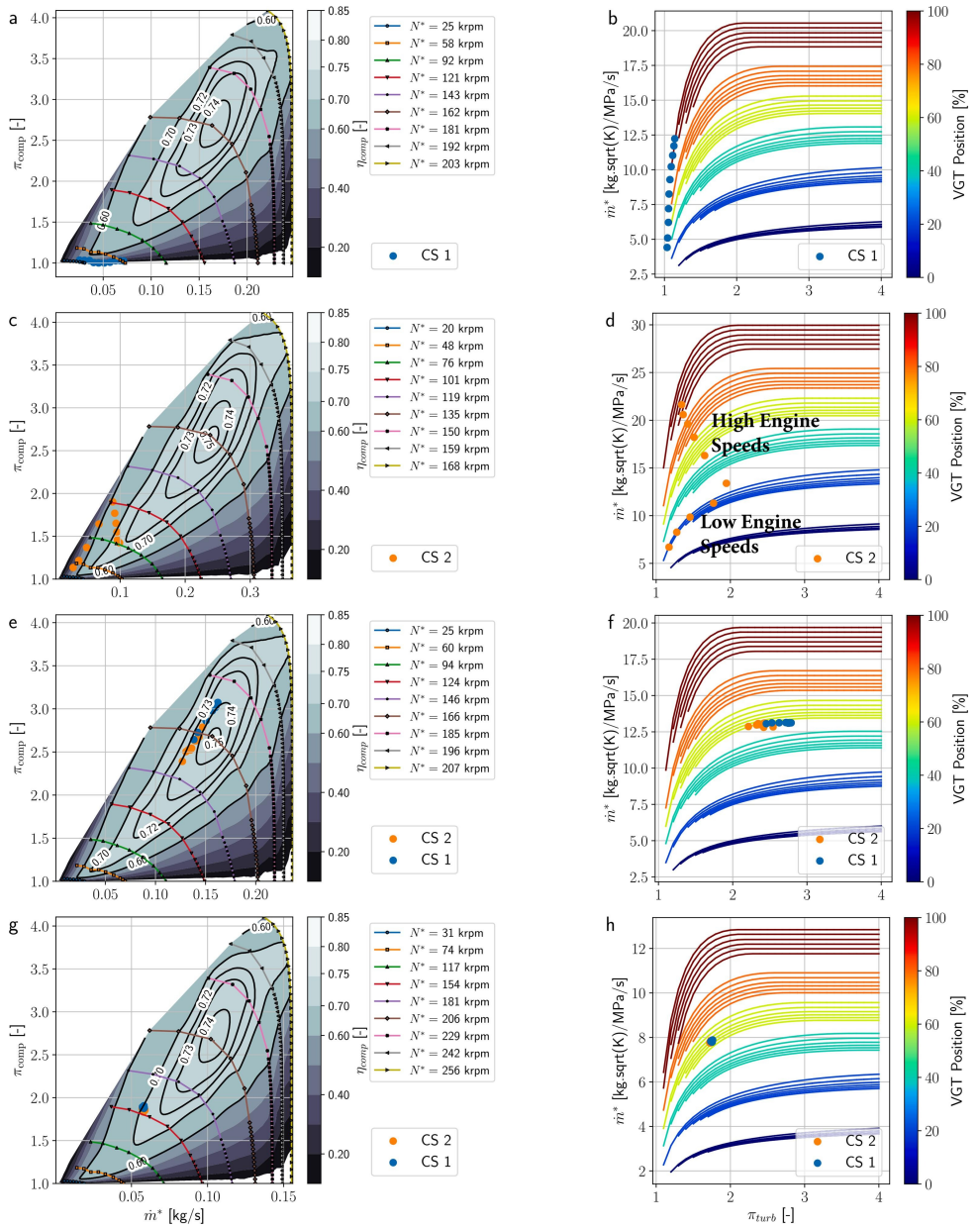

Figure 3.18: Turbochargers maps: CS1 VGT-G/O (Compressor a and Turbine b), CS2 VGT-G/O (Compressor c and Turbine d), VGT-N/A-1 (Compressor e and Turbine f), VGT-N/A-2 (Compressor g and Turbine h).

In summary, the behavior differences between both layout can be enumerated as follow:

- At low engine speeds, EGR CS2 operates with higher cylinder intake and exhaust pressure (Figure 3.15e-f) due to the energy recovered by the turbine (Figure 3.18c-d). The pumping losses are higher (Figure 3.16g) due to turbine back-pressure; the membrane efficiency is bigger (Figure 3.16a) and so it is the O_2 production (Figure 3.16b).

- That allows to trap more mass at low engine speeds and more O_2 (Figure 3.14f), burn more fuel (working at constant equivalence ratio) and, thus, produce more torque (Figure 3.14b). It also allows to introduce more EGR inside the cylinder (Figure 3.15c). Due to this last effect, the O_2 mass fraction trapped inside the cylinder is then lower (Figure 3.12d), so the combustion needs to be slightly delayed (Figure 3.14d) to obtain the desired T_{exh}. This produces a loss in efficiency and an increase in fuel consumption (Figure 3.14c).

- However, as the engine speed increases with EGR CS2 configuration, the backpressure valve must be opened to regulate the temperature (Figure 3.16h) until it saturates at its maximum opening. After the maximum backpressure valve opening, the temperature is regulated varying the geometry of the turbine (VGT) (Figure 3.4b). As the turbine opens, its capacity to recover energy decreases. Then, EGR CS2 is working with lower pressures in the permeate side of the membrane (Figure 3.16d), what makes the feed side to also work with lower pressures if the partial pressure difference is to be kept constant. This reduces the mass flow passing through the Brayton cycle (Figure 3.18f and Figure 3.14e). With a lower mass flow in the feed side, the O_2 production is reduced even with a higher membrane efficiency, which presents an asymptotic behavior against the rotational speed (Figure 3.16a).

- From all these results, on the one hand, it can be concluded that EGR CS1 presents a smoother behavior throughout the whole full load curve, although with a lower low-end torque. The turbine placed in the EGR line (VGT-G/O) does not work in any point of the whole full load line (Figure 3.18a-b), so it may be removed from this configuration leading to a decrease in the cost and complexity of the system.

- On the other hand, a configuration like EGR CS2 may have higher acquisition costs, but its low-end torque is higher, and its high-speed full-load power is like that of EGR CS1 with a reduced BSFC.

Chapter 3 Bibliography

[1] J. Serrano, F. Arnau, L. García-Cuevas, and V. Farias. "Oxy-fuel combustion feasibility of compression ignition engines using oxygen separation membranes for enabling carbon dioxide capture". *Energy Conversion and Management* 247 (Nov. 2021), p. 114732. DOI: 10.1016/j.enconman.2021.114732 (cit. on pp. xii, 25, 40).

[35] A. Van Blarigan, D. Kozarac, R. Seiser, R. Cattolica, J.-Y. Chen, and R. Dibble. "Experimental Study of Methane Fuel Oxycombustion in a Spark-Ignited Engine". *Journal of Energy Resources Technology* 136 (Mar. 2013), p. 9. DOI: 10.1115/1.4024974 (cit. on pp. 5, 18, 46).

[39] Z. Kang, S. Chen, Z. Wu, J. Deng, Z. Hu, and L. Li. "Simulation Study of Water Injection Strategy in Improving Cycle Efficiency Based on a Novel Compression Ignition Oxy-Fuel Combustion Engine". *SAE International Journal of Engines* 11 (Apr. 2018). DOI: 10.4271/2018-01-0894 (cit. on pp. 5, 20, 21, 46).

[56] A. Osman. "Feasibility Study of a Novel Combustion Cycle Involving Oxygen and Water". *SAE Technical Papers* (Nov. 2009), p. 14. DOI: 10.4271/2009-01-2808 (cit. on pp. 18, 46).

[60] T. Sharma, A. Rao, and M. K. "Homogeneous Charge Compression Ignition (HCCI) Engines: A Review". *Archives of Computational Methods in Engineering* 23 (May 2015). DOI: 10.1007/s11831-015-9153-0 (cit. on pp. 19, 46).

[61] R. Mobasheri, A. Aitouche, Z. Peng, and X. Li. "Influence of Oxy-Fuel Combustion on Engine Operating Conditions and Combustion Characteristics in a High Speed Direct Injection (HSDI) Diesel Engine under Homogenous Charge Compression Ignition (HCCI) Mode". In: *SAE Technical Paper*. WCX SAE World Congress Experience, Apr. 2020, p. 10. DOI: 10.4271/2020-01-1138 (cit. on pp. 19, 46).

[62] A. Mohammed, A. Elkhazraji, S. Jan, and B. Johansson. "A Study on the Performance and Emissions of HCCI Oxy-Fuel Combustion in a CFR Engine with Recirculated Carbon Dioxide". In: *SAE Powertrains, Fuels and Lubricants Meeting*. Sept. 2020, p. 13. DOI: 10.4271/2020-01-2065 (cit. on pp. 20, 46).

[71] G. D. Perry R. *Perry's chemical engineers's handbook eighth edition*. McGraw-Hill, 2008 (cit. on pp. 21, 58, 113, 125).

[74] D. Catalán Martínez, M. Santafé-Moros, J. Gozálvez-Zafrilla, J. García Fayos, and J. Serra. "Characterization of oxygen transport phenomena on BSCF membranes assisted by fluid dynamic simulations including surface exchange". *Chemical Engineering Journal* 387 (May 2020), p. 124069. DOI: 10.1016/j.cej.2020.124069 (cit. on pp. 22, 24, 40, 41, 70).

[101] F. J. Arnau, J. Benajes, J. M. Desantes, J. R. Serrano, J. M. Serra, D. Catalán-Martínez, and L. M. García-Cuevas. *Motor de combustión interna de hidrocarburos auto transportable que no emite gases nocivos ni CO_2; secuestra CO_2 atmosférico y fabrica CO_2 líquido subcrítico*. P201930285. Mar. 2019 (cit. on pp. 40, 43, 44, 71).

[102] J. Martín, F. Arnau, P. Piqueras, and A. Auñón. "Development of an Integrated Virtual Engine Model to Simulate New Standard Testing Cycles". *SAE Technical Papers* 2018-April (2018). DOI: 10.4271/2018-01-1413 (cit. on p. 40).

[103] F. Payri, F. J. Arnau, P. Piqueras, and M. Ruiz. "Lumped Approach for Flow-Through and Wall-Flow Monolithic Reactors Modelling for Real-Time Automotive Applications". In: *SAE International*. Apr. 2018. DOI: 10.4271/2018-01-0954 (cit. on p. 41).

[104] D. T. Guide. *Engine Emission Control*. URL: https://dieselnet.com/tech/engine_emission-control.php (cit. on p. 46).

[105] B. N.C. *Fundamentals of turbocharging*. Concepts NREC, 2005 (cit. on p. 47).

Chapter 4

Strategies to extend power plant load operation map range in oxy-fuel combusiton mode

Contents

4.1 Introduction

The works, analysis and ideas described in this chapter were the origins of publication number [2] from the publications list of the author of this thesis. In the sake of readiness and to protect the thesis writing style, the publication number [2] from author's list of publications have not been specifically cited every time that ideas, figures or discussions contained in it are bring to this chapter again. This disclaimer corrects, compensates and justify this fact; being the Ph.D. candidate and the works of his thesis are the origin of the innovation component in the publication number [2] listed in the referred section.

This chapter aims to continue the study developed in chapter 3 wherein the oxy-fuel combustion is applied to a CIE over the full speed-load range using an O_2 supply system based on ionic-electronic conducting membrane (MIEC) technology. Therefore, this second part intends to extend the power plant operating map towards part-load conditions assessing the system performance in oxy-fuel combustion mode. To do so, the regenerative cycle layout built in previous chapter, as well as the BSCF MIEC model based on results obtained by Serra et al. [74] for O_2 production are maintained, and the EGR CS1 depicted in that chapter is considered to propose a strategy to lower the engine load controlling the amount of injected fuel combining the following approaches:

1. The first approach consists of working with a constant λ, lowering the T_{exh} and, thereby, decreasing the MIEC O_2 production capacity.
2. The second approach is based on keeping T_{exh} constant while the load is reduced by decreasing the amount of injected fuel.

Actually, EGR CS1 was selected to pursue with this study since VGT-G/O turbine had been completely open throughout the engine full-load curve for this configuration in precedent chapter and, thereby, the VGO-G/O turbine uselessness may be confirmed at engine partial-load operation and, then it may be removed for the sake of system simplification in succeeding chapters.

By modifying T_{exh} and λ, temperature-lambda maps are generated to decide the optimal combination in terms of power plant performance. Thus, the system behavior is analyzed at three engine speeds (1250 rpm, 2500 rpm and 3500 rpm) with different load levels and CR of 20. For that purpose, the

baseline engine model is calibrated with experimental data within part-load operation ranges, and combustion reduced order model calibrated with CFD data is applied to simulate the combustion process under oxy-fuel combustion conditions.

Indeed, that combustion model uses the apparent combustion time (ACT) characteristic of a diffusion combustion process to find out clear relations between the rate of heat release, in-cylinder conditions (O_2 concentration, air density, ...) and the injection rate law [106] [107]. As shown by Arregle et al. [108], a genetic algorithm adjusts some constants of the model with experimental data from several engines, and the model validation is based on a vast range of tested engines with different operating conditions.

Finally, specific parameters are researched to verify whether the system produces enough energy to heat up the MIEC for generating the necessary oxygen. Therefore, they might be very useful as design parameters for finding out oxy-fuel power plant operation limits and estimating MIEC design features.

4.2 Methodology

The engine model employed in this study is built up and implemented into VEMOD as done in previous chapter. Moreover, the same 2.2 L turbocharged and direct injection CIE used as a baseline for modeling the oxy-fuel power plant considering the full-load operation depicted in chapter 3 is utilized in this chapter.

Figure 4.1 shows how part-load points are reasonably calibrated, indicating that the VEMOD model is still valid to simulate the same baseline engine within a broader operating range. Also, the benchmark power plant optimized model calibrated in that previous chapter is preserved as well as the sub-models of auxiliary elements composing the oxy-fuel layout such as VGTs, HEs and gas flow regulation components (valves, plenums, and pipes). In particular, the combustion chamber geometry and injection system are deeply optimized considering the CFD outputs presented by Serrano et al. [58] in their study of a SC CIE in oxy-fuel combustion mode. Some heat-exchanger and turbocharger layouts were previously proposed in patent [101]. However, the optimized one in terms of engine efficiency, energy recovery and packaging presented in

chapter 3 is still contemplated maintaining the EGR CS1 described there as starting point to study methods to reduce the power plant load as shown in Figure 4.2.

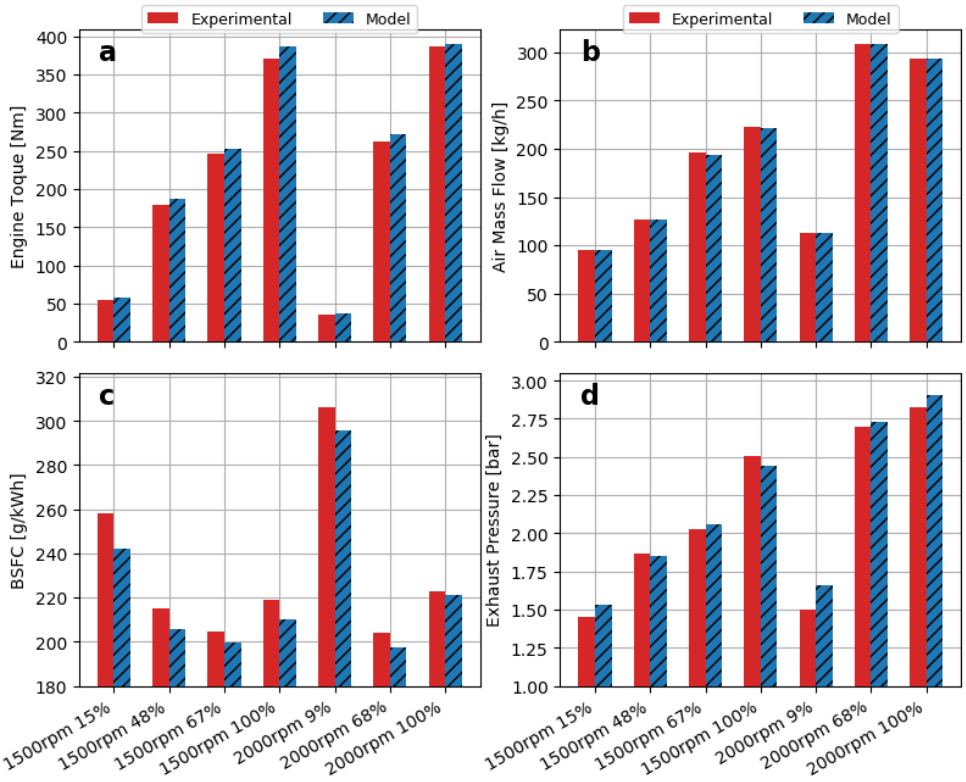

Figure 4.1: Comparison between experimental and simulation data for the baseline turbocharged IC standard air engine considering various load levels for two engine speeds. (a) Engine torque; (b) Air mass flow entering the cylinders; (c) BSFC; (d) Exhaust manifold pressure.

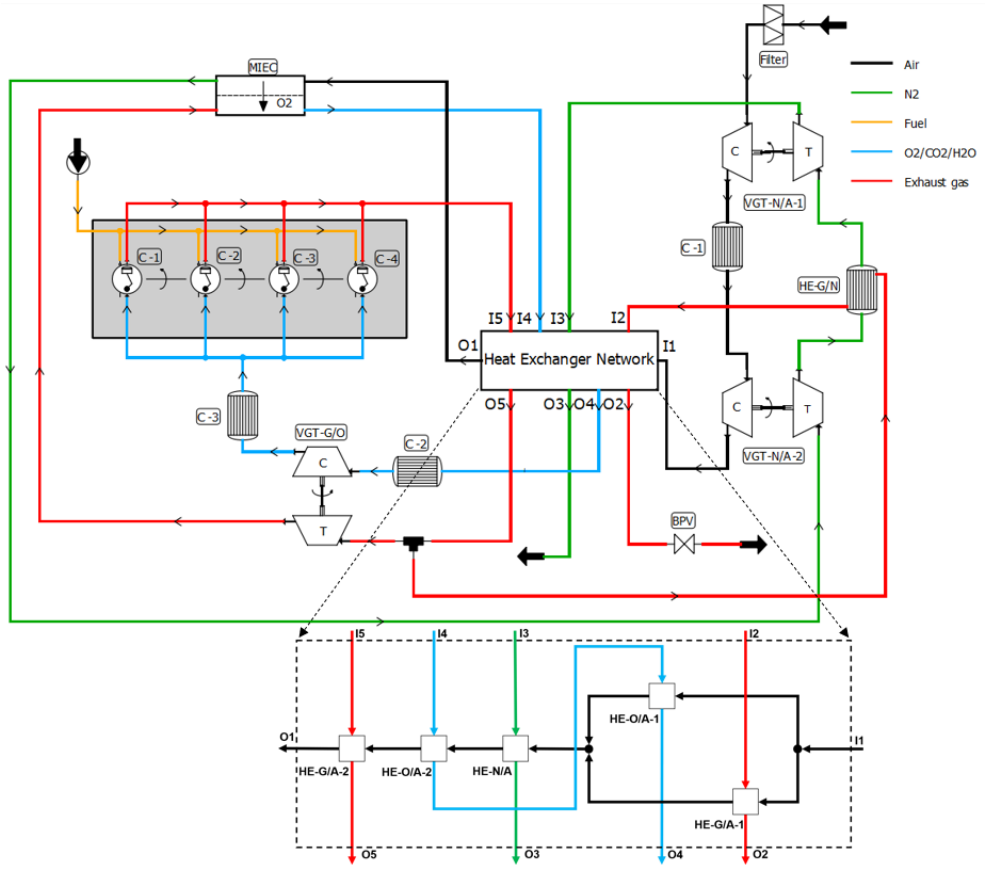

Figure 4.2: Layout of the oxy-fuel combustion concept

4.2.1 Brief model description

As mentioned above, ACT is used in this study to simulate the combustion behavior for predicting the SOC and heat power released, taking into account premixed and diffusion zones. In this case, that model was calibrated and validated by Arregle and al. [106] [107] [108] testing several engines at various operating situations. Moreover, it has been calibrated with CFD simulation data obtained by Serrano et al. [58] for an oxy-fuel combustion SC CIE with the same geometry, fuel, and injection system as the one used in this chapter. The ACT model has been adjusted based on a wide parametric study using results presented in [58] as described by Serrano et al. [109].

The tuning of the model has been made to consider the larger specific heat capacity of the CO_2 molecule compared with O_2 and N_2 (the dominant parts of the air). An increment of CO_2 in the combustion chamber (maintaining the same intake temperature and pressure) will vary the specific heat capacity of the mixture causing a lower temperature rise, and a larger ignition delay period in the combustion phase. It is important to note that this 3D physical model used as reference to adjust ACT has turbulence, atomization and combustion models which presumably guarantees its reliability. Figure 4.3 indicates that ACT was satisfactorily calibrated, predicting the outcomes of the diffusive region and premixed phase during combustion process for a particular case studied by Serrano et al. [109].

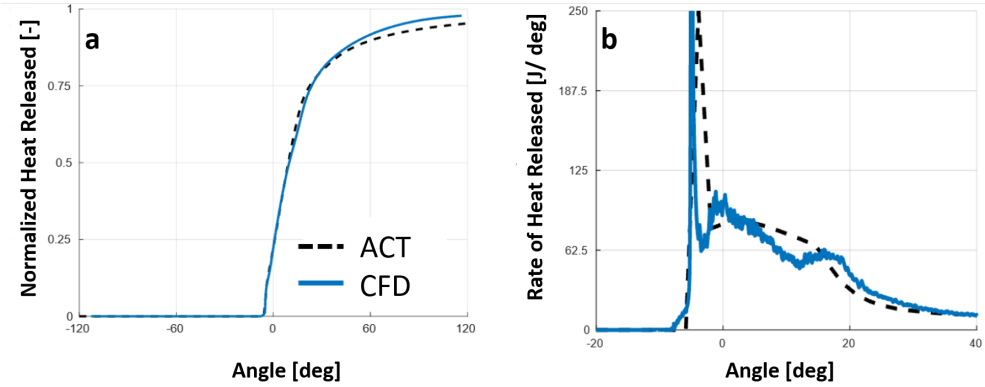

Figure 4.3: Comparison between ACT and CFD at same operating conditions [109].

For all studies carried out in this chapter, same control philosophy depicted in Figure 3.4a with same operating range is employed, membrane surface is still fixed at $10\,m^2$ and the cooler C-3 model is still operated to maintain a $85\,°C$ cylinder intake temperature in order to avoid in-cylinder water condensation.

4.2.2 Compression ratio study

As a starting point, the power plant full-load curve from 1250 rpm to 3500 rpm is built up taking into account ACT as combustion model and CR = 28. Actually, that value is found in chapter 3 after a geometry assessment for the same multi-cylinder engine employed in this chapter, but using a heat released law (HRL) as the combustion model. Therefore, in this subsection CR = 28

is ascertained whether it is still the best value regarding engine performance, otherwise it would have to be modified.

The SOI is submitted to an optimization process with constrains (T_{exh} = 1000 °C and Maximum In-cylinder Pressure $\leq$ 180 bar) to maximize torque and engine efficiency as depicted in Equation 3.4. Figure 4.4 shows a comparison in terms of average and instantaneous results between ACT and HRL combustion models, maintaining $\lambda = 1.1$ for both cases.

If compared to imposed HRL outputs, engine brake power using ACT model adapted to oxy-fuel combustion is slightly lower (Figure 4.4a), and its BSFC is mainly more elevated at high-intermediate engine speeds (on average, more than 7 %) (Figure 4.4b) due to significant unburnt fuel (around 5 %) present at the end of combustion phase (Figure 4.4a). That issue is not observed using the HRL model due to its assumption of complete fuel burn. Indeed, as oxy-fuel combustion modeled with ACT has a peak of heat release at SOC (Figure 4.4b), which is not seen in conventional combustion, SOI must be delayed not to surpass maximum in-cylinder pressure (Figure 4.4c). In that case, BPV must be closer which entails more in-chamber trapped mass (Figure 4.4d) to control combustion temperature (Figure 4.4d). Furthermore, from 1250 rpm to 2000 rpm the engine brake torque is relatively constant for ACT (Figure 4.4c) because in-cylinder maximum pressure is almost reached only with compression phase and, thereby, exhaust temperature had to be reduced from 1000 °C to 925 °C so as to fulfill the pressure constrain. In fact, 925 °C is the maximum exhaust temperature allowed within that engine speed range wherein in-chamber maximum pressure may be lesser or equal than 180 bar and, consequently, that suggests that CR should be reduced (Figure 4.4c).

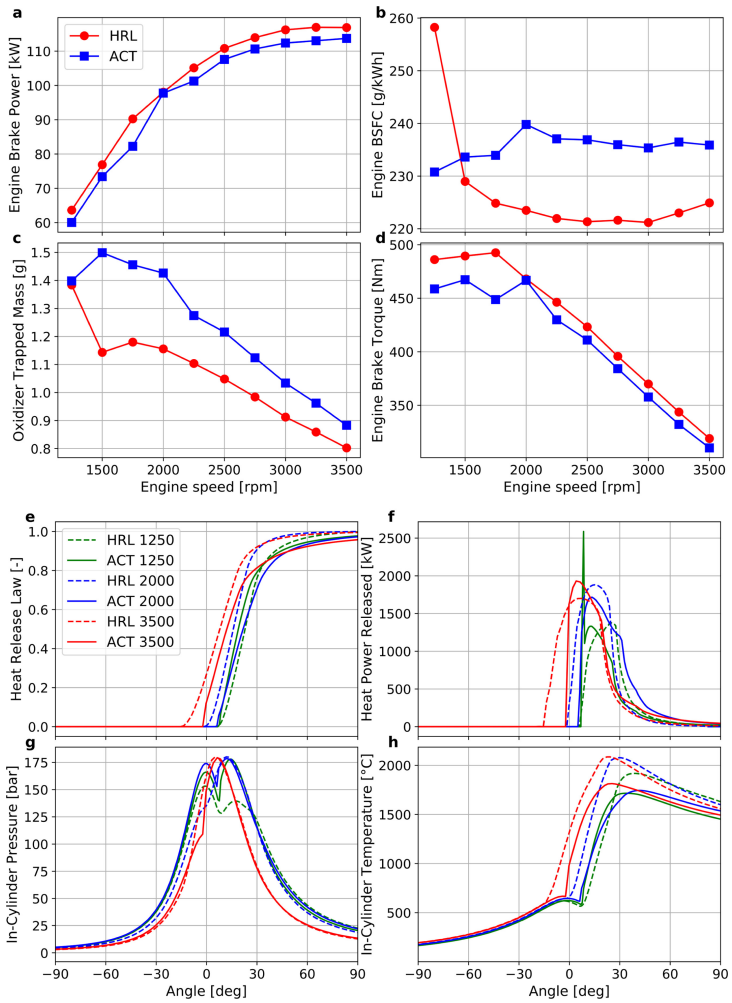

Figure 4.4: Full-load curve average results of relevant engine variables with CR=28 and for both combustion models (a, b, c and d). Instantaneous results of in-cylinder parameters at 1250 rpm, 2000 rpm and 3500 rpm at full load with CR = 28 for both combustion models (e, f, g and h).

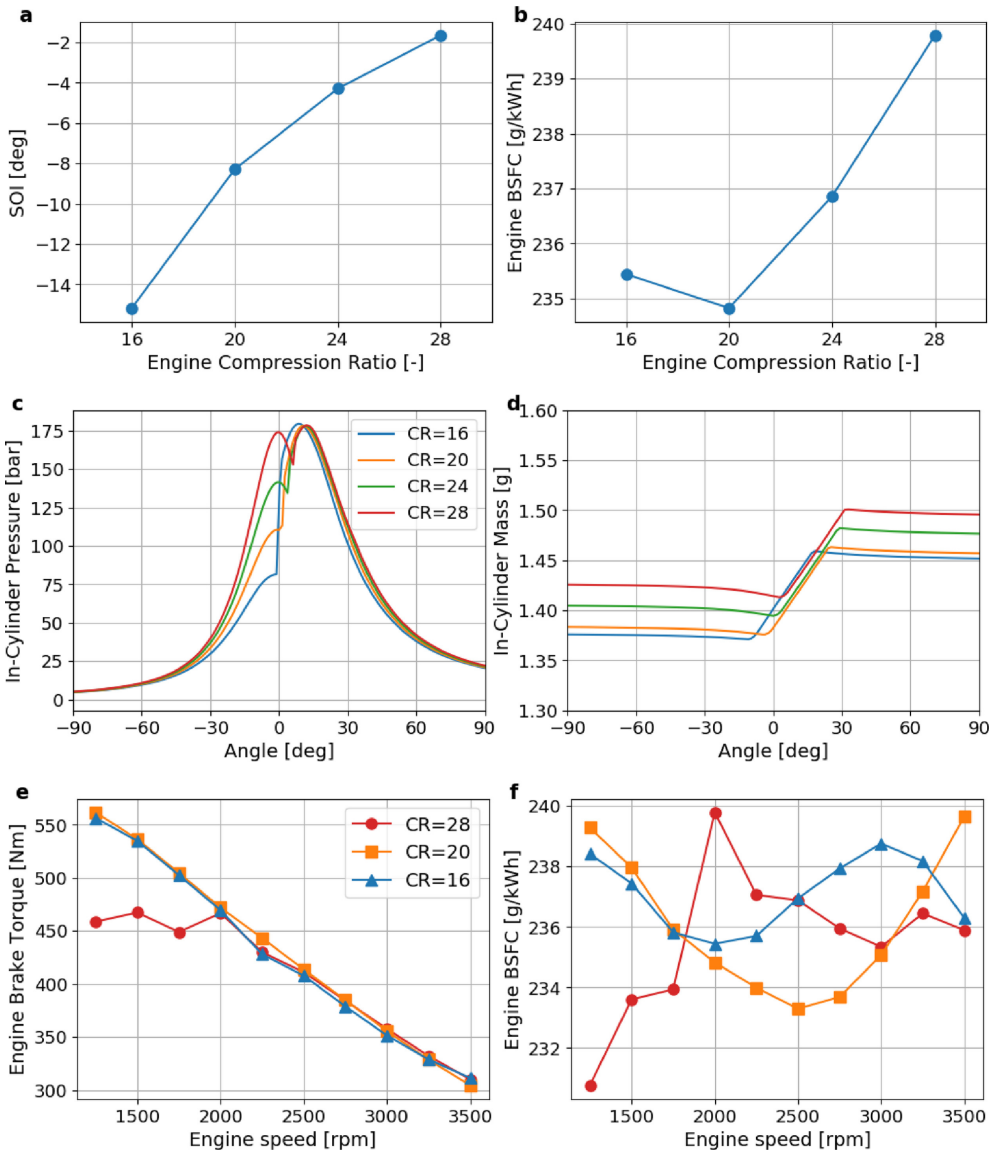

Figure 4.5: Average results for CR curve at 2000 rpm (a and b). Instantaneous results for different CRs at 2000 rpm (c and d). Full-load curve average results for different CRs (e and f).

Thus, a study of CR is carried out at 2000 rpm, that is the maximum-torque engine speed, wherein compression stage pressure peak begins to be around 180 bar. In this regard, other variables are held constant, and SOI is optimized as already described. As shown in Figure 4.5, with lower CR there is more room to bring forward SOI (Figure 4.5a) without exceeding pressure constrain (Figure 4.5c). At high CRs, the compression process already achieves elevated pressures, forcing SOI delay and increasing BSFC. In addition, more delayed SOI implies more EGR to control T_{exh}, which is reflected on more trapped mass (Figure 4.5d), and a minimum BSFC is reached with CR = 20 (Figure 4.5b). Likewise, to conclude this study, a full-load curve is generated optimizing SOI and taking into account three CRs of interest: 16 (power plant baseline original CR), 28 (best CR found in chapter 3 and [58]), and 20 (optimum CR at 2000 rpm). Also, calculations for CR = 16 and CR = 20 could be performed using $T_{exh} = 1000\,°C$, not imposing a limitation on torque improvement from 1250 rpm to 1750 rpm (Figure 4.5e). In addition, as shown in Figure 4.5f, CR = 20 appears to have slightly better effective efficiency in general, especially within intermediate engine speeds and, thereby, that value is considered satisfactory to be set for carrying out all calculations from high to low power plant loads.

4.3 Results and discussion

As mentioned before, the strategy to extend the engine map towards part-load conditions at fixed rotation speed is based on combining two approaches, generating a vast amount of operating points. The first one is based on operating the system with less T_{exh} at constant λ, decreasing MIEC thermal energy and, consequently, O_2 generation, which results in less injected fuel. Furthermore, in-cylinder convective heat losses may be reduced with lower T_{exh}. The second approach maintains T_{exh} constant at any value, and λ is increased by decreasing the amount of injected, leading to less brake power. In the latter situation, combustion may be enhanced due to more in-chamber O_2 enrichment at the cost of "wasting" unused O_2 produced at MIEC. Accordingly, the objective is to look for the optimum combination of both approaches regarding power plant minimum consumption. Finally, the optimization method outlined in Equation 3.4 is also applied for each combination of actions, and some indicators are proposed to analyze limitations encountered to lower power at a given engine speed.

4.3.1 Average and instantaneous results and turbocharger maps

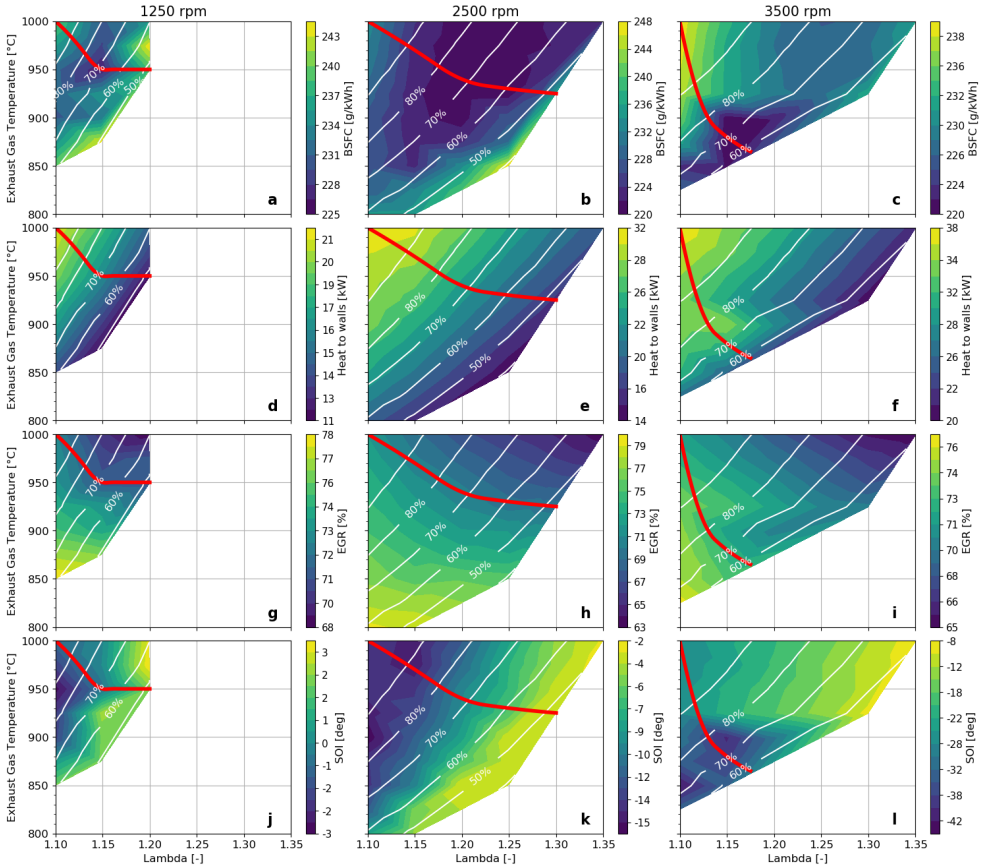

Figure 4.6: Part-load maps for average results of relevant engine variables for 1250 rpm, 2500 rpm and 3500 rpm. The white lines drawn on maps represent level curve for engine load relative to maximum power achieved at corresponding engine speed.

In Figure 4.6, Figure 4.7 and Figure 4.8 x-axis represents λ and y-axis T_{exh}. White lines represent the percentage of power plant load as shown on color maps. As may be seen, the full-load point would be located in the upper-left corner and would correspond to the operating point with the highest T_{exh}=1000 °C and the lowest λ=1.1. As these simulations are very time-consuming, the points of T_{exh} and λ are created with discrete intervals of 25 °C and 0.05 respectively without impairing data analysis accuracy.

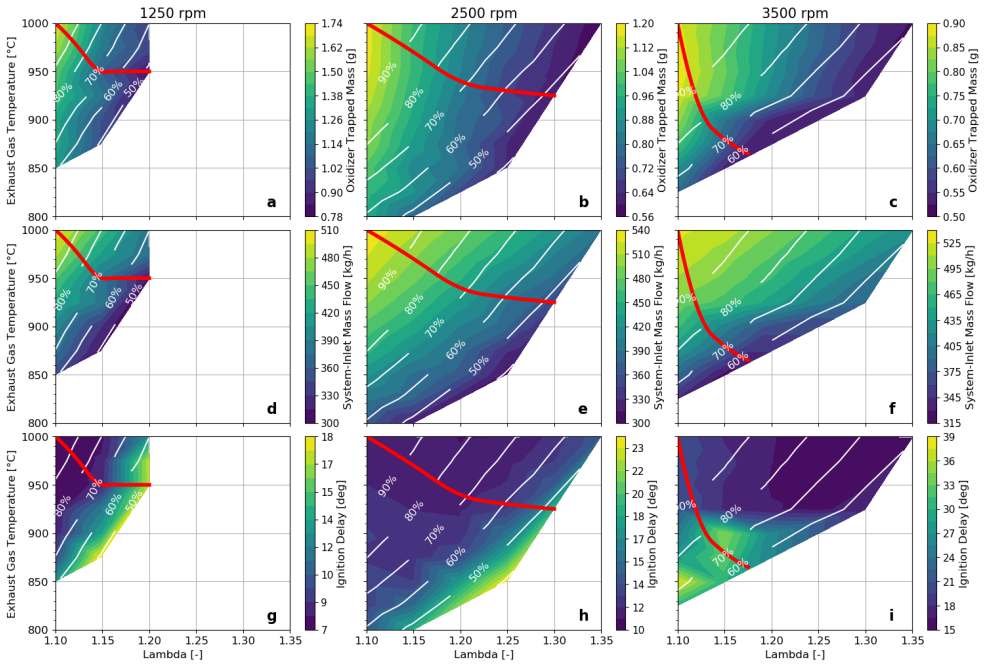

Figure 4.7: Part-load maps for average results of relevant engine variables for 1250 rpm, 2500 rpm and 3500 rpm. The white lines drawn on maps represent level curve for engine load relative to maximum power achieved at corresponding engine speed.

As depicted in Figure 4.6a-c, there is a sort of minimum consumption zone due to low exhaust temperatures, with less convective heat losses (Figure 4.6d-f), coupled to excess of oxygen, that enhances combustion performance. BSFC values down to 220 g/kWh are reached for 2500 rpm and 3500 rpm and 225 g/kWh for 1250 rpm. Actually, the best effective-efficiency temperature-lambda paths are present as the red lines in Figure 4.6, Figure 4.7 and Figure 4.8 for different engine speeds. In addition, when Figure 4.6a-c is contrasted with Figure 4.6g-i, the red lines similarly follow iso-EGR trends, indicating that an increase in λ should be followed by around 71 % to 73 % EGR rate in order to reduce power plant load optimally.

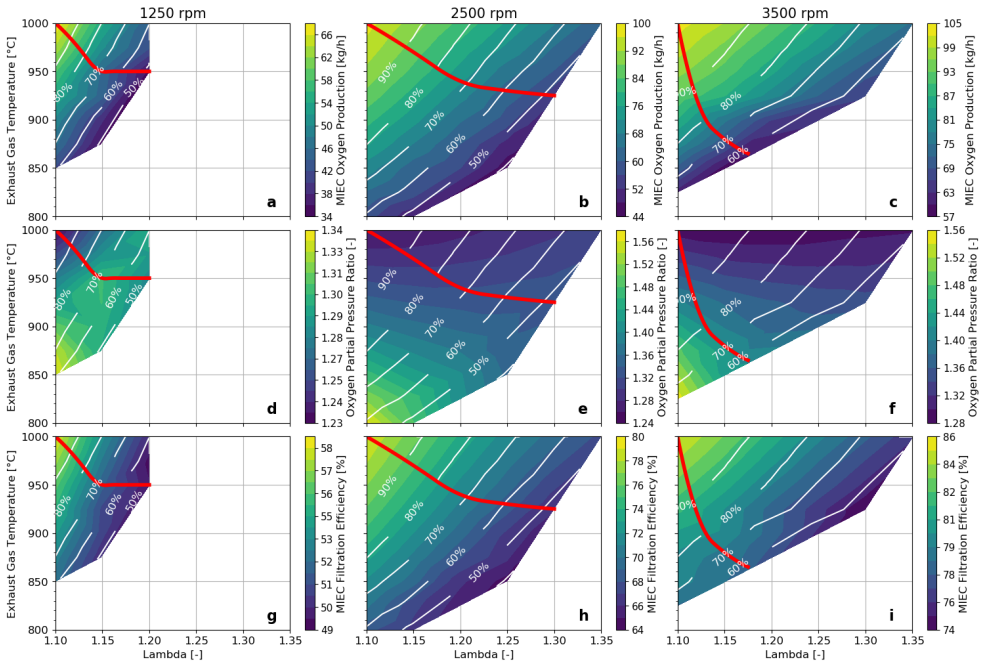

Figure 4.8: Part-load maps for average results of relevant MIEC variables for 1250 rpm, 2500 rpm and 3500 rpm. The white lines drawn on maps represent level curve for power plant load relative to maximum power achieved at corresponding engine speed.

Also, SOI must be delayed (Figure 4.6j-l) mainly at a fixed temperature so as to provide more energy for exhaust gas in favor of keeping MIEC thermal requirements for O_2 generation at the cost of less mechanical power. Indeed, if SOI is delayed, more sensible enthalpy is available at the exhaust gas. Accordingly, more energy may be transferred to system inlet air via HEs in order to heat up the MIEC feed side for O_2 production. In addition, more λ entails more production of useless oxygen; however, that may reduce combustion-end HCs due to more in-chamber O_2 availability. In general, low engine speed points have SOI more delayed in order to center combustion. As expected, increasing inerts recirculation (Figure 4.6g-i) decreases cylinder-out temperature since inert gas may absorb a substantial part of heat power released. The reverse effect is seen, though to a lesser extent, when intake gases are diluted with an excess of O_2 increasing λ and less EGR is required to control combustion temperature. Despite the EGR behavior being quite similar in all engine speeds, more oxidizer trapped mass is observed at low engine speeds due to

more in-cylinder gas residence time (Figure 4.7a-c). As this research is mainly focused on proposing minimum-consumption temperature-lambda paths for lowering power plant load, only three engine speeds are contemplated in this study. However, the same process may be carried out for other engine speeds to find out their corresponding effective-efficiency paths and extend the power plant part-load operating range.

When the engine load is reduced, less sensible enthalpy is available in the exhaust line, reflecting on less energy for the regenerative Brayton cycle and, consequently, depletion of system-inlet air mass flow (Figure 4.7d-f). In this case, less O_2 is produced by the MIEC (Figure 4.8a-c), diminishing oxidizer trapped mass. Although O_2 partial pressure ratio increases with less T_{exh} due to lower O_2 concentration at MIEC permeate side with more EGR rate (Figure 4.8d-f), MIEC filtration capacity decreases with power plant load reduction (Figure 4.8g-i). Indeed, a decrease in the exhaust gas heat availability lowers MIEC feed side temperature and, thereby, harms membrane filtration.

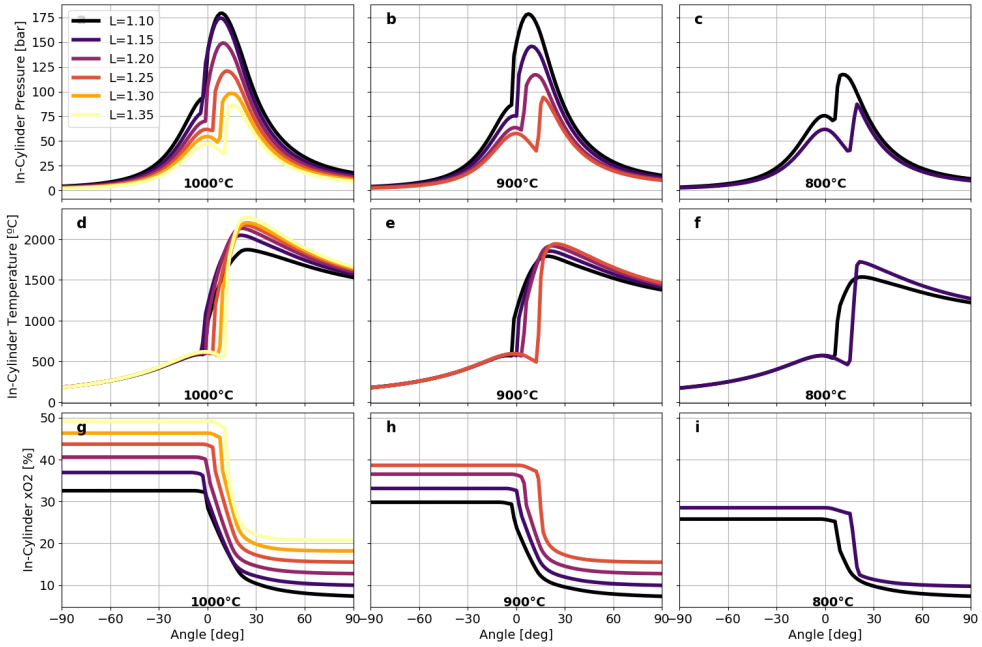

Figure 4.9: In-cylinder variable instantaneous results at fixed engine speed = 2500 rpm for different values of T_{exh} (1000 °C, 900 °C and 800 °C). x_{O2} represents O_2 mass fraction.

Figure 4.9 shows some in-cylinder variable instantaneous results for a particular engine speed = 2500 rpm which is taken for the sake of simplicity, the same trends may be observed at other engine speeds. As depicted in Figure 4.9a-c, in-cylinder maximum pressure varies from 180 bar to 75 bar when λ increases and T_{exh} is reduced for lowering load. Also, when λ increases, the sudden rise in pressure at SOC is delayed and the pressure during compression phase is lower due to less trapped mass and need of more energy at exhaust gas, moving SOI towards ascending crank angle degree (CAD). In particular, ignition pressure is reduced, though to a lesser degree, lowering exhaust temperature and, apparently, a required minimum pressure is observed (around 40 bar) whereby combustion may be ignited regardless of λ and exhaust temperature, setting limits of feasible combustion. Figure 4.9d-f shows that the maximum combustion temperature increases with more λ due to combustion decentralization caused by SOI delay. Moreover, if Figure 4.7g-i is compared to Figure 4.9d-f, when λ increases, the ignition delay may be longer or shorter depending on conditions change. Thus, if the ignition time is too long, the fuel is mainly burnt during the premixed phase and, hence, the combustion process is sharper. Nevertheless, ignition temperature seems to be around 550 °C for all engine speeds and part-load points with more dependence on SOI. As expected, more λ raises in-cylinder O_2 concentration that is reduced with lower exhaust temperature at constant λ due to less O_2 production (Figure 4.9g-i). Although more λ entails more O_2 availability, that is not enough to trigger combustion if the in-cylinder pressure is not suitable, as already explained.

Figure 4.10 presents similar trends to those depicted in Figure 4.9, varying engine speed at constant T_{exh} = 1000 °C. In this case, maximum pressure Figure 4.10a-c, maximum temperature Figure 4.10d-f and O_2 concentration Figure 4.10g-i have relatively same values, varying engine speed at fixed λ. Furthermore, SOI must be advanced at high engine speeds so as to center the combustion properly (Figure 4.6e-f), which is seen comparing instantaneous (Figure 4.10a-c) results for 3500 rpm, 2500 rpm and 1250 rpm at same λ and T_{exh}. Thus, once SOI is very advanced at 3500 rpm, the combustion ignition usually takes place during compression phase with high ignition pressure (Figure 4.10a) and, hence, ignition delay decreases when load is reduced at T_{exh} = 1000 °C increasing λ (Figure 4.6f and i). However, a reverse effect is seen for 2500 rpm and 1250 rpm because combustion usually occurs after 0 CAD when in-cylinder pressure is already decreasing (Figure 4.10b and c) and, thereby, ignition time increases due to SOI delay (Figure 4.6d,e, g and h).

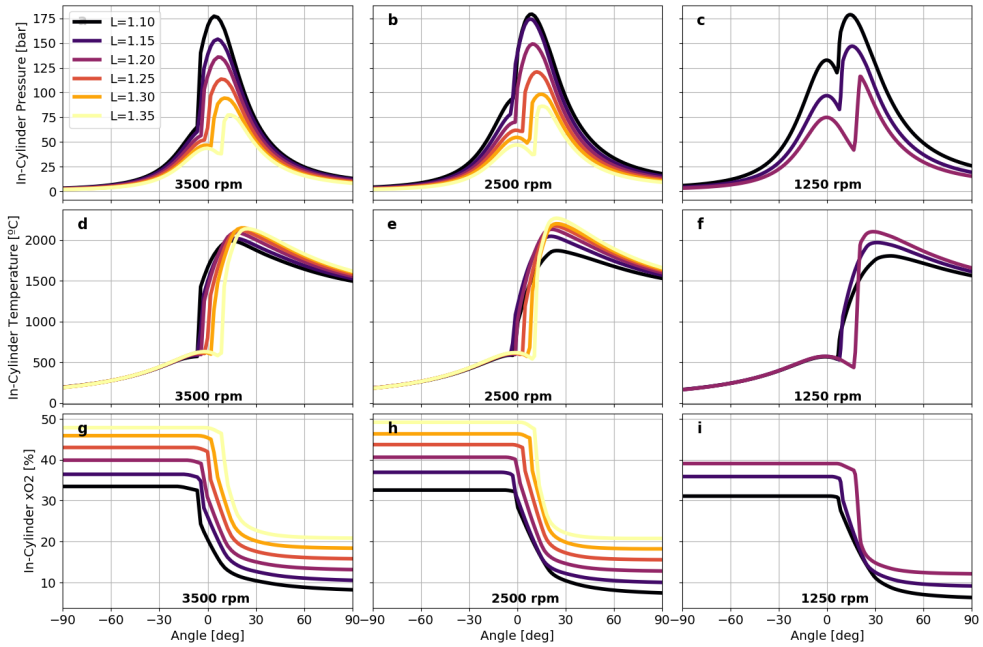

Figure 4.10: In-cylinder variable instantaneous results at constant $T_{exh} = 1000\,°C$ for different values of engine speeds (3500 rpm, 2500 rpm and 1250 rpm). x_{O2} represents O_2 mass fraction.

Regarding the Brayton cycle compressors, they present their full-load operating points reunited nearby maximum efficiency zones with compression ratios from 2.0 to 3.5 (Figure 4.11a and c). Also, their turbines operate with a suited expansion ratio from 1.5 to 3.0 at VGT position = 60 % (Figure 4.11b and d). Nonetheless, when power plant load decreases, less energy is available at turbines (expansion ratio is reduced primary for VGT-N/A-1), and independently of engine speed, air compressors tend to be operated with lower compression ratios (minimum value reached around 1.7) and with worse efficiencies. Concerning VGT-G/O, the exhaust temperature is mainly controlled by the BPV in all part-load points regardless of engine speed because its turbine is continuously operated at maximum rack position with low compression- and expansion ratios.

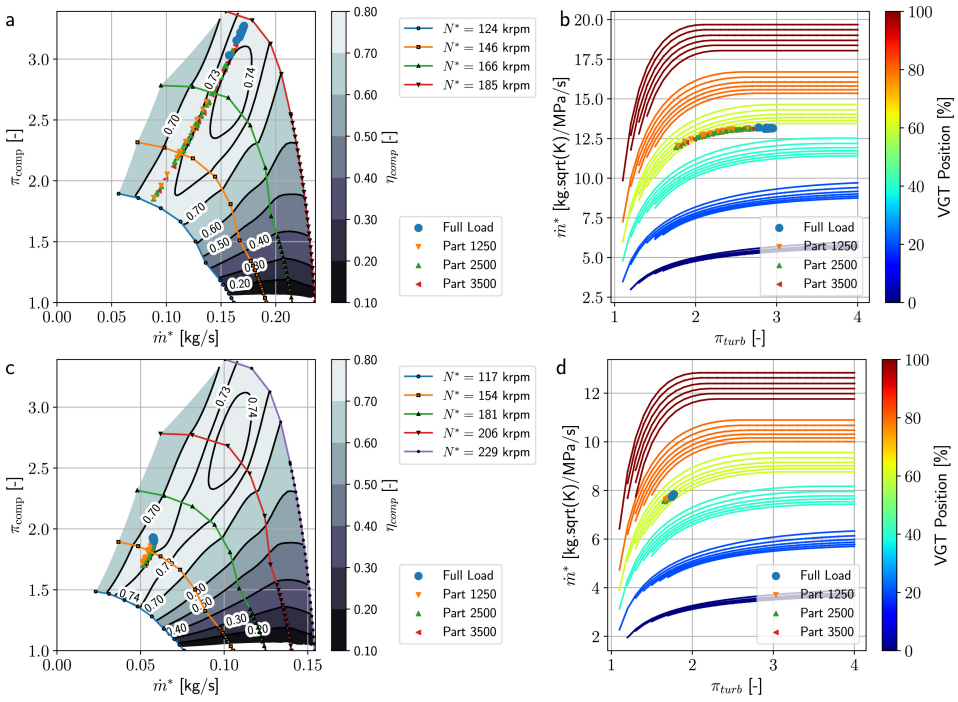

Figure 4.11: Turbochargers maps: VGT-N/A-1 (Compressor a and Turbine b), VGT-N/A-2 (Compressor c and Turbine d) and VGT-G/O (Compressor e and Turbine f).

4.3.2 Temperature, pressure and mass flow diagrams

Figure 4.12 presents temperature and power diagram for highest and lowest power plant loads at 2500 rpm which is an intermediate speed for the sake of analysis. That part-load point corresponds to $T_{exh} = 850\,°C$ and $\lambda = 1.25$ where load is around 40 % if compared to full-load point at same engine speed. Calculated temperatures are shown next to each flow line in degrees Celsius, with bottom values for low load and top ones for high load. Furthermore, heat power exchanged between fluids is depicted next to coolers and HEs in kW following the same temperature arrangement. That analogous representation scheme is also employed on pressure and mass flow diagrams (Figure 4.13 and Figure 4.14).

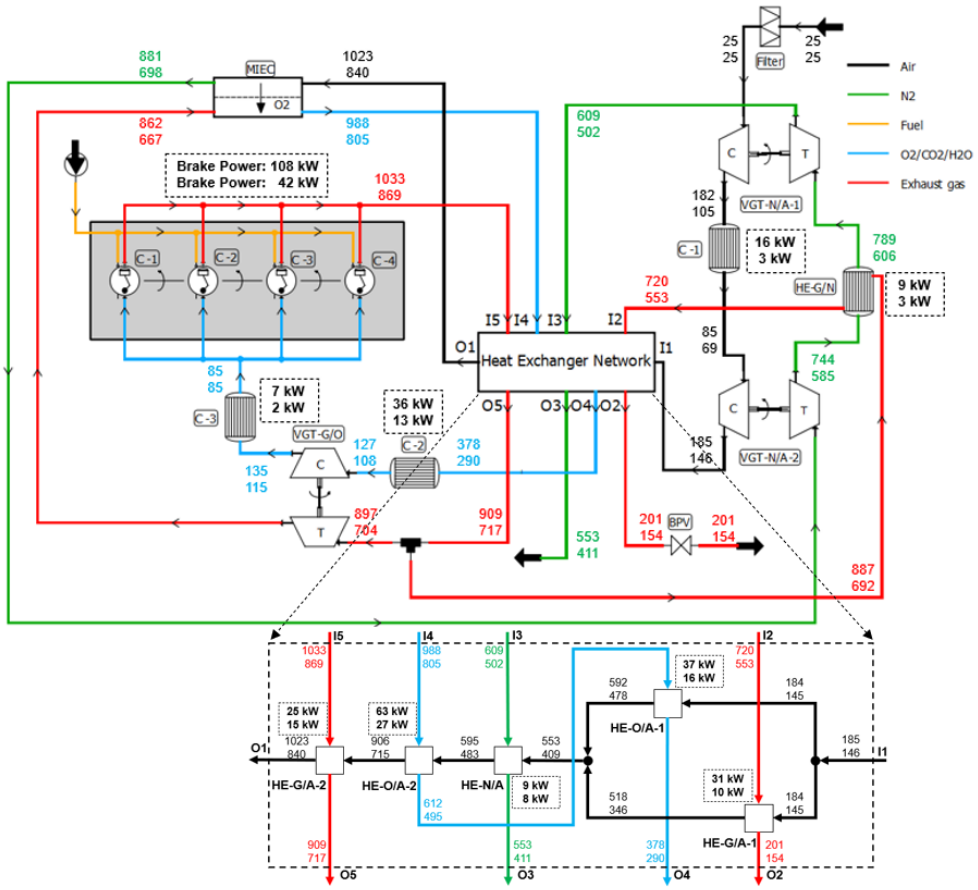

Figure 4.12: Power (in kW) and temperature (in °C) distribution diagram at 2500 rpm for full-load point (top values) and 40 % part-load point (bottom values)

Low load point posses lower heat exchanged, implying colder fluids due to less energy produced in the combustion chamber, reflecting on less exhaust gas heat. In fact, some HEs present power reduction of up to around 50 % and 70 % for HEs and coolers, respectively. In addition, as this system is based on a regenerative process, that cut in energy availability may also justify pressure and mass flow declines (Figure 4.13 and Figure 4.14) since N_2 VGTs may no longer supply enough air to generate high pressure at MIEC feed side for O_2 production. Indeed, pressure and mass flow are reduced by half in general. One may see that more O_2 content is seen in the exhaust gas at low power plant load as a consequence of working with more λ.

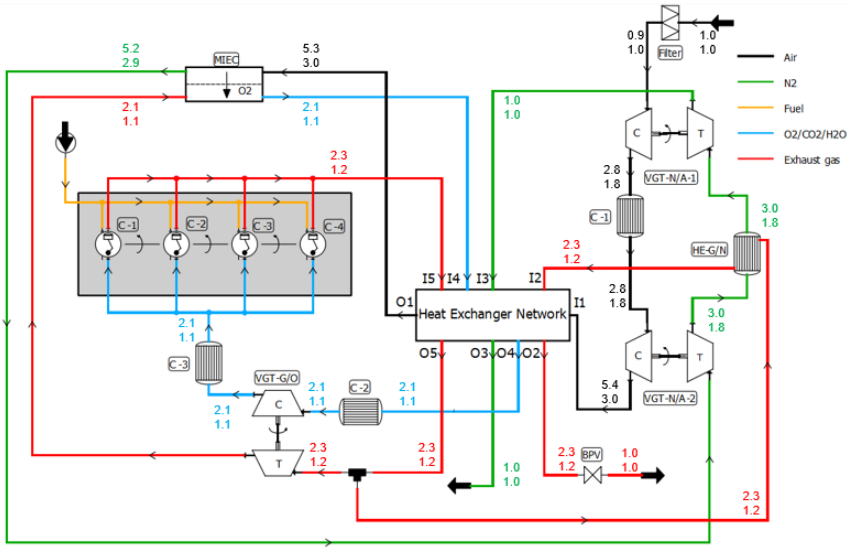

Figure 4.13: Pressure (in bar) distribution diagram at 2500 rpm for full-load point (top values) and 40 % part-load point (bottom values)

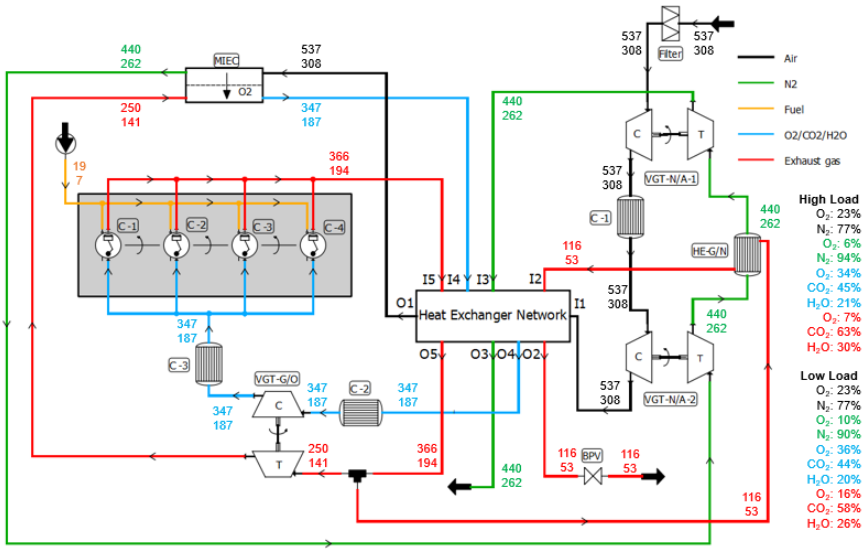

Figure 4.14: Mass flow (in $\mathrm{kg\,h^{-1}}$) distribution diagram at 2500 rpm for full-load point (top values) and 40 % part-load point (bottom values)

4.3.3 Part-load limit analysis indicators

With the purpose of analyzing the system energy performance within different operating conditions, some variables must be indicated beforehand such as: mass flow of O_2 generated by the membrane ($\dot{m}_{O_2}$ in $\mathrm{kg\,s^{-1}}$), cooling power at cooler C-1 (Q_{C-1} in kW), flow sensible enthalpies at MIEC feed side and system air inlets ($H_{air,in,MIEC}$ and $H_{air,in,system}$ respectively in kW), heat released by combustion (HR in kW), brake power (W in kW) and convective heat losses at cylinder walls and exhaust pipes (Q_{htw} and Q_{pipes} respectively in kW). Afterwards, total thermal energy transferred to air from system entry until MIEC feed side inlet ($H_{MIEC,real}$ in kW), mass flow of O_2 generated by membrane per engine cycle ($\dot{m}^*_{O_2}$) and analysis variables (*parameter* 1, *parameter* 2, *parameter* 1^* and *parameter* 2^*) may be defined as follows:

$$\dot{m}^*_{O_2}[\mathrm{g/cycle}] = \frac{\dot{m}_{O_2}[\mathrm{kg\,s^{-1}}] \times 2 \times 60 \times 1000}{Engine\ Speed[\mathrm{rpm}]} \tag{4.1}$$

$$H_{MIEC,real}[\mathrm{kW}] = H_{air,in,MIEC} - H_{air,in,system} + Q_{C-1} \tag{4.2}$$

$$parameter\ 1[\,-\,] = \frac{H_{MIEC,real}}{HR} \tag{4.3}$$

$$parameter\ 2[\,-\,] = \frac{H_{MIEC,real}}{HR - W - Q_{htw} - Q_{pipes}} \tag{4.4}$$

$$parameter\ 1^*[\mathrm{g/cycle}] = \frac{\dot{m}^*_{O_2}}{parameter\ 1} \tag{4.5}$$

$$parameter\ 2^*[\mathrm{g/cycle}] = \frac{\dot{m}^*_{O_2}}{parameter\ 2} \tag{4.6}$$

Parameters 1 and 2 present a ratio of the required energy for producing necessary O_2 by MIEC with respect to fuel caloric value and exhaust gas available thermal energy, respectively. The denominator of parameter 2 is an energy balance between the intake manifold and exhaust pipes considering major heat losses and mechanical power released, and consequently, it measures the gas enthalpy leap surrounding cylinders. Parameters 1* and 2* are basically parameters 1 and 2, respectively, taking into account the amount of generated O_2 per four-stroke cycle. Their values can be read as how much energy is needed in the MIEC to produce 1 g of O_2 per four-stroke engine cycle, and with respect to either the energy released in the fuel (parameter 1*) or delivered by the exhaust gases (parameter 2*).

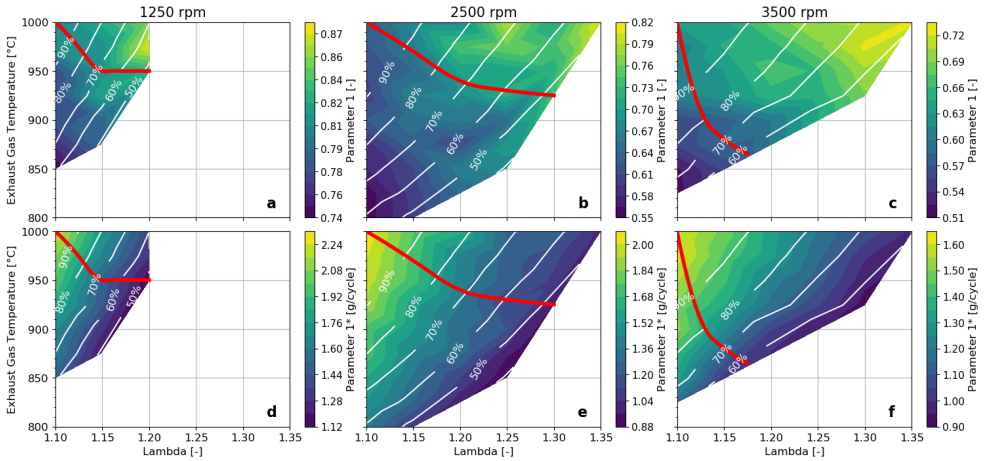

Figure 4.15: Part-load maps for average results of parameter 1 for 1250 rpm, 2500 rpm and 3500 rpm. The white lines drawn on maps represent level curve for engine load relative to maximum power achieved at corresponding engine speed.

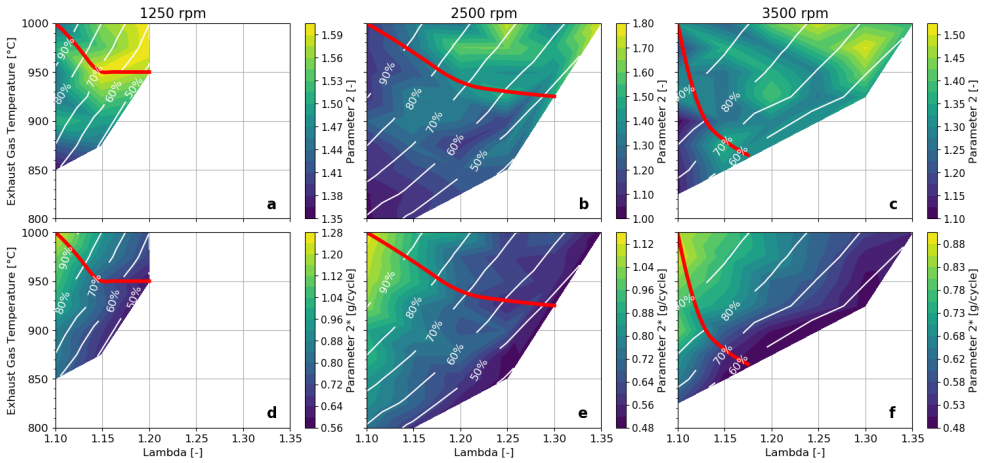

Figure 4.16: Part-load maps for average results of parameter 2 for 1250 rpm, 2500 rpm and 3500 rpm. The white lines drawn on maps represent the level curve for engine load relative to maximum power achieved at corresponding engine speed.

Attention should be drawn to the fact that many parameters were studied but the ones depicted here seem to be the most representative for analyzing power plant part-load conditions. Figure 4.15 shows how parameter 1 is not reliant on neither engine speed nor load degree. By contrast, parameter 1* follows the power reduction trend with almost constant values on iso-load lines, and, besides that, it tends to a minimum value around 1 from which load may not be decreased regardless of engine speed. One may interpret parameter 1* as how many times HR must be greater than $H_{MIEC,real}$ for producing 1 g/cycle of oxygen, and those limit values observed on maps show that HR must be at least equal to $H_{MIEC,real}$ in order to ensure suitable thermal-energy availability for O_2 generation of 1 g/cycle. If that value is still lower to produce every gram of O_2 per four-stroke engine cycle, it would not be enough with just recovering the waste energy of the exhaust gases. Therefore, more energy should be added to have a self-sustaining stable system. Parameter 1* it is a very simple parameter, which can be used for design purposes as a priori parameter, that allows scaling up the whole system to any membrane and 4-stroke engine cycle.

A similar observation is verified in Figure 4.16 whereby no clear trend is found for parameter 2, and parameter 2* is almost steady concerning the same power plant load points. In this case, parameter 2* may be interpreted as how many times gas enthalpy increment must be greater than $H_{MIEC,real}$ for

producing 1 g/cycle of oxygen, and their values tend to a minimum one around 0.5 independent of engine speed. In addition, that smallest value indicates that gas enthalpy gain must be at least half the $H_{MIEC,real}$ to guarantee proper MIEC thermal conditions for 1 g/cycle O_2 production just recovering waste energy from the exhaust gases. The value is lower than 1 due to the regenerative cycle behavior and the virtuous cycle effect caused by the HEs.

Thus, if parameters 1* and 2* present values lesser than the minimum ones already explained, the regenerative process would not be enough to maintain power plant stability, and O_2 should be provided by an external source apart from the membrane. Finally, parameter 2* may be useful for analysis since it considers the effective enthalpy increment necessary for appropriate MIEC operating conditions. In contrast, parameter 1* may be employed for system design since fuel calorific value is commonly known and may be used to estimate MIEC O_2 production capacity and membrane minimum mass-transfer area.

Chapter 4 Bibliography

[2] F. Arnau, G. Bracho, L. García-Cuevas, and V. Farias. "A strategy to extend load operation map range in oxy-fuel compression ignition engines with oxygen separation membranes". *Applied Thermal Engineering* 226 (2023), p. 120268. ISSN: 1359-4311. DOI: https://doi.org/10.1016/j.applthermaleng.2023.120268. URL: https://www.sciencedirect.com/science/article/pii/S1359431123002971 (cit. on pp. xii, 70).

[58] J. R. Serrano, G. Bracho, J. Gomez-Soriano, and C. Fernandes. "Development of an oxy-fuel combustion system in a compression-ignition engine for ultra-low emissions powerplants Using CFD and evolutionary algorithms". *Applied Sciences* 12.(14) (2022). ISSN: 2076-3417. DOI: 10.3390/app12147104. URL: https://www.mdpi.com/2076-3417/12/14/7104 (cit. on pp. 18, 71, 73, 78).

[74] D. Catalán Martínez, M. Santafé-Moros, J. Gozálvez-Zafrilla, J. García Fayos, and J. Serra. "Characterization of oxygen transport phenomena on BSCF membranes assisted by fluid dynamic simulations including surface exchange". *Chemical Engineering Journal* 387 (May 2020),

p. 124069. DOI: 10.1016/j.cej.2020.124069 (cit. on pp. 22, 24, 40, 41, 70).

[101] F. J. Arnau, J. Benajes, J. M. Desantes, J. R. Serrano, J. M. Serra, D. Catalán-Martínez, and L. M. García-Cuevas. *Motor de combustión interna de hidrocarburos auto transportable que no emite gases nocivos ni CO_2; secuestra CO_2 atmosférico y fabrica CO_2 líquido subcrítico.* P201930285. Mar. 2019 (cit. on pp. 40, 43, 44, 71).

[106] J. Arrègle, J. J. López, J. M. García, and C. Fenollosa. "Development of a Zero-Dimensional Diesel Combustion Model. Part 1: Analysis of the Quasi-Steady Diffusion Combustion Phase". *Applied Thermal Engineering* 23.(11) (11 2003), pp. 1301–1317. ISSN: 13594311. DOI: 10.1016/S1359-4311(03)00079-6 (cit. on pp. 71, 73).

[107] J. Arrègle, J. J. López, J. M. García, and C. Fenollosa. "Development of a Zero-Dimensional Diesel combustion Model: Part 2: Analysis of the Transient Initial and Final Diffusion Combustion Phases". *Applied Thermal Engineering* 23.(11) (11 2003), pp. 1319–1331. ISSN: 13594311. DOI: 10.1016/S1359-4311(03)00080-2 (cit. on pp. 71, 73).

[108] J. Arrègle, J. J. López, J. Martín, and E. M. Mocholí. "Development of a Mixing and Combustion Zero-Dimensional Model for Diesel Engines". *SAE Technical Papers* (2006), p. 1381. ISSN: 26883627. DOI: 10.4271/2006-01-1382 (cit. on pp. 71, 73).

[109] J. Serrano, J. Lopez, J. Martín, and G. Bracho. "Extension of a Zero-Dimensional Mixing-Controlled Combustion Model for the Development of a NOx–Free System Based on the Oxy-Combustion Concept". *Johnson Matthey Technology Review* (Jan. 2023). DOI: 10.1595/205651324X16963284171824 (cit. on pp. 73, 74, 135).

Chapter 5

Design of the carbon capture system for the oxy-fuel power plant with exhaust water recirculation.

Contents

5.1 Introduction

The works, analysis and ideas described in this chapter were the origins of publication number [3] from the publications list of the author of this thesis. In the sake of readiness and to protect the thesis writing style, the publication number [3] from author's list of publications have not been specifically cited every time that ideas, figures or discussions contained in it are bring to this chapter again. This disclaimer corrects, compensates and justify this fact; being the Ph.D. candidate and the works of his thesis are the origin of the innovation component in the publication number [3] listed in the referred section.

The current chapter aims to continue the work conducted in chapter 3 and chapter 4 whereby a feasibility study of the oxy-fuel combustion applied to a CIE using O_2 separation membranes was carried out. The heat exchanger- and turbocharging layout, as well as the model for a BSCF MIEC are preserved, and a CC system is coupled to the previous model at the tailpipe outlet. The CC system is essentially composed of two inter-cooled compression steps with intermediate water removal followed by a CO_2 purifier whereby the CO_2 is separated from O_2 when the combustion process is performed in lean combustion conditions. Therefore, such CO_2 drying and purification processes have to be simulated considering the thermodynamic equilibrium between liquid and vapor at different separation stages within the CC system.

In this case, as cubic EOS are more straightforward for calculation procedure than state-of-the-art EOS due to their simple structure, the PR EOS is employed in this chapter to model the vapor-liquid phase equilibrium (VLE) concerned in CC system with the temperature-dependent binary interaction parameters calibrated with experimental results given by the literature within the operating conditions (temperature, pressure and composition) of interest for CO_2 capture related to oxy-fuel combustion. In general, the CO_2 capture process chains found in literature may approximately cover temperatures from 25 °C to 1346 °C and pressures from 0.5 bar to 80 bar [110] [111].

Initially, two approaches are compared when the CC is coupled to the O_2 generation unit considering the recirculation of the unburned excess of O_2 from the CC back to combustion chamber since the system is operated with *lambda* = 1.1. In addition and afterwards, water recirculation is applied to both reduce intake oxidant charge temperature and increase the intake flow water composition, improving the power plant thermal efficiency. For this purpose,

a mixer model is developed to recirculate part of the water condensed in the CC towards the cylinder inlet. Basically, the proposed power plant concept is optimized by maximizing the product of useful effective efficiency and engine brake power, actuating on the SOI as done in precedent chapters. Nevertheless, the additional cooling power required by the CC system is also contemplated in order to find out the most suitable system operating conditions.

In summary, this chapter presents the whole picture the process to highlight the feasibility of this system (membrane-based oxy-fuel combustion with CC for zero-emission power generation) taking into account different systems operating together and their respective submodels.

5.2 Materials and methods

In this section the thermodynamic model is calibrated with experimental data to predict the behavior of several elements whereby there is phase change. Afterwards, initial amendments are proposed to the reference oxy-fuel combustion layout in order to check the need of a turbocharger upstream the intake manifold. Also, a CC model is proposed finding the best operating conditions in terms of energy requirement and CO_2 purity, and once developed, it is coupled to oxy-fuel combustion layout considering the reuse of the excess of O_2 coming from the CC system. Finally, a water mixer model is proposed to recirculate part of the water condensed in the flashes in order to enhance the engine thermal efficiency and net mechanical power.

5.2.1 Thermodynamic model for the VLE

The calibration processes of EOSs used in this chapter may be performed based on Equation 2.6 and, hence, the binary parameters for major pairs of substances within CC and oxy-fuel combustion scenario (CO_2-O_2, O_2-H_2O and CO_2-H_2O) are adjusted with experimental data from the literature. As SRK and PR EOSs are widely used by the industry to simulate VLE behavior of fluids considering the ω of substances [100], and thereby more elaborated than RK, which only predicts the fluid state of a limited range of substances, they are contemplated in this work to model the complex phase change for the CO_2-O_2 binary system. In this case, constant-temperature phase diagrams are

built considering 15 °C and 25 °C, which are common ambient temperatures for capturing CO_2 without the need for substantial cooling power. Therefore, k_{CO_2,O_2} is determined by minimizing the sum of squared errors between model and data for the partial pressure of CO_2 in equilibrium with the bubble point for a given composition as depicted in Figure 5.1. The interaction parameter values found using PR and SRK are depicted in Table 5.1, with PR EOS fitting better the experimental data taken from the work published by Westman *et al.* [112]. As shown in Figure 5.1, these EOSs are not able to predict the critical point with reasonable accuracy; however, both are satisfactory for simulating the VLE within a pressure range (around from 50 bar to 80 bar) whereby the CO_2 may be captured and separated from O_2 at environment temperatures with high purity.

Table 5.1: The best k_{CO_2,O_2} for PR and SRK EOSs

	PR	**SRK**
$k_{\mathbf{CO_2,O_2}}$	0.17431	0.20298

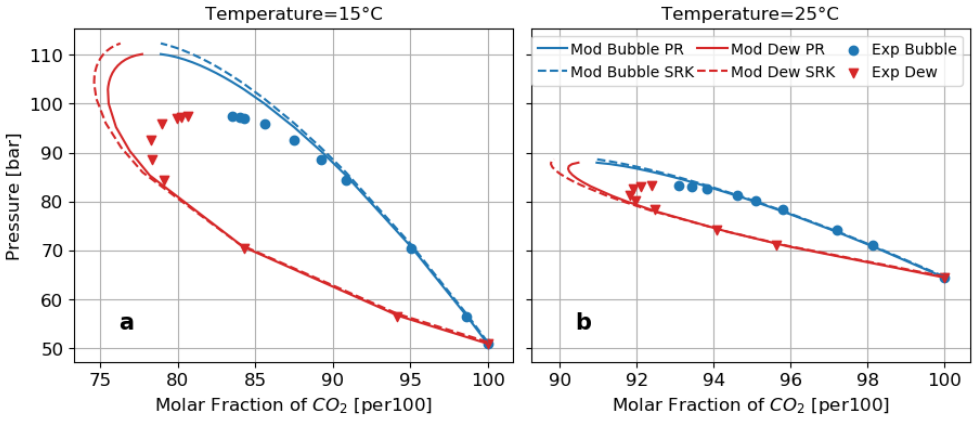

Figure 5.1: Phase diagram at constant temperature for the CO_2-O_2 binary system comparing model and experimental data.

As PR EOS slightly provides better results than SRK in the previous assessment, it is selected and applied to other water-mixture binary systems, such as water-O_2 and water-CO_2, since the binary CO_2-O_2 is the most critical system wherein more elaborated models like cubic EOS are really necessary [113]. Thus, a similar procedure is followed to calibrate the PR EOS for the O_2-H_2O binary (Figure 5.2) with experimental data taken from the work published

by Stephan *et al* [114]. However, in such a study, a k_{O_2,H_2O} value is found for each temperature and, thereby, after a fitting procedure, a temperature-dependent linear function is proposed for the interaction parameter, where temperature is employed in °C as depicted in Equation 5.1. Figure 5.2 presents the VLE in terms of O_2 solubility in the liquid phase in equilibrium with O_2 partial pressure in the vapor phase. As vapor and liquid phases contain mostly O_2 and water, respectively, system pressure may be approximated by O_2 partial pressure. Therefore, one may see that the proposed model is suitable to predict the VLE at a low-pressure range (around from 15 bar to 125 bar), which is interesting for CC applications, whereas its accuracy is undermined at high-pressure values.

$$k_{O_2,H_2O} = 0.003T - 0.3428 \tag{5.1}$$

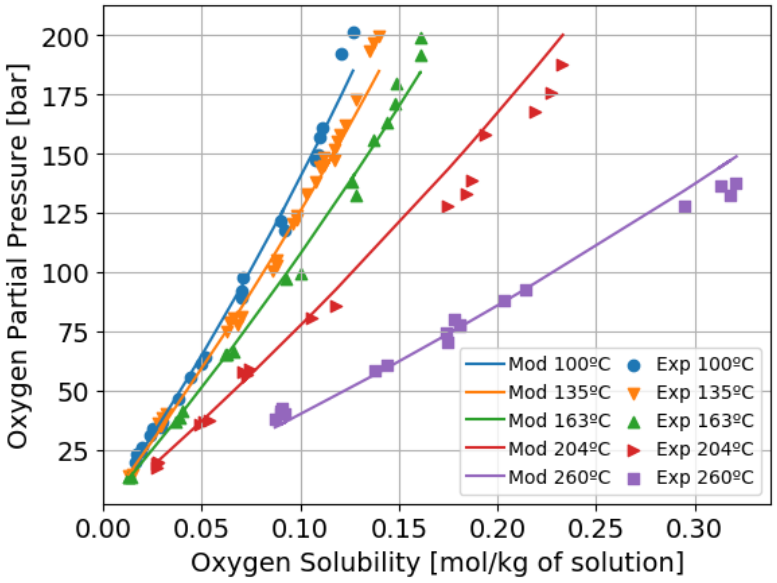

Figure 5.2: VLE for the O_2-H_2O binary system comparing model and experimental data. The solution is only composed of water and O_2.

$$k_{CO_2,H_2O} = 0.0009T - 0.1455 \tag{5.2}$$

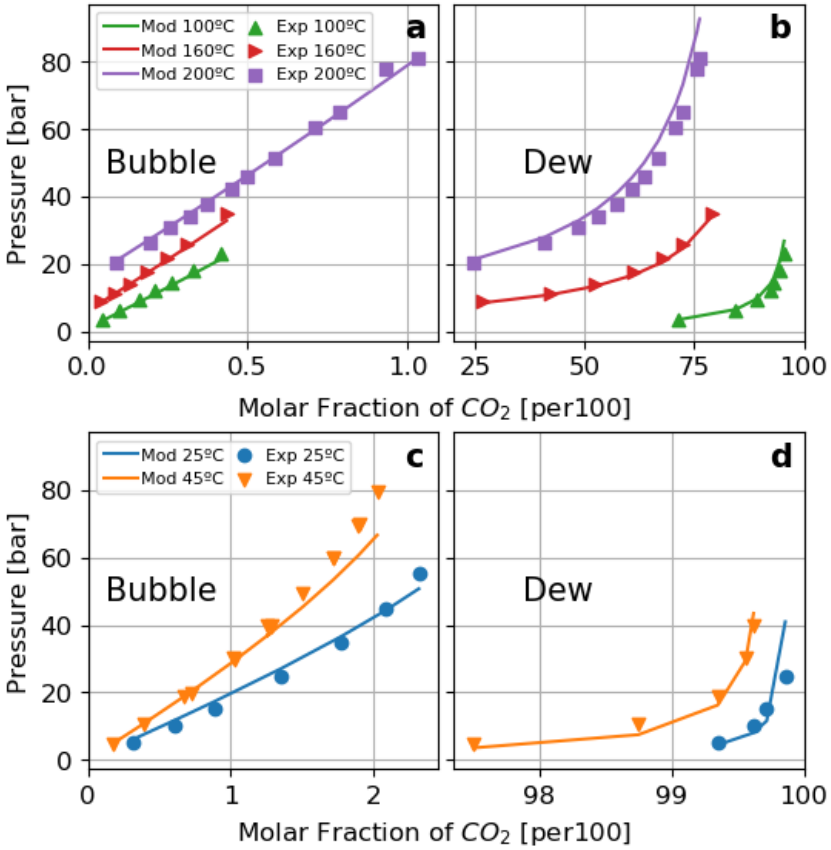

Figure 5.3: VLE for the CO_2-H_2O binary system comparing model and experimental data. Left and right plots represent the bubble and dew points, respectively.

Analogous method is applied to CO_2-H_2O system in order to calibrate its corresponding interaction parameter k_{CO_2,H_2O} for each temperature data, as represented in Figure 5.3. In that case, the experimental data for temperatures from 25 °C to 45 °C, and from 100 °C to 200 °C are taken from works published by Valtz et al. [115] and Muller et al. [116], respectively. Thus, a temperature-dependent linear function is also suggested with temperature used in °C as shown in Equation 5.2 after a fitting procedure considering phase change data. Experimental data found in literature [115] [116] are separated for bubble

(Figure 5.3a and c) and dew (Figure 5.3b and d) pressures, so the left and right experimental points in Figure 5.3 are not necessarily in equilibrium for a given CO_2 overall composition and a given temperature, and consequently, bubble and dew points are calculated independently. Although model accuracy is not so satisfactory for low temperatures when the slope of pressure as a function of CO_2 composition appears to be too sharp for dew points, it fits the experimental data properly for high temperatures within a broad pressure range considering the CO_2 capture context.

Thus, after having the binary parameters calibrated for PR EOS, this thermodynamic approach is applied to simulate the flash processes in this study taking into account the VLE plus mass and energy balances solving a non-linear system with $2n+2$ equations (Equation 2.6, Equation 5.3, Equation 5.4 and Equation 5.5) and $2n+2$ unknowns (ζ, y_i, x_i and Q) for given overall mole fraction (z_i), pressure (P), inlet mole flow (F) and inlet and outlet temperatures (T_{in} and T_{out}), assuming vapor and liquid flows are in equilibrium, where n is the number of components, ζ is the vapor mole ratio and Q is the heat exchanged with the surroundings:

$$z_i = \zeta y_i + (1-\zeta)x_i \tag{5.3}$$

$$\sum_{i=1}^{n} y_i - \sum_{i=1}^{n} x_i = 0 \tag{5.4}$$

$$Q = F\left[h_{in}(T_{in}, P, z_i) - \zeta h_{vap}(T_{out}, P, y_i) - (1-\zeta)h_{liq}(T_{out}, P, x_i)\right] \tag{5.5}$$

5.2.2 Initial amendment to oxy-fuel power plant layout.

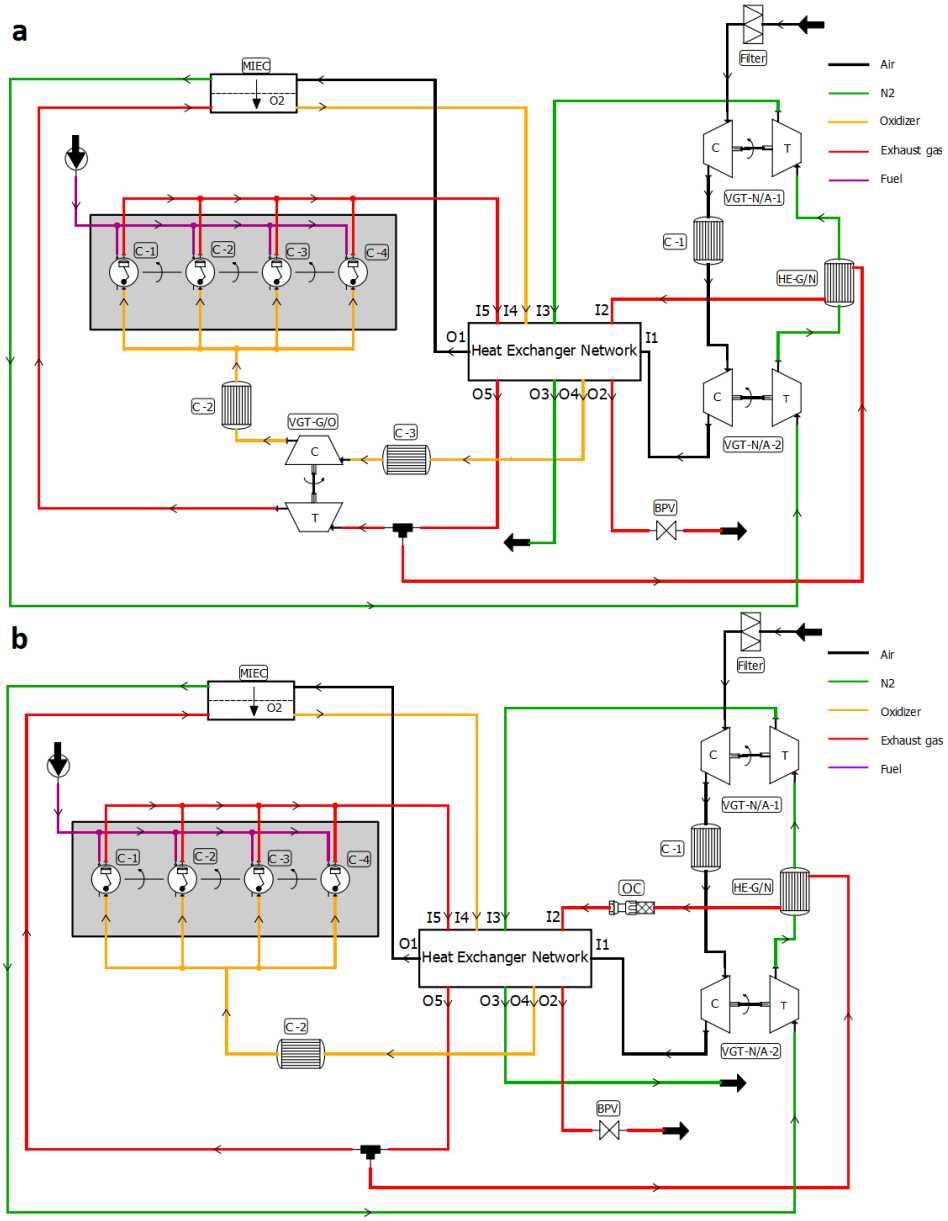

Figure 5.4: (a) Original layout established in chapter 3 and chapter 4; (b) New layout without VGT-G/O and cooler C-3, and adding an OC.

This chapter contemplates the power plant full-load point at 3500 rpm with exhaust manifold temperature (T_{exh}) = 1000 °C and O_2 to fuel equivalence ratio (λ) = 1.1 as a point of departure, and thereby, all calculations shown in this chapter are performed taking into account those conditions. Figure 5.4a shows the original layout used in chapter 4 to be employed as baseline in this study. In addition, chapter 4 confirmed the uselessness of VGT-G/O proposed in chapter 3, since the engine operating range, covering the power plant full-load curve and part-load points for some engine speeds, did not require it for controlling T_{exh}, being enough the BPV for that purpose. Thus, as displayed in Figure 5.4b, VGT-G/O and its corresponding cooler C-2 are removed in this work due to its advantage in packaging. Moreover, as the exhaust gas contains unburnt fuel due to incomplete combustion, an after-treatment system, particularly an oxidation catalyst (OC), is placed at the hot-fluid outlet of the heat exchanger (HE) GN to abate CO and HC engine-out emissions, and increase the exhaust gas purity in terms of CO_2 and its temperature at HEN inlet. In particular, the HEN proposed in chapter 3 is preserved for all the layouts depicted in this chapter.

Table 5.2 displays the main average results comparing the model with first amendments (without VGT-G/O and with OC) to its previous version (with VGT-G/O and without OC). To do so, an optimization process was carried out actuating on the SOI to maximize the optimization (Opt.) function, equivalent to Equation 3.4, defined as the product of effective efficiency and engine brake power. There is no considerable difference between the two cases in power plant performance which demonstrates that VGT-G/O is not necessary. Besides, the OC conversion efficiency was 98%, reducing the amount of unburnt hydrocarbons from 2147 ppm to 30 ppm thanks to a temperature around 750 °C at the catalyst inlet.

Table 5.2: Comparison table for model with and without VGT-G/O.

	Brake Power [kW]	**Effective Efficiency [-]**	**BSFC [g/kWh]**	**SOI [CAD]**	**Maximum In-cylinder Pressure [bar]**	**Opt. Function [kW]**
VGT-G/O	111.6	0.337	239.7	-27.4	177	37.68
No VGT-G/O & OC	111.3	0.338	238.8	-24.6	164	37.71

5.2.3 Combustion model adaptation

In order to avoid the combustion effect on energy fluxes and independently study the power requirements for CC, an average HRL is built up and interpolated based on the HRLs provided by ACT for last 1000 engine cycles considering the first amendments and its corresponding optimum SOI as shown in Figure 5.5a and b. Also, as combustion models based on imposed HRL requires a value for SOC, instead of SOI, the distance in CAD between average SOC and SOI, is preserved and employed in all simulations coupling the CC system and the oxy-fuel layout.

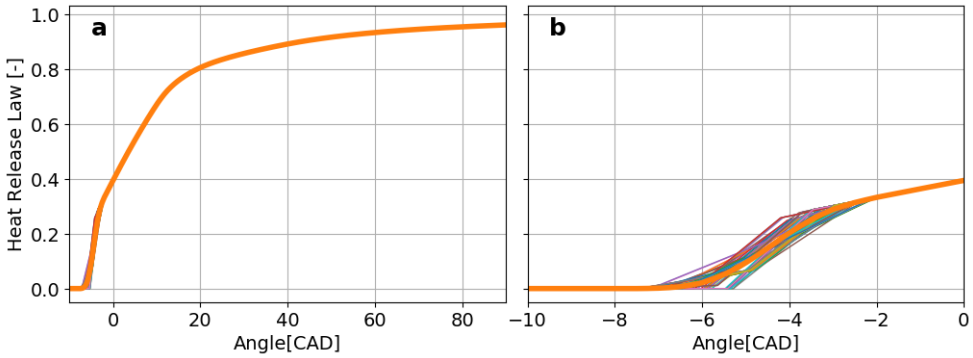

Figure 5.5: (a) Average HRL interpolated (orange line) with results of the last 1000 cycles provided by ACT; (b) Zoom-in on premixed combustion zone.

5.2.4 Coupling carbon capture model to oxy-fuel layout.

This section proposes a CC model based on EOS for VLE calculation built in a Python script , considering how to couple it to the modified oxy-fuel power plant modeled in VEMOD (no VGT-G/OGO with OC) and studying the intake cooling effect on system performance. Therefore, parametric studies were performed in order to determine the CC unit operating conditions in terms of temperature, pressure, and composition with the purpose of capturing the CO_2 at near-ambient temperature. In this context, the complete model was established using VEMOD along with a Python script working simultaneously and interdependently, i.e., the VEMOD outputs are the Python script inputs and vice versa.

5.2.4.1 CC modeling.

With the aim of developing a CC model with essential equipment and suitable operating parameters (i.e., temperature, pressure, and composition), average temperature and pressure of the system-out exhaust gas upstream the BPV found for the modified oxy-fuel layout (described in subsection 5.2.2) are imposed and held constant as inlet conditions for the CC system at point 1 in Figure 5.6. Therefore, the CC system basically consists of two compression steps, three cooling processes with water removal, and a CO_2 storage tank as shown in Figure 5.6. Furthermore, only the mass balance with reaction is employed in this work step for the element engine, and O_2 mass flow generated by the membrane found in that last layout configuration is imposed at point 0, assuming the CC system operates regardless of the Brayton cycle. Thus, heat transfer and generation, as well as fluid dynamics are not taken into account to design a preliminary CC model and specify its basic features.

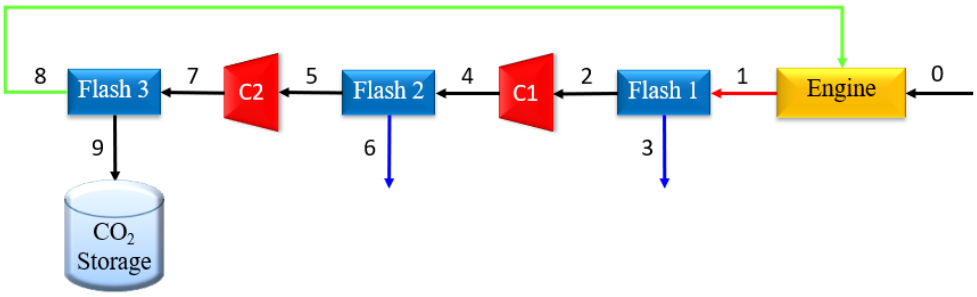

Figure 5.6: CC system schematic layout for modeling proposals.

Considering a CO_2-O_2 binary system with CO_2 overall mole composition of 88%, which was obtained using the system-out exhaust gas composition assuming water is completely removed, flash 3 operating conditions are fixed analyzing the phase diagram for that system at 20 °C (Figure 5.7). Indeed, CO_2 may be captured without high cooling energy requirements at that ambient temperature. As shown in Figure 5.1b, if that binary system has an 88% CO_2 mole composition, no matter the pressure, there is no phase change and, thereby, CO_2 may not be purified from O_2 at temperatures from approximately 25 °C upward. Thus, fixing 20 °C for flash 3, 80 bar seems to be a pressure high enough to liquefy around one-third of overall mole flow, with a reasonable CO_2 purity (around 93% mole composition = 95% mass composition) as displayed in Figure 5.7, where y, z, and x represent vapor, overall

and liquid CO_2 mole composition respectively, and red and blue horizontal bars denote vapor and liquid mole fraction portions respectively. Indeed, on the one hand, lower pressures would generate more surplus vapor, which must be recirculated to the engine in order to avoid CO_2 emissions. Consequently, more mass flow would be recirculated through the compressors, increasing the energy required by the compression process. On the other hand, higher pressures would decrease captured CO_2 purity.

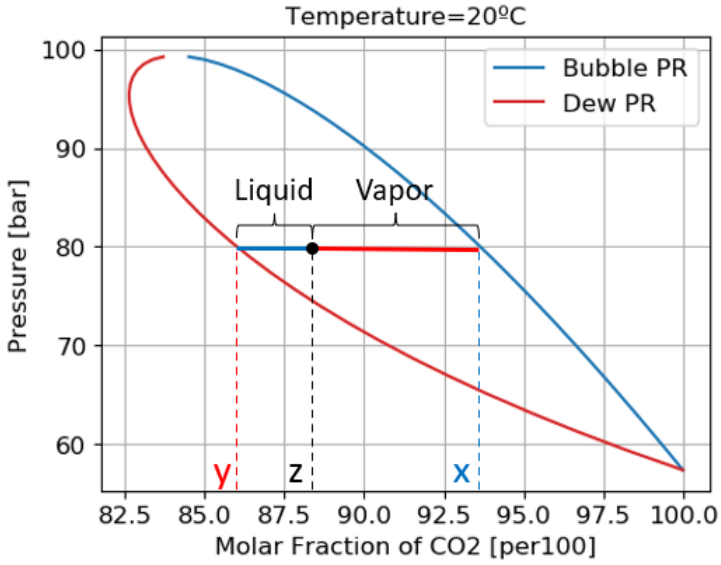

Figure 5.7: Phase diagram at 20 °C for the CO_2-O_2 binary system calculated with PR EOS.

The 180 L CO_2 tank volume was estimated considering complete combustion of the fuel (n-heptane), and assuming fuel and CO_2 densities at normal conditions and, 20 °C and 80 bar, respectively. Thus, taking into account those densities and supposing a fuel tank capacity of 50 liter (a conventional value for automotive applications), the CO_2 tank volume must be approximately three times higher than the fuel one in order to assure all CO_2 produced by the combustion may be stored when all fuel in the tank is completely consumed. The compressors were calculated as reciprocating compressors assuming 85% isothermal efficiency with the same pressure ratio (around 7) so as to minimize the total compression work to pressurize the CO_2 from 1.65 bar (suction pressure at system-out exhaust gas) to 80 bar in two compression stages. Reciprocating compressors were considered due to their capacity to generate

high-discharge pressures compared to other compressors without the need for numerous compression stages [117]. The flash model was defined as a cooling step through a HE wherein the liquid generated during this process is separated from the vapor phase. As already mentioned in the previous subsection subsection 5.2.1, all-flash calculations were based on VLE thermodynamic behavior calculated with PR EOS. Thus, liquid water is essentially removed from the exhaust gas through flashes 1 and 2, and liquid CO_2 is captured at point 9 after flash 3.

Also, the surplus vapor contains a substantial amount of oxygen, which may be considered in the combustion process to provide extra power for the engine. Otherwise, there would be an accumulation of O_2 within the system and the CO_2 overall mole fraction would move gradually leftwards in Figure 5.7 reducing little by little the amount of CO_2 captured in the liquid phase. In addition, if the reciprocating compressors are coupled to the engine, that extra power delivered by combustion may be useful to move the compressors. Therefore, all O_2 (from points 8 and 0) entering the element engine in Figure 5.6 is employed in the combustion keeping the O_2 to fuel ratio equal to 1.1. The injected fuel to achieve that value was computed as expressed in Equation 5.6, where *st* refers to the stoichiometric conditions, $\dot{m}_{fuel}$ and $\dot{m}_{O_2}$ represent the mass flows of fuel and O_2 respectively. In this case, attention should be let to the fact that $\dot{m}_{O_2,0}$ and $\dot{m}_{O_2,8}$ mean O_2 produced by the membrane and recirculated from flash 3 (the product of mass flow and O_2 mass fraction), respectively.

$$\lambda = \frac{\dot{m}_{O_2,0} + \dot{m}_{O_2,8}}{\left(\frac{\dot{m}_{O_2}}{\dot{m}_{fuel}}\right)_{st}} \tag{5.6}$$

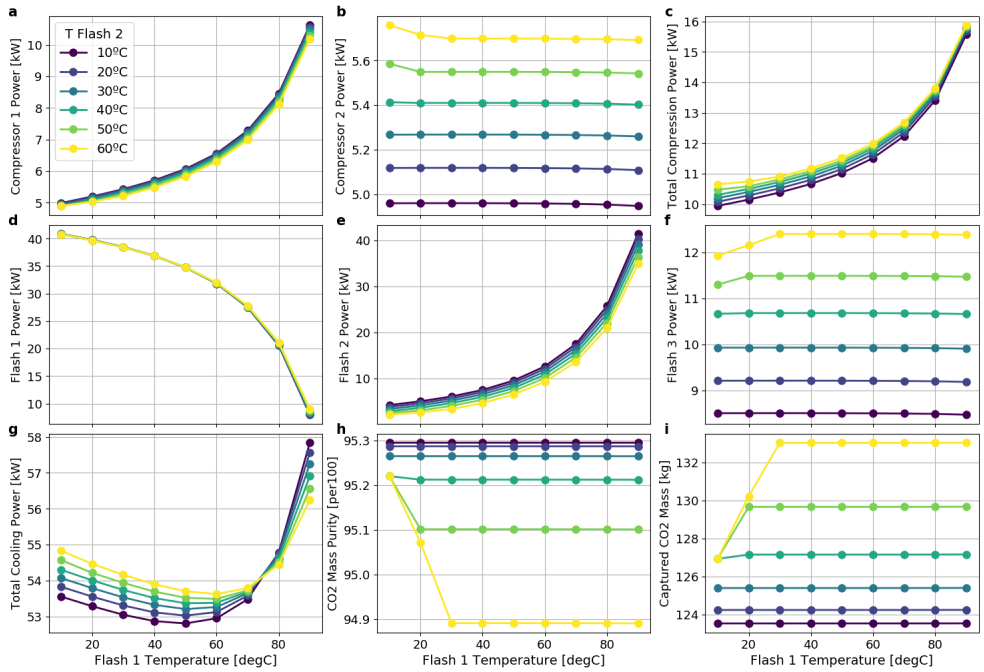

Figure 5.8: The main results of the CO_2 capture system performance sweeping flash 1 and flash 2 outlet temperatures.

With the aim of defining flash 1 and flash 2 outlet temperatures (TF1 and TF2, respectively) and verifying their effects on the CC system performance as operating parameters, a parametric study was carried out varying those variables from 10 °C to 90 °C, and from 10 °C to 60 °C for flashes 1 and 2 respectively (Figure 5.8). The flash 2 outlet temperature intends to remove the remaining water (from the flash 1 vapor outlet), purify and dry the CO_2, and decrease the compressor 2 inlet temperature to avoid damaging the compressor and prevent very high temperatures at the Flash 3 inlet. As shown in Figure 5.8a, compressor 1 power increases significantly when TF1 is high because of higher compressor inlet temperatures, and less water is condensed in the flash 1, and thereby, more mass flow passes through that compressor. Besides that, compressor 2 is more dependent on TF2 (Figure 5.8b) but with less variation when compared to compressor 1 due to lower water content at its inlet, which entails more dependency on the total compression power (defined as the sum of the compressor 1 and compressor 2 powers) on TF1 (Figure 5.8c). Flash 1 and flash 2 powers are essentially relying on TF1 (Figure 5.8d and e) and, thereby, when TF1 rises, flash 1 power is reduced due to

less condensation in this stage, also provoking an increase in mass flow passing through flash 2 and, consequently, raising its cooling power. Thus, since flash 3 power varies slightly with respect to TF2 and it is TF1-independent, the total cooling power (defined as the sum of flash 1, flash 2, and flash 3 powers) presents a minimum value within a narrow TF1 range (approximately from 50 °C to 60 °C) for each TF2 (Figure 5.8f and g).

The amount of CO_2 captured as well as its purity is basically relying on TF2 (Figure 5.8h and i) because whenever there is phase change at flash 2, its outlet temperature controls water content at flash 3 inlet since water saturation pressure is fundamentally temperature-dependent. Hence, if TF2 rises, less liquid water is condensed at flash 2, increasing the mass flow entering flash 3 with more water content, which boosts CO_2 liquefaction at flash 3 (Figure 5.8i) and increases its cooling power (Figure 5.8f), reducing CO_2 purity (Figure 5.8h) due essentially to water presence at liquid phase. Nevertheless, there is no condensation in flash 2 at low TF1 (approximately from 10 °C to 30 °C) and high TF2 (approximately from 40 °C to 60 °C), because water vapor pressure is lower than water saturation pressure at TF2 in this case. Thus, the amount of CO_2 captured as well as its purity is essentially TF1-dependent under those conditions, having an effect equivalent to varying TF2 when there is condensation at flash 2. Finally, TF1=50 °C and TF2=30 °C were deemed optimum points to pursue the work presented in this chapter. In fact, the higher the TF2, the worse the total energy consumption as seen in Figure 5.8c and g. However, as temperatures lower than 30 °C could be challenging to achieve due to utility structural limitations using refrigerant fluid or water, that value was set to TF2. Moreover, TF1=50 °C yields a minimum total cooling power at TF2=30 °C (Figure 5.8g) without substantial penalty in total compression power (Figure 5.8c).

5.2.4.2 Inner cylinder vapor injection and intake cooling effect

After having designed the CC system and defined its process variables, the next step consisted of determining the best way to recirculate the flash-3-out vapor to the engine, coupling the CC model to the complete oxy-fuel combustion layout with O_2 generation. Towards that end, the CC model replaced the BPV in the modified oxy-fuel combustion layout (no VGT-G/O with OC described in subsection 5.2.2) and, thereby, the system-out exhaust gas properties were the inputs at point 1 in Figure 5.6. The exhaust manifold gas temperature was maintained at its set value (1000 °C), employing the pressure imposed on the compressor 1 inlet, which controls the EGR rate and the O_2 dilution level.

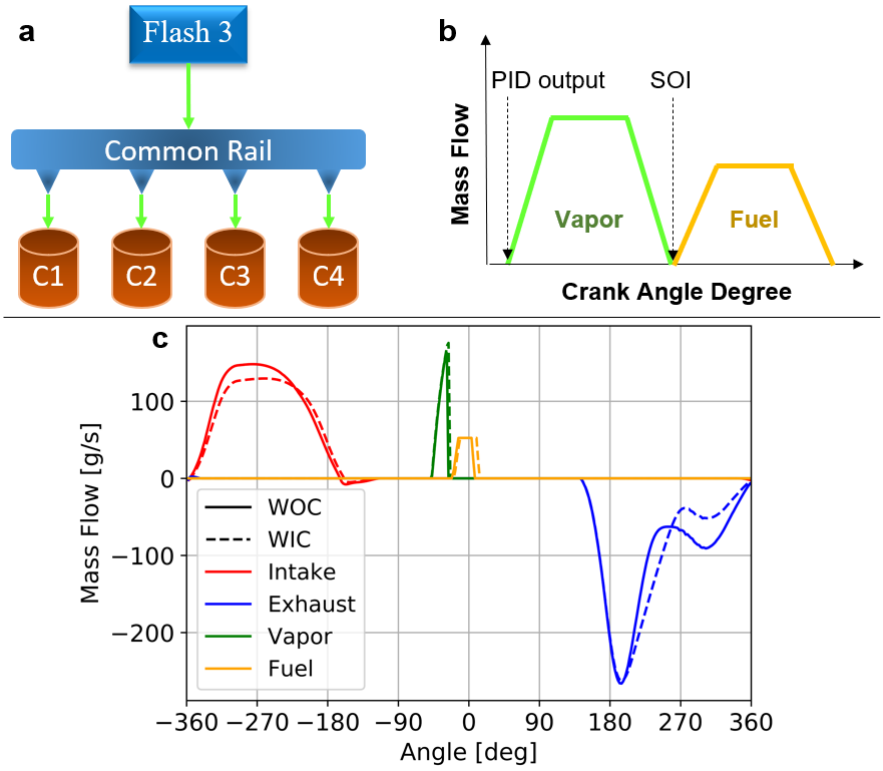

Figure 5.9: Common rail for injecting vapor from flash 3 directly into cylinders. (a) Scheme; (b) Pressure control system; (c) Instantaneous inbound and outbound mass flows inside a cylinder for the best SOI of each proposed configuration (WIC and WOC).

Also, a common rail was proposed to receive the vapor coming from flash 3 and re-inject it directly inside the cylinders in order to take advantage of its high pressure (80 bar) and low temperature (20 °C), increasing the in-cylinder trapped mass and, hence, the engine volumetric efficiency (Figure 5.9a). To do so, a proportional-integral-derivative controller (PID) was used to keep the vapor common rail pressure at 80 bar actuating on the start of vapor injection whose value is the same for all cylinders (Figure 5.9b). Moreover, the end of injection was fixed equal to SOI to ensure all O_2 contained in the vapor is available to react with the fuel. In this way, the discharge pressure (in-cylinder instantaneous pressure) is not very low, which enables to recover part of vapor momentum and pressure through vapor expansion. Also, the amount of vapor injected was uniform throughout cylinders guaranteeing no mass accumulation inside vapor common rail, which had a volume equal to 2.0 L to avoid huge pressure fluctuations and PID instability.

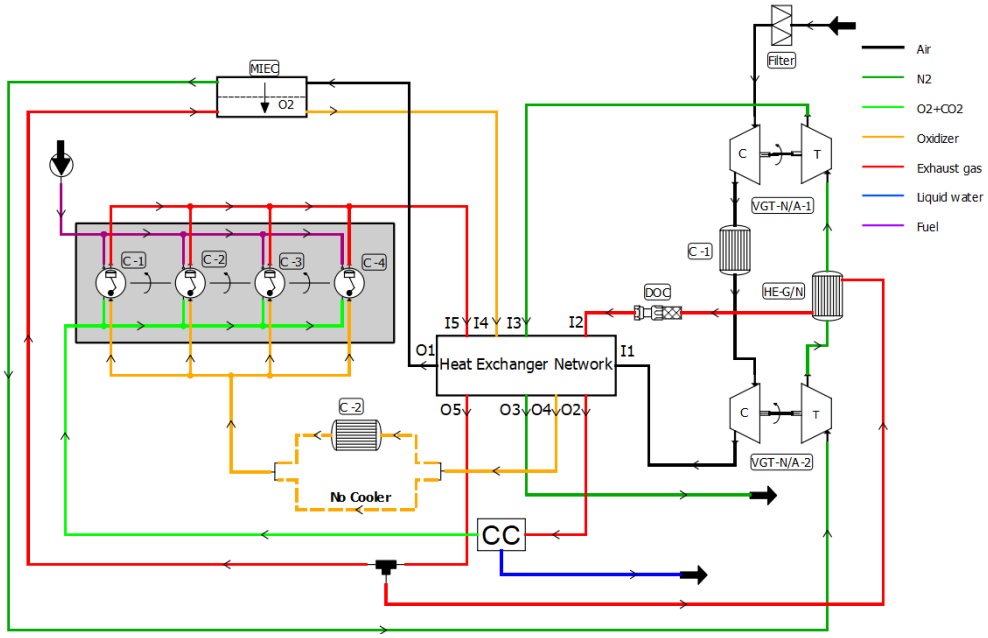

Figure 5.10: Oxy-fuel combustion layout coupled to CO_2 capture system with vapor recirculation.

Figure 5.10 presents the oxy-fuel combustion layout coupled to the CC system with surplus vapor recirculation comparing two cases: with and without a cooler (WIC and WOC, respectively) before the intake manifold. The cooler

C-2 model was established by maintaining a cylinder intake temperature equal to 85 °C to avoid in-cylinder water condensation. The idea is to assess the impact of a cooling step at the cylinder inlet on power plant performance and verify if C-2 is not really advantageous and may be removed, facilitating the system packaging.

Table 5.3: Average results of relevant power plant performance variables comparing WIC and WOC for the oxy-fuel combustion layout with CC: Part 1.

	BSFC [g/kWh]	**Brake Power [kW]**	**Opt. Function [kW]**	**SOI [CAD]**	**Maximum In-cylinder Pressure [bar]**	**MIEC Permeate Pressure [bar]**
WIC	240.3	118.0	39.7	-25.7	164	1.55
WOC	256.4	92.7	29.2	-28.7	180	2.67

Table 5.4: Average results of relevant power plant performance variables comparing WIC and WOC for the oxy-fuel combustion layout with CC: Part 2.

	Net BSFC [g/kWh]	**Net Brake Power [kW]**	**Net Opt. Function [kW]**	**EGR [%]**	**Intake Temperature [°C]**	**Total ICE Additional Cooling Power [kW]**
WIC	264.7	107.2	32.7	70.3	85	109
WOC	278.9	85.2	24.7	76.4	374	60

As the reciprocating compressors were connected to the engine crankshaft, part of the mechanical energy produced by combustion was used to move those compressors and, hence, both engine brake power and BSFC must consider that reduction of available mechanical energy. As a result, net brake power is defined as engine brake power minus the power of the reciprocating compressors, and engine net BSFC is established as the amount of injected fuel by the engine cycle divided by net mechanical energy generated within the same engine cycle. In this circumstance, the net optimization function, defined as the product of net effective efficiency (equivalent to engine net BSFC) and net brake power, was maximized actuating on SOI for the proposed cases (WIC and WOC), whose average results of relevant power plant performance variables are compared in Table 5.3 and Table 5.4. WOC presents higher in-cylinder maximum pressure than WIC because more EGR is required to control T_{exh} at the set point due to the lack of intake cooling. Within this context, once the total ICE additional cooling is defined as the sum of cooler C-1, flash 1, flash 2 and flash 3 powers (plus cooler C-2 power for WIC), WOC requires lower cooling energy than WIC. However, WIC shows higher gross brake power than WOC because it needs less EGR, which implies lower MIEC permeate pressure, higher MIEC pressure ratio, and, consequently more O_2

generation to produce heat released power. As WIC presents a lower intake temperature, engine volumetric efficiency and gross BSFC are better for that case, since it increases inlet flow density and reduces heat losses. Moreover, the net variables follow the same trend as the gross BSFC and brake power due to the reasons mentioned above based on intake temperature. Those assertions are better proven and detailed in section 5.3 whereby more process variables (regarding MIEC, HEN and engine performances) are studied considering the entire system with the final amendments.

One may see that there is an increment in BSFC (around 10%) by comparing both gross and net BSFC values as well as a reduction in brake power (around 9%) due to energy penalty related to the CO_2 capture. Although the net optimization function presents better results for WIC, its cooling energy penalty is not negligible compared to WOC. Indeed, the total ICE additional cooling power for WIC is around twice as high as for WOC, suggesting the best configuration must contemplate an intermediate solution between WIC and WOC. In both cases, the amount of CO_2 captured as well as its purity is the same since flash temperatures are fixed and, as already seen in Figure 5.8, those variables basically depend on the CC system specifications.

Figure 5.9c depicts the inbound and outbound mass flows inside one of the cylinders for both cases, WIC and WOC. Therefore, it may be seen how the vapor injection controller is operating satisfactorily without overlapping fuel injection, and vapor injection is very narrow with a significant peak due to the high-pressure difference between common rail (80 bar) and combustion chamber during the compression phase (around 15 bar). The effects of vapor in-chamber direct injection on the in-cylinder instantaneous variables (pressure, temperature and trapped mass) are appropriately presented and discussed in section 5.3.

5.2.5 Water recirculation.

In order to take advantage of the main benefits of each solution, i.e., WIC with higher net optimization function and WOC with lower total ICE additional cooling power, a new amendment was proposed. It consisted of recovering part of the liquid water generated by flashes 1 and 2, and blending it with the oxidizer flow to decrease the intake manifold temperature and increase the γ of the intake gas. In fact, as water has greater γ than CO_2 [71], that strategy may be favorable in terms of power plant indicated efficiency. To do so, a pump was added to the CC system to recuperate part of the water leaving flash 1, increasing its pressure until the flash 2 operating pressure Figure 5.11. Therefore, liquids from flashes 1 and 2 were mixed and recirculated towards engine intake gases. Figure 5.12 displays the proposed layout with a desuperheater (named mixer on the diagram) used to blend water from the CC system with oxidizer flow coming from HEN.

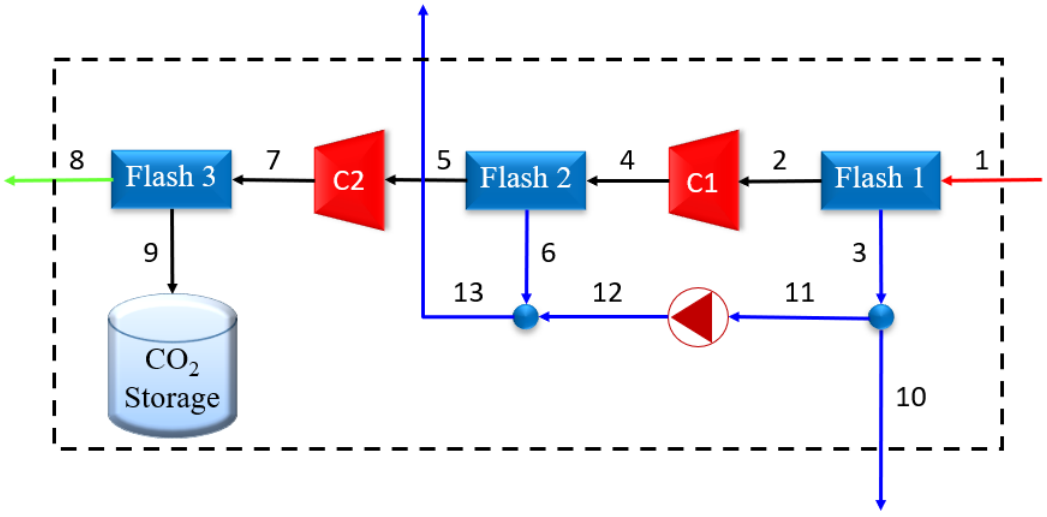

Figure 5.11: CC model with water recirculation.

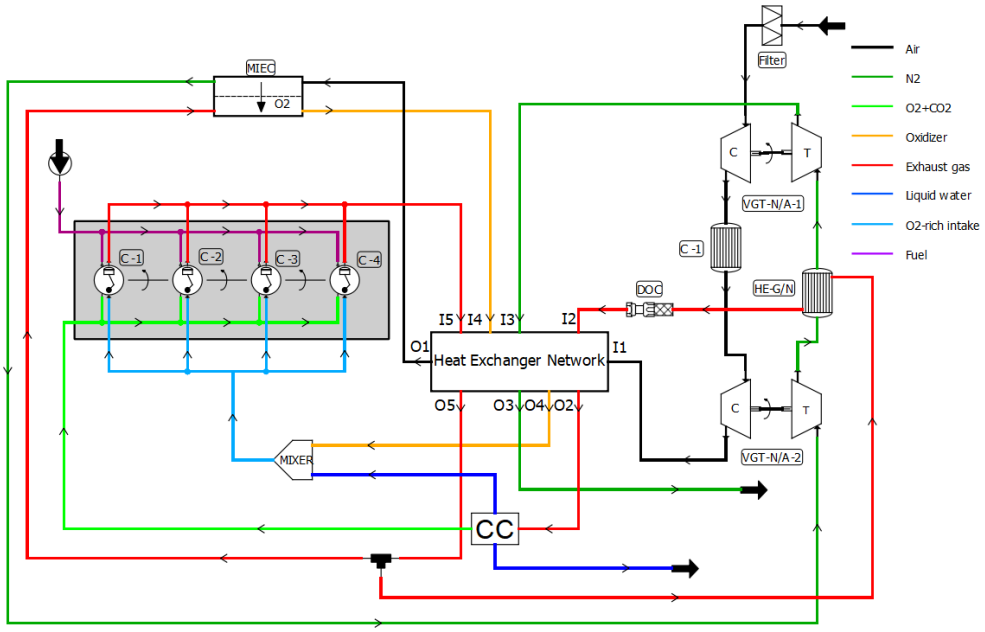

Figure 5.12: Oxy-fuel combustion layout coupled to CO_2 capture system with water recirculation.

Regarding the complete model, VEMOD was modeling the vapor injection from the common rail into the cylinders as described in subsubsection 5.2.4.2, while the Python script was simulating in steady-state the water-oxidizer mixer and the CC system comprising compressors 1 and 2, and flashes 1, 2 and 3. The flow conditions at the oxidizer line (HEN output 4 in Figure 5.12) and oxy-fuel layout tailpipe (HEN output 2 in Figure 5.12) are the Python script inputs. Indeed, as the EOS-based VLE calculation in different elements of the CC system and mixer is very time-consuming regarding the fluid dynamic as done in VEMOD, the Python script was only activated during certain periods considering the input average values generated by VEMOD. Thus, after VEMOD initialization in order to stabilize the Brayton cycle, and subsequent Python activation, the Python script outputs were returned to the VEMOD-built oxy-fuel layout as inputs (surplus vapor and water recirculations) in an iterative process between VEMOD and Python script until the system could converge as shown in Figure 5.13.

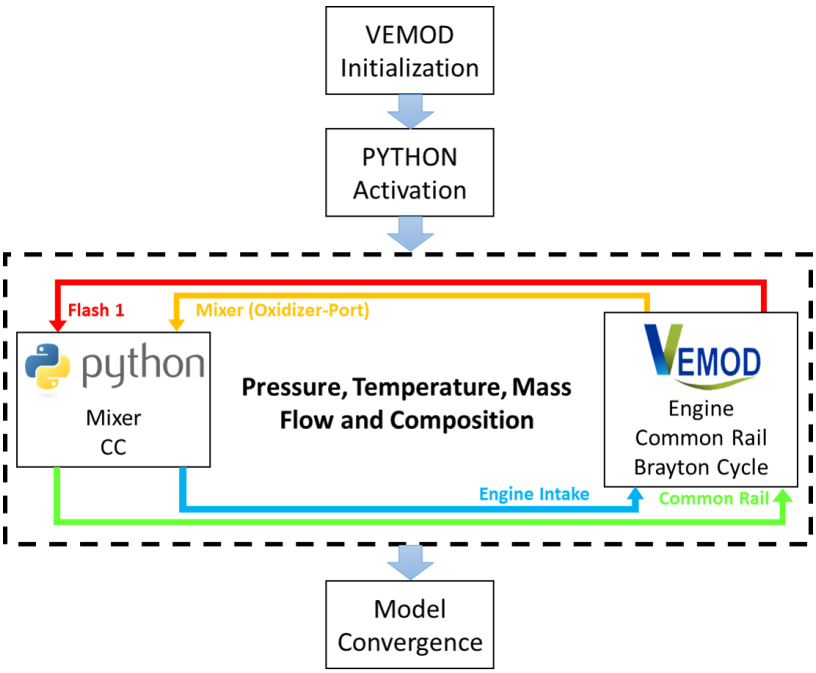

Figure 5.13: Model flowchart diagram.

5.2.5.1 Mixer model.

Consequently, a mixer model was developed regarding the above context. The mixer outlet may contain either a vapor phase, which means all liquid water is evaporated by the oxidizer flow, or a VLE phase with considerable liquid water content depending on mixer inlet flow conditions. In order to determine the mixer outlet conditions (mass flow, composition, temperature and phase), the mixer model algorithm solved mass and energy balances coupled to VLE equations, considering the mixer as adiabatic and the inlet liquid water discharge pressure equal to the inlet oxidizer flow pressure. Mixer outlet phase was verified by comparing the mixture dew enthalpy with the mixture outlet vapor enthalpy, which was calculated assuming the oxidizer has enough thermal energy to evaporate all liquid water and, hence, mixer outlet phase was assured to be vapor. Both enthalpies were respectively calculated using Equation 2.5 with dew-point vapor mole composition and outlet overall mole composition considering the mixer mass balance. In short, if the mixture outlet vapor enthalpy is greater than the mixture dew enthalpy, the outlet phase

is a vapor; otherwise, it is a VLE mixture for a given operating pressure.

For the purpose of demonstrating the mixer model performance itself, oxidizer conditions (mass flow, composition, temperature and pressure) were held constant for the point with a better net optimization function for the WOC case. Therefore, a sweeping process varying inlet liquid water temperature (from 30 °C to 90 °C) and mass flow (from $0\,\mathrm{kg\,h^{-1}}$ to $150\,000\,\mathrm{kg\,h^{-1}}$) was carried out by tending to infinite the amount of water injection for the sake of better illustrating the physics of the process.

As shown in Figure 5.14b, there are two distinct zones: one where the outlet phase is a vapor corresponding to low water mass flows (WMFs) (approximately from $0\,\mathrm{kg\,h^{-1}}$ to $50\,\mathrm{kg\,h^{-1}}$), and another where outlet phase is a VLE corresponding to high WMFs (approximately from $50\,\mathrm{kg\,h^{-1}}$ to $150\,000\,\mathrm{kg\,h^{-1}}$). The mixer outlet temperature profoundly decreases when inlet WMF increases within the vapor zone because little-by-little significant latent energy is required to evaporate all liquid water. In contrast, it tends to the respective water inlet temperature when oxidizer mass flow is not comparable to WMF anymore inside the VLE zone (Figure 5.14a). Water vapor pressure increases with WMF inside the vapor region because more water content is present in the outlet gas until achieving saturation condition and, consequently, the VLE zone (Figure 5.14c).

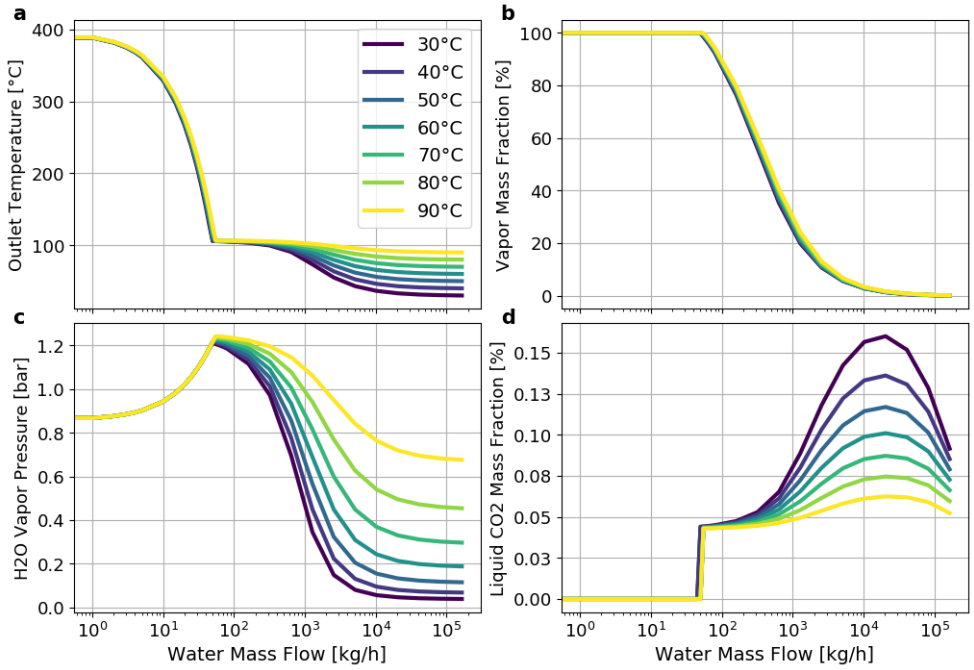

Figure 5.14: Main mixer model outlet variables sweeping water temperature and mass flow for given EGR conditions.

Indeed, that saturation point corresponds to a stable temperature area (around 100 °C in Figure 5.14a), wherein water pressure vapor is basically equal to its saturation pressure, which is significantly temperature-dependent. Still in Figure 5.14c, when WMF is much higher than the oxidizer mass flow, water vapor pressure is WMF-independent because the temperature is essentially equal to the water inlet temperature. The mixer model may predict the solubility of both O_2 and CO_2 in liquid water, which is illustrated in Figure 5.14d. On the one side, the liquid CO_2 mass fraction is majorly temperature-dependent, analyzing both Figure 5.14a and Figure 5.14d, and the lower temperature is, the higher CO_2 solubility due to lower gas kinetic energy level. On the other side, a water dilution effect is seen when there is a considerable amount of WMF at constant outlet temperature, which reduces CO_2 solubility (after the peak in Figure 5.14d). Also, information about CO_2 solubility is important to define the use of that CO_2-contaminated water since CO_2 dissolving into the water may form carbonic acid, which may corrode alloys and steels present in the power plant components.

5.3 Results and discussion.

After having proposed a complete oxy-fuel combustion layout with CC and with vapor and water recirculations (Figure 5.12), SOI and WMF are swept to verify their impact on the performance of relevant power plant variables attempting to find out the best operating conditions for the system. In order to avoid liquid water inside the cylinders, this study pursues operation zones wherein intake temperature is above the dew point at the intake manifold. As a result, saturation conditions limit the increase in recirculated water for a given SOI. Therefore, in this section, critical average results are analyzed to define the system optimum operating point with insights into the instantaneous results for the cases of interest. In particular, temperature, pressure and mass flow along the system are discussed for the best cases without and with water. Finally, an overall analysis of the final results is made subsection 5.3.4.

5.3.1 Average results.

Figure 5.15 and Figure 5.16 present relevant average results in contour maps varying SOI and total ICE additional cooling power, which is basically WMF-dependent (the amount of recirculated water is represented by white lines drawn over maps). As expected, the higher WMF is, the lower intake temperature is (Figure 5.15a). Also, if SOI is delayed for a specific WMF, more thermal energy is available at the exhaust manifold and, hence, more EGR is required to control the target temperature (Figure 5.15b), heating up the oxidizer flow. Indeed, for producing more EGR, the intake pressure must be increased (Figure 5.15c), which entails more intake mass flow (Figure 5.15d). The in-cylinder maximum pressure is essentially SOI-dependent (Figure 5.15e) and its value decreases when SOI is delayed because the combustion is moved towards the expansion process. Actually, MIEC O_2 generation increases with recirculated water (Figure 5.16a) due to the MIEC permeate pressure reduction (following the EGR and intake pressure behaviors) (Figure 5.16b), reflecting on an enhancement of the MIEC pressure ratio (Figure 5.16c), since MIEC feed pressures scarcely vary (Figure 5.16d). Thus, it improves the MIEC filtration efficiency defined by the ratio between the O_2 produced and the total O_2 which enters the MIEC feed side (Figure 5.16e). Additionally, the O_2 permeated by the MIEC increases due to higher MIEC feed temperature (Figure 5.16f) risen by the higher exhaust gas thermal power with greater water content. As a re-

sult, the increment of in-cylinder available O_2 produces more energy released by combustion and, consequently, more mechanical power (Figure 5.15h) and cylinder-out gas sensible enthalpy to heat up the MIEC. Also, as water specific heat capacity is greater than that of CO_2, if more water is recirculated, the better is the efficiency in many HEs. In other words, once this system is self-sufficient, the more O_2 generated by the MIEC, the better the entire system works, increasing even its O_2 production rate.

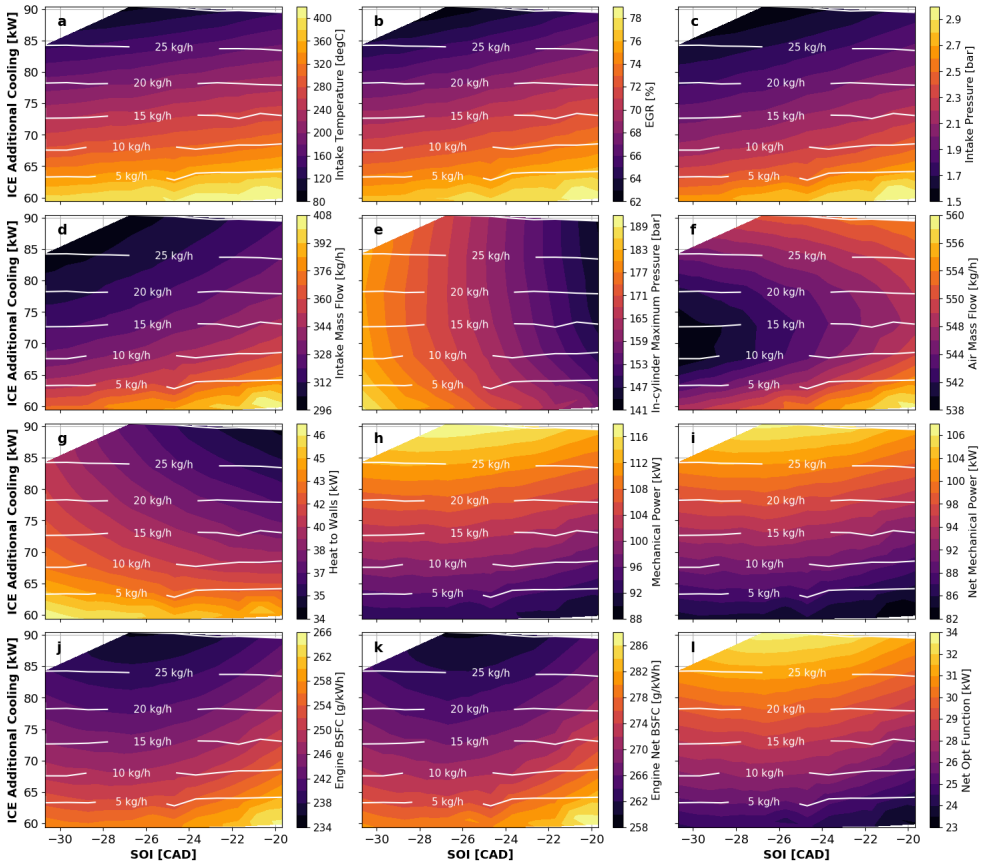

Figure 5.15: Maps for average results of relevant engine variables sweeping SOI and total ICE additional cooling power (reflected by the amount of water blended with EGR at mixer). The white lines drawn on maps represent the amount of recirculated water.

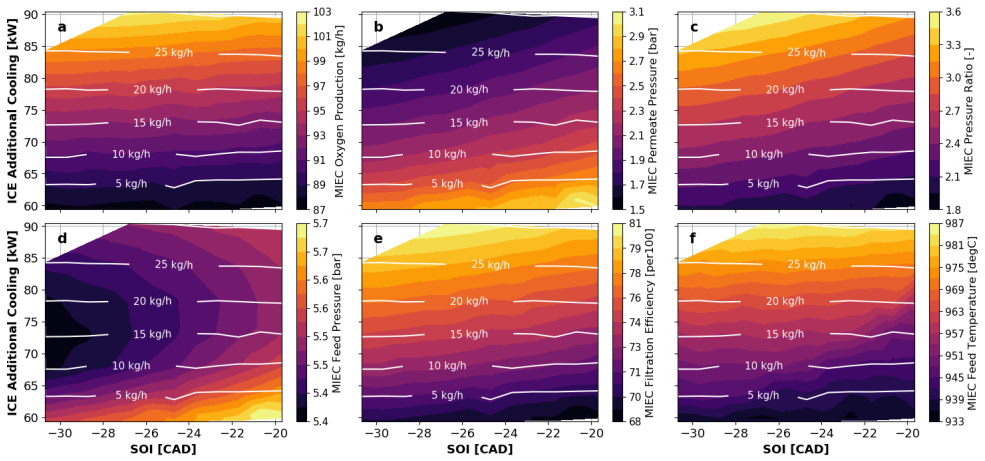

Figure 5.16: Maps for average results of relevant MIEC variables sweeping SOI and total ICE additional cooling power (reflected by the amount of water blended with EGR at mixer). The white lines drawn on maps represent the amount of recirculated water.

Figure 5.15f shows minimum values for system-inlet air mass flow when the WMF varies at a constant SOI, which is also observed on the MIEC feed pressure (Figure 5.16d). On the one hand, if the MIEC filtration efficiency is improved, less mass flow is present at the N_2-rich line and less energy is available to move N_2 turbines of VGT-N/A-1 and VGT-N/A-2 (bottom part over Figure 5.15f with WMF range from $0\,kg\,h^{-1}$ to $15\,kg\,h^{-1}$). On the other hand, when O_2 production is high, more exhaust mass flow is generated leading to more heat power exchanged at the HEs, producing more thermal power to move the N_2 turbines (Figure 5.16d and Figure 5.16f), which compensates the increase in MIEC filtration efficiency (top part over Figure 5.15f with WMF range from $15\,kg\,h^{-1}$ to $30\,kg\,h^{-1}$). In turn, convective heat losses decrease when WMF increases due to the intake cooling effect (Figure 5.15a and g), and at constant WMF, if SOI is delayed, more intake fresh mass flow with more inert is sucked by the engine, reducing the heat transfer to walls due to the presence of more mass that absorbs the heat released by the combustion (Figure 5.15b and d). The main advantage of using recirculated water is reflected in the improvement of the system performance variables such as engine power, net engine power, BSFC, net BSFC and net optimization function (Figure 5.15h-l). In fact, as more O_2 is produced and less convective heat is wasted when the WMF increases, more useful energy is available to yield worthwhile mechanical power with better efficiency, since the gamma of

the cylinder oxidizer charge is also higher. In general, the penalty for capturing CO_2 in-situ (moving the reciprocating compressors coupled to the engine) is seen in the reduction of mechanical power (around 8%) and the increase in BSFC (around 9%), comparing Figure 5.15h and i as well as Figure 5.15j and k, respectively. Figure 5.15l depicts a trade-off between the cost of chilling and system performance since improvement on net optimization function entails higher total ICE additional cooling power. Therefore, WMF=20 $kg\,h^{-1}$ and SOI=-26.5 CAD is considered the preferred point without excessive cooling power and with satisfactory power plant output.

5.3.2 Instantaneous results.

Figure 5.17 displays instantaneous results of in-cylinder variables for the edges of the contour maps (blue and green lines) and the chosen combination of SOI and WMF, taking into account the trade-off between total ICE additional cooling power and net optimization function (red line). Green and blue lines represent the most advanced and delayed SOIs, respectively, whereas solid and dashed lines represent the highest and lowest WMFs for each specific SOI. One may see that when the combustion is more centered at top dead center (Figure 5.17a and c), the effective efficiency is improved (Figure 5.15j and k). The effect of in-cylinder direct vapor injection is observed in Figure 5.17b and d, with a slight increment of in-cylinder O_2 mass which decreases the temperature during the compression phase. Still within that phase, the cases without water recirculation present higher pressure (Figure 5.17c) due to more EGR need (Figure 5.15b) to keep T_{exh} of 1000 °C, also reflecting on more elevated maximum pressure (Figure 5.15e). In addition, once more O_2 is employed for cases with water recirculation, more heat power is released during combustion (Figure 5.17a), generating more brake power (Figure 5.15h and i).

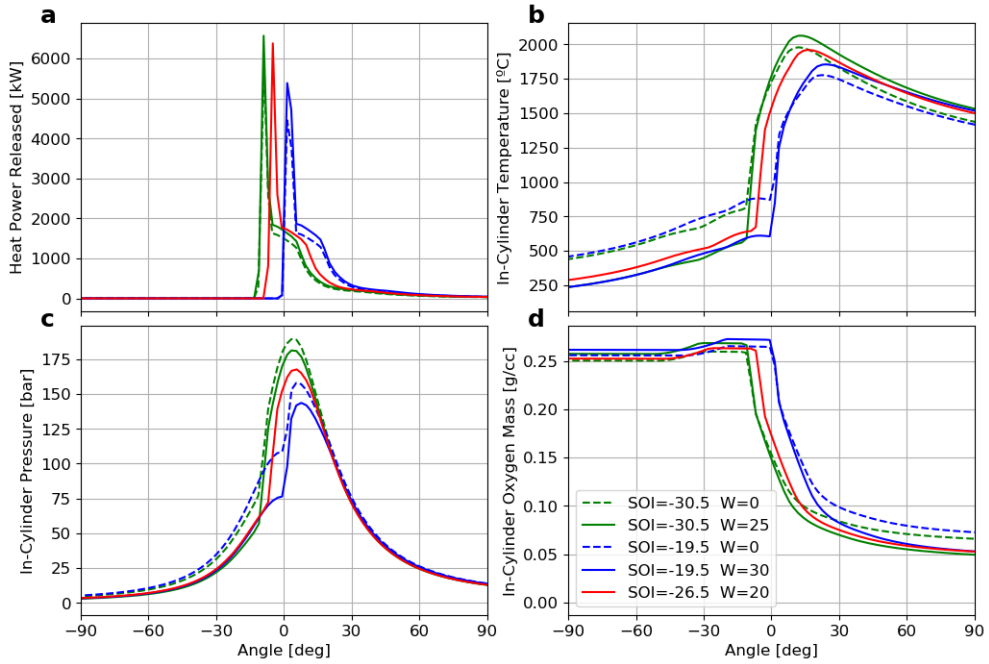

Figure 5.17: Instantaneous results of in-cylinder parameters for the edges of the contour maps and the chosen combination of SOI and amount of recirculated water, taking into account the trade-off between total ICE additional cooling power and net optimization function. In figure legend, SOI is in CAD and W represents the amount of water recirculated in kg/h.

5.3.3 Temperature, mass flow and pressure diagrams.

This subsection analyzes the preferred point (in terms of total ICE additional cooling power and net optimization function) for each case with and without water recirculation (WIR and WOR, respectively) by checking the process variables drawn over distribution diagrams (Figure 5.18 and Figure 5.19):

- WMF=20 kg h^{-1} and SOI=-26.5 CAD for WIR.
- WMF=0 kg h^{-1} and SOI=-27.5 CAD for WOR.

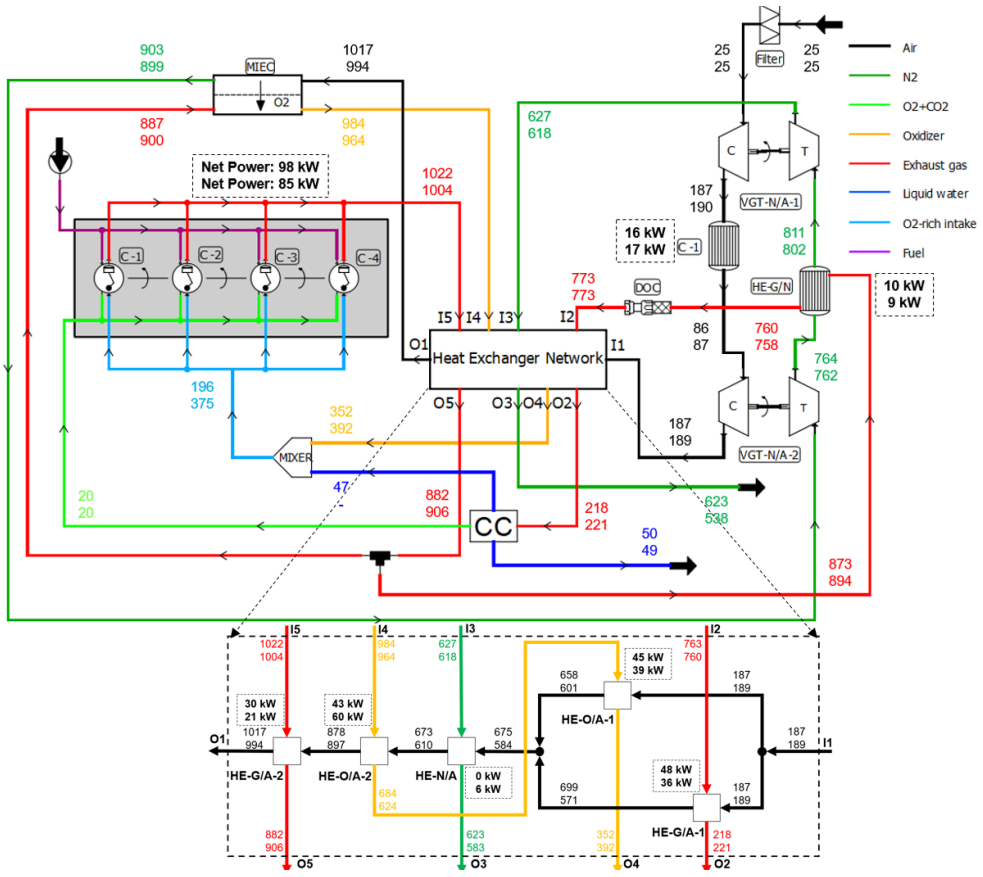

Figure 5.18: Power (in kW) and temperature (in °C) distribution diagram for both cases at 3500 rpm: with (top values) and without (bottom values) water recirculation.

Figure 5.18 displays powers and temperatures on different lines and elements of the system, including the HEN. Numerical values are added next to each flow line with top values for WIR and bottom ones for WOR. In addition, the heat power exchanged is shown next to each HE and cooler, as well as the net system power over the engine itself, following the representation mentioned above. Also, Figure 5.19 shows the effect of each case on mass flow and pressure distributions, following the same depiction scheme as for the temperature diagram (with top values for WIR and bottom ones for WOR).

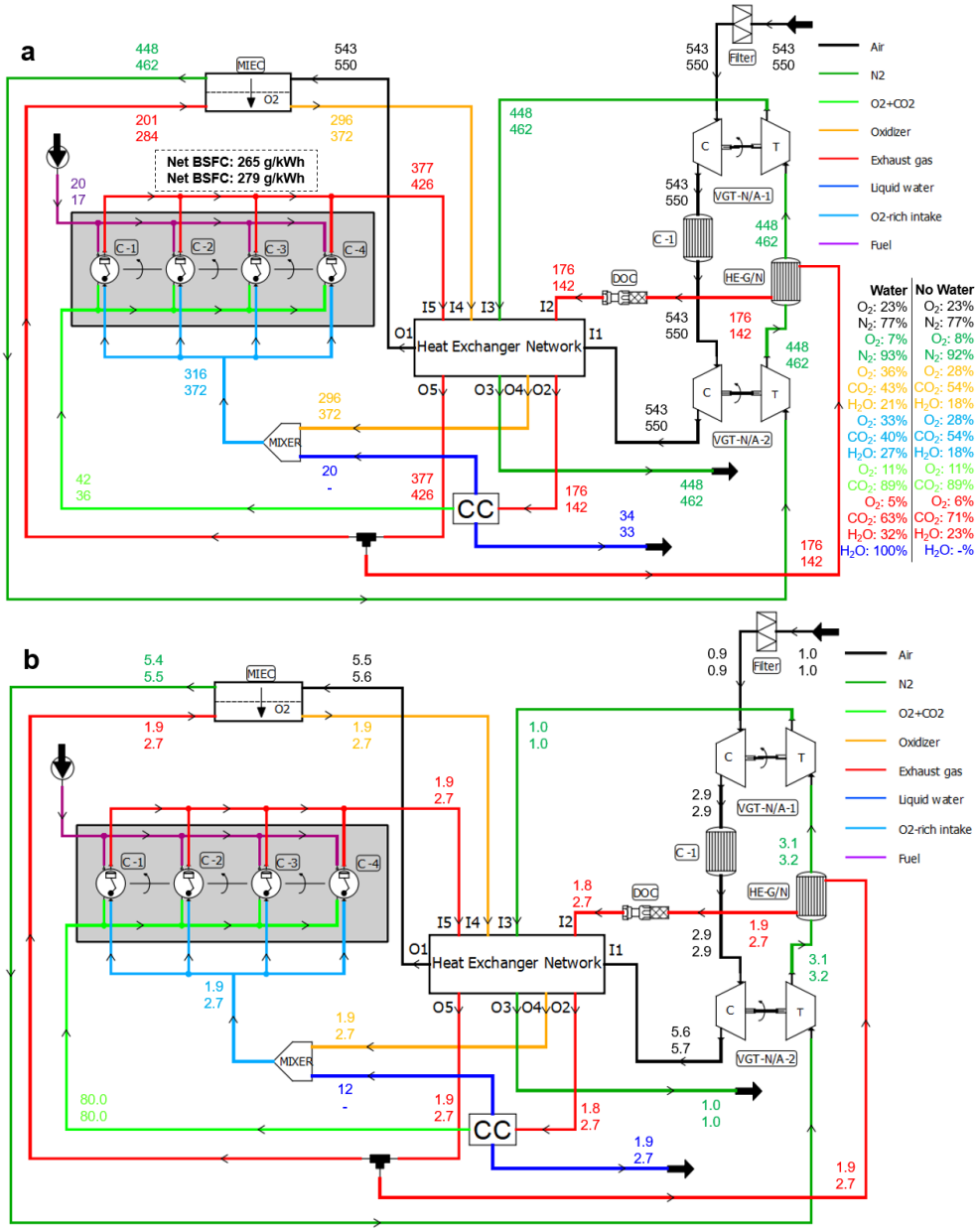

Figure 5.19: Distribution diagram for both cases at 3500 rpm: with (top values) and without (bottom values) water recirculation. (a) Mass flow (in kg h^{-1}) and composition; (b) Pressure (in bar).

Indeed, those diagrams confirm the analyzes carried out for contour maps (Figure 5.15 and Figure 5.16), demonstrating the benefits of water recirculation on system performance (see Net BSFC and Net Power on Figure 5.19a and Figure 5.18, respectively). Compared to WIR, WOR has higher pressure at MIEC permeate side with more EGR mass flow to maintain T_{exh}=1000 °C, and, thereby, less O_2 is generated by the MIEC, since its feed pressure is almost constant. However, less EGR is required to control that temperature when there is water recirculation, which improves the pressure ratio at the MIEC and its O_2 production. If more O_2 is available for combustion, the engine power output increases, and more mechanical power is free to move the reciprocating compressors in the CC. Once λ is fixed in both cases, when more O_2 permeates the MIEC, more fuel is also injected and, thereby, more combustion products (CO_2 and water vapor) are generated. Thus, that increment of mass flow going towards CC, also due to water recirculation, causes more heat transfer in the HE-G/A-1, and, hence, changes the power distribution through the HEs. In addition, as the specif heat capacity for water is almost double that for CO_2 [71], the better the heat exchange is in a particular HE when there is more water content on any of its sides. Also, the intake manifold water content increases from 18% to 27%, enhancing the in-cylinder γ and, hence, the power plant indicated efficiency.

Nonetheless, as WIR possesses more water vapor at exhaust gas going towards CC, Flash 1 cooling power must be higher because TF1 is the same for both cases, which increases the total ICE additional cooling power as explained in subsubsection 5.2.4.1. In any case, the heat exchanged in the Flash 1 is much higher than for Flashes 2 and 3 due to their outlet temperatures, which are defined in subsubsection 5.2.4.1. Whenever there is water recirculation, the pump shown in Figure 5.11 is required; however, once the liquid density is much higher than for gases, its pumping power (around 0.005 kW) is negligible compared to the gas compression power on reciprocating compressors (around 7 kW and 9 kW for the first and second compression stages respectively) as shown in Figure 5.20. As more CO_2 is produced for WIR case than for WOR one, its corresponding time to consume the fuel (at this particular operating point) and fill up the CO_2 storage tank is shorter (around 93 min and 104 min for WIR and WOR, respectively) to capture the same amount of mass (around 125 kg) at 20 °C and 80 bar with the same CO_2 purity equal to 95% (mass fraction) as displayed in Figure 5.21.

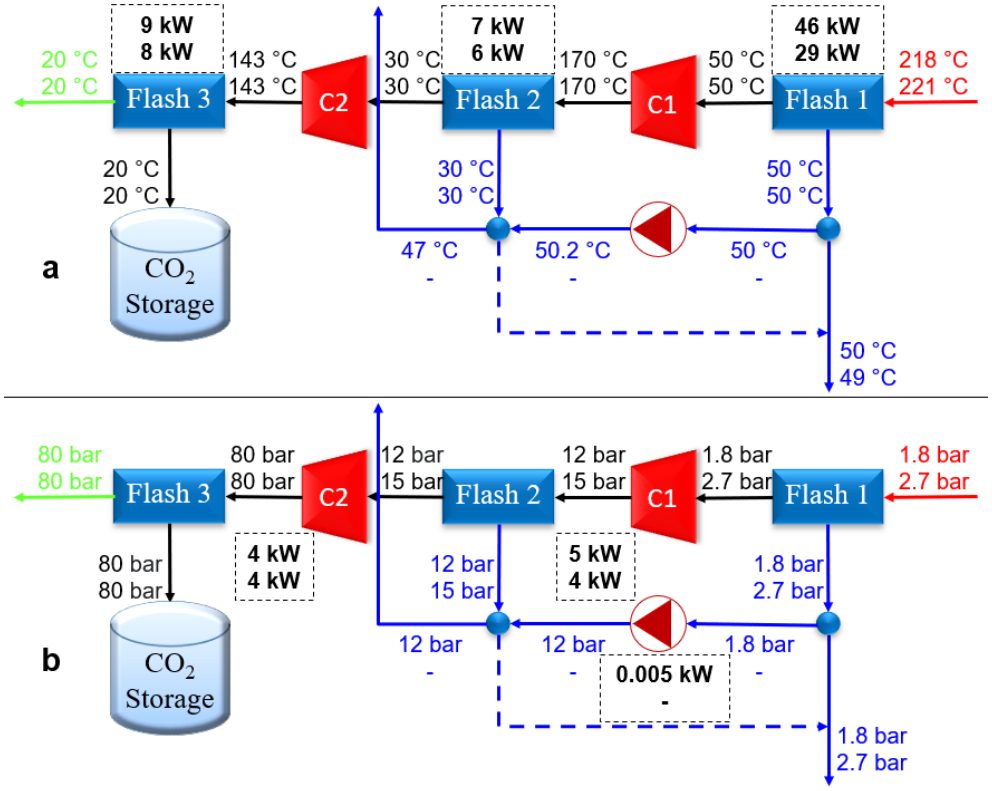

Figure 5.20: Diagram inside CC for both cases: with (top values) and without (bottom values) water recirculation. (a) Temperature (in °C) and cooling power (in kW); (b) Pressure (in bar) and compression power (in kW).

As the blow-by flow generated in the cylinders is recirculated into the intake manifold and vapor generated in the Flash 3 is directly re-injected into the combustion chamber, the only losses of CO_2 from the system are related to non-recirculated condensed water on Flash 1 (and Flash 2 for the WOR case), which contains some traces of CO_2 diluted in the liquid phase. Thus, CO_2 capture efficiency may be calculated for the optimum points of the WIR and WOR cases, carrying out a mass balance for the CO_2 considering its mass flows and compositions in the non-recirculated water and CO_2 tank inlet streams. Accordingly, the CO_2 capture efficiencies (or CO_2 recovery rates) calculated for WIR and WOR are 99.94% and 99.87%, respectively using the values presented in the supplementary material.

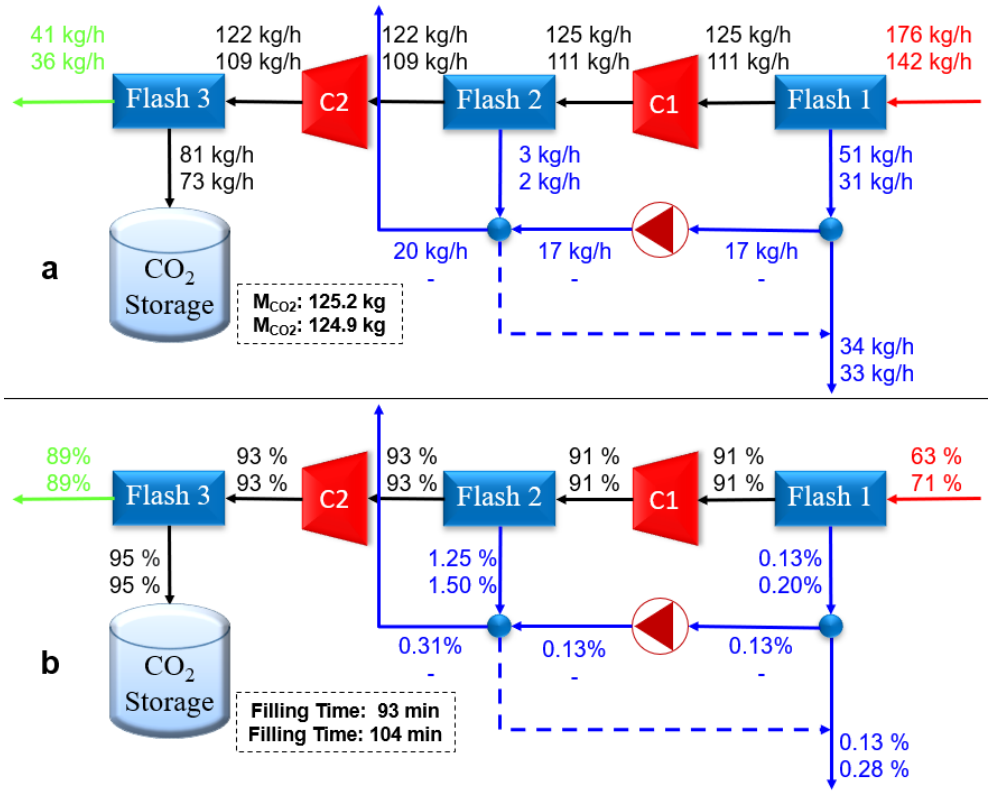

Figure 5.21: Diagram inside CC for both cases: with (top values) and without (bottom values) water recirculation. (a) Mass flow (in $\mathrm{kg\,h^{-1}}$) and captured CO_2 (in kg); (b) CO_2 mass composition (in %) and filling time (in min)

5.3.4 Overall results.

Figure 5.22 summarizes the preferred results of each amendment proposed in this chapter. In fact, the abbreviation depicted in that figure and used in this subsection represents the following modifications of the layout:

- Original layout established in chapter 4 (M1).
- Layout M1 without VGT-G/O and its corresponding cooler, adding a OC (M2).
- Layout M2 with a cooler upstream the intake manifold and the coupling of the CC system. This configuration is equivalent to the WIC case shown in subsubsection 5.2.4.1 (M3).
- Layout M2 with the coupling of the CC system. This structure is equivalent to WOC and WOR cases seen, respectively, in subsubsection 5.2.4.1 and subsection 5.3.3 (M4).
- Layout M4 with water recirculation. This configuration represents the WIR case depicted in subsection 5.3.3 (M5).

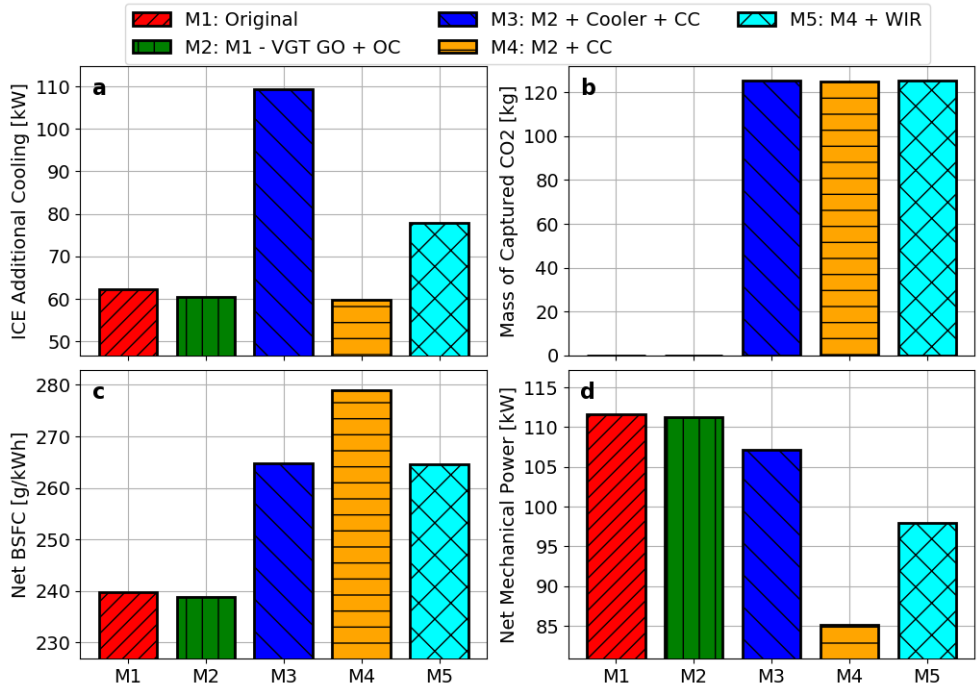

Figure 5.22: Overall results comparing the main amendments.

The results shown for M1, M2, M3 and M4 consider the preferred SOI only with regard to net optimum function, while M5 takes into account that variable combined with the total ICE additional cooling power as explained in subsection 5.3.1. In general, a worsening of the power plant performance (higher net BSFC and lower net mechanical power) is seen (Figure 5.22c and d) due to the system capability of capturing the CO_2 present in the exhaust gas (Figure 5.22b). As already discussed in subsection 5.2.2, M1 and M2 present similar performance, because VGT-G/O and its corresponding cooler are useless in M1. M5 is able to combine the advantages of M3 and M4 when the CC is deemed with in-cylinder direct-injection of the surplus vapor coming from flash 3. Thus, M5 yields the same net BSFC as M3, with a slight reduction in net mechanical power, but decreasing considerably total ICE additional cooling power (approximately from 110 kW to 80 kW) (Figure 5.22a). In addition, although M5 presents more cooling energy than M4, an important improvement in power plant efficiency and output power is observed for M5 (on average, more than 5% and 13% respectively), what confirms M5 as the best layout discussed in this work.

Chapter 5 Bibliography

[3] J. Luján, F. Arnau, P. Piqueras, and V. Farias. "Design of a carbon capture system for oxy-fuel combustion in compression ignition engines with exhaust water recirculation". *Energy Conversion and Management* 284 (May 2023), p. 116979. DOI: 10.1016/j.enconman.2023.116979 (cit. on pp. xii, 95).

[71] G. D. Perry R. *Perry's chemical engineers's handbook eighth edition.* McGraw-Hill, 2008 (cit. on pp. 21, 58, 113, 125).

[100] S. I. Sandler. *Chemical, biochemical and engineering thermodynamics.* Harvard, 2016 (cit. on pp. 28, 96).

[110] L. Hailong. "Thermodynamic properties of CO2 mixtures and their applications in advanced power cycles with CO2 capture processes". PhD thesis. Stockholm, Sweden: Royal Institute of Technology, Jan. 2008 (cit. on p. 95).

[111] B. Metz, O. Davidson, H. de Coninck, M. Loos, and L. Meyer. "IPCC special report on carbon dioxide capture and storage". *Policy Stud.* (Jan. 2005) (cit. on p. 95).

[112] S. Westman, J. Stang, S. Løvseth, A. Austegard, I. Snustad, and I. Ertesvåg. "Vapor-liquid equilibrium data for the carbon dioxide and oxygen (CO2 + O2) system at the temperatures 218, 233, 253, 273, 288 and 298 K and pressures up to 14 MPa". *Fluid Phase Equilibria* 421 (Apr. 2016), pp. 67–87. DOI: 10.1016/j.fluid.2016.04.002 (cit. on p. 97).

[113] R. W. Kugel. "Raoult's Law: Binary Liquid-Vapor Phase Diagrams: A Simple Physical Chemistry Experiment". *Journal of Chemical Education* 75.(9) (1998), p. 1125. DOI: 10.1021/ed075p1125. URL: https://doi.org/10.1021/ed075p1125 (cit. on p. 97).

[114] E. F. Stephan, N. S. Hatfield, R. S. Peoples, and H. A. Pray. "THE SOLUBILITY OF GASES IN WATER AND IN AQUEOUS URANYL SALT SOLUTIONS AT ELEVATED TEMPERATURES AND PRESSURES" (Jan. 1956). URL: https://www.osti.gov/biblio/4379406 (cit. on p. 98).

[115] A Valtz, A. Chapoy, C Coquelet, P Paricaud, and D Richon. "Vapour-liquid equilibria in the carbon dioxide-water system, measurement and modelling from 278.2 to 318.2K". English. *Fluid Phase Equilibria* 226 (Dec. 2004), pp. 333–344. ISSN: 0378-3812. DOI: doi:10.1016/j.fluid.2004.10.013 (cit. on p. 99).

[116] G. Müller, E. Bender, and G. Maurer. "Das Dampf-Flüssigkeitsgleichgewicht des ternären Systems Ammoniak-Kohlendioxid-Wasser bei hohen Wassergehalten im Bereich zwischen 373 und 473 Kelvin". *Berichte der Bunsengesellschaft für physikalische Chemie* 92.(2) (1988), pp. 148–160. DOI: https://doi.org/10.1002/bbpc.198800036. URL: https://onlinelibrary.wiley.com/doi/abs/10.1002/bbpc.198800036 (cit. on p. 99).

[117] R. E. Sanders. *9 - Accidents involving compressors, hoses, and pumps*. Ed. by R. E. Sanders. Fourth Edition. Butterworth-Heinemann, 2015, pp. 235–267. ISBN: 978-0-12-801425-7. DOI: https://doi.org/10.1016/B978-0-12-801425-7.00009-1. URL: https://www.sciencedirect.com/science/article/pii/B9780128014257000091 (cit. on p. 106).

Chapter 6

Final oxy-fuel carbon-capture layout for prototype construction.

Contents

6.1 Introduction

A final version of the oxy-fuel carbon-capture power plant developed throughout this manuscript is presented in the current chapter, preparing the oxy-fuel carbon-capture layout to be set up and tested at CMT - Clean Mobility and Thermofluids facilities. Therefore, the aim of this chapter is to improve the system sub-models in order to make them more down-to-earth for easier equipment acquisition and implementation.

At first, preliminary sub-models for reciprocating compressors and fluid mixing used in preceding chapters are improved and tailored for easy realistic application at laboratory scale. Indeed, better models for system design may provide decision supports for selecting equipment suppliers and proper interaction with them. Secondly, a control philosophy is proposed for the CC system considering the pressure and temperature regulation among the HEs and reciprocating compressors.

Finally, the final version of the layout is depicted and described, assessing its performance at 3500 rpm full-load point via analysis on average and instantaneous results as well as distribution diagrams for temperature, pressure, mass flow and composition.

6.2 Adaptation and improvement of sub-models

Considering the previous layout (Figure 5.12) shown in chapter 5, some market research was performed regarding industrial devices for in-cylinder direct injection of the vapor coming from flash 3, however the required mass flow was too high for conventional injectors found in the market and a tailor-made solution would be very high-priced, which makes this approach unfeasible at the present time for prototype construction. Thus, for the final oxy-fuel carbon-capture engine layout proposed in this section(see Figure 6.1), the common rail (Figure 5.9) used in precedent chapter is removed, and a dual-stage desuperheater model (Mixers 1 and 2) is located upstream the intake manifold to simulate the mixing of fluids recirculating from CC system. In this case, flash 3 outlet vapor and part of the liquid water generated at flashes 1 and 2 are mixed with the oxidizer flow at the dual-stage desuperheater to decrease the intake temperature, increase the γ of the intake gas and consume the recycled

O_2 in the combustion process, yielding further power for the engine.

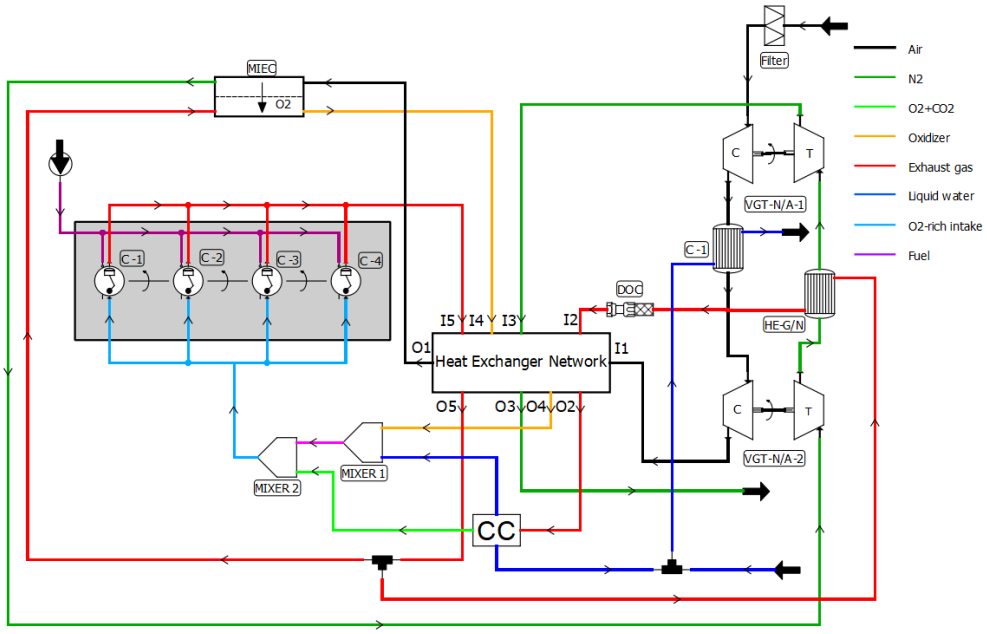

Figure 6.1: Final oxy-fuel combustion layout coupled to CO_2 capture system with dual-stage mixer.

The other portion of water condensed in the CC at flashes 1 and 2 is reused for system inlet air cooling at Cooler C-1, diminishing the additional cooling power in terms of water consumption. Indeed, this water stream is not enough to maintain cooler C-1 outlet air temperature around 85 °C and, thereby, some extra water must be used for that purpose. The sub-model for recipocrating compressors is also enhanced and discussed to better simulate the system behavior for experimental development. In addition, values for some design variables such as TFs, CO_2 capturing pressure, T_{exh} and oxygen-to-fuel ratio (see Equation 5.6) found and used in previous chapter are likewise maintained in the present study for the layout modification.

At last, the combustion model was improved when compared to the one employed in previous chapter since the current approach makes use of ACT in order to simulate the combustion behavior. In fact, ACT is able to identify and quantify the main physical variables which directly affect the mixing process within combustion phenomena ([109]). Moreover, two additional ACT

calibrating parameters (K-factor and mixing constant) had to be refined because the effect of greater water content at intake valve closed, when water is recycled from CC, was not properly predicted underestimating the combustion completeness by around 4% if compared to CFD results for same scenario.

6.2.1 Dual-stage mixer model

Apart from the market constrains regarding injector acquisition as already exposed, the previous vapor injection model was not considering the phase change for CO_2-O_2 mixture and, besides that, this fluid was expanded in an isentropic process. Therefore, a dual-stage desuperheater model is proposed taking into account the phase change during expansion for the recirculating fluids, mixing them in a isenthalpic process concerning the stagnation enthalpy (static enthalpy plus kinetic energy) with outlet pressure equal to the lowest inlet pressure in order to obtain more conservative results at engine intake. Indeed, this model is fundamentally an improvement of the mixer model proposed in subsubsection 5.2.5.1.

The dual-stage mixer model input conditions (pressure, temperature, mass flow and composition) for oxidizer, water and CO_2-O_2 vapor are depicted in Figure 6.2 based on the preferred operating point (in terms of net optimization function and total ICE additional cooling power) for M5 layout modification shown in subsection 5.3.4. Thus, a sweeping process was carried out varying sprayed liquid WMF (from $0\,kg\,h^{-1}$ to $85\,kg\,h^{-1}$) and injected CO_2-O_2 vapor mass flow (from $0\,kg\,h^{-1}$ to $120\,kg\,h^{-1}$).

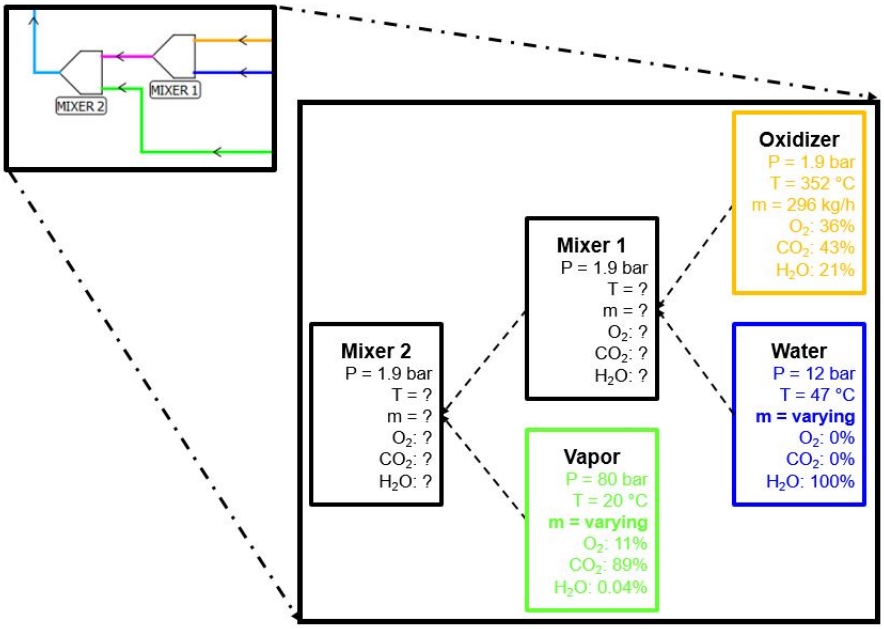

Figure 6.2: Input conditions for dual-stage mixer model

Similarly to mixer model exposed in subsubsection 5.2.5.1, Figure 6.3a shows that there are essentially two separate zones: one where mixer 2 outlet fluid is subject to a VLE phase corresponding to high CO_2-O_2 and WMFs, and another where the outlet phase is a vapor for low CO_2-O_2 and water mass flows. Within the vapor zone, the outlet temperature remarkably diminishes when water mass flow gets greater due to notable latent energy required to evaporate all liquid water. In fact, that temperature drop effect is less marked with respect to vapor injection increase. When water mass flow is high enough (greater than about $25\,\mathrm{kg\,h^{-1}}$) , the outlet temperature is basically water- and vapor-independent because the vapor phase water content reaches the saturation point which also relies on outlet fluid composition (Figure 6.3b). As one may see, that exact point, wherein zone change occurs, slightly depends on vapor mass flow due to its cooling effect contribution when mixed with water. Furthermore, there is a change in vapor mass fraction trend at around $40\,\mathrm{kg\,h^{-1}}$ water mass flow since, for values lower than this figure, the recirculating vapor is more capable to generate cold (more liquid water) via its expansion. Nonetheless, for higher values, when the amount of injected gas increases the vapor mass fraction also rises up due to recirculating vapor com-

position (essentially CO_2 and O_2).

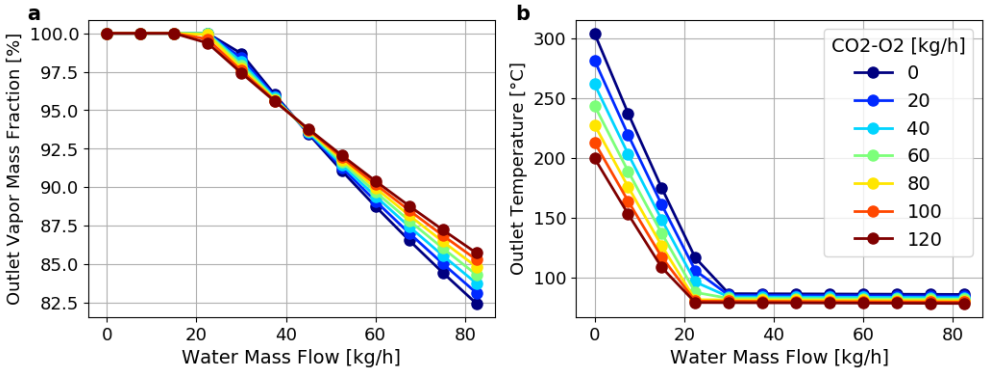

Figure 6.3: Mixer 2 outlet variables sweeping water and CO_2-O_2 mass flows for given oxidizer conditions.

6.2.2 Compressor design

The reciprocating compressor model was improved to consider the fluid dynamic inside the compression cylinder and its surroundings since the model present in chapter 3 is a 0D basic approach which does take into account compressor geometry and operating speed. Thus, the reciprocating compressors shown in Figure 5.11 were designed in VEMOD, separating the CC model from the oxygen-generating layout and imposing at flash 1 inlet the flow conditions (mass flow, temperature, pressure and composition) at same location of the preferred operating point for M5 layout modification which was already used for dual-stage mixer design in subsection 6.2.1.

The engine cylinder geometry was used as reference for compressor cylinder geometry design, keeping same connecting rod length and crank radius as in the engine but varying cylinder diameter of both compressors in order to find optimal stroke volumes in terms of CC performance. Moreover, a CR of 11 was applied for both compressors once normal clearance found literature may vary between 4 and 16% for most standard cylinders ([118]). A PID was employed to actuate on compressors speed to maintain the CC inlet flow constant at the value found at flash 1 inlet for M5 layout. In addition, the compressors were running 180 CAD out of phase to avoid interconnecting piping over-pressure and unstable flow.

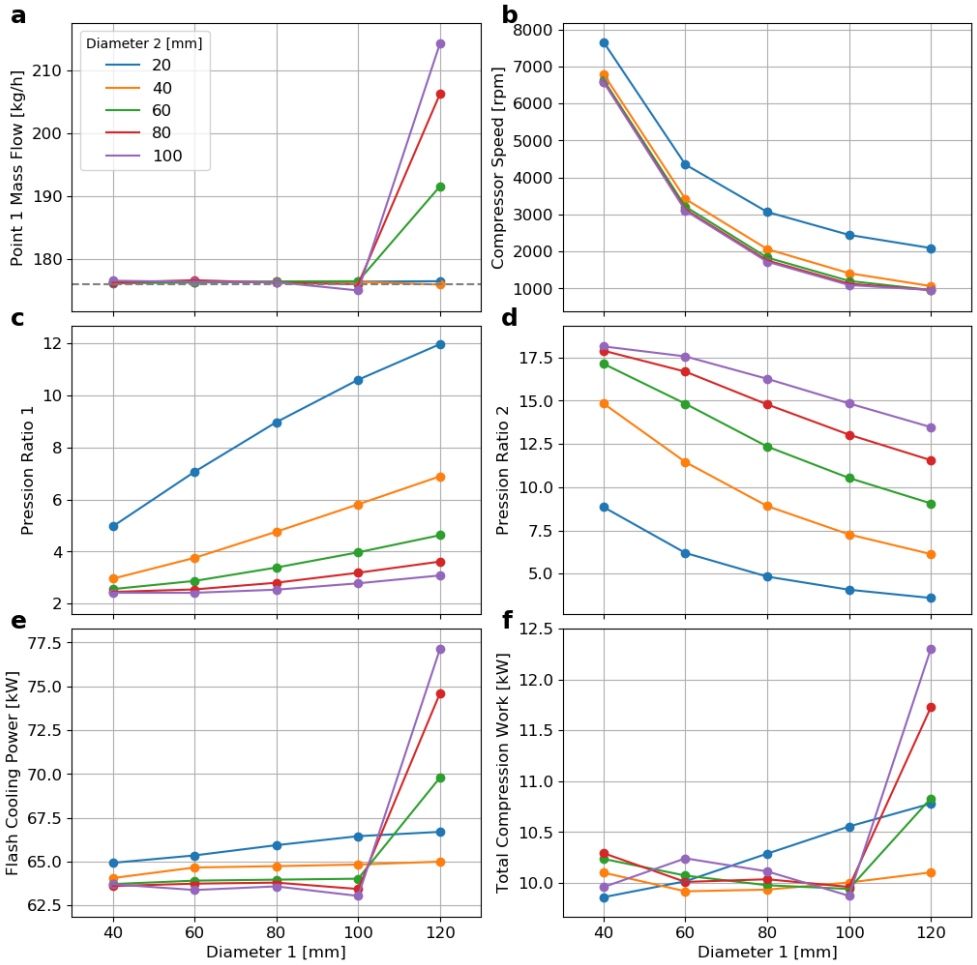

Figure 6.4: Compressor design results varying first- and second-stage compressors diameters.

Figure 6.4a shows that the PID controller was able to control the inlet flow for most of the cases, except for cases with big diameters for both compressors. As expected, the higher the diameters, the lower the speed should be to keep the inlet mass flow constant (Figure 6.4b). As the CC inlet and outlet pressures were fixed at 1.8 bar and 80 bar respectively, compressors present opposite trends regarding the pressure ratio (Figure 6.4c and d). Indeed, when first-stage volume increases, keeping the second-stage compressor volume constant, more mass from first compressor is compressed against second compressor

volume, rising the pressure between them.

Also, flash cooling power (the sum of flash 1, flash 2 and flash 3 powers) and total compression work (the sum of compressors powers) do not vary significantly regarding volume changes on compressors because their individual values present opposite trend as well (Figure 6.4e and f). For instance, when first-stage compressor power consumption increases, second-stage compressor work reduces, and analogous behavior may be seen on cooling power through flashes. In addition, the worked performed by both compressors are similar by analyzing the areas depicted in Figure 6.5. Thus, 80 mm and 40 mm were chosen as diameters for first- and second-stage compressors respectively since low- to medium compressor speed should be applied for reciprocating compressors ([118]). The final geometries will be really decided after interacting and agreement with compressor supplier, checking up their availability, cost and limitations.

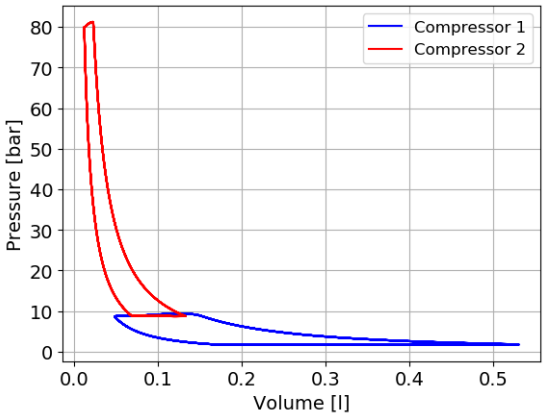

Figure 6.5: pV Diagram.

6.3 Control philosophy proposal

With the aim of offering a more practical and down-to-earth process regulation and achieving the desired outputs of system variables, i.e. T_{exh}, compressor N/A-1 outlet temperature, TFs and CO_2 capturing pressure already specified in chapter 5, a control philosophy is proposed for this arrangement basically actuating on pump and reciprocating compressor speeds, and cooling WMF as

shown in Figure 6.6. The flashes 1 and 2 are broken down into heat exchangers HEF1 and HEF2, and condensed water separators SF1 and SF2 respectively, whereas flash 3 is composed by heat exchanger HEF3 and CO_2 storage tank with vapor recirculation back to mixer 2. In addition, cooling water is supplied at pressure greater than atmospheric to remove heat generated by the system and returned to heat-dissipation equipment such as air coolers. A water tank is used to blend water condensed at SF1 with further supply water to provide refrigerant flow towards cooler C-1 for cooling down air between N_2 compressors. Also, CO_2-enriched liquid generated in HEF3 is collected and stocked in CO_2 storage tank wherein CO_2 capturing pressure is controlled via the control valve VP, releasing CO_2-O_2 vapor back to engine oxidizer intake.

Basically, T_{exh} is controlled by actuating on variable frequency drives of reciprocating compressors RC1 and RC2 simultaneously, while gas outlet temperatures at coolers HEF1, HEF2 and HEF3 are regulated by either opening or closing control valves VT1, VT2 and VT3 respectively, which limit the necessary amount of water for cooling effect. Furthermore, valves VL1 and VL2 control the liquid level within water separators SF1 and SF2, respectively so as temperature and pressure conditions may be maintained for water removal and no liquid accumulation expected during steady-state. Pump P1 is employed to provide certain amount of water set by user to be sent to mixer 1, by varying its driver speed. In this case, water from pump P1 is blended with condensed water in separator SF2 and then forwarded to first-stage desuperheater. Last but not least, compressor N/A-2 inlet temperature is regulated by actuating directly on pump P2 driver speed and indirectly on valve VL3 opening as a way of furnishing enough cooling water at cooler C-1 when more extra water supply is required.

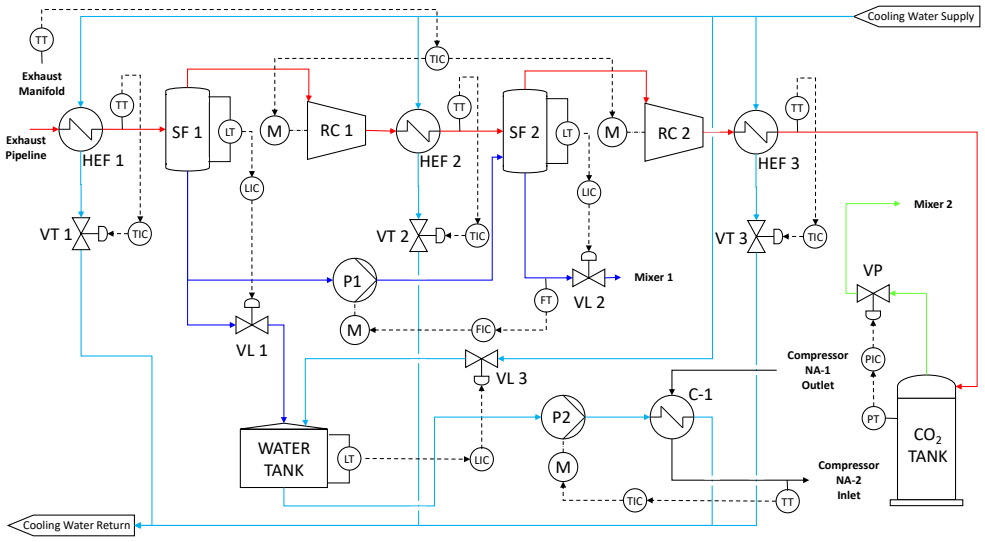

Figure 6.6: Control philosophy scheme.

6.4 Final layout results

The reciprocating compressors and dual-stage desuperheater designed in subsection 6.2.2 and subsection 6.2.1, respectively, were employed in the final oxy-fuel carbon-capture engine layout shown in Figure 6.1. In this case, equivalent procedure depicted in section 5.3 is applied in this section varying recycled WMF and SOI in order to optimize system performance regarding energy requirements. As already mentioned, reciprocating compressor speed is used to control $T_{exh} = 1000\,°C$ via a PID controller.

Similarly to what was done in chapter 5 and shown in Figure 5.13, the entire model was calculated using Python script along with VEMOD working interdependently and simultaneously, i.e., the Python script outputs are VEMOD inputs and vice versa. Actually, Python script was still the tool used in advanced calculation for predicting mixture phase change properties with the equation-of-state approach mainly in Flash 3 and dual-stage mixer, whereas VEMOD was modeling fluid dynamics throughout the rest of layout elements. Furthermore, to run the final model in this new layout, VEMOD had to be adapted to consider liquid water presence inside engine cylinders during intake, compression, power and exhaust stages. Nonetheless, attention should

be paid to the fact that the amount of liquid water used in this thesis present at cylinder intake is completely evaporated well before the end of the compression stage and, hence, engine hydrolock is prevented. Thus, key average and instantaneous results are exposed and assessed in this section aiming to determine the best engine operating conditions. At last, mass flow, temperature and pressure distribution diagrams are analyzed for the optimum point in terms of SOI and WMF.

6.4.1 Average results

In Figure 6.7, Figure 6.8 and Figure 6.9 x-axis and y-axis denote SOI and WMF respectively, while green lines represent the points with 180 bar (maximum allowed in-cylinder pressure). Thus, engine should operate on right side of that green line not to surpass pressure limit. Although SOC follows a linear trend with respect to SOI, the ignition delay increases with more recirculated water and advanced SOIs because lower intake temperatures, and consequently lower ignition temperatures, are achieved within these zones (Figure 6.7a, b and c). In fact, intake temperature rises up when less liquid is mixed with intake gas and when SOI is delayed because more high-temperature exhaust gas needs to be recirculated by the compressors (Figure 6.7d). After ignition time reaches a maximum value at constant advanced SOI by increasing WMF, its value starts to reduce due to lower intake mass flow which is heated by the intake-port wall, increasing in-chamber temperature at intake valve closing. In addition, ignition lag slightly starts to increase at constant WMF by delaying SOI when combustion occurs after top-dead center (0 CAD) because proper fuel diffusion is achieved when pre-combustion temperature is already dropping down (Figure 6.7c).

When intake temperature is diminished, reciprocating compressors have to run faster for decreasing O_2 concentration and, hence, maintaining T_{exh} = 1000 °C as seen on intake pressure and mass flow decline (Figure 6.7e and f). Besides that, in-cylinder maximum pressure increases for advanced SOC because combustion would be more centered at top-dead center. Nevertheless, when combustion occurs on the expansion phase, the in-cylinder maximum pressure is already attained at compression phase which fundamentally relies on intake pressure (Figure 6.7g).

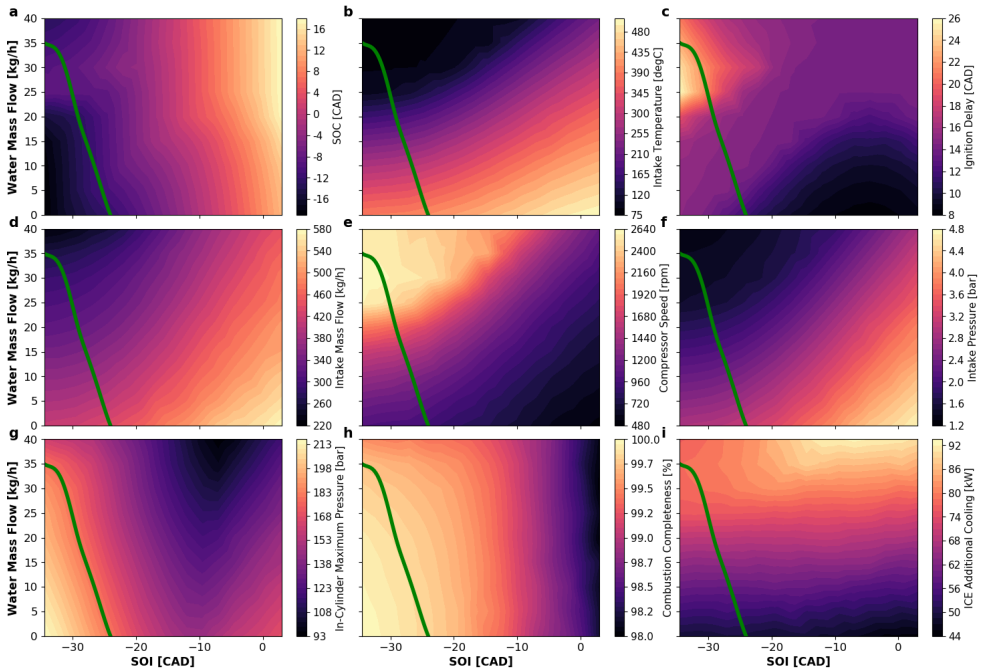

Figure 6.7: Maps for average results of relevant engine variables sweeping SOI and WMF: Part 1.

Combustion completeness basically improves when SOI is advanced once the injected fuel would have more time to meet O_2 and, thereby, a more homogeneous pre-mixture phase may be achieved. Anyway, system combustion efficiency is broadly quite good with values greater than 98% (Figure 6.7h). ICE additional cooling, which is still defined as the sum of flash powers plus cooler C-1 power provided by extra cooling water, increases with more WMF because further recirculated water is condensed at flash 1 (Figure 6.7i). Also, a slight increment in ICE additional cooling is seen when SOI is delayed at constant high WMF because more O_2 is generated by MIEC and, consequently, further mass flow passes through flash 1 (see Figure 6.9a). As depicted in Figure 6.8a and Figure 6.9b, Air mass flow and MIEC feed pressure decrease from high-SOI low-WMF zone to low-SOI high-WMF zone due to recirculating flow reduction, declining exhaust sensible enthalpy and, thereby, less energy would be accessible for moving N_2 turbines of VGT N/A-1 and VGT-N/A-2 at Brayton cycle as observed on MIEC feed temperature trend (Figure 6.9c).

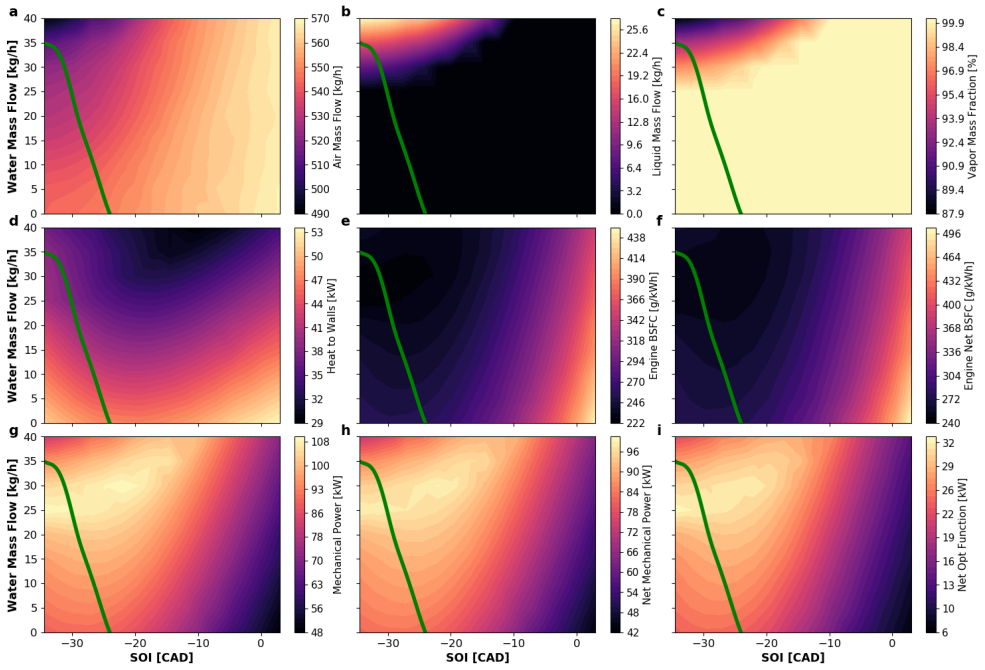

Figure 6.8: Maps for average results of relevant engine variables sweeping SOI and WMF: Part 2.

Furthermore, up to 25 kg h^{-1} of liquid is generated at intake line within low-SOI high-WMF region in which water vapor pressure already reaches its saturation point (Figure 6.8b and c). On the one hand, as more trapped inert mass inside the cylinder absorbs more heat released from combustion, whether SOI increases at constant WMF, less convective heat is lost through chamber walls if SOC occurs before top-dead center. On the other hand, in-chamber temperatures are too high when combustion starts on expansion phase, generating more heat to walls when SOI is delayed. Still, the intake cooling effect is intensified when WMF augments, diminishing convective heat losses as seen in Figure 6.8d. Within same scenario, gamma of the oxidizer charge enhances with higher water content and O_2 production improves since MIEC permeate pressure reduces and, subsequently, MIEC pressure ratio and filtration efficiency increase when reciprocating compressors speed up as displayed in Figure 6.9d, e and f, resulting in better engine performance in terms of BSFC, net BSFC, engine power, net engine power and net optimization function (Figure 6.8e, f, g, h and i). It must be underline that net performance variables defined in chapter 5 were also applied in this chapter. Also, heat transferred

from fuel to piston is enhanced when combustion is properly centered, which gives grounds for BSFC variation over SOI at constant WMF (Figure 6.8e and f).

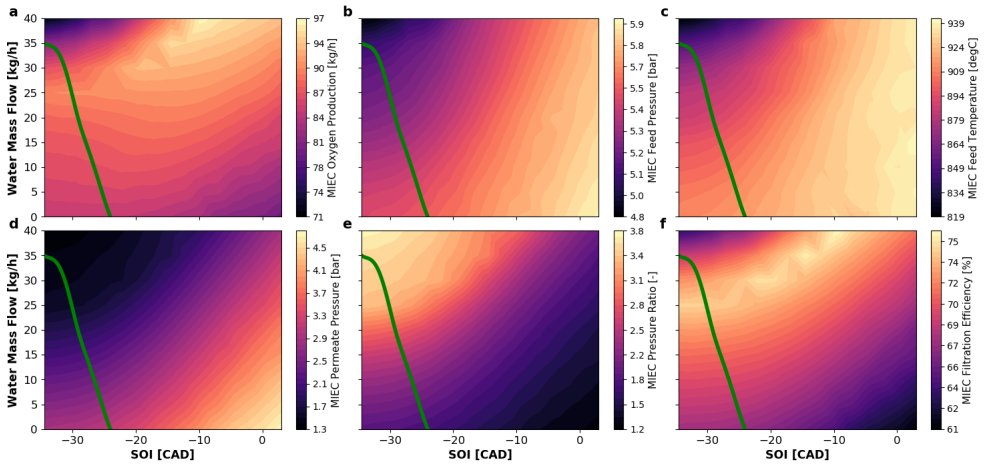

Figure 6.9: Maps for average results of relevant MIEC variables sweeping SOI and WMF.

Diminution in MIEC feed temperature caused by low exhaust mass flow within high-WMF low-SOI zone provokes a depletion of the MIEC filtration efficiency and consequent little O_2 generation, worsening engine gross and net mechanical powers (see Figure 6.9a, c and f along with Figure 6.8a, g and h). Additionally, combustion completeness is moderately undermined within that same zone at constant SOI due to lower intake temperature and pressure, decreasing somewhat gross and net BSFCs (see Figure 6.7b and h along with Figure 6.8e and f). As a whole, a deterioration of around 10% on BSFC and mechanical power is noted due to on-site CO_2 capture with reciprocating compressor coupling, comparing Figure 6.8e and f as well as Figure 6.8g and h, respectively. Again, a trade-off between system output and cost of cooling may be assessed and, given that best point chosen in previous chapter had a chilling energy of about 80 kW and net optimization function in this study presents a maximum figure enclosed by a zone whereby such cooling power value is not surpassed, WMF=30 $kg\,h^{-1}$ and SOI=-22 CAD are deemed the preferred input parameters for adequate power plant performance.

6.4.2 Instantaneous results

As represented in subsection 5.3.2, in-cylinder instantaneous outputs are depicted in Figure 6.10 for most delayed and advanced SOIs with highest and lowest WMF. In addition, the preferred point selected in preceding subsection is compared to these contour-map corner conditions. One may see more explicitly in that figure the cooling effect on combustion lag since when more water is recycled at constant SOI, the ignition temperature and pressure decrease (Figure 6.10a and b), provoking delay on SOC on shown Figure 6.10c. Although optimum point (red line) presents moderate lower in-cylinder O_2 mass than delayed-SOI cases (blue line), it yields higher gross and net mechanical powers because those cases have worse combustion efficiency and, besides that, more elevated thermal energy wasted through cylinder walls and exhaust gas.

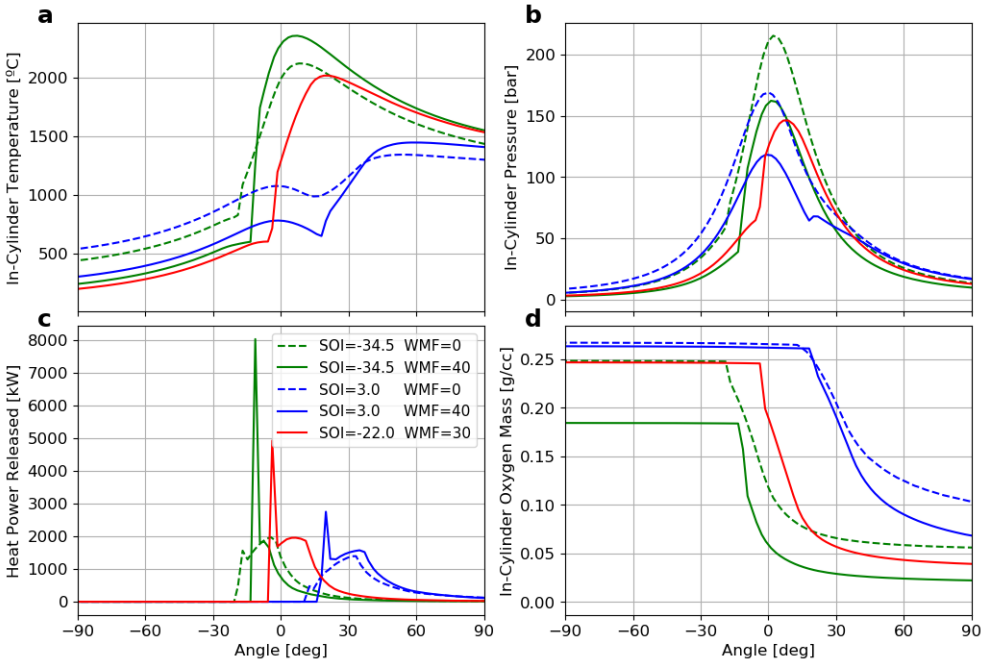

Figure 6.10: Instantaneous results of in-cylinder parameters for the edges of the contour maps and the chosen combination of SOI and WMF. In figure legend, SOI is in CAD and WMF in kg/h.

Despite WMF=40 kg h^{-1} points (solid lines) have lower intake temperature and in-cylinder O_2 mass than WMF=0 kg h^{-1} points (dashed lines), their

combustion temperature peaks are higher due to less trapped mass caused by greater reciprocating compressor speeds (Figure 6.10a and d). Furthermore, WMF=0 kg h^{-1} cases present higher in-cylinder O_2 than WMF=40 kg h^{-1} ones once oxygen-to-fuel ratio is kept at 1.1 (system operating with excess of oxygen) and more EGR is required to maintain T_{exh} = 1000 °C as depicted in Figure 6.10d.

6.4.3 Diagram results

The preferred point found in this study is assessed through distribution diagrams in this subsection following terminology and representation already depicted on diagrams analyzed in previous chapters. Power disposition through out the HEs inside HEN are similar to what was observed in preceding chapters as shown in Figure 6.11. In such situation, HE G/A-1 presents the highest power exchanged due to notable contrast between its inlet temperatures. Again, the lowest power exchanged is seen for HE N/A-1 since HE O/A-1 and HE G/A-1 are able to heat air up to temperature close to turbine N/A-1 outlet temperature. Moreover, oxidizer temperature drops down from 349 °C to 92 °C when mixed with recirculating liquid water and CO_2-O_2 vapor, and its O_2 concentration decreases as more water and CO_2 mass flows are injected at engine intake via dual-stage mixer as seen in Figure 6.12 and Figure 6.13, respectively.

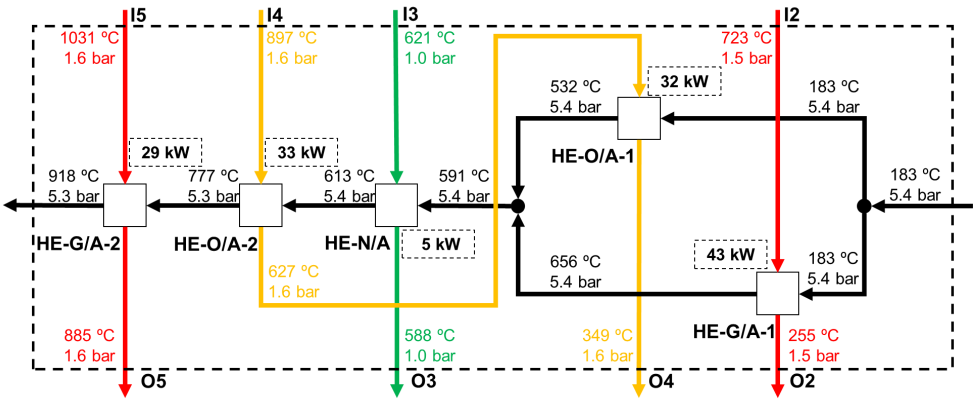

Figure 6.11: Power, temperature and pressure distribution diagram for the preferred case inside HEN.

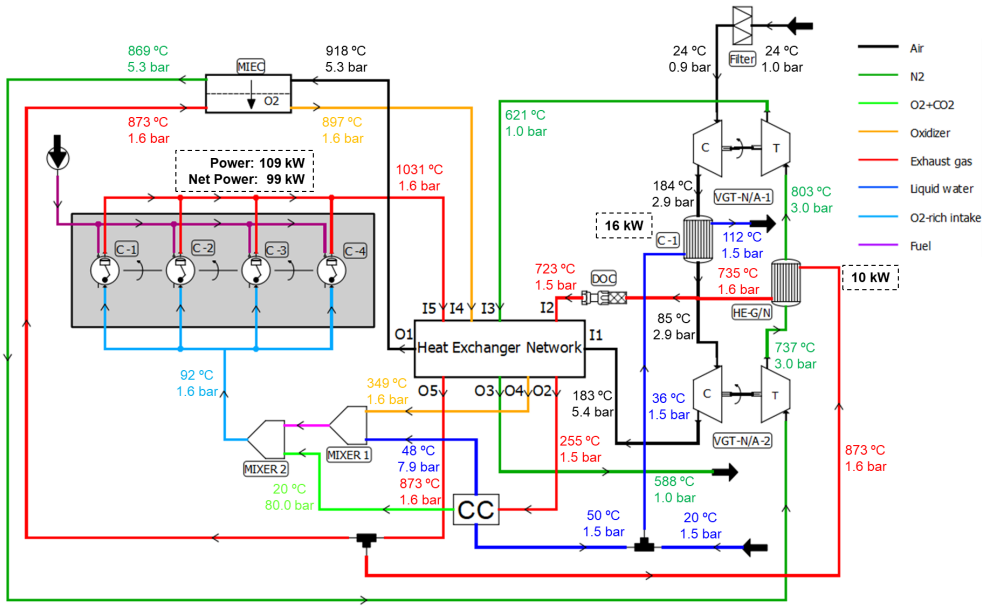

Figure 6.12: Power, temperature and pressure distribution diagram for the preferred case.

The term "X" in Figure 6.13 represents the vapor mass faction in streams wherein liquid may appear. In this context, no liquid is noted at intake flow because basically its water saturation pressure is higher than its vapor pressure for that given temperature of 92 °C. Also, 29 kg h^{-1} extra cooling water at 20 °C is blended with liquid released by CC to reduce air temperature from 184 °C to 85 °C, generating 24% of vapor at C-1 cold-side outlet. Mixer 1 water inlet pressure of 7.9 bar is lower than theoretical intermediate pressure of around 11 bar in case both CC compressors possess same pressure ratio, indicating second-stage reciprocating compressor is consuming more power than first-stage one. As expected, since CC reciprocating compressors are coupled to engine shaft, preferred point power output decreases from 109 kW to 99 kW and BSFC increases from 228 g kW^{-1} h^{-1} to 252 g kW^{-1} h^{-1}, however approximately 74 kg h^{-1} of CO_2 in liquid phase is captured thanks to that slight energy penalty.

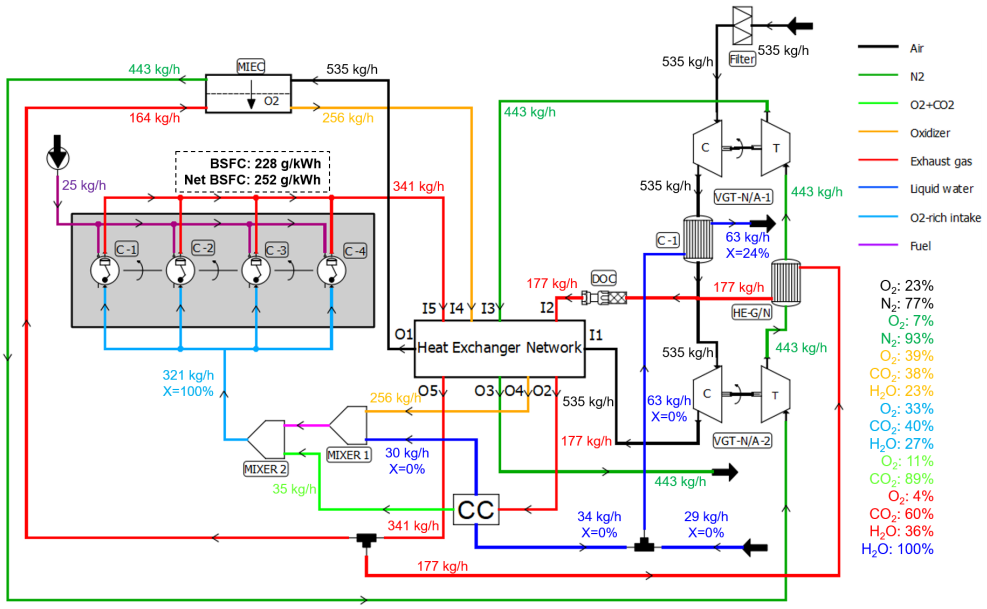

Figure 6.13: Composition and mass flow diagram for the preferred case.

Chapter 6 Bibliography

[109] J. Serrano, J. Lopez, J. Martín, and G. Bracho. "Extension of a Zero-Dimensional Mixing-Controlled Combustion Model for the Development of a NOx–Free System Based on the Oxy-Combustion Concept". *Johnson Matthey Technology Review* (Jan. 2023). DOI: 10.1595/205651324X16963284171824 (cit. on pp. 73, 74, 135).

[118] P. Heinz. *A Practical Guide to Compressor Technology*. John Wiley and Sons, Ltd, 2006. DOI: 10.1002/9780471929789 (cit. on pp. 138, 140).

Chapter 7

Conclusions and way forward

Contents

7.1 Conclusions

This manuscript presented the development of an oxy-fuel combustion power plant layout with in-situ O_2 generation and CC. The evolution of this zero-emission power plant was studied throughout different design and operation aspects facing a prototype construction and installation to be tested at CMT facilities.

Although the modeling of the system was applied to an automotive engine, the aim of this thesis is to highlight the feasibility in generally using such self-sustaining clean-combustion concept in CIEs with various features regarding size, application and technological maturity. Moreover, taking into account the system packaging and potential utility consumption, this novel power plant layout would be better applied to high-duty engines for maritime transport and electricity generation with easy access to cooling medium (e.g., seawater) and enough space for system disposal concerning O_2 generation and CC

The main breakthrough outcome of this work may be reflect on the final proposed layout in which the system is self-sustainably operated recovering part of the wasted exhaust gas energy to produce the necessary O_2 for a clean combustion, preventing emissions of NOx, CO and soot, and capturing the CO_2 in critcal/liquid phase at ambient temperature.

The milestones and achievements made throughout this thesis may be gathered as follows:

- Oxy-fuel power plant layout with in-situ O_2 production
- Proposed strategy to extend oxy-fuel power plant load operation map range with O_2 generation.
- Design and integration of the CC system for the oxy-fuel power plant with exhaust water recirculation.
- Model improvement facing oxy-fuel prototype construction and installation.

7.1.1 Oxy-fuel power plant layout with in-situ O_2 production

In chapter 3, the oxy-fuel combustion concept was study in a CIE applying MIEC as a from-air O_2 provider. EGR, composed mainly by CO_2 and water, was used to control the in-cylinder temperature and exhaust gases wasted energy was recovered for producing the O_2 required by the engine by heating up the MIEC. For this purpose, different engine configurations were analyzed in order to find out an optimum one in terms of energy efficiency and engine performance. Basically, two different EGR CSs were studied: one with a turbine on EGR line (CS1) and other with a turbine on cylinder exhaust line (CS2). Thus, the two oxy-fuel combustion power plant configurations were compared with each other and with conventional baseline and optimized baseline engine configurations for full load operating points from 1250 rpm to 3500 rpm.

The temperature, pressure and mass flow diagrams at 3500 rpm showed that the two proposed CSs present similar results in terms of thermal energy and mass flow distributions because O_2 production mainly depends on regenerative Brayton cycle structure (heat exchanger and turbocharger disposal) which was preserved in both CSs. As the global optimization objectives were the same with both configurations (same merit function, same exhaust gases temperature, same maximum efficiency objective in turbomachinery, ...) the global system converges to the same thermodynamic and flow variables with both CS1 and CS2. Moreover, in both cases the critical data, MIEC feed temperature and O_2 partial pressure ratio, which control the O_2 production for the power plant proper operation varies similarly with respect to engine speed; i.e: from 860 °C to 930 °C and from 1.25 to 1.28, respectively. But the difference was how VGT-G/O operates and, also, the size of this specific turbocharger. It is much bigger in the case CS2 than in CS1. Therefore, one conclusion was that CS1 is a more convenient solution in sake of layout simplicity and lower-cost, since on the one hand the turbocharger is smaller (lower inertia and lower cost). And on the other hand, it could be probably avoided when the whole engine was completed with the CC subsystem, i.e.. VGT-G/O in CS1 case is not more useful that a regulation flow valve or any other flow regulation system, since the compressor of CS1 does not provide any pressure.

Comparing the instantaneous results, the oxy-fuel combustion cases distinguished from optimized baseline case especially with respect to in-cylinder

O_2 content which, coupled with higher CR, SOC optimization process and different CS in oxy-fuel combustion configurations, led to higher in-chamber temperature and higher maximum pressure at 1250 rpm. Moreover, in spite of the oxy-fuel combustion presented a smaller area enclosed by the high-pressure loop due to its smaller amount of trapped mass and lower of the oxidizer, the pumping losses reduction thanks to a different power plant control system could compensate part of that mechanical work loss.

The average results showed that, if compared to a conventional CIE, at high engine speeds the proposed oxy-fuel combustion engine provided similar brake power and indicated efficiency, whereas at low engine speeds, despite of it yielded higher BSFC (on average, more than 10%), a brake power enhancement (on average, more than 30%) was observed. Also, there were no clear differences between the EGR CSs on power plant performance, since they produced similar amount of O_2 as a result of both having same T_{exh} and equivalent O_2 partial pressure ratio. In addition, one could see how the engine power with regard to engine speed was practically function of the O_2 production which was conditioned to membrane temperature and pressure ratio (between feed and permeate sides). Although VGT-G/O of CS 1 seemed to be useless at full load operating points, it could be required to control the power plant in studies considering the CO_2 capture system and engine partial load points requirements.

Although the EGR CSs presented similar results in terms of power plant performance, the EGR CS 1 proposal seemed to offer more advantages regarding the engine T_{exh} control in other operating points (e.g. part-load conditions). Thus, the VGT-G/O turbine of CS 1 could be useful at engine lower loads, since the VGT rack would choke the EGR line when high temperature is required by the MIEC, whereas a valve would be necessary at that line under same conditions if the VGT-G/O turbine of CS 2 is chosen. Indeed, the VGT racks are usually more thermally robust than basic valves. At last, the breakthrough result was the feasible end of correlation between BSFC and CO_2 emissions due to CO_2 capture.

7.1.2 Proposed strategy to extend oxy-fuel power plant load operation map range with O_2 generation.

A strategy was analyzed to extend the load operation map range of the oxy-fuel layout with on-board O_2 generation in chapter 4. The method consists basically of modifying T_{exh} and λ, generating temperature-lambda maps to decide the optimal load reduction combination in terms of power plant performance. Therefore, the system behavior was assessed at three engine speeds (1250 rpm, 2500 rpm and 3500 rpm) actuating on SOI. The baseline engine model was calibrated with experimental data within part-load operation ranges, and an ACT model calibrated with CFD data was applied to simulate the combustion process under oxy-fuel combustion conditions.

There was a minimum consumption zone on those maps wherein the benefits of low exhaust temperature were observed due to less convective heat losses and more excess of O_2 that improves combustion performance. In those cases, if compared to the corresponding full-load point, a BSFC enhancement was seen, around 6.2 %, 6.8 % and 7.5 % for 1250 rpm, 2500 rpm and 3500 rpm respectively. For those engine speeds, minimum-consumption paths were proposed combining T_{exh} and λ, and a similar procedure may be carried out to extend this methodology towards other engine speeds. In addition, a minimum ignition pressure of around 40 bar was found to trigger combustion with ignition temperature of around 550 °C, establishing limits of combustion feasibility regardless of in-cylinder O_2 content.

Comparing a full-load point with a 40 % load one at the same engine speed, a heat exchanged reduction was seen over several HEs for the part-load case due to less exhaust gas heat generated by combustion. Indeed, a decline in energy availability decreases air mass flow and MIEC feed side pressure boosted by N_2 VGTs because the system is based on a regenerative process. Thus, reductions of up to around 50 % in heat exchanged in HEs decreased pressure and mass flow by half over the system different parts.

Finally, four parameters were proposed to evaluate system stability in terms of combustion energy availability for generating O_2 and finding out oxy-fuel power plant operation limits. On the one hand, Parameter 1* may be employed for system design since fuel calorific value is commonly known and may be used to estimate MIEC O_2 production capacity and membrane design features such as minimum mass-transfer area depending on MIEC energy

requirements. On the other hand, Parameter 2* may be useful for analyzing suitable energy distribution since it takes into account the energy balance surrounding cylinders to calculate the outlet and inlet sensible enthalpy difference necessary for MIEC proper O_2 generation. Parameter 1* and Parameter 2* tended to have a minimum value of 1 and 0.5, respectively, from which a decrease in engine load was not possible. Accordingly, the minimum value of power plant load achieved in this proposed oxy-fuel layout was around 50 % considering 1250 rpm, 2500 rpm and 3500 rpm.

7.1.3 Design and integration of the carbon capture system for the oxy-fuel power plant with exhaust water recirculation.

In chapter 4, the oxy-fuel combustion power plant concept with in-situ O_2 separation was studied integrating a CC system through several amendments to the layout proposed in chapter 3. Indeed, the oxy-fuel combustion applied to power plants enables to capture CO_2 in the liquid phase by means of intercooling compression stages with water removal. Also, the energy cost of that carbon capture system was assessed as well as the ways to design and integrate it into the oxy-fuel layout. To do so, the PR EOS was calibrated with experimental data found in the literature regarding the binary interaction parameter for each pair of substances and used to predict the VLE behavior in many elements to model the CO_2 purification process properly. The product of engine brake power and effective efficiency was optimized actuating on SOI for every oxy-fuel engine layout.

The first layout modification was based on removing VGT-G/O with its corresponding cooler and adding an OC. Afterwards, the CC system, composed of two reciprocating compressors, three flash units and one CO_2 storage tank, was designed taking into account the TF1, TF2 and TF3 and pressures. Thus, the best values found in terms of energy consumption for TF1, TF2 and TF3 and flash 3 pressure were 50 °C, 30 °C, 20 °C and 80 bar. Moreover, the surplus vapor leaving flash 3 was directly injected into the cylinders in order to increase the in-cylinder trapped mass and produce extra mechanical power with the excess of O_2 to move the reciprocating compressors. Although a cooler upstream the intake manifold enhanced the power plant performance because it increased engine volumetric efficiency and collaborated with O_2 production by decreasing the MIEC permeate side pressure, its cooling power

may not be negligible. Consequently, a mixer model was developed to recirculate part of water condensed in flashes 1 and 2 towards the cylinder inlet to lower intake gas temperature and increase the γ of the oxidizer, improving the engine effective efficiency. Moreover, a sweeping process was carried out varying SOI and WMF with the purpose of finding out the best power plant operating conditions.

In general, a deterioration in engine performance occurred when the power to move reciprocating compressors was also provided by the combustion, decreasing net mechanical power by about 8% and increasing the BSFC by about 9%. A lower EGR rate is required when more water is recirculated to control the T_{exh} at 1000 °C, which decreases MIEC permeate side pressure and, hence, raises O_2 production at the membrane. In this way, more mass flow passes through HE G/N and HE G/A-1, increasing their transferred heat and changing power distribution through other HEs. Furthermore, if more liquid water is recirculated, more water vapor is present in the exhaust gas, which improves the heat exchanged in many HEs because specific heat capacity for CO_2 is worse than for water vapor. In summary, if MIEC generates more oxygen, the better the complete system works, producing even more O_2 since this system is self-sufficient.

After the sweeping process, WMF=20 kg h^{-1} and SOI=-26.5 CAD was deemed the optimum point, taking into account the trade-off between chilling power and power plant performance. In fact, this case merged the main benefits of the configurations with and without intake cooler (WIC and WOC, respectively), reducing WIC total ICE additional cooling power from 110 kW to 80 kW and increasing the WOC net optimization function from 25 kW to 30 kW.

7.1.4 Model improvement facing an oxy-fuel prototype construction and installation.

The oxy-fuel carbon-capture engine layout developed through chapter 3, chapter 4 and chapter 5 was improved in chapter 6 for upcoming experimental set-up. In fact, CC reciprocating compressors were designed regarding their geometry taking into account process variables from preferred point chosen in chapter 5. Therefore, 80 mm and 40 mm were selected as diameters for first- and second-stage compressors, respectively, with same crank radius and

connecting rod length present in the engine cylinders but with a CR of 11.

In addition, a dual-stage mixer model was proposed for injecting the CO_2-O_2 vapor stream at engine intake pipeline since its direct injection into combustion chamber was not feasible nowadays. Indeed, that model is able to predict vapor expansion behavior, outward mixture temperature and composition, and liquid presence at mixer outlet. Also, a CC control philosophy was proposed in order to regulate process variables for capturing CO_2 with minimum 95% mass purity at near-ambient temperature. A SOI-WMF sweeping procedure was carried put in order to find out the best combination with respect to energy requirements and system performance, and hence the point with SOI=-22 CAD and WMF=30 $kg\,h^{-1}$ is selected as the most suitable. Furthermore, the main outcomes for the preferred point found in chapter 6 are compared with the equivalent ones for the best case (M5) seen in chapter 5 on summary Table 7.1 below:

Table 7.1: Average results of relevant powerplant performance variables comparing best solutions found in chapter 5 and chapter 6.

	Net BSFC [g/kWh]	**Net Brake Power** [kW]	**Net Opt. Function** [kW]	**Combustion Completeness** [%]	**Intake Temperature** [°C]	**Total ICE Additional Cooling Power** [kW]
chapter 5	265	98	30	95	196	78
chapter 6	252	99	32	99	92	80

Thanks to better combustion completeness and lower intake temperature, net BSFC and optimization function for chapter 6 are improved by around 5% when compared to ones for chapter 5, generating akin net mechanical power and requiring similar additional cooling power. Combustion model used in chapter 5 was underestimated because the calibration process of the HRL carried out at that stage was not updated with new in-cylinder conditions when water is recirculated. Thus, combustion model employed in chapter 6 took that effect into consideration when its ACT parameters were calibrated with CFD results. Indeed, many back-and-forth discussions with CFD team from CMT were necessary to properly predict the combustion behavior in oxy-fuel conditions. Also, since part of water condensed in CC is reused in cooler C-1 in chapter 6, extra cooling water consumption is less critical allowing selection of operating points with better energy performance. As CO_2-O_2 vapor is directly injected inside cylinders for chapter 5, its volumetric efficiency is better than for chapter 6, wherein vapor injection is conducted at engine intake, most likely explaining, alongside discrepancy in heat losses caused

by intake temperature divergence, why both models present analogous brake power but with a difference in effective efficiency.

At last, one may see how this final oxy-fuel carbon-capture engine layout roughly ready for experimental installation could be still competitive in terms of energy and efficiency performance in spite of some deterioration in net BSFC and power output when compared to baseline conventional engine case at 3500 rpm (Figure 3.14) used as starting point in chapter 3. In fact, although net brake power and BSFC get worse from 140 kW and 212 g kW^{-1} h to 99 kW and 252 g kW^{-1} h, respectively, due to system limitations and additional energy requirement, this engine layout is actually self-sustaining avoiding tailpipe emissions and capturing the CO_2 from flue gas. Thus, this proposed novel concept for CIE may be considered a technological advance which, along with alternative emerging technologies, might contribute for achieving zero-emission powerplant development on industrial scale.

7.2 Way forward

Further future works are proposed to continue enhancing the oxy-fuel carbon-capture powerplant layout regarding its simulation and experiments considering more constructional constrains and industrial specific applications. Thus, the following aspects should be addressed:

7.2.1 Modeling and Control

Full-load curve from 1250 rpm to 3500 rpm should be studied for the final layout depicted in chapter 6 with the aim of observing system performance in other operating points. In this case, some numerical variables for model initialization and convergence should reviewed and modified if necessary such as initial amount of fuel and recirculating water, number of cycles for transition between calculation phases, stabilization criteria, initial turbocharger speeds, PID parameters and so on.

Similarly to what was done in chapter 4, the final layout operation map should extended towards lower loads. In this context, strategies to reduce load until reaching powerplant energy self-sufficiency limits should be investigated such as by decreasing either system inlet air, e.g. via a throttle valve at turbine

N/A-1 outlet, or T_{exh} to restrict membrane O_2 production. It must underline that increasing λ more than 1.1 would jeopardize CO_2 purification from O_2 at ambient temperatures as already seen in chapter 5 and, thereby, this strategy should be avoided.

Control logic sequence should be proposed for safe and proper operation of the system during startup and shutdown. Actually, an external motor would be likely necessary to rotate the nitrogen-line turbochargers during Brayton cycle initialization. Furthermore, CC system will have two different phase which must be contemplated, e.i. CO_2 capture tank pressure will firstly have to achieve 80 bar and, then, CO_2-O_2 vapor could be recycled via a self-acting pressure control valve. In general, transient states should be simulated for taking into account system inertia and dynamic behaviors during operating point changeover.

7.2.2 Experimental campaign

At final stage of the thesis project, a prototype has been built at CMT facilities based on oxy-fuel carbon-capture powerplant layout developed and studied in this thesis to enable its technological demonstration (Figure 7.1).

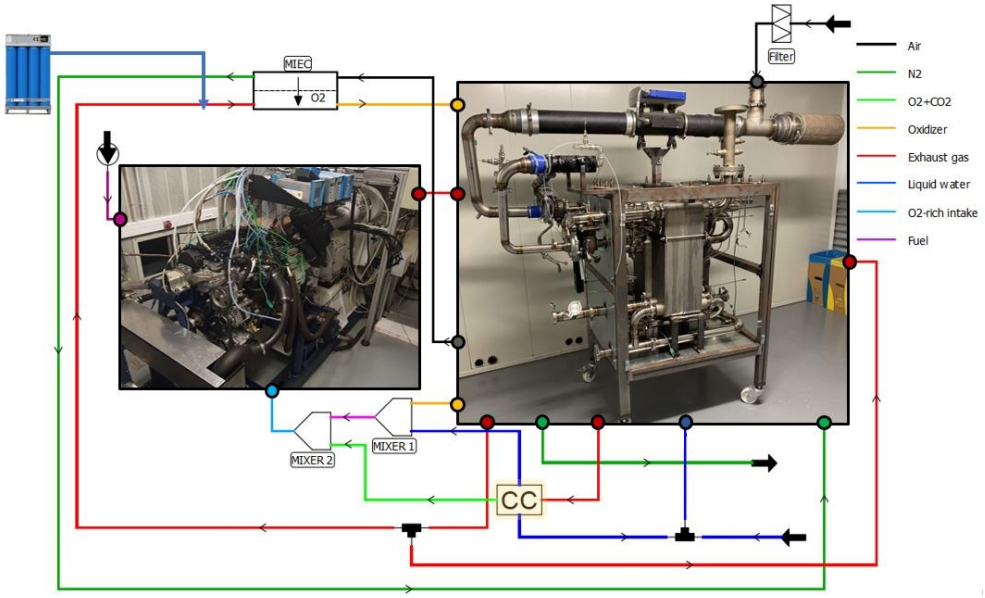

Figure 7.1: Oxy-fuel carbon-capture engine layout as built-up at CTM facilities.

Once the research team has faced many challenges to acquire a MIEC membrane for O_2 generation, it was replaced by a conventional HE to allow heat exchanged between air and oxidizer streams. Since the HE is not able to transfer O_2 from one stream to another, bottles with pressurized O_2 were connected next to that HE to feed the oxidizer streams, simulating the MIEC membrane behavior. In addition, turbocharges and HEN were mounted and integrated in an instrumented device over a mobile support, which includes covers surrounding the components and, consequently, minimizing heat losses to the environment. Also, a desuperheater (Figure 7.2) was purchased and included in the layout as well a mixing device for water and vapor recirculation, respectively, following the strategy already shown in chapter 6.

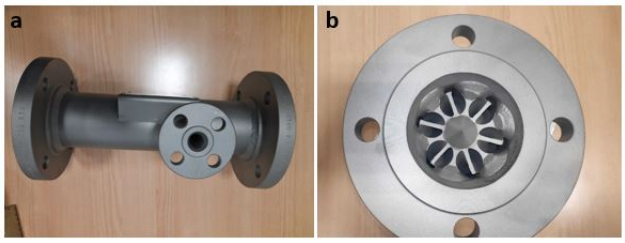

Figure 7.2: Desuperheater for oxidizer-water mixing: (a) Top view; (b) Front view.

The energy recovery device designed and built to provide temperature and pressure to the MIEC feeding air was coupled and allocated next to a multi-cylinder CIE in a test room as shown in Figure 7.3. The experimental set-up has been completely instrumented for measuring variables such as mass flow, pressure or temperature at the most relevant points.

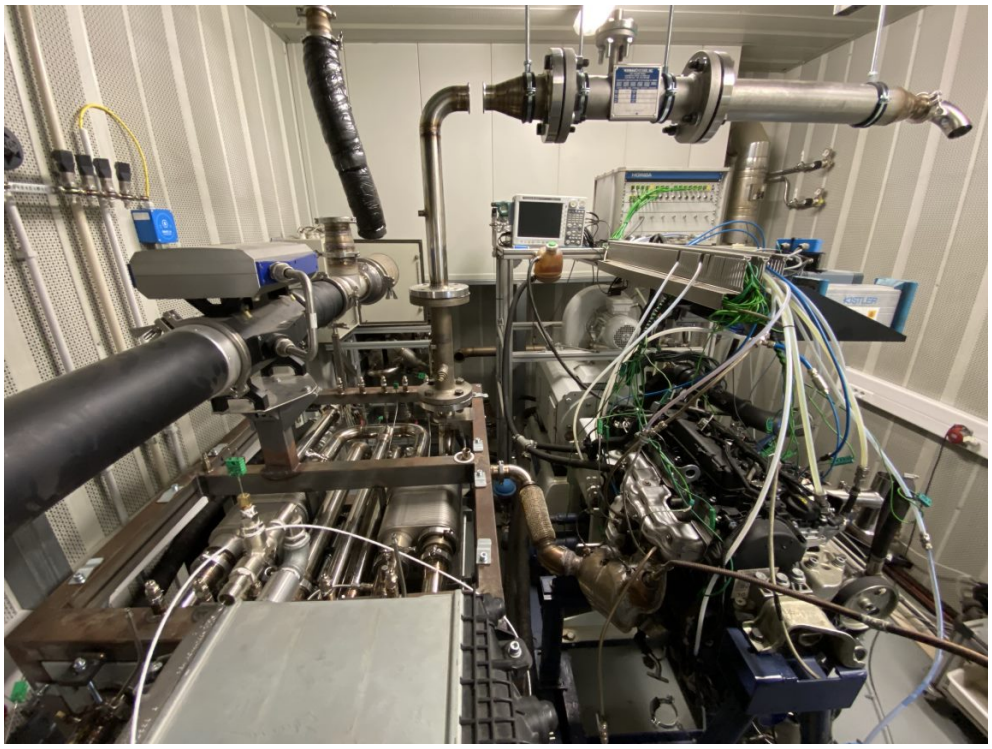

Figure 7.3: Test room with the engine and energy recovery system integrated.

Regarding the CC system, some amendments to scheme studied in chapter 5 were required after contact with its component suppliers. Due to difficulty in finding positive-displacement compressors for meeting pressures and mass flows required in chapter 6, the number of compression stages were changed from 2 to 3. Furthemore, part of high-pressure liquid CO_2 stored in the tank is recirculated and expanded into inlets of the second- and third-stage compressors to produce a joule-thomson cooling effect and dry their suction flows. Apart from that, three coolers were placed upstream the first-stage compressor in order to condense water as much as possible from the flue gas due to compressor suction constraints. Figure 7.4b displays a scheme of the proposed CC system wherein images of real components used for its construction are shown. Accordingly, once all necessary components were selected, including auxiliary and safety devices, the CC system was built and installed in a separate test room next to the one enclosing the engine and energy recovery system for oxy-fuel combustion. Figure 7.4a shows the CC system already assembled in the test room and ready to perform prototype demonstration tests.

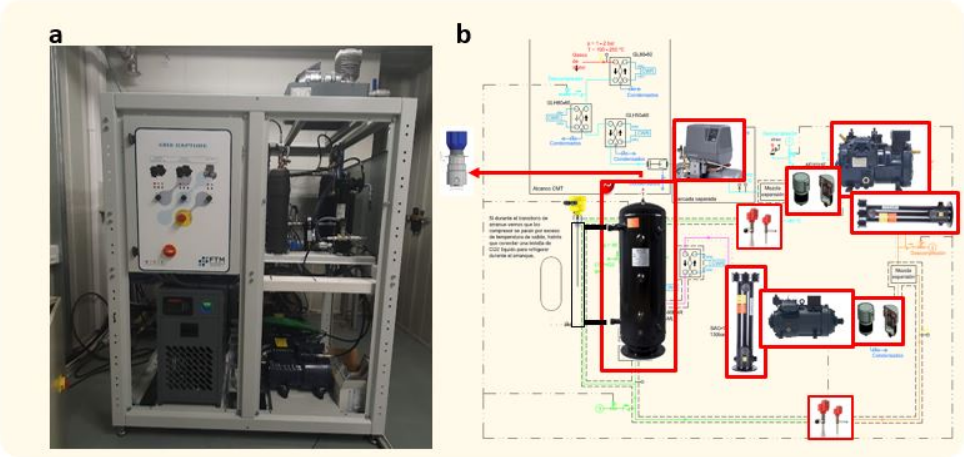

Figure 7.4: CC system as built-up at CTM facilities: (a) Components integrated and compact inside CC; (b) CC with images of the components used.

As shown above, since the original oxy-fuel carbon-capture layout has undergone some modifications due to experimental adaptation, prototype simulation development should be carried out as well as an optimization of its process variables such TFs, recycled WMF, T_{exh}, SOI, etc. Moreover, an assessment of usage of pilot fuel pre-injection to mitigate the rapid pressure rise

during SOC which may provoke excessive noise.

To conclude, an extensive testing campaign should be carried out with this pilot plant as a fundamental part of the proof of concept of this technology. Thus, the oxy-fuel carbon-capture powerplant model outputs seen throughout the thesis could be actually confirmed after the engine testing through that experimental campaign at CMT facilities. In such a circumstance, some parameters previously found for modeling heat transfer, wave dynamic and combustion reaction for in-place components will probably have to be readjusted to fit experimental results. Finally, market analysis and interactions with companies should be carried out in order to take note of industrial needs to be considered when adapting this novel oxy-fuel carbon-capture technology for each particular application.

Global bibliography

[1] J. Serrano, F. Arnau, L. García-Cuevas, and V. Farias. "Oxy-fuel combustion feasibility of compression ignition engines using oxygen separation membranes for enabling carbon dioxide capture". *Energy Conversion and Management* 247 (Nov. 2021), p. 114732. DOI: 10.1016/j.enconman.2021.114732 (cit. on pp. xii, 25, 40).

[2] F. Arnau, G. Bracho, L. García-Cuevas, and V. Farias. "A strategy to extend load operation map range in oxy-fuel compression ignition engines with oxygen separation membranes". *Applied Thermal Engineering* 226 (2023), p. 120268. ISSN: 1359-4311. DOI: https://doi.org/10.1016/j.applthermaleng.2023.120268. URL: https://www.sciencedirect.com/science/article/pii/S1359431123002971 (cit. on pp. xii, 70).

[3] J. Luján, F. Arnau, P. Piqueras, and V. Farias. "Design of a carbon capture system for oxy-fuel combustion in compression ignition engines with exhaust water recirculation". *Energy Conversion and Management* 284 (May 2023), p. 116979. DOI: 10.1016/j.enconman.2023.116979 (cit. on pp. xii, 95).

[4] I. P. on Climate Change. *AR5 Climate Change 2014: Mitigation of Climate Change*. URL: https://www.ipcc.ch/report/ar5/wg3/ (cit. on p. 2).

[5] G. M. Laboratory. *Trends in Atmospheric Carbon Dioxide*. URL: https://gml.noaa.gov/ccgg/trends/global.html# (cit. on p. 2).

[6] E. Commission. *2030 climate and energy framework in European Union*. URL: https://ec.europa.eu/clima/policies/strategies/2030_en (cit. on p. 2).

[7] B. Buhre, L. Elliott, C. Sheng, R. Gupta, and T. Wall. "Oxy-fuel combustion technology for coal-fired power generation". *Progress in Energy and Combustion Science* 31 (Dec. 2005), pp. 283–307. DOI: 10.1016/j.pecs.2005.07.001 (cit. on pp. 2, 4).

[8] A. D. of Environmental Quality. *Nitrogen Oxide Pollution*. URL: https://azdeq.gov/nitrogen-oxide-nox-pollution#:~:text=The%20nitrogen%20oxides%20family%20can,disease%2C%20leading%20to%20premature%20death. (cit. on p. 2).

[9] R. D. Reitz et al. "IJER editorial: The future of the internal combustion engine". *International Journal of Engine Research* 21.(1) (2020), pp. 3–10. DOI: 10.1177/1468087419877990. URL: https://doi.org/10.1177/1468087419877990 (cit. on pp. 2, 3).

[10] European Commission. *An european strategy for low-emission mobility*. URL: https://ec.europa.eu/clima/policies/transport_en#tab-0-0 (cit. on p. 2).

[11] E. E. Agency. *Greenhouse Gas Emissions from Transport in Europe*. URL: https://www.eea.europa.eu/ims/greenhouse-gas-emissions-from-transport (cit. on p. 2).

[12] United States Environmental Protection Agency. *Greenhouse gas emissions from a typical passenger vehicle*. URL: https://www.epa.gov/greenvehicles/greenhouse-gas-emissions-typical-passenger-vehicle (cit. on p. 3).

[13] E. E. Agency. *Nitrogen Oxides Emissions*. URL: https://www.eea.europa.eu/data-and-maps/indicators/eea-32-nitrogen-oxides-nox-emissions-1/assessment.2010-08-19.0140149032-3 (cit. on p. 3).

[14] R. Babayev, A. Andersson, A. Dalmau, H. Im, and B. Johansson. "Computational optimization of a hydrogen direct-injection compression-ignition engine for jet mixing dominated nonpremixed combustion". *International Journal of Engine Research* 23.(5) (Dec. 2021), pp. 754–768. DOI: 10.1177/14680874211053556 (cit. on p. 3).

[15] M. S. Wooldridge, R. Singh, L. G. Gutierrez, and S. Clancy. "Survey of strategies to reduce cold-start particulate, CO, NOx,and hydrocarbon emissions from direct-injection spark-ignition engines". *International Journal of Engine Research* (2022). DOI: 10.1177/14680874211068576. URL: https://doi.org/10.1177/14680874211068576 (cit. on p. 3).

[16] J. V. Pastor, J. M. García-Oliver, C. Micó, and A. Garcia. "An experimental study with renewable fuels using ECN spray A and D nozzles". *International Journal of Engine Research* (July 2021), p. 146808742110312. DOI: 10.1177/14680874211031200 (cit. on p. 3).

[17] S. Bouzalakos and M. Maroto-Valer. "Overview of carbon dioxide (CO2) capture and storage technology". In: vol. 2. June 2010, pp. 1–24. ISBN: 1 84569 533 X. DOI: 10.1533/9781845699574.1 (cit. on p. 3).

[18] X. Li, Z. Peng, T. Ajmal, A. Aitouche, R. Mobasheri, Y. Pei, B. Gao, and M. Wellers. "A feasibility study of implementation of oxy-fuel combustion on a practical diesel engine at the economical oxygen-fuel ratios by computer simulation". *Advances in Mechanical Engineering* 12 (Dec. 2020), p. 168781402098018. DOI: 10.1177/1687814020980182 (cit. on p. 4).

[19] M. Kanniche, R. Gros-Bonnivard, P. Jaud, J. Valle-Marcos, J.-M. Amann, and C. Bouallou. "Pre-combustion, Post-combustion and Oxy-combustion in thermal power plant for CO capture". *Applied Thermal Engineering* 30 (Jan. 2010), pp. 53–62. DOI: 10.1016/j.applthermaleng.2009.05.005 (cit. on p. 4).

[20] M. Pamminger, W. Buyu, C. Hall, R. Vojtech, and T. Wallner. "The impact of water injection and exhaust gas recirculation on combustion and emissions in a heavy-duty compression ignition engine operated on diesel and gasoline". *International Journal of Engine Research* 21 (Jan. 2019), pp. 1555–1573. DOI: 10.1177/1468087418815290 (cit. on pp. 4, 17).

[21] R. Mobasheri and S. Khabbaz. "Modeling the Effects of High EGR Rates in Conjunction with Optimum Multiple Injection Techniques in a Heavy Duty DI Diesel Engine". *SAE Technical Papers* 1 (Apr. 2014). DOI: 10.4271/2014-01-1124 (cit. on pp. 4, 17).

[22] A. Simpson and A. Simon. "Second law comparison of oxy-fuel combustion and post-combustion carbon dioxide separation". *Energy Conversion and Management* 48 (Nov. 2007), pp. 3034–3045. DOI: 10.1016/j.enconman.2007.06.047 (cit. on p. 4).

[23] C. N. del Medio Ambiente CONAMA 10. *CAPTURA Y ALMACENAMIENTO DE CO_2*. URL: http://www.conama10.conama.org/conama10/download/files/GTs\%202010/2_final.pdf (cit. on p. 4).

[24] E. Portillo, B. Alonso-Fariñas, F. Vega, M. Cano, and B. Navarrete. "Alternatives for oxygen-selective membrane systems and their integration into the oxy-fuel combustion process: A review". *Separation and Purification Technology* 229 (June 2019), p. 115708. DOI: 10.1016/j.seppur.2019.115708 (cit. on pp. 4, 5, 22).

[25] A. Escudero, S. Espatolero, and L. Romeo. "Oxy-combustion power plant integration in an oil refinery to reduce CO_2 emissions". *International Journal of Greenhouse Gas Control* 45 (Feb. 2016), pp. 118–129. DOI: 10.1016/j.ijggc.2015.12.018 (cit. on pp. 4, 16).

[26] X. Wei, V. Manovic, and D. Hanak. "Techno-economic assessment of coal-or biomass-fired oxy-combustion power plants with supercritical carbon dioxide cycle". *Energy Conversion and Management* 221 (July 2020), p. 113143. DOI: 10.1016/j.enconman.2020.113143 (cit. on p. 4).

[27] F. Carrasco Maldonado, R. Spörl, K. Fleiger, V. Hoenig, J. Maier, and G. Scheffknecht. "Oxy-fuel combustion technology for cement production - State of the art research and technology development". *International Journal of Greenhouse Gas Control* 45 (Feb. 2016), pp. 189–199. DOI: 10.1016/j.ijggc.2015.12.014 (cit. on pp. 4, 16).

[28] A. Leo, S. Liu, and J. Costa. "Development of mixed conducting membranes for clean coal energy delivery". *International Journal of Greenhouse Gas Control* 3 (July 2009), pp. 357–367. DOI: 10.1016/j.ijggc.2008.11.003 (cit. on p. 5).

[29] S. Hashim, A. Mohamed, and S. Bhatia. "Oxygen separation from air using ceramic-based membrane technology for sustainable fuel production and power generation". *Renewable and Sustainable Energy Reviews* 15 (Feb. 2011), pp. 1284–1293. DOI: 10.1016/j.rser.2010.10.002 (cit. on p. 5).

[30] R. Kriegel, L. Kiesel, R Kircheisen, and U Pippardt. "Performance of various Archetypes of Oxygen Membranes for local Oxygen Supply." In: *DKG-Jahrestagung, 10. München*. Apr. 2018, p. 10. DOI: 10.13140/RG.2.2.16996.83842 (cit. on p. 5).

[31] F. Wu, M. Argyle, P. Dellenback, and M. Fan. "Progress in O_2 separation for oxy-fuel combustion–A promising way for cost-effective CO_2 capture: A review". *Progress in Energy and Combustion Science* 67 (July 2018), pp. 188–205. DOI: 10.1016/j.pecs.2018.01.004 (cit. on pp. 5, 23).

[32] A. Arratibel, A. Labella, Y. Liu, N. Porras, D. Tanaka, M. Annaland, and F. Gallucci. "Mixed Ionic-Electronic Conducting Membranes (MIEC) for Their Application in Membrane Reactors: A Review". *Processes* 7 (Mar. 2019), p. 128. DOI: 10.3390/pr7030128 (cit. on p. 5).

[33] X. Li, Z. Peng, Y. Pei, T. Ajmal, K. Rana, A. Aitouche, and R. Mobasheri. "Oxy-fuel combustion for carbon capture and storage in internal combustion engines – A review". *International Journal of Energy Research* 46 (Aug. 2021), pp. 505–522. DOI: 10.1002/er.7199 (cit. on pp. 5, 16, 18, 21).

[34] X. Li, Y. Pei, Z. Peng, T. Ajmal, K.-J. Rana, A. Aitouche, and R. Mobasheri. "Numerical study on the effects of intake charge on oxy-fuel combustion in a dual-injection spark ignition engine at economical oxygen-fuel ratios". *International Journal of Engine Research* 23 (May 2021). DOI: 10.1177/14680874211022292 (cit. on pp. 5, 18).

[35] A. Van Blarigan, D. Kozarac, R. Seiser, R. Cattolica, J.-Y. Chen, and R. Dibble. "Experimental Study of Methane Fuel Oxycombustion in a Spark-Ignited Engine". *Journal of Energy Resources Technology* 136 (Mar. 2013), p. 9. DOI: 10.1115/1.4024974 (cit. on pp. 5, 18, 46).

[36] Z. Wu, Z. Kang, D. Jun, H. Zongjie, and L. Li. "Effect of oxygen content on n-heptane auto-ignition characteristics in a HCCI engine". *Applied Energy* 184 (Dec. 2016). DOI: 10.1016/j.apenergy.2016.10.050 (cit. on p. 5).

[37] H.-W. Wu, R.-H. Wang, Y.-C. Chen, D.-J. Ou, and T.-Y. Chen. "Influence of port-inducted ethanol or gasoline on combustion and emission of a closed cycle diesel engine". *Energy* 64 (Jan. 2013). DOI: 10.1016/j.energy.2013.11.027 (cit. on pp. 5, 20, 21, 25).

[38] Y. Gao, L. Li, X. Yu, J. Deng, and Z. Wu. "Effect of Compression Ratio on Internal Combustion Rankine Cycle Based on Simulations". In: vol. 328. Jan. 2015, pp. 129–138. ISBN: 978-3-662-45042-0. DOI: 10.1007/978-3-662-45043-7_14 (cit. on p. 5).

[39] Z. Kang, S. Chen, Z. Wu, J. Deng, Z. Hu, and L. Li. "Simulation Study of Water Injection Strategy in Improving Cycle Efficiency Based on a Novel Compression Ignition Oxy-Fuel Combustion Engine". *SAE International Journal of Engines* 11 (Apr. 2018). DOI: 10.4271/2018-01-0894 (cit. on pp. 5, 20, 21, 46).

[40] R. Bilger and Z. Wu. "Carbon Capture for Automobiles Using Internal Combustion Rankine Cycle Engines". *Journal of Engineering for Gas Turbines and Power* 131 (May 2009), p. 034502. DOI: 10.1115/1.3077657 (cit. on pp. 5, 21, 25).

[41] B. Abraham, J. Asbury, E. Lynch, and A. Teotia. "Coal-Oxygen Process Provides CO_2 for Enhanced Recovery". *Oil and Gas Journal* 80 (Jan. 1982) (cit. on p. 16).

[42] D. Hanak, D. Powell, and V. Manovic. "Techno-economic analysis of oxy-combustion coal-fired power plant with cryogenic oxygen storage". *Applied Energy* 191 (Jan. 2017), 193–203. DOI: 10.1016/j.apenergy.2017.01.049 (cit. on p. 16).

[43] N. Kimura, K. Omata, T. Kiga, S. Takano, and S. Shikisima. "The characteristics of pulverized coal combustion in O_2/CO_2 mixtures for CO_2 recovery". *Energy Conversion and Management* 36 (Jan. 1996), pp. 805–808. DOI: 10.1016/0196-8904(95)00126-X (cit. on p. 16).

[44] W. Sanz, H. Jericha, B. Bauer, and E. Göttlich. "Qualitative and Quantitative Comparison of Two Promising Oxy-Fuel Power Cycles for CO_2 Capture". *Journal of Engineering for Gas Turbines and Power-transactions of The Asme - J ENG GAS TURB POWER-T ASME* 130 (May 2008). DOI: 10.1115/1.2800350 (cit. on p. 16).

[45] O. Biyiklioğlu and M. Tat. "Tribological assessment of NiCr, Al_2O_3/TiO_2 , and Cr_3C_2/NiCr coatings applied on a cylinder liner of a heavy-duty diesel engine". *International Journal of Engine Research* (July 2020), p. 146808742093016. DOI: 10.1177/1468087420930164 (cit. on p. 16).

[46] J. Guo, Z. Liu, X. Huang, T. Zhang, W. Luo, F. Hu, P. Li, and C. Zheng. "Experimental and numerical investigations on oxy-coal combustion in a 35MW large pilot boiler". *Fuel* 187 (2017), pp. 315–327. ISSN: 0016-2361. DOI: https://doi.org/10.1016/j.fuel.2016.09.070 (cit. on p. 16).

[47] F. Hu, P. Li, W. Li, C. Ding, J. Guo, and Z. Liu. "Experimental and kinetic study of NO-reburning by syngas under high CO2 concentration in a jet stirred reactor". *Fuel* 304 (2021), p. 121403. ISSN: 0016-2361. DOI: https://doi.org/10.1016/j.fuel.2021.121403 (cit. on p. 17).

[48] S. Yan, Q. Liu, Y. Shao, and W. Zhong. "Energy and exergy analysis of oxy-fuel combustion based on circulating fluidized bed power plant firing coal, lignite and biomass". *Fuel* 269 (June 2020), p. 117424. DOI: 10.1016/j.fuel.2020.117424 (cit. on p. 17).

[49] C. Ye, Z. Ye, Z. Zhu, and Q. Wang. "Thermodynamic and Economic Analysis of Oxy-Fuel-Integrated Coal Partial Gasification Combined Cycle". *ACS Omega* XXXX (Feb. 2021). DOI: 10.1021/acsomega.0c05277 (cit. on p. 17).

[50] I. Mohsin, T. Al-Attas, K. Sumon, J. Bergerson, S. McCoy, and M. Kibria. "Economic and Environmental Assessment of Integrated Carbon Capture and Utilization". *Cell Reports Physical Science* 1 (July 2020), p. 100104. DOI: 10.1016/j.xcrp.2020.100104 (cit. on pp. 17, 25).

[51] L. Cai, L. Tan, Y. Liang, X. Yin, C. Liu, and Y. Guan. "Numerical study on sulfur-bearing natural gas oxy-fuel combustion power plant". *Applied Thermal Engineering* 196 (July 2021), p. 117292. DOI: 10.1016/j.applthermaleng.2021.117292 (cit. on p. 17).

[52] Y. Liang, L. Cai, Y. Guan, W. Liu, Y. Xiang, J. Li, and T. He. "Numerical study on an original oxy-fuel combustion power plant with efficient utilization of flue gas waste heat". *Energy* 193 (Dec. 2019), p. 116854. DOI: 10.1016/j.energy.2019.116854 (cit. on p. 17).

[53] J. Alvarez, A. Sleiti, W. Al-Ammari, and E. Fernández. "Study of recirculating water-based and carbon-based working fluids on the combustion flow field and the cycle performances of semi-CO2-capturing Brayton-derived cycles". *Applied Thermal Engineering* 218 (Sept. 2022), p. 119296. DOI: 10.1016/j.applthermaleng.2022.119296 (cit. on p. 17).

[54] S. Yadav and S. Mondal. "A review on the progress and prospects of oxy-fuel carbon capture and sequestration (CCS) technology". *Fuel* 308 (2022), p. 122057. ISSN: 0016-2361. DOI: https://doi.org/10.1016/j.fuel.2021.122057. URL: https://www.sciencedirect.com/science/article/pii/S0016236121019335 (cit. on p. 18).

[55] S. Yadav and S. Mondal. "Numerical investigation of 660 MW pulverized coal-fired supercritical power plant retrofitted to oxy-coal combustion". *International Journal of Greenhouse Gas Control* 105 (2021), p. 103227. ISSN: 1750-5836. DOI: https://doi.org/10.1016/

j.ijggc.2020.103227. URL: https://www.sciencedirect.com/science/article/pii/S1750583620306526 (cit. on p. 18).

[56] A. Osman. "Feasibility Study of a Novel Combustion Cycle Involving Oxygen and Water". *SAE Technical Papers* (Nov. 2009), p. 14. DOI: 10.4271/2009-01-2808 (cit. on pp. 18, 46).

[57] J. R. Serrano, J. Martín, J. Gomez-Soriano, and R. Raggi. "Theoretical and experimental evaluation of the spark-ignition premixed oxy-fuel combustion concept for future CO2 captive powerplants". *Energy Conversion and Management* 244 (Sept. 2021), p. 114498. DOI: 10.1016/j.enconman.2021.114498 (cit. on pp. 18, 19).

[58] J. R. Serrano, G. Bracho, J. Gomez-Soriano, and C. Fernandes. "Development of an oxy-fuel combustion system in a compression-ignition engine for ultra-low emissions powerplants Using CFD and evolutionary algorithms". *Applied Sciences* 12.(14) (2022). ISSN: 2076-3417. DOI: 10.3390/app12147104. URL: https://www.mdpi.com/2076-3417/12/14/7104 (cit. on pp. 18, 71, 73, 78).

[59] R. Mobasheri, A. Abdel, Z. Peng, and X. Li. "A Numerical Study of the Effects of Oxy-Fuel Combustion under Homogeneous Charge Compression Ignition". *International Journal of Engine Research* (Feb. 2021). DOI: 10.1177/1468087421993359 (cit. on p. 19).

[60] T. Sharma, A. Rao, and M. K. "Homogeneous Charge Compression Ignition (HCCI) Engines: A Review". *Archives of Computational Methods in Engineering* 23 (May 2015). DOI: 10.1007/s11831-015-9153-0 (cit. on pp. 19, 46).

[61] R. Mobasheri, A. Aitouche, Z. Peng, and X. Li. "Influence of Oxy-Fuel Combustion on Engine Operating Conditions and Combustion Characteristics in a High Speed Direct Injection (HSDI) Diesel Engine under Homogenous Charge Compression Ignition (HCCI) Mode". In: *SAE Technical Paper*. WCX SAE World Congress Experience, Apr. 2020, p. 10. DOI: 10.4271/2020-01-1138 (cit. on pp. 19, 46).

[62] A. Mohammed, A. Elkhazraji, S. Jan, and B. Johansson. "A Study on the Performance and Emissions of HCCI Oxy-Fuel Combustion in a CFR Engine with Recirculated Carbon Dioxide". In: *SAE Powertrains, Fuels and Lubricants Meeting*. Sept. 2020, p. 13. DOI: 10.4271/2020-01-2065 (cit. on pp. 20, 46).

[63] Z. Kang, Z. Wu, Z. Zhang, J. Deng, Z. Hu, and L. Li. "Study of the Combustion Characteristics of a HCCI Engine Coupled with Oxy-Fuel Combustion Mode". *SAE International Journal of Engines* 10 (Mar. 2017). DOI: 10.4271/2017-01-0649 (cit. on p. 20).

[64] J. Hawley, G. Reader, M. Zheng, I. Potter, and O. Frauvel. "Investigations on Carbon Dioxide/Oxygen Breathing Diesel Engines—Results from an International Collaborative Project". *Underwater Technology: The International Journal of The Society for Underwater* 23 (Dec. 1998), pp. 109–121. DOI: 10.3723/175605498783259218 (cit. on p. 20).

[65] J Hawley, S Ashcroft, and M Patrick. "The Effects of Non-Air Mixtures on the Operation of a Diesel Engine by Experiment and by Simulation". *Proceedings of The Institution of Mechanical Engineers Part A-journal of Power and Energy - PROC INST MECH ENG A-J POWER* 212 (Feb. 1998), pp. 55–68. DOI: 10.1243/0957650981536691 (cit. on p. 20).

[66] Q. Tan and Y. Hu. "A study on the combustion and emission performance of diesel engines under different proportions of O2-N2-CO2". *Applied Thermal Engineering* 108 (July 2016). DOI: 10.1016/j.applthermaleng.2016.07.151 (cit. on p. 20).

[67] H.-W. Wu and C.-T. Shu. "Effects of operating parameters on steady and transient behaviors of a closed cycle diesel engine". *Energy Conversion and Management - ENERG CONV MANAGE* 47 (Sept. 2006), pp. 2070–2080. DOI: 10.1016/j.enconman.2005.12.023 (cit. on p. 21).

[68] Z. Wu, X. Yu, L. Fu, J. Deng, and L. Li. "Experimental study of the effect of water injection on the cycle performance of an internal-combustion Rankine cycle engine". *Proceedings of the Institution of Mechanical Engineers, Part D: Journal of Automobile Engineering* 228 (Mar. 2014), pp. 580–588. DOI: 10.1177/0954407013511069 (cit. on pp. 21, 25).

[69] X. Yu, Z. Wu, L. Fu, J. Deng, Z. Hu, and L. Li. "Study of Combustion Characteristics of a Quasi Internal Combustion Rankine Cycle Engine". *SAE Technical Papers* 11 (Oct. 2013). DOI: 10.4271/2013-01-2698 (cit. on p. 21).

[70] S. Zhu, B. Hu, S. Akehurst, C. Copeland, A. Lewis, H. Yuan, I. Kennedy, J. Bernards, and C. Branney. "A review of water injection applied on the internal combustion engine". *Energy Conversion and Management* 184 (Mar. 2019), pp. 139–158. DOI: 10.1016/j.enconman.2019.01.042 (cit. on p. 21).

[71] G. D. Perry R. *Perry's chemical engineers's handbook eighth edition.* McGraw-Hill, 2008 (cit. on pp. 21, 58, 113, 125).

[72] Z. Kang, S. Feng, Y. Lv, J. Wu, and Z. Wu. "Effect of direct water injection temperature on combustion process and thermal efficiency within compression ignition internal combustion Rankine engine". *Case Studies in Thermal Engineering* 28 (Oct. 2021), p. 101592. DOI: 10.1016/j.csite.2021.101592 (cit. on p. 21).

[73] S. Engels, F. Beggel, M. Michael, and H. Stadler. "Simulation of a membrane unit for oxyfuel power plants under consideration of realistic BSCF membrane properties". *Journal of Membrane Science - J MEMBRANE SCI* 359 (Sept. 2010), pp. 93–101. DOI: 10.1016/j.memsci.2010.01.048 (cit. on p. 22).

[74] D. Catalán Martínez, M. Santafé-Moros, J. Gozálvez-Zafrilla, J. García Fayos, and J. Serra. "Characterization of oxygen transport phenomena on BSCF membranes assisted by fluid dynamic simulations including surface exchange". *Chemical Engineering Journal* 387 (May 2020), p. 124069. DOI: 10.1016/j.cej.2020.124069 (cit. on pp. 22, 24, 40, 41, 70).

[75] F. Gutiérrez, L. García-Cuevas, and W. Sanz. "Comparison of cryogenic and membrane oxygen production implemented in the Graz cycle". *Energy Conversion and Management* 271 (Nov. 2022), p. 116325. DOI: 10.1016/j.enconman.2022.116325 (cit. on p. 22).

[76] J. Serrano, F. Arnau, L. García-Cuevas, and F. Gutiérrez. "Thermoeconomic analysis of an oxygen production plant powered by an innovative energy recovery system". *Energy* 255 (June 2022), p. 124419. DOI: 10.1016/j.energy.2022.124419 (cit. on p. 22).

[77] P. Lemes, G. Garcia, R. Machado, D. Hotza, and J. Costa. "Current Developments of Mixed Conducting Membranes on Porous Substrates". *Materials Research* 17 (Dec. 2012). DOI: 10.1590/S1516-14392013005000175 (cit. on p. 23).

[78] Z. Shao, G. Xiong, J. Tong, H. Dong, and W. Yang. "Ba effect in doped $SrCo_{0.8}Fe_{0.2}O_{3-\delta}$ on the phase structure and oxygen permeation properties of the dense ceramic membranes". *Separation and Purification Technology - SEP PURIF TECHNOL* 25 (Oct. 2001), pp. 419–429. DOI: 10.1016/S1383-5866(01)00071-5 (cit. on p. 23).

[79] Y. Teraoka, H.-M. Zhang, S. Furukawa, and N. Yamazoe. "Oxygen Permeation Through Perovskite-Type Oxides". *Chemistry Letters - CHEM LETT* 11 (Nov. 1985), pp. 1743–1746. DOI: 10.1246/cl.1985.1743 (cit. on p. 23).

[80] S. Baumann, J. Serra, M. Lobera, S. Escolástico, F. Schulze-Kuppers, and W. Meulenberg. "Ultrahigh Oxygen Permeation Flux Through Supported $Ba_0 \cdot {}_5Sr_0 \cdot {}_5Co_0 \cdot {}_8Fe_0 \cdot {}_2O_{3-\delta}$ Membranes". *Journal of Membrane Science* 377 (July 2011), pp. 198–205. DOI: 10.1016/j.memsci.2011.04.050 (cit. on p. 23).

[81] E. Shubnikova and A. Nemudry. "Perovskites Based on SCF and BSCF Oxides and Their Application as Membrane Materials and Electrodes for Solid Oxide Fuel Cells". *Membranes and Membrane Technologies* 3 (Nov. 2021), pp. 377–388. DOI: 10.1134/S251775162106007X (cit. on p. 23).

[82] M. Exter, W. Haije, and J. Vente. "Viability of ITM Technology for Oxygen Production and Oxidation Processes: Material, System, and Process Aspects". *Inorganic Membranes for Energy and Environmental Applications* (Jan. 2009). DOI: 10.1007/978-0-387-34526-0_2 (cit. on p. 23).

[83] M. Balaguer, C. Solís, J. García Fayos, E. Palafox, and J. Serra. "Progress in $Ce_{0.8}Gd_{0.2}O_{2-\delta}$ Protective Layers for Improving the CO_2 Stability of BSCF O2-Transport Membranes". *Sustainable Energy and Fuels* 4 (May 2020), pp. 3747–3752. DOI: 10.1039/D0SE00324G (cit. on p. 24).

[84] C. Solís, F. Toldrá Reig, M. Balaguer, S. Somacescu, J. García Fayos, E. Palafox, and J. Serra. "Mixed Ionic-Electronic Conduction in $NiFe_2O_4$−$Ce_{0.8}Gd_{0.2}O_{2-\delta}$ Nanocomposite Thin Films for Oxygen Separation". *ChemSusChem* 11 (July 2018), pp. 2818–2827. DOI: 10.1002/cssc.201800420 (cit. on p. 24).

[85] F. J. Arnau, R. Novella, L. M. García-Cuevas, and F. A. Gutierrez. "Adapting an internal combustion engine to oxy-fuel combustion with in-situ oxygen production". In: *Internal Combustion Engine Division*

Fall Technical Conference 2021. Oct. 2021, p. 12. DOI: 10.1115/ICEF2021-67707 (cit. on pp. 24, 25).

[86] J. R. Serrano, F. J. Arnau, L. M. García-Cuevas, and F. A. Gutiérrez. "Coupling an oxygen generation cycle with an oxy-fuel combustion spark ignition engine for zero NOx emissions and carbon capture: A feasibility study". *Energy Conversion and Management* 284 (2023), p. 116973. ISSN: 0196-8904. DOI: https://doi.org/10.1016/j.enconman.2023.116973. URL: https://www.sciencedirect.com/science/article/pii/S0196890423003199 (cit. on p. 24).

[87] S. Sharma and F. Maréchal. "Carbon Dioxide Capture From Internal Combustion Engine Exhaust Using Temperature Swing Adsorption". *Frontiers in Energy Research* 7 (Dec. 2019), p. 143. DOI: 10.3389/fenrg.2019.00143 (cit. on p. 25).

[88] S. Valluri, V. Claremboux, and S. Kawatra. "Opportunities and challenges in CO2 utilization". *Journal of Environmental Sciences* 113 (2022), pp. 322–344. ISSN: 1001-0742. DOI: https://doi.org/10.1016/j.jes.2021.05.043. URL: https://www.sciencedirect.com/science/article/pii/S1001074221002217 (cit. on p. 25).

[89] O. Bushuyev, P. Luna, C. T. Dinh, L. Tao, G. Saur, J. Lagemaat, S. Kelley, and E. Sargent. "What Should We Make with CO_2 and How Can We Make It?" *Joule* 2 (Mar. 2018). DOI: 10.1016/j.joule.2017.09.003 (cit. on p. 25).

[90] Z. Wu, X. Yu, L. Fu, J. Deng, Z.-J. Hu, and L. Li. "A high efficiency oxyfuel internal combustion engine cycle with water direct injection for waste heat recovery". *Energy* 70 (June 2014). DOI: 10.1016/j.energy.2014.03.095 (cit. on p. 25).

[91] S. T. Munkejord, M. Hammer, and S. Løvseth. "CO2 transport: data and models – A review". *Applied Energy* 169 (May 2016), 499–523. DOI: 10.1016/j.apenergy.2016.01.100 (cit. on p. 26).

[92] O. Redlich and J Kwong. "On the Thermodynamics of Solutions: An Equation of State, Fugacities of Gaseous Solutions". *Chemical Reviews* 44 (Mar. 1949), pp. 233–44. DOI: 10.1021/cr60137a013 (cit. on p. 26).

[93] G. Soave. "Equilibrium Constants From a Modified Redlich-Kwong Equation of State". *Chemical Engineering Science* 27 (June 1972), pp. 1197–1203. DOI: 10.1016/0009-2509(72)80096-4 (cit. on p. 26).

[94] D. Peng and D. Robinson. "New Two-Constant Equation of State". *Industrial and Engineering Chemistry Fundamentals* 15 (Feb. 1976). DOI: 10.1021/i160057a011 (cit. on p. 26).

[95] H. Li, J. Jakobsen, O. Wilhelmsen, and J. Yan. "PVTxy properties of CO2 mixtures relevant for CO2 capture, transport and storage: Review of available experimental data and theoretical models". *Applied Energy* 88 (Apr. 2013), pp. 3567–3579. DOI: 10.1016/j.apenergy.2011.03.052 (cit. on p. 26).

[96] M. D. Bermejo and M. J. Cocero. "Supercritical water oxidation: a technical review". *American Institute of Chemical Engineers Journal* 52.(11) (2006), pp. 3933–3951. DOI: https://doi.org/10.1002/aic.10993. URL: https://aiche.onlinelibrary.wiley.com/doi/abs/10.1002/aic.10993 (cit. on p. 26).

[97] F. Mangold, S. Pilz, S. Bjelic, and F. Vogel. "Equation of state and thermodynamic properties for mixtures of H2O, O2, N2, and CO2 from ambient up to 1000 K and 280 MPa". *The Journal of Supercritical Fluids* 153 (Mar. 2019), p. 104476. DOI: 10.1016/j.supflu.2019.02.016 (cit. on pp. 26, 27).

[98] J. M. Smith, H. C. Van Ness, M. M. Abbott, and M. T. Swihart. *Introduction to chemical engineering thermodynamics*. Harvard, 2018 (cit. on pp. 26, 27).

[99] P. M. Mathias. "A versatile phase equilibrium equation of state". *Industrial & Engineering Chemistry Process Design and Development* 22.(3) (1983), pp. 385–391. DOI: 10.1021/i200022a008. URL: https://doi.org/10.1021/i200022a008 (cit. on p. 27).

[100] S. I. Sandler. *Chemical, biochemical and engineering thermodynamics*. Harvard, 2016 (cit. on pp. 28, 96).

[101] F. J. Arnau, J. Benajes, J. M. Desantes, J. R. Serrano, J. M. Serra, D. Catalán-Martínez, and L. M. García-Cuevas. *Motor de combustión interna de hidrocarburos auto transportable que no emite gases nocivos ni CO_2; secuestra CO_2 atmosférico y fabrica CO_2 líquido subcrítico*. P201930285. Mar. 2019 (cit. on pp. 40, 43, 44, 71).

[102] J. Martín, F. Arnau, P. Piqueras, and A. Auñón. "Development of an Integrated Virtual Engine Model to Simulate New Standard Testing Cycles". *SAE Technical Papers* 2018-April (2018). DOI: 10.4271/2018-01-1413 (cit. on p. 40).

[103] F. Payri, F. J. Arnau, P. Piqueras, and M. Ruiz. "Lumped Approach for Flow-Through and Wall-Flow Monolithic Reactors Modelling for Real-Time Automotive Applications". In: *SAE International*. Apr. 2018. DOI: 10.4271/2018-01-0954 (cit. on p. 41).

[104] D. T. Guide. *Engine Emission Control*. URL: https://dieselnet.com/tech/engine_emission-control.php (cit. on p. 46).

[105] B. N.C. *Fundamentals of turbocharging*. Concepts NREC, 2005 (cit. on p. 47).

[106] J. Arrègle, J. J. López, J. M. García, and C. Fenollosa. "Development of a Zero-Dimensional Diesel Combustion Model. Part 1: Analysis of the Quasi-Steady Diffusion Combustion Phase". *Applied Thermal Engineering* 23.(11) (11 2003), pp. 1301–1317. ISSN: 13594311. DOI: 10.1016/S1359-4311(03)00079-6 (cit. on pp. 71, 73).

[107] J. Arrègle, J. J. López, J. M. García, and C. Fenollosa. "Development of a Zero-Dimensional Diesel combustion Model: Part 2: Analysis of the Transient Initial and Final Diffusion Combustion Phases". *Applied Thermal Engineering* 23.(11) (11 2003), pp. 1319–1331. ISSN: 13594311. DOI: 10.1016/S1359-4311(03)00080-2 (cit. on pp. 71, 73).

[108] J. Arrègle, J. J. López, J. Martín, and E. M. Mocholí. "Development of a Mixing and Combustion Zero-Dimensional Model for Diesel Engines". *SAE Technical Papers* (2006), p. 1381. ISSN: 26883627. DOI: 10.4271/2006-01-1382 (cit. on pp. 71, 73).

[109] J. Serrano, J. Lopez, J. Martín, and G. Bracho. "Extension of a Zero-Dimensional Mixing-Controlled Combustion Model for the Development of a NOx–Free System Based on the Oxy-Combustion Concept". *Johnson Matthey Technology Review* (Jan. 2023). DOI: 10.1595/205651324X16963284171824 (cit. on pp. 73, 74, 135).

[110] L. Hailong. "Thermodynamic properties of CO2 mixtures and their applications in advanced power cycles with CO2 capture processes". PhD thesis. Stockholm, Sweden: Royal Institute of Technology, Jan. 2008 (cit. on p. 95).

[111] B. Metz, O. Davidson, H. de Coninck, M. Loos, and L. Meyer. "IPCC special report on carbon dioxide capture and storage". *Policy Stud.* (Jan. 2005) (cit. on p. 95).

[112] S. Westman, J. Stang, S. Løvseth, A. Austegard, I. Snustad, and I. Ertesvåg. "Vapor-liquid equilibrium data for the carbon dioxide and oxygen (CO2 + O2) system at the temperatures 218, 233, 253, 273, 288 and 298 K and pressures up to 14 MPa". *Fluid Phase Equilibria* 421 (Apr. 2016), pp. 67–87. DOI: 10.1016/j.fluid.2016.04.002 (cit. on p. 97).

[113] R. W. Kugel. "Raoult's Law: Binary Liquid-Vapor Phase Diagrams: A Simple Physical Chemistry Experiment". *Journal of Chemical Education* 75.(9) (1998), p. 1125. DOI: 10.1021/ed075p1125. URL: https://doi.org/10.1021/ed075p1125 (cit. on p. 97).

[114] E. F. Stephan, N. S. Hatfield, R. S. Peoples, and H. A. Pray. "THE SOLUBILITY OF GASES IN WATER AND IN AQUEOUS URANYL SALT SOLUTIONS AT ELEVATED TEMPERATURES AND PRESSURES" (Jan. 1956). URL: https://www.osti.gov/biblio/4379406 (cit. on p. 98).

[115] A Valtz, A. Chapoy, C Coquelet, P Paricaud, and D Richon. "Vapour-liquid equilibria in the carbon dioxide-water system, measurement and modelling from 278.2 to 318.2K". English. *Fluid Phase Equilibria* 226 (Dec. 2004), pp. 333–344. ISSN: 0378-3812. DOI: doi:10.1016/j.fluid.2004.10.013 (cit. on p. 99).

[116] G. Müller, E. Bender, and G. Maurer. "Das Dampf-Flüssigkeitsgleichgewicht des ternären Systems Ammoniak-Kohlendioxid-Wasser bei hohen Wassergehalten im Bereich zwischen 373 und 473 Kelvin". *Berichte der Bunsengesellschaft für physikalische Chemie* 92.(2) (1988), pp. 148–160. DOI: https://doi.org/10.1002/bbpc.198800036. URL: https://onlinelibrary.wiley.com/doi/abs/10.1002/bbpc.198800036 (cit. on p. 99).

[117] R. E. Sanders. *9 - Accidents involving compressors, hoses, and pumps*. Ed. by R. E. Sanders. Fourth Edition. Butterworth-Heinemann, 2015, pp. 235–267. ISBN: 978-0-12-801425-7. DOI: https://doi.org/10.1016/B978-0-12-801425-7.00009-1. URL: https://www.sciencedirect.com/science/article/pii/B9780128014257000091 (cit. on p. 106).

[118] P. Heinz. *A Practical Guide to Compressor Technology*. John Wiley and Sons, Ltd, 2006. DOI: 10.1002/9780471929789 (cit. on pp. 138, 140).

"You will know the truth, and the truth will set you free."

Jesus Christ.